

**POLARIZED LIGHT APPLICATIONS TOWARDS BIOMEDICAL DIAGNOSIS
AND MONITORING**

A Dissertation

by

CASEY WILLIAM-MUNZ PIRNSTILL

Submitted to the Office of Graduate and Professional Studies of
Texas A&M University
in partial fulfillment of the requirements for the degree of

DOCTOR OF PHILOSOPHY

Chair of Committee, Gerard L. Coté
Committee Members, Javier Jo
Kristen Maitland
Prasad Enjeti

Head of Department, Gerard L. Coté

August 2015

Major Subject: Biomedical Engineering

Copyright 2015 Casey William-Munz Pirstill

ABSTRACT

Utilization of polarized light for improved specificity and sensitivity in disease diagnosis is occurring more often in fields of sensing, measurement, and medical diagnostics. This dissertation focuses on two distinct areas where polarized light is applied in biomedical sensing/monitoring: The first portion of worked reported in this dissertation focuses on addressing several major obstacles that exist prohibiting the use of polarized light as a means of developing an optical based non-invasive polarimetric glucose sensor to improve the quality of life and disease monitoring for millions of people currently afflicted by diabetes mellitus. In this work there are two key areas, which were focused on that require further technical advances for the technology to be realized as a viable solution.

First, *in vivo* studies performed on New Zealand White (NZW) rabbits using a dual-wavelength polarimeter were conducted to allow for performance validation and modeling for predictive glucose measurements accounting for the time delay associated with blood aqueous humor glucose concentrations in addition to overcoming motion induced birefringence utilizing multiple linear regression analysis. Further, feasibility of non-matched index of refraction eye coupling between the system and corneal surface was evaluated using modeling and verified with *in vitro* testing validation. The system was initially modeled followed by construction of the non-matched coupling configuration for testing *in vitro*.

The second half of the dissertation focuses on the use of polarized light microscopy designed, built, and tested as a low-cost high quality cellphone based polarimetric imaging system to aid medical health professionals in improved diagnosis of disease in the clinic and in low-resource settings. Malaria remains a major global health burden and new methods for, low-cost, high-sensitivity diagnosis of malaria are needed particularly in remote low-resource areas throughout the world. Here, a cost effective optical cellphone based transmission polarized light microscope system is presented utilized for imaging the malaria pigment known as hemozoin. Validation testing of the optical

resolution required to provide diagnosis similar to commercial polarized imaging systems will be conducted and the optimal design will be utilized in addition to image processing to improve the diagnostic capability.

DEDICATION

The work described herein is dedicated to my parents David and Rhonda Pirstill for instilling in my brothers and me, at an early age, the value of an education and learning particularly in the area of science and medicine. Additionally, I would like to dedicate the work to my girlfriend Hoangha Dao for her continued support and encouragement through the graduate school process.

ACKNOWLEDGEMENTS

I would like to thank the various people whose support and assistance made the work presented in this dissertation a reality. First, and foremost, I would like to thank my advisor Dr. Gerard Coté for being a great mentor, colleague, and friend during the course of my graduate studies. I could not have asked for a better mentor and advisor. I would also like to acknowledge my committee members contributions in providing useful comments and constructive feedback on my project over the course of my graduate studies. Further, I would like to thank Professor John Hanks for his guidance and support throughout the course of this research. Additionally, I would like to thank my mentor and colleague, Dr. Bilal Malik, for all the advice and mentorship he provided when I started in the Optical Biosensing Laboratory followed my continued collaboration throughout my time at Texas A&M University. I also want to extend my gratitude to the Erwin Thomas III and Dr. Vincent Gresham for providing training and active cooperation in the research described in this dissertation. Thanks also go to my friends, including but not limited to, Drs. Tony Akl, Melodie Benford, Dustin Ritter, Ryan Shelton, and Brian Cummins in addition to Javier Garza, Daniel Grunden, Haley Marks, and Andrea Locke, other lab mates, colleagues, and the department faculty and staff for making my time at Texas A&M University a great experience.

Finally, thanks to my mother and father for their encouragement and to my girlfriend, Hoangha, for their patience and love over the past five years of my studies. I am forever grateful for their love and support.

TABLE OF CONTENTS

	Page
ABSTRACT	ii
DEDICATION	iv
ACKNOWLEDGEMENTS	v
TABLE OF CONTENTS	vi
LIST OF FIGURES.....	x
LIST OF TABLES	xvi
1. INTRODUCTION.....	1
1.1. Noninvasive Glucose Monitoring	1
1.1.1. Diabetes Mellitus: Overview of Pathology and History of Monitoring.....	1
1.1.2. Current Commercial Blood Glucose Monitoring Technologies	4
1.1.3. Optical Approaches for Glucose Monitoring	6
1.1.3.1. Absorption and Scattering Spectroscopy	7
1.1.3.1.1. Near Infrared Absorption and Scattering.....	7
1.1.3.1.2. Raman Spectroscopy	7
1.1.3.2. Photoacoustic Spectroscopy.....	9
1.1.3.3. Optical Coherence Tomography	10
1.1.3.4. Polarimetric Measurements of Aqueous Glucose.....	11
1.2. Polarization Histopathology of Malaria Blood Smears.....	13
1.2.1. Malaria: Overview.....	13
1.2.2. Current Commercial Malaria Diagnostic Techniques.....	14
1.2.2.1. Conventional Brightfield Microscopy	14
1.2.2.2. Rapid Diagnostic Testing Strips	14
1.2.3. Polarized Microscopy for Malaria Diagnosis.....	15
1.2.4. Mobile Phone Microscopy Overview	16
2. POLARIMETRIC GLUCOSE SENSING	19
2.1. Polarized Light Theory.....	20
2.1.1. Fundamentals of Polarized Light	20
2.1.2. Optical Activity and Polarimetry	21
2.1.3. Specific Rotation	23
2.1.4. Optical Rotatory Dispersion and Glucose.....	24
2.1.5. Corneal Birefringence	25
2.1.6. Single Wavelength Polarimeter.....	27
2.1.7. Dual-wavelength Polarimeter.....	29
2.1.8. Polarimetric Faraday Rotation	30
2.1.9. Electric Field Derivation of Experimental Polarimetric Setup	31
2.2. Polarimetric System Design	34

2.2.1.	In Vivo Dual-wavelength Polarimeter	34
2.2.2.	Control System and Signal Acquisition	35
2.2.3.	Faraday Rotators	36
2.2.4.	Eye Coupling Mechanism	37
2.2.5.	Theoretical Description of Overcoming Corneal Birefringence in the Presence of Motion Using Dual-wavelength Optical Polarimetry	39
2.3.	Required Components and Modeling Time Delay for Clinical Use	41
2.3.1.	In Vivo Experiments in Rabbits	41
2.3.2.	Design, Build, and Characterize a High Permeability Ferromagnetic, Air Gapped Magneto-Optic Faraday Rotator	43
2.4.	Materials and Method.....	44
2.4.1.	In Vivo Animal Protocol	44
2.4.2.	Improved Faraday Modulator Design	46
2.5.	Results and Discussion.....	49
2.5.1.	In Vivo Experiments in Rabbits	49
2.5.1.1.	Results Within a Rabbit: On a Single Day.....	50
2.5.1.2.	Results Within Each Rabbit: Across Multiple Days.....	54
2.5.1.3.	Results for All 3 Rabbits: Across Multiple Days.....	55
2.5.2.	Faraday Device Magnetic Field Measurements	57
3.	MODELING OF CORNEAL BIREFRINGENCE	60
3.1.	Introduction	60
3.1.1.	Anterior Chamber of the Eye	63
3.1.2.	Cornea Description.....	64
3.1.3.	Eye Model Parameters	65
3.2.	Non-index Coupling Design Tasks	71
3.2.1.	Develop a Birefringent Eye Model for Non-index Matched Light Coupling Design.....	71
3.2.2.	Test the Eye-Coupling Device	73
3.2.3.	If Needed Develop Alternative Modeling Utilizing Scleral Lens Coupling Approach	73
3.3.	Materials and Methods	74
3.3.1.	Modeling Index-unmatched Coupling of Light	74
3.3.1.1.	Anatomical Constraint Analysis	78
3.3.1.2.	Polarization Analysis of Dual-wavelength System.....	78
3.3.2.	Modeling Scleral Index-matched Coupling of Light	82
3.4.	Results and Discussion.....	82
3.4.1.	Modeling Index-unmatched Coupling of Light Ray Trace Analysis	82
3.4.1.1.	Anatomical Boundary Analysis	85
3.4.1.2.	Polarization Ray Tracing (MATLAB)	86
4.	DUAL-WAVELENGTH POLARIMETER SYSTEM MINIATURIZATION	96
4.1.	System Miniaturization Tasks	97

4.1.1. Design and Build Cart Based Miniaturized Dual-wavelength Polarimetric System	97
4.1.2. Perform In Vitro Testing Using a Birefringent Plastic Cuvette	99
4.2. Materials and Methods	99
4.2.1. High Frequency Modulation with Improved Faraday Rotator Design	99
4.2.2. Miniaturized Optical Polarimeter For Human Use	102
4.3. Results and Discussion.....	104
4.3.1. In Vitro Experiments Using Glucose in Cuvette High Frequency	104
4.3.2. PID Closed-Loop Control Design	107
4.3.2.1. LabVIEW FPGA PID Configuration and Stabilization Testing.....	107
4.3.3. Miniaturized Optical Polarimeter Design.....	108
5. POLARIZED MICROSCOPY FOR CELL-PHONE BASED MALARIA DIAGNOSIS	110
5.1. Introduction	113
5.1.1. Design, Build, and Characterize a Mobile Phone Based Transmission Polarized Imaging Microscope.....	113
5.1.2. Comparison of Design with Traditional Polarized Microscope Using Blood Smears Infected with Malaria.....	114
5.2. Materials and Methods	115
5.2.1. Polarized Light Systems.....	115
5.2.2. Blood Smear Sample Preparation	118
5.2.3. Method for Polarized Light Microscopy Imaging.....	118
5.2.4. Image Analysis	119
5.3. Results and Discussion.....	120
5.3.1. Performance Testing	121
5.3.2. Non-Malaria Polarized Light Comparative Sample Images	123
5.3.3. Brightfield and Polarized Imaging of Malaria	124
6. CONCLUSIONS AND FUTURE WORK.....	128
6.1. Noninvasive Polarimetric Glucose Monitoring Conclusions.....	128
6.1.1. Conclusions In Vivo.....	128
6.1.2. Conclusions Ferrite Core.....	128
6.1.3. Conclusions Eye Modeling	129
6.2. Noninvasive Polarimetric Glucose Monitoring Future Work	130
6.3. Polarization Histopathology of Malaria Blood Smears Conclusions.....	130
6.4. Polarization Histopathology of Malaria Blood Smears Future Work	131
REFERENCES.....	132
APPENDIX A ANIMAL STUDY PROTOCOL.....	162
APPENDIX B AMENDMENTS ANIMAL STUDY PROTOCOL.....	174
APPENDIX C EXCISED CORNEA IBC PROTOCOL	183
APPENDIX D FARADAY ROTATOR DESIGN	207

APPENDIX E PRELIMINARY EYE MODELING DATA	212
APPENDIX F ZEMAX EYE MODELING.....	216
APPENDIX G LABVIEW FPGA CONTROL.....	219

LIST OF FIGURES

	Page
Figure 2.1: An illustration of how un-polarized light becomes linearly polarized through the application of a polarizer.....	21
Figure 2.2: Schematic representation illustrating the different ways glucose forms in solution.	25
Figure 2.3: Illustration of optical rotation of plane-polarized light.....	27
Figure 2.4: CAD model of the <i>in vivo</i> dual-wavelength polarimetric glucose detection system. Note that the rabbit's eye was coupled to the system via the refractive index matching eye coupling device shown after the Faraday modulator (FM).....	30
Figure 2.5: Photograph (left) and CAD model (right) of the eye-coupling device. The glass test tube is filled with PBS solution to allow for index-matched coupling with isolated corneas clamped on the artificial phantom and <i>in vivo</i>	38
Figure 2.6: Photograph of eye coupling device used during <i>in vivo</i> NZW rabbit experiments.....	39
Figure 2.7: (a) CAD dimensions of air-core solenoid modulator and (b) CAD rendering of air-core solenoid device with eight rows of 26 AWG wire wound.	41
Figure 2.8: (a) CAD schematic showing dimensions of the custom-machined ferrite modulator with a C core geometry and (b) CAD rendering of air gapped high permeability rotator design.	41
Figure 2.9: (a) CAD rendering of setup used to measure the polarization rotation; (b) photograph of MOPLM; and (c) dimensional schematic of the ferrite modulator in millimeters.....	48
Figure 2.10: <i>In vivo</i> glucose estimation for a single day using a linear regression model for (a) the individual 532 nm laser, (b) the individual 635 nm laser, and (c) the combined laser wavelengths shown on a Clarke error grid.....	51
Figure 2.11: <i>In vivo</i> time profile of measured and predicted glucose concentrations for an individual rabbit trial.....	51

Figure 2.12 (A) Spectral analysis of the time-based polarimetric feedback signal – Run 1; top: 635-nm feedback, bottom: 532-nm feedback. (B) Run 2; top: 635-nm feedback, bottom: 532-nm feedback.	53
Figure 2.13: <i>In vivo</i> glucose estimation using linear regression (a) with 532 nm wavelength and (b) 635 nm wavelength as well the (c) dual wavelength MLR glucose estimation for all 9 rabbit studies (3 rabbits across 3 separate days) shown on a Clarke error grid	54
Figure 2.14: <i>In vivo</i> glucose prediction within rabbits across multiple days using linear regression model for individual wavelengths (a) 532 nm and (b) 635 nm as well as the (c) dual wavelength data using MLR shown on a Clarke error grid	56
Figure. 2.15: Mean value of each device comparing (a) measured and theoretical change in DC rotation; (b) DC power with rotation; and (c) change in current with frequency.....	57
Figure 3.1: Frequency analysis indicating the common sources of motion artifact caused by the cardiac (3.4 HZ) and respiratory (1.6 Hz) cycles (1) – Reproduced by permission of the author.	62
Figure 3.2: Modeling of the optical path through the anterior chamber of the eye for unmatched refractive indices	72
Figure 3.3: Modeling of the optical path through the anterior chamber of the eye using the new optical coupling method	76
Figure 3.4: CODE V simulation of proposed non-index matched eye-coupling scheme utilizing two 90 degree off-axis parabolic mirrors re-collimating the beam exiting the cornea in addition to a round mirror guiding the entrance beam into the cornea at a specified glancing angle.....	83
Figure 3.5: CODE V simulation of proposed non-index matched eye-coupling scheme utilizing two 90 degree off-axis parabolic mirrors re-collimating the beam exiting the cornea in addition to a round mirror guiding the entrance beam into the cornea at a specified glancing angle with solid fill.....	84
Figure 3.6: CODE V simulation, detector beam profile at the detector for model shown in Figure 3.4 and Figure 3.5	84
Figure 3.7: Theoretical polarization rotation results for a simulated dual-wavelength polarimeter passing through an eye model with parameters comparable to recorded in vivo data.....	86

Figure 3.8: 3D anatomical analysis for proposed non-index matched design configuration utilizing CODE V ray trace exported in CAD format.....	92
Figure 3.9: Theoretical polarization rotation results for a simulated dual-wavelength polarimeter passing through an eye model with parameters comparable to recorded in vivo data.....	93
Figure 3.10: Theoretical eye dimensions for the Navarro model and the two extreme cases reported by Winkler et. al (a) represents the size and spacing of the average eye parameters based on the model produced by Navarro, (b) represents the first extreme case where the two corneal surfaces meet near the temple and nose and, (c) the case discussed by Winkler regarding a large separation between corneal layers at the base of the eye near the temple and nose.....	94
Figure 4.1: (a) SolidWorks model of the caged optical system; left to right are the two lasers (L1 & L2), two polarizers (P1 & P2), two faraday rotators (FR1 & FR2), mirror (M1) and beam combiner (BC), mirror (M2) up to the eye and mirror (M3) to the detection system including crossed polarizer (P3) and detector (D), (b) transparent view of the system with optics, electronics, and eye coupling extension.....	98
Figure 4.2: Computer-aided design of the single-wavelength polarimetric glucose detection system.....	101
Figure 4.3: Compensation voltage as a function of actual glucose concentration for 635nm single-wavelength model from 0 mg/dL–600 mg/dL in increments of 100 mg/dL, first data set for multiple runs over 2 repeated tests collected at different times.	104
Figure 4.4: Predicted glucose concentration as a function of actual glucose concentration for 635nm single-wavelength model from 0 mg/dL–600 mg/dL in increments of 100 mg/dL, model for multiple runs over 2 repeated tests collected at different times.....	105
Figure 4.5: (A) Optics of miniaturized dual-wavelength polarimeter on a mount to hold the device steady in envisioned case	108
Figure 4.6: (A) Azimuth angle measured across three different human corneas mounted for three angles of incidence.....	109
Figure 5.1: Plasmodium falciparum malaria pigment on a thick blood film from a patient with malaria (a) the image was taken using conventional light microscopy (b) image was taken using polarized light microscopy.....	111

Figure 5.2: CAD prototype of the single-lens on-chip polarized biosensor (left) off axis view of the system with optics, cellphone mount for slide based transmission microscopy applications, (middle) side view illustrating LEDs and compartments for polarizers and (right) additional off axis view of the design illustrating the slots for the polarizer sheets.....	112
Figure 5.3: (left) Leica DMLM polarized white light microscope used as reference for comparison in this study; and (right) A microscope lens combination implemented into a 3D-printed fitting to allow similar function to a traditional polarized laboratory microscope.	118
Figure 5.4: USAF resolution target images utilized to determine FOV, resolution, in addition to other optical system parameters with a reference Leica microscope using A.) 20x magnification; and B.) 40x magnification Images.....	121
Figure 5.5: iPhone 5s (left) configuration USAF target image and (right) the calculated derivative for a line spread across Group 7 Element 6.....	122
Figure 5.6: Images of a microscope slide coated with wheat starch acquired using a Leica microscope with a 40X objective with a.) No polarizers present in the imaging plane and b.) With a polarizer and analyzer crossed at 90 degrees in the imaging plane	124
Figure 5.7: Images acquired of mouse malaria strain blood smear using (A) a Leica microscope in non-polarized transmission mode with a 40X magnification objective and (B) the same area of the slide imaged utilizing the iPhone 5s mobile phone based design shown in Figure 5.3b	125
Figure 5.8: Images of a Giemsa stained mouse blood smear using a Leica microscope with a 40X objective and A.) No-polarizers present in the image plane and B.) With a polarizer and analyzer crossed at 90 degrees in the image plane.....	126
Figure D3.1: Oscilloscope recording of (a) ~1 kHz, 1f, modulation signal of the 324 turn ferrite coil and (b) the 2f modulated signal.	210
Figure D3.2: Impedance matched response with both the 324 turn ferrite and 3364 turn air-core using power amplifier polarimetric setup as described in polarized system description.....	211
Figure E1: CODE V simulation of proposed non-index matched eye-coupling scheme (A) utilizing two 90 degree off-axis parabolic mirrors recollimating the beam exiting the cornea in addition to a round mirror guiding the entrance beam into the cornea at a specified glancing angle	

and (B) close-up image of the model illustrating the ray trace change within the cornea and aqueous humor surfaces.	214
Figure E2: CODE V simulation spot ray trace simulation output at the detector for model shown in Figure D1 (A) profile showing repeatable beam shape under 3 mm x 3 mm which is the current size of the detector surface and (B) spot diagram using rays in circular pattern 5x5 rays of red and green beams with the total surface area set to 3 mm x 3 mm the detector area size.	214
Figure E3: 3D anatomical analysis for proposed non-index matched design configuration utilizing CODE V ray trace exported in CAD format. (A) 3D rendering top view of proposed design coupled to eye with facial anatomy included and (B) additional side view of proposed setup illustrating the collimated beam profile for input and output beams.	215
Figure F1: Zemax simulation of proposed non-index matched eye-coupling scheme utilizing two 90 degree off-axis parabolic mirrors re-collimating the beam exiting the cornea in addition to a round mirror guiding the entrance beam into the cornea at a specified glancing angle.	216
Figure F2: Zemax simulation spot ray trace simulation output at the detector for model shown in Figure E1 profile showing repeatable beam shape under 6 mm x 5 mm which is the current size of the detector surface.	217
Figure F3: Zemax simulation of proposed non-index matched eye-coupling scheme utilizing two 90 degree off-axis parabolic mirrors re-collimating the beam exiting the cornea in addition to a round mirror guiding the entrance beam into the cornea at a specified glancing angle where, M1 & M2 are round mirrors; α is glancing angle of input beam; M1-90P & M2-90P are 90 degree off-axis parabolic mirrors; and D is detector.	217
Figure F4: (A) Zemax simulation of proposed non-index matched eye-coupling scheme utilizing two 90 degree off-axis parabolic mirrors re-collimating the beam exiting the cornea in addition to two round mirrors guiding the entrance beam into the cornea at a specified glancing angle and (B) the beam profile at the detector for an optimized setup configuration. Multiple simulation runs were conducted and minimal change in the profile was observed.	218
Figure G1: A screen capture of the block diagram for the FPGA LabVIEW PID controller is illustrated below in addition to the user interface for the VI.	219
Figure G2: (A screen capture of the block diagram for the FPGA LabVIEW PID controller. Area marked with 2 in the image above is used in the VI to	

keep track of the number of iterations that are cycled of the while loop in addition to keeping track of the amount of time the while loop is running.220

Figure G3: (A screen capture of the block diagram for the FPGA LabVIEW PID controller. Sections 4, 5, and 6 in the block diagram represent the PID loop on the FPGA side is illustrated below in addition to the user interface for the VI.....220

Figure G4: (A screen capture of the block diagram for the FPGA LabVIEW PID controller. Section marked 7 in the block diagram. Data collection and output occurs through implementation of a FIFO output methodology.221

Figure G5: A screen capture of the front panel for the FPGA VI.222

Figure G6: A screen capture of the block diagram schematic for the host PC PID control VI.....222

Figure G7: A screen capture of the front panel schematic for the host PC PID control VI.....223

LIST OF TABLES

	Page
Table 3.1: Eye Model Parameters	68
Table 3.2: Eye Model Parameters Navarro	70
Table 3.3: Corneal Retardance Value Range Used in Simulation	70
Table 3.4: Diattenuation Value Range for Simulation	70
Table 3.5: Corneal Diattenuation Parameters.....	81
Table 3.6: Polarization Model Analysis 635nm Wavelength	89
Table 3.7: Polarization Model Analysis 532nm Wavelength	91
Table 4.2: Standard Error for Each Data Set in mg/dL.....	107
Table D3.1: RL Measurements of Faraday Modulation Devices.....	209

1. INTRODUCTION^{*}

Over the past several decades, novel biomedical optical techniques have been implemented for health related applications, providing solutions in various biomedical diagnostic and monitoring applications. While the use of such optical imaging and sensing has led to many breakthroughs in biomedical diagnostic applications, several areas exist that have yet to produce solutions for various disease states. Specifically, two of such areas where optics is currently being applied for biomedical diagnostics and monitoring are glucose sensing and malaria diagnosis. In the work presented in this dissertation, the use of polarized light imaging techniques to determine if it can potentially be useful in these two key areas of medical diagnosis to allow for improved monitoring capabilities.

1.1. Noninvasive Glucose Monitoring

1.1.1. *Diabetes Mellitus: Overview of Pathology and History of Monitoring*

The disease diabetes mellitus is a condition marked by the body's inability to control blood glucose levels. The disease is a chronic systemic disease where the role of hormone insulin is held up resulting in an inability of cells to uptake glucose in a subject (1). Diabetes currently affects over 346 million people worldwide and nearly 29.1 million adults and children in the United States (2, 3). Diabetes and its associated complications rank as the seventh leading cause of death in the United States (2, 3). Based on findings released by the National Institute of Health (NIH), it has been shown that improved glycemic control can significantly reduce the risk of many secondary microvascular-associated complications such as kidney failure, heart disease, gangrene, and blindness (2, 3). It has been shown that education and proper self-management of the disease such as accurate monitoring of blood sugar, healthy eating, and being active, can significantly improve health outcomes and the quality of life in people with diabetes (3). Elevated glucose concentrations give rise to increased passing of glucose in urine and excessive urination. It is from this symptom the disease gets its name, diabetes

* Part of this chapter is reprinted from Pirstill, C.W., Cummins, B., Coté, G.L., and McNichols, R.J., (2014). Glucose Monitoring. Biomedical Photonics Handbook, Second Edition, CRC Press: 47-76 with kind permission of CRC press.

Part of this chapter is reprinted from Pirstill, C.W. and Coté, G.L. "Malaria Diagnosis Using a Mobile Phone Polarized Microscope," Scientific Reports (2015), with kind permission of Nature Publishing Group.

mellitus, where 'diabetes' in Greek means 'a siphon' and 'mellitus' originates from the Greek and Latin word for honey. The increased passing of glucose in urine also later became the first method for diagnosing the condition.

Diabetes mellitus traditionally presents in one of two forms. The two main types of the disease are Type I: insulin-dependent or juvenile diabetes and Type II: non-insulin dependent diabetes mellitus (2, 4, 5). Type I diabetes is often known as juvenile diabetes from the fact that it usually develops in childhood. Type I diabetes occurs in a much smaller percentage of the population as compared to Type II diabetes. Type I diabetes is usually caused by autoimmune destruction of the beta cells, insulin-producing islets of Langerhans, in the pancreas (2, 4, 5). Type II diabetes results from the impairment of insulin secretion and a resistance to insulin action by the body, which is often secondary to obesity (2, 4, 5). Type II is the most common form of diabetes with over 95% of all reported cases being Type II. The disease often occurs later in life around the age of 40. In Type II diabetes, the beta cells remain viable; however, their insulin production is suppressed.

The physiological range of glucose values seen in the normal human body may range from 80 mg/dL to 120 mg/dL and should ideally remain around 100 mg/dL (5.5 mM). In people suffering from diabetes, blood sugar may rise as high as 500 mg/dL. The generally accepted figure of merit for required sensitivity of a useful glucose meter is 10 mg/dL (0.55 mM). However, in each form of diabetes the blood levels vary from the normal range. Blood glucose levels becoming abnormally low is known as hypoglycemia and when the blood glucose level is considerably high, at time as high as 600 mg/dL, the condition is known as hyperglycemia (2, 4, 5). While the course of action is often the same at any level of hyperglycemia the accurate level of hypoglycemia is very important for recommendation of the course of treatment (2, 4, 5).

The Ebers papyrus (1550 B.C.) appears to be the earliest and most comprehensive reference to diabetes as it covers one of the principal associated symptoms, excessive urination. It was not until the second century A.D. that the condition was described in more detail by Aretus of Cappadocia. The word diabetes was first used to describe the

condition by Aretaeus, and his description of the disease focused on increased urination, weight loss, degradation of tissue, and unquenchable thirst. The first known method of diagnosing diabetes mellitus occurred in the second millennium A.D., where “water tasters” tasted a patient’s urine to determine if it had a sweet taste. It was suggested in 1776 by Mathew Dobson, a British physician and chemist, the sweetness in both the blood serum and urine was due to sugar (5-7). This led to urine tasting as an indicator of diabetes throughout the seventeenth and eighteenth centuries (5, 7). Then in 1778 an Englishman by the name of Thomas Cowley was successful in separating saccharine matter from urine in a free state (4). In the early 1800's attention towards diabetes began considering the condition as a metabolic disease and resulted in the conclusion that the development of analytical devices and techniques would allow for reliable glucose monitoring. Initial research into analytical methods for determining glucose measurements can be greatly attributed to work of Cowley, Bernard, Bouchardat, Priestly, Lavoisier, Chevreul, Wöhler, and Benedict (4-6). As noted by prominent French physiologist Claude Bernard in his lecture at the College de France in the late 1800s the three prominent methods used during that time for the detection of glucose included polarimetry, reduction of Cu(II) to Cu(I) by the reduction of sugars, and the development of CO₂ from the fermentation of a glucose-containing solution (7). Although it was known at the time that the reduction of Cu(II) is not specific to glucose, it was this method involving the reduction of Cu(II) to Cu(I) by reducing sugars through the use of Fehling's solution or the closely related Benedict's solution that became the dominant method for analyzing glucose over the next 100 years until the early 1940s.

In 1941, the Ames Division of Miles Laboratories (now known as Bayer), developed a tablet known as the Clinitest®, essentially the Benedict's reagent in the form of a tablet, which could be combined with a few drops of a glucose containing sample such as urine to produce an exothermic reaction resulting in color change (7, 8). This color change could then be compared to a reference sheet for an estimate of the approximate level of glucose within the sample. Then in 1956 Bayer developed a dip-and-read test for glucose in urine known as Clinistix®, which represented the first technology to use

glucose oxidase and peroxidase as opposed to the previous reagents to detect the presence of glucose. Although urine based test strips for determining glucose still exist today, it has been shown that the glucose present in urine is a poor index for blood glucose concentrations (5). Some of the current handheld meters used to date still employ the use of glucose oxidase and peroxidase as discussed later in this chapter. It was this technique that led to the development of the first test strip used for measuring blood glucose by the name Dextrostix®, named after dextrose, developed at Ames by Anton (Tom) Clemens in 1964. The Dextrostix® was designed to be read using a reflectance meter that was called the Ames Reflectance Meter, a departure from previous techniques that relied on the individual to use their eyes to assess a comparison of color change on the test strip to a color scale chart. Due to the expensive price of the device for that period in time (\$400), it was primarily meant for use in a doctor's office but was used by a limited number of patients. Another significant development in 1979 by Ames was the first fingerpick lancet device for simplifying blood sampling in patients call the Ames Autolet®.

1.1.2. Current Commercial Blood Glucose Monitoring Technologies

Many of the home blood glucose monitors currently in use rely on the so-called electro-enzymatic and colorimetric approach to glucose sensing. These methods consists of three basic steps: 1.) the invasive withdrawal of a small blood sample, 2.) the application of the blood sample to a specially formulated "test strip", and 3.) the automated reading of the test strip results via an electrical or optical meter.

Glucose monitor test strips are available from a number of manufacturers and in several varieties. However, many commercially available glucose monitor test strips (be they electro-enzymatic or colorimetric) rely on the quantification of reaction of glucose with the naturally occurring enzyme glucose oxidase (GOx) while some use glucose dehydrogenase because it does not require oxygen. While a number of red-ox reaction based methods for determining the concentration of reducing sugars exists, the specificity afforded by glucose oxidase makes it the standard practiced assay. Glucose oxidase is a protein approximately 160,000 Daltons in size and is composed of two

identical 80 kD sub-units linked by disulfide bonds. Each sub-unit contains one mole of Fe and one mole of flavin-adenine-dinucleotide (FAD). During the oxidation of glucose, the FAD groups become temporarily reduced, thus glucose oxidase is one of the family of flavoenzymes. In the presence of oxygen, reduced glucose oxidase further reacts to drive the reaction to the right. Commercially available colorimetric sensors employ a peroxidase enzyme (commonly horseradish peroxidase) and a red-ox coupled dye pair to generate chromophore concentrations, which are proportional to the amount of hydrogen peroxide produced. One such dye pair is the oxygen acceptor 3-Methyl-2-benzothiazolinone hydrazone plus 3-(dimethylamino) benzoic acid (MBTH-DMAB) which has an absorption peak at 635 nm. Production of hydrogen peroxide by oxidation of glucose and reduction of oxygen drives the peroxidase-catalyzed production of active MBTH-DMAB chromophore and thus results in a measurable increase in absorbance of light at 635 nm. Oxygen acceptor dyes which can also be used include O-dianisidine, Benzidine, and 4-aminoantipyrine and chromotropic acid (AAP-CTA) among others (9).

Optical measurement of the dye product (and hence glucose concentration) is based on the Beer's law increase in absorbance of the dye product. In practice, this increase in absorbance is usually quantified by measuring the attendant decrease in reflectance of the active site on a test strip. The relationship between absorbance and reflectance is described by the Kubelka-Munk equation (see for example, (10)), $K/S = (1-R)^2/2R$ where K is the concentration dependent absorbance, S is a constant related to the scattering coefficient, and R is the measured reflectance.

Practical colorimetric measurement systems typically employ a multi-wavelength detection scheme to increase accuracy and account for variables like the background absorbance of blood, the oxygenation state of blood, and the hematocrit of the blood under test. For the case of the MBTH-DMAB dye pair, the absorbance peak at 635 nm is sharp and absorbance by the dye at 700 nm is negligible. Therefore, a second reflectance measurement at 700 nm affords a correction factor, which accounts for background and sample variations. Since the glucose oxidase reaction is progressive, the timing of measurements is also extremely important. Early measurement systems required that a

timer be started when blood was placed on the strip and that a reading be taken after a specific period (typically 15-60 seconds). Modern systems overcome this inconvenience by taking continuous reflectance measurements as soon as a new test-strip is inserted into the meter. When a drop of blood is placed on the meter, an immediate change in the reflectance signals the start of the reaction and multiple reflectance readings may be taken during the reaction to further increase accuracy or dynamic range of the sensor.

Findings released by the National Institute of Health (NIH) have shown that improved glycemic control can significantly reduce the risk of many secondary microvascular associated complications such as kidney failure, blindness, heart disease, and gangrene (2, 11, 12). Current commercial methods of sensing are invasive, requiring a finger or forearm stick to draw blood each time a reading is needed or by using an implanted sensor for continuous glucose monitoring (CGM). Although, it has been shown that proper education and self-management of the disease can significantly improve health outcomes and the quality of life in people with diabetes (2, 11, 12) these current approaches are painful, cumbersome, embarrassing, and raise concerns about blood borne pathogens. CGMs also require calibration with the finger stick devices one or more times daily. Thus, it is often times difficult to obtain the appropriate motivation and dedication on the part of the patients to commit to an intensive blood sugar monitoring regiment.

1.1.3. Optical Approaches for Glucose Monitoring

Over the past few decades there has also been significant research performed in the development of non-invasive optical methods including: near-infrared (NIR) absorption and scatter spectroscopy (13-17), Raman inelastic scatter spectroscopy (18-20), photoacoustic spectroscopy (PAS) (21, 22), optical coherence tomography (OCT) (23-27), and polarimetry (28-42). While these approaches show promise, all of them have limitations preventing successful realization of a commercial device. The Raman, OCT, NIR absorption and scatter spectroscopy, and PAS based techniques hold some potential but suffer primarily from a lack of glucose specificity (7, 43-46).

1.1.3.1. Absorption and Scattering Spectroscopy

1.1.3.1.1. Near Infrared Absorption and Scattering

Further, near infrared (NIR) absorption spectroscopy and NIR scattering techniques can be confounded by changes in chemical and physical physiological parameters present in blood. NIR spectroscopy suffers from the fact that the glucose absorption band overlaps with the much stronger absorption bands of water, fats, and many other proteins such as hemoglobin present in tissue (7, 43-47). For example, hyperglycemia can lead to increased perfusion because of vasodilation in addition to the potential for accelerated aging of collagen in skin (1, 48, 49).

1.1.3.1.2. Raman Spectroscopy

In addition to NIR absorption and elastic scatter, the optical method known as Raman spectroscopy is an inelastic scattering technique that has been investigated as a method for potentially rapid, precise and accurate analysis of glucose concentration and biochemical composition (50). Raman spectroscopy provides information about the inelastic scattering that occurs when vibrational or rotational energy is exchanged with incident probe radiation. As with infrared spectroscopic techniques, Raman spectra can be utilized to identify molecules such as glucose since these spectra are characteristic of variations in the molecular polarizability and dipole moments. However, in contrast to infrared and near-infrared spectroscopy, Raman spectroscopy has a spectral signature that is less influenced by water. In addition, Raman spectral bands are considerably narrower than those produced in near-infrared spectral experiments are. Raman also has the ability to permit the simultaneous estimation of multiple analytes, requires minimum sample preparation, and would allow for direct sample analysis (i.e. would be on-line) and since different bonds scatter different wavelengths of EM radiation, this method gives quantitative information about the total biochemical composition of a sample, without its destruction. Although these early attempts to employ Raman techniques to directly measure glucose concentration on-line and in aqueous solutions, serum and plasma have met with some success *in vitro* (51-55), efforts to utilize these techniques *in*

in vivo for transcutaneous measurement of whole blood glucose levels have met with considerable difficulty (55, 56). This is partly because whole blood and most tissue are highly absorptive. In addition, most tissues contain many fluorescent and Raman-active confounders (56). As a surrogate to blood glucose measurement, several investigators have suggested using Raman spectroscopy to obtain the glucose signal from the aqueous humor of the eye (56-58). The glucose content of the aqueous humor reflects an age-dependent steady-state value of approximately 70% of that found in blood and the time lag between aqueous humor and blood glucose has been shown to be on the order of minutes. For Raman sensing, the aqueous humor of the eye is relatively non-absorptive and contains much fewer Raman-active molecules than whole blood. However, even though only four or five Raman-active constituents are present in significant concentrations in the aqueous humor, it is still necessary to use both linear and nonlinear multifactor analytical techniques to obtain accurate estimates of glucose concentrations from the total Raman spectrum (56). In addition, as with other tissues, when excited in the near infrared region (700-1300 nm) Raman spectra encounter less fluorescence background. However, although the background fluorescence falls off when excitation is moved to the NIR region, the Raman signal also falls off to the fourth power with wavelength. Thus, unlike the polarization approach through the eye, Raman requires higher power and it remains to be seen if the Raman approach could be measured at laser intensities that can be used safely in the eye. Due to the power required and the associated safety concerns related to the use of Raman for glucose monitoring in the eye this technique has been extended to alternative sensing locations. Due to the low signal to noise associated with traditional Raman techniques *in vivo*, multivariate analyses have been employed that are similar to those used in glucose related NIR spectroscopic approaches (59-61). Alternatively, the Raman effect can be greatly enhanced (by some 10^6 - 10^8 -fold) if the molecules of interest are sufficiently close to a suitably roughened metal surface (i.e. Cu, Ag or Au) (62). This method, called surface-enhanced Raman scattering (SERS), (63, 64) has received much attention within biomedicine (64) and genomics (65). Since the development of reproducible SERS on a silver-coated alumina

substrate by Vo-Dinh and his colleagues (66), this technology has emerged as a very powerful bio-chemical detection method. It is noteworthy as well that the fluorescence background typically observed in many on-line samples using dispersive Raman may potentially be reduced by using SERS. Recently, an approach utilizing surface enhanced spatially offset Raman spectroscopy (SESORS) was used for *in vivo* monitoring of glucose in rats (19, 20). Spatially offset Raman spectroscopy (SORS) is used to increase the sensing depth of SERS techniques for *in vivo* applications (67, 68). This work used silica nanoparticles covered with a silver film, termed AgFONs (silver or Ag Film Over Nanoparticles), which have displayed enhancement factors of up to 10^7 (7). These films were then functionalized with a self-assembled monolayer to increase the number of glucose molecules probed, allowing continuous glucose monitoring *in vivo* up to 17 days without the need for multiple calibrations (19, 20).

1.1.3.2. Photoacoustic Spectroscopy

Photoacoustic spectroscopy can be used to acquire absorption spectra from samples including biological ones noninvasively. The photoacoustic signal is obtained by probing the sample with a monochromatic radiation that is modulated or pulsed. Absorption of probe radiation by the sample results in localized short-duration heating. Thermal expansion then gives rise to a pressure wave, which can be detected with a suitable transducer. An absorption spectrum for the sample can be obtained by recording the amplitude of generated pressure waves as a function of probe beam wavelength. Because high signal-to-noise measurements require reasonable penetration of the sample by the probe radiation, the near infrared region holds the same attraction as the more conventional NIR spectroscopy approaches. A purported advantage of PAS, however, is that the signal recorded is a direct result of absorption alone, and scatter or dispersion does not play a role in the acquired signal.

Photoacoustic spectroscopy techniques in the NIR region face many of the same challenges attendant to other NIR spectroscopic methods, namely that complicated and empirical calibration models must be created in order to account for the broad overlapping spectral bands associated with the NIR spectrum, temperature changes,

pressure changes, and varied glucose compartments. Further, the technique requires expensive instrumentation and the measurements are particularly sensitive to variables including temperature, transducer pressure, and sample morphology. Some examples of PAS techniques applied to glucose sensing include (69-74).

1.1.3.3. Optical Coherence Tomography

Optical coherence tomography (OCT) provides a means for measuring the optical properties of turbid media including scatter and refractive index. OCT is an optical ranging technique in which a very short coherence length source is coupled to an interferometer with a sample in one arm and a reference reflector in the other. As the reference reflector is scanned, depth resolved interference fringes are produced with amplitude dependent on the amplitude of backscattered radiation. Since the scattering coefficient of tissue is dependent on the bulk index of refraction, an increase in refractive index and a decrease in scatter can be detected as a change in the slope of fall-off of the depth resolved OCT amplitude. As the glucose concentration present in interstitial fluid rises, a change in the refractive index occurs. Using OCT the delay in backscattered light is compared to light that is reflected by the reference arm. As similar scatter and refractive index approaches described earlier, it has yet to be shown that OCT can overcome specificity and other limitations when applied *in vivo*. In addition, OCT techniques also suffer from large signal fluctuations due to motion artifact along with other environmental and physiological conditions (23, 44). Several groups have explored this detection technique for measurement of glucose *in vivo* (7, 23-27, 75-79). To enhance specificity, an additional variation on OCT-based glucose sensing has also been proposed in which the bulk refractive index and scattering change of a suspension of small polysaccharide beads and cross-linked dextran molecules was mediated by the competitive binding of both glucose and dextran to Concanavalin A bound to the beads. Encapsulated within a dialysis membrane, this sensor displayed varying optical turbidity with glucose which was discernible by OCT (80).

1.1.3.4. Polarimetric Measurements of Aqueous Glucose

In comparison to the aforementioned techniques, polarimetry has the potential to interrogate the anterior chamber of the eye as a glucose sensing site. The development of a polarimetric sensor to determine blood glucose levels noninvasively could greatly facilitate patient compliance by eliminating the invasive nature of current glucose monitoring techniques. As mentioned above, each optical technique for non-invasive measurement of glucose has its own advantages and disadvantages; however, the polarimetric approach has the advantage of being highly specific to changes in glucose while remaining completely non-invasive to the subject. Polarimetric detection of glucose is based on the concept of optical activity, the ability of glucose molecules to rotate the plane of polarization of linearly polarized light transmitted through the sample in direct proportion to the concentration of the glucose.

Polarimetric glucose sensing through the aqueous humor of the eye has the advantage of being highly specific to changes in glucose while remaining completely non-invasive to the subject. Previous research in the area of polarimetric glucose sensing can be classified into two groups: one consists of approaches that detect phase change in polarization caused by the chiral sample, and the second group includes approaches that measure changes in amplitude. Although many of these techniques have shown good repeatability *in vitro*, *in vivo* application has been limited mainly due to time varying birefringence of the cornea caused by motion artifact. Previous research has demonstrated the concept of overcoming birefringence with a dual-wavelength system approach (35, 81, 82).

Dual-wavelength polarimetry utilizing a closed-loop approach has shown success in measuring glucose concentrations in the presence of motion-induced birefringence *in vitro*, *ex vivo*, and limited *in vivo* applications. Thus, although polarimetric glucose techniques utilizing both dual and single wavelength schemes have shown good repeatability and sub-millidegree sensitivity *in vitro* they lack sensitivity *in vivo*. The two largest obstacles that need to be overcome before any polarimetric technique can be utilized to probe the anterior chamber of the eye *in vivo* are: **(1)** time-variant corneal

birefringence due to motion artifact and **(2)** unavailability of a non-index matched approach to coupling light in and out of the cornea (81).

Most biological tissues are optically turbid making a polarimetric detection technique for glucose sensing *in vivo* difficult. Thus, polarimetric glucose sensing in such a media becomes challenging due to multiple scattering events that scramble the potentially useful information encoded in the state of polarization of the reflected or transmitted light. These problems can be overcome by probing the anterior chamber of the eye, since the absorption effects are minimal, loss of polarization information due to scattering effects is insignificant, and glucose is the principal chiral component within the aqueous fluid (83). Our group has previously determined that the major optical rotatory component in aqueous humor is glucose, which contributes to approximately 95% of the total observed optical rotation (84). In addition, it has been shown that a direct correlation exists between the glucose concentration in the eye and blood glucose concentration with a time lag of less than 5 minutes (83). To date, dual-wavelength polarimetry utilizing a closed-loop approach has been shown to have some success in measuring glucose concentrations in the presence of motion induced birefringence within a cuvette, *in vitro* (with a plastic eye phantom), and *ex vivo* (with excised New Zealand White (NZW) rabbit corneas), and *in vivo* (with NZW rabbits) (35, 81, 82). Our group has characterized and overcame the main confounder toward making this approach viable, primarily, motion artifact coupled with corneal birefringence. However, further work is needed for this technique to be viable; in particular, noninvasive coupling of light across the eye, designing the system for human studies, and developing a calibration algorithm for within, and between, patients.

The final long-term goal of this research is the development of an inexpensive, noninvasive, glucose monitor, based on optical polarimetry through the anterior chamber of the eye. Previous work has made strides toward this goal but for this dissertation, there are three primary areas requiring further technical advance for the technology to become a viable solution. The research discussed in this dissertation addresses certain aspects of these remaining problems associated with noninvasive glucose sensing

utilizing optical polarimetry through the anterior chamber. The problems associated with corneal birefringence, and the design and development of this polarimetric glucose monitoring technology would ultimately provide a means for noninvasive measurement of glucose, thereby facilitating increased frequency of measurement, which will allow the patient/end user to modify their insulin/glucose regimen in an effort to repress the long-term secondary complications associated with diabetes. Optical polarimetries as a method for noninvasively diagnosing glucose, along with the remaining obstacles addressed in this research are covered in further details in Chapters II-IV. The driving methodology is that optical polarimetry relies on optical activity for of glucose to induce rotation in the linear polarization of light proportionally to the glucose concentration present. Specifically, the studies described in this dissertation address the following questions regarding optical polarimetry through the anterior chamber of the eye. “Can light be coupled without index matching into and out of the anterior chamber of the cornea without significant loss in polarization information?” “Can a model be formed evaluating the relationship between the two wavelengths of light and the birefringence observed within the cornea?” and “Can a system be built encompassing the above two solutions that results in a benchtop solution usable in pre-clinical human testing?”

1.2. Polarization Histopathology of Malaria Blood Smears

1.2.1. Malaria: Overview

Malaria is a life-threatening disease caused by parasites that most often infect a subject via transmission from a mosquito bite. Following infection, the parasite begins invading the host red blood cells and liver cells, modifying the biochemistry and structural properties of the cells. According to the World Health Organization (WHO), an estimated 584,000 deaths were caused by malaria in 2013 with an estimated 198 million new cases in the span of time (85). Worldwide, the mortality rates associated with the disease have fallen, however, a significant portion of deaths still primarily affect African children (85).

1.2.2. *Current Commercial Malaria Diagnostic Techniques*

1.2.2.1. Conventional Brightfield Microscopy

The recommended gold standard and primary method for evaluating blood samples for malaria detection still utilized around the world is observation of Giemsa-stained thick and thin blood smears via brightfield microscopy. This technique offers the ability to detect parasitemia associated with 5-10 parasites in 1 μ l of blood (86-88). Thick blood smears most commonly provide a positive or negative screening test to determine if the parasite is present in a blood smear for diagnosing if a subject is infected with malaria, while thin smears are most commonly used to determine the species of malaria infection. Thick smears result in lysed red blood cells (RBCs), consist of larger volumes and have greater parasite density as compared to thin smears. For thin smears, white light microscopic imaging with a higher magnification and resolution is utilized to identify the species present and evaluate parasite morphology (89). However, conventional white light microscopy often requires a clinical laboratory structure in addition to trained microscopy technicians, which are both rare in regions where malaria is most prevalent (89-99). Further, current microscopy techniques results in a subjective measure, reported to vary significantly, based on the training and equipment utilized by the expert microscopy technician (100, 101). Thus, the need for devices capable of malaria diagnosis in remote areas has led to the design and implementation of mobile health (mHealth) based portable systems (99).

1.2.2.2. Rapid Diagnostic Testing Strips

Rapid diagnostic tests (RDTs) have become widely used throughout the world and offer a cheaper less time consuming alternative for diagnosis of malaria using a finger-prick of blood (90, 101-104). However, RDTs currently employed for malaria detection consist of an antigen-based detection scheme. Thus, RDT performance has been reported to degrade in tropical areas where the disease is most prevalent due to the sensing chemistry (87, 105). Additionally, existing RDTs detection limits tend to be much worse than the current gold standard tool for detection of early-stage infections, white light

microscopy. The current sensitivity threshold for RDT tests is greater than 100 parasites/ μ l of blood. Further, these devices do not provide quantitative parasitemia results and suffer from reported inconsistent performance, specifically in diagnosing strain specific malaria infections (86, 90, 106). Additionally, RDTs are ineffective at diagnosing low parasite densities (104). This lack of quantification of the parasitemia level leads to individuals who test positive, showing some indication of the parasite, but does not allow identification of patients requiring urgent treatment (104, 107). A recent study reported a substantial misdiagnosis rate for malaria currently exists in parts of Asia using RDTs (108, 109). Misdiagnosis then leads to substantial mistreatment and over diagnosis of malaria, often resulting in wasted drugs and potential immunity build up in these populations to the anti-malaria drugs (108, 109). Accurate diagnosis has become more important as the drug resistant malaria continues to spread causing medications to become costly (87).

1.2.3. Polarized Microscopy for Malaria Diagnosis

Other traditional microscopy techniques applied for malaria diagnosis have included cross-polarization microscopy and dark-field microscopy (87, 89-91). Both techniques utilize imaging contrast enhancement from hemozoin to improve diagnostic capability for the presence of malaria in blood smear samples (89-91, 104, 110). Hemozoin crystals occur in varying amounts within malaria infected blood smear samples. The crystals are created as the byproduct of hemoglobin metabolism by the malaria parasite in an infected host. These crystals are optically birefringent, meaning they result in speed of light or effective refractive index being dependent on the direction of propagation of light, based on the anisotropies (86, 91, 107, 110-114). Hence, it is much easier to observe hemozoin under polarized light microscopy as compared to traditional white light microscopy. Specifically, studies using polarized microscopy have shown that it may even be better than conventional staining, particularly for the less severe cases of malaria infection (91, 111). Maude et al. demonstrated that when examining histologic specimens, polarized microscopy sensitivity was approximately double that of conventional light microscopy for the detection of the malaria parasite (91, 110).

Further, the conventional staining approach is also potentially inferior because it can include many false positive indications for the presence of malaria, specifically in diagnosis of tissue samples or placental malaria diagnostics (91, 110). Unfortunately, similar to traditional white light microscopy, polarized microscopy is rarely implemented for field-based diagnosis or even in the clinic because it often requires costly and complex microscope configurations in addition to sophisticated maintenance with the microscope systems tending to be bulky in size (85, 86, 90, 91, 111, 115-118). Thus, further research in the design, development, and testing of low-cost polarized microscopic imaging systems as an alternative approach to current microscopy in malaria diagnosis is needed. The polarized light cell-phone design described in this report intends to overcome these drawbacks and assist medical professionals in the clinic and in low-resource settings to improve correct diagnosis of malaria with enhanced detection via a field-based modular polarized microscope.

1.2.4. Mobile Phone Microscopy Overview

Mobile phones offer an ideal platform for creating field-based modular polarized microscope. Currently, over 6 billion cell-phone subscriptions exist worldwide (accounting for approximately 75% of the world having access to mobile phone networks),⁽¹¹⁹⁻¹²²⁾ and the vast majority of these users (~5 billion) are located in developing countries. Utilizing the existing mobile infrastructure allows for significant reduction in cost and size of mobile-based designs (119, 123). Additionally, the number of active mobile phone subscriptions is continually increasing, particularly in low-resource settings, and was expected to surpass the world population by the end of 2014 (122). Due to the large volume of wireless communication users, mobile phones continually remain at relatively low-costs, even with constant advancements in hardware and software specifications on new models. Because of increased access to these mobile networks and the fact that many mobile phones currently available are equipped with advanced camera features and other technologies, they have become an ideal platform for many advanced imaging and sensing mHealth applications resulting in several portable field ready point-of-care (POC) devices (89, 119, 124-130). These mobile POC

platforms offer great opportunities for improved healthcare throughout the world in developed and developing nations by offering high quality alternatives to existing imaging modalities that are low-cost, portable, and energy efficient. This is particularly important for the clinic and field-testing in remote areas and in low resource settings where the medical infrastructure is often times limited or even non-existent.

In recent years, a significant number of studies have focused on introducing new cell-phone based systems that provide low-cost alternatives to conventional microscopy techniques for mHealth applications (89, 126-130). Mobile phone based microscopy approaches can be broken down into three specific design areas including: lensless approaches^(126, 128), on-lens approaches⁽¹²⁷⁾, and attachment based approaches (89, 129, 130). Research in each of these design categories has produced promising scientific approaches towards cell-phone microscopy designs capable of significantly affecting healthcare standards in remote developing countries, particularly in the area of single cell resolution for disease diagnosis. More specifically, several cell-phone based microscopy designs for malaria diagnostic applications have been reported. For example the lensless design using holography is capable of offering resolution comparable to traditional brightfield microscopic techniques (~40x magnification, NA=0.65 objective) without the use of any additional lenses after the cell-phone camera on a mobile device. Using a lensless design approach can allow for more compact designs and eliminates the need for optical alignment (126, 128). Additionally, this technique allows for decoupling of the relationship between field-of-view (FOV) and resolution, thus allowing for significant improvements in large FOV imaging without sacrificing system resolution as compared to traditional microscopy techniques (128, 131-136). This design approach has resulted in systems to look for the presence of malaria parasites on standard blood smears have been reported (119, 124, 129, 131, 132, 137-142). The two main limitations of the approach are **1.)** Cell-phone microscopy systems used in this configuration must contain enough processing power to reconstruct the resultant images from holograms or process the images remotely on a server and **2.)** Samples to image require placement

relatively close to the camera optical detector limiting this approach in certain applications (128, 131-136).

Previous reported on-lens device designs typically employs a refractive element directly attached to the cell-phone camera at the focus or a ball lens mounted in front of the camera lens (127, 130). This approach allows for a low-cost alternative and produces comparable resolution to other reported cell phone based microscope systems. The ball lens creates a spherical focal surface; thus, the technique only allows for a small FOV of a captured image to be in focus. The out of focus areas in the FOV then need to be adjusted using image processing correction techniques or implementing correction algorithms while processing the images (127, 130).

The majority of reported cell phone based microscopy designs use an attachment-based approach, where additional hardware is required for microscopic imaging (89, 124, 143). The hardware attachment is often a variation of lenses: commonly combining a clip-on attachment for a cell-phone^(89, 127), a commercial microscope objective⁽⁸⁹⁾, or even low-cost singlet lenses (130). The limitations of this approach are that a separate attachment can often be required for each individual cell-phone model and complex optical elements may be required, thus potentially limiting the application of such a design in developing countries.

In the second part of this dissertation, the examination of polarized light microscopy on a cellular phone platform to evaluate feasibility of a low-cost portable alternative to current malaria diagnostic testing practices is explored. This research is presented in Chapter V of the dissertation and focuses on the development and preliminary testing of a modular platform design.

2. POLARIMETRIC GLUCOSE SENSING^{*}

In this chapter, a description of polarized light starting with the theory and then discussing the various components of a polarimetric sensing system is presented. The first half of the chapter focuses on a study, which a glucose detection algorithm was developed capable of compensating for birefringence with motion and time lag between blood and aqueous humor glucose levels. First, the critical issue of corneal birefringence in the presence of eye motion for glucose monitoring using optical polarimetry was addressed *in vivo* utilizing animal models. Eye motion occurs primarily as saccadic motion, heart rate, and respiration. Saccadic motion is a high frequency involuntary fixation (50 to 80 movements per second), where heart rate and respiration signal occurs at a middle range frequency (3.5 beats/second and 1.5 movements/second in a rabbit respectively). Additional low frequency voluntary fixation that occurs when a person moves their eyes to find the object they wish to focus on. These eye movements contribute noise to the polarized measurement technique by causing changes in corneal birefringence during a measurement equivalent to hundreds of millidegrees as compared to the millidegree rotations observed due to glucose. In an anesthetized rabbit the voluntary motion artifact is insignificant but the motion due to respiration and heart rate has been shown to be problematic (1). This work has previously demonstrated the potential in utilizing a closed-loop dual-wavelength polarimetric approach to detect glucose concentration in the presence of motion induced corneal birefringence through the combination of computer modeling, *in vitro* testing, and *ex vivo* testing of the optical system (35, 81). However, only recently has this approach been tested and shown to work *in vivo* (82).

^{*} Part of this chapter is reprinted from Pirmstill, C.W., Cummins, B., Coté, G.L., and McNichols, R.J., (2014). Glucose Monitoring. Biomedical Photonics Handbook, Second Edition, CRC Press: 47-76 with kind permission of CRC press.

Part of this chapter is reprinted from Pirmstill, C.W., Malik, B.H., Gresham V.C., and Coté, G.L. "In Vivo Glucose Monitoring Using Dual-Wavelength Polarimetry to Overcome Corneal Birefringence in the Presence of Motion," *Diabetes Technol. Ther.* 14(9), (2012), with kind permission of Mary Ann Liebert, Incorporated.

Part of this chapter is reprinted from Pirmstill, C.W., Malik, B.H., Thomas E. III, and Coté, G.L. "Design and Characterization of a Ferromagnetic, Air Gapped Magneto-Optic Faraday Rotator," *Opt. Letters.* 30(8), (2013), with kind permission of Optical Society of America.

2.1. Polarized Light Theory

2.1.1. Fundamentals of Polarized Light

Polarization is a property of light and it can exist in three polarization states that are circular, elliptical, and linear. You may not be aware of it, but polarized light and technologies that utilize the concepts of polarization are all around you. For example, do you own a laptop, LCD flat screen TV, calculator, cellular phone, or any other liquid crystal display device? If so, then you have been exposed to polarized light. Another product, you are likely familiar with, that is designed to interact with and eliminate polarized light, created after being reflected from a non-metallic surfaces (such as snow, roads, a tabletop, or water) is polarized sunglasses. The production of polarized light can occur through several different methods such as reflection, double refraction, selective absorption, and scattering.

Most types of light sources, including sunlight and most indoor lighting, generate light that exists in an unpolarized state. Unpolarized light is composed of several transverse waves each oscillating in a sinusoidal fashion. However, these oscillations occur in an infinite number of planes as illustrated in Figure 2.1. Linear polarizer sheets are designed in a way such that they only transmit light that exists in a single plane. Thus, when putting a linear polarizer in-line with an unpolarized light source, (see Figure 2.1 below), all the light that is not oscillating in the same plane as the initial linear polarizers orientation will be blocked, or eliminated, resulting in light oriented in a single plane (oriented in parallel with the initial polarizers orientation) transmitted through the polarizer. The light exiting the polarizer is termed linearly polarized light. As shown in Figure 2.1, the beam of light transmitted through the initial linear polarizer is transformed from an unpolarized light beam consisting of sinusoidal electromagnetic oscillations in many planes into a beam consisting of an electromagnetic oscillation in a single plane (the Vertical plane) oriented parallel to the initial polarizers preferred axis.

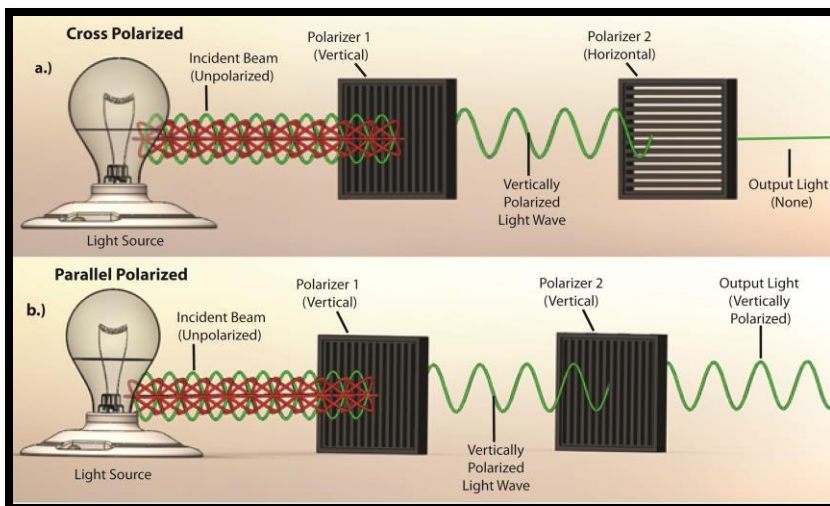


Figure 2.1: An illustration of how un-polarized light becomes linearly polarized through the application of a polarizer.

2.1.2. *Optical Activity and Polarimetry*

Certain materials have the ability to “rotate” the plane of polarization of linearly polarized light. This is termed optical rotation and the amount of rotation within a sample is wavelength dependent. Karo and corn syrup are both optically active liquids. Meaning they can rotate the plane of polarization of light transmitted through them by an amount proportional to their path length. Common optically active substances include sugar solutions, turpentine, amino acids, Karo syrup, corn syrup and some crystals. Many naturally occurring organic compounds such as sugar, tartaric acid and turpentine, are optically active and thus rotate the light passing through a sample when in the liquid state. The equation used to describe the optical rotation, Biot’s law, of polarized light is shown in Equation 2.1 below. This illustrates that optical activity is associated with the individual molecules themselves. Thus, when linearly polarized light from a white light source transmits through an optically active fluid each wavelength, or color, in the underlying spectrum changes in polarization independently from the other light. As a result, at each angle the second polarizer rotation will result in a change in the observed color with respect to angle of polarization when examined between two polarizer sheets. The majority of light sources, including sunlight and most indoor lighting, generate light

existing in an un-polarized state. Linear polarizers are devices that block un-polarized light (light waves) from passing through the polarizer traversing all planes except the plane matching the orientation of the polarizer.

The use of optical polarimetry for the detection of sugar concentrations has its origins in the late 1800s, where it has been used in the sugar industry for monitoring the production processes of sugar (144-147). The sensing mechanism for optical polarimetry relies on the fact that the polarization vector of light rotates when it interacts with an optically active material, such as glucose. Therefore, the amount of rotation in the plane of polarization is directly proportional to the glucose concentration and sample path length. However, it was not until the early 1980s when the use of polarized light had begun to focus on physiologically relevant glucose measurements. March, Rabinovich, and Adams (28, 29) first proposed the application of optical polarimetry to measure the glucose level in the aqueous humor of the eye as a way to noninvasively sense blood glucose levels. Their design utilized an optical feedback system that consisted of two Faraday rotators, one for feedback and the second for compensation. Then Coté et al. developed a technique based on true phase measurement, which demonstrated the potential for millidegree sensitivity in glucose based water solutions (148). The system, utilized by Coté et al., employed a rotating linear polarizer for modulation and a fixed linear polarizer as an analyzer for detection. Later, Goetz et al. investigated a polarimetric system, which used an integrator as the feedback element. Their system was able to measure incremental rotation with micro degree sensitivity, using a precision rotational mount (149). King et al. reported a multispectral polarimetric system, utilizing a Pockels cell for modulation and compensation, in order to account for other optically active components present in the aqueous humor (150). Cameron et al. reported a single wavelength system similar to Rabinovich and March, with a digital closed-loop controller allowing for significantly enhanced stability and repeatability of the system (151).

In later work by Coté et al., a multi-spectral system was utilized to overcome the effect of optical confounders in aqueous humor, and potentially, motion induced corneal

birefringence (152). Additionally, utilizing this technique they were able to investigate the time delay between blood glucose concentration and the glucose concentration in the aqueous humor of the eye. This resulted in finding that the average transport time lag was measured to be less than 5 minutes (83). In subsequent work, Cameron et al. reported on development of a real-time polarimetric glucose sensor which utilized a dedicated birefringence compensator in order to account for corneal birefringence (153). This system was later tested *in vivo* on New Zealand White (NZW) rabbits. More recently, Malik et al. reported on the development and testing of a real-time closed-loop dual-wavelength polarimeter for glucose sensing using three dedicated Faraday rotators, one for modulation and two for compensation of the individual wavelengths (81). This system employed multi-variable analysis of the two beams to overcome corneal birefringence. This technique was then tested *in vitro* on a plastic eye model and *ex vivo* utilizing excised NZW rabbit corneas (35, 81).

Several research groups have demonstrated the application of optical polarimetry to glucose sensing *in vitro* with acceptable repeatability of less than 15 mg/dl standard error (29, 151, 154). Additionally, we have previously modeled, designed, built, and tested the world's most sensitive and accurate dual-wavelength polarimeter that could measure polarization rotations for each wavelength to less than 0.4 millidegrees, which is equivalent to less than 10 mg/dL glucose levels in a 1 cm pathlength cuvette within our lab. Further, our group successfully demonstrated the ability to compensate for the presence of confounding molecules and motion artifact. We calculated glucose concentrations across the physiologic range *in vitro* with a birefringent cuvette and *ex vivo* using excised rabbit corneas and found the dual-wavelength model produced 100% of hits that fall within zone A, MARD of 5.3%, and a standard error of 22.4 mg/dL (35). Utilizing a dual-wavelength setup the single wavelength error of over 100 mg/dL in many cases was reduced to less than 15 mg/dL (35).

2.1.3. *Specific Rotation*

The polarimetric detection of molecules such as glucose result from the fact the molecule of interest is a chiral molecule, which means it does not have a structural plane

of symmetry. All chiral molecules cause linearly polarized light to rotate upon contact and are known as optically active molecules. Glucose is a chiral molecule, which allows it to be detected using polarimetry (144-147). The equation used to describe the rotation of linearly polarized light in the presence of an optically active compound is shown in Equation 2.1:

$$[\alpha]_{\lambda} = \frac{\alpha}{L \times C} \quad (2.1)$$

Where $[\alpha]_{\lambda}$ is the specific rotation of light dependent on wavelength (λ), α is the observed rotation, C is the concentration of the optically active material, and L is the path length of the sample.

Polarimetry is a sensitive, nondestructive technique for measuring the optical activity exhibited by inorganic and organic compounds. A compound is chiral if it has at least one center about which no structural symmetry exists. Such molecules are optically active since linearly polarized light rotation occurs when passing through them. The amount of optical rotation determination from the molecular structure of the molecule, the concentration of chiral molecules in the substance, and the pathlength the light traverses through the sample. Each optically active substance has its own specific rotation as defined by Biot's law described in Equation 2.1. A common setup for observing optical rotation measurements using is depicted in Figure 2.2 below.

2.1.4. Optical Rotatory Dispersion and Glucose

Using Equation 2.1, the determination of the concentration of an optically active sample can occur, if the pathlength distance is known. The wavelength dependence is known as optical rotatory dispersion and can be further defined using a modified version of the Drude equation for wavelengths away from or between the absorption bands namely (155),

$$[\alpha]_{\lambda} = \frac{k_o}{\lambda^2 - \lambda_o^2} \quad (2.2)$$

Where λ is the wavelength of interest, and k_o is a rotational constant that corresponds to the wavelength λ_o of maximal absorption. For glucose, the values of k_o and λ_o are 16.74° and $0.17236 \mu\text{m}$, respectively.

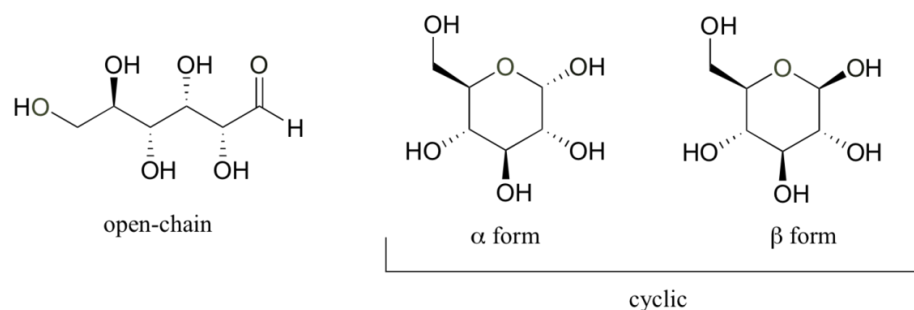


Figure 2.2: Schematic representation illustrating the different ways glucose forms in solution.

The main concept that the focus of utilizing polarimetry for glucose sensing research focuses on the optical activity of exhibited by glucose. When glucose dissolves in water, the glucose molecule will adopt one of two cyclical form(s) as shown in Figure 2.2. For example once dissolve in water glucose will undergo a configurational change into one of two known optical isomers either α -D-glucose or β -D-glucose. The two isomers known as anomers only differ in the configuration of the chiral center of the molecule. Further, after dissolution occurs the conversion between α form and β form glucose is a dynamic process that is known as maturation. The process continues until thermodynamic equilibrium occurs between the two forms. The specific rotation for α form glucose is $+122.8^\circ$ and the specific rotation of β form glucose is $+18.7^\circ$. Upon equilibrium the two forms reach a balance present at the ratio of 36:64 (α : β) resulting in a net specific rotation of $+52.6^\circ$. Equations 2.1 and 2.2 describe the relationship between glucose concentration, the rotation in the plane of light polarization, optical path length, and the specific rotation as a function of wavelength in a clear optical media. However, neither equation takes into account the effect of birefringence similar to the amount observed in the cornea.

2.1.5. Corneal Birefringence

To address this concern, our group reported a theoretical framework for modeling corneal birefringence and its effect on dual-wavelength polarimetry for glucose sensing (156). The results indicated that a multi-wavelength polarimetric approach can potentially be utilized to eliminate the effect of motion induced time-varying corneal

birefringence *in vitro*, *ex vivo*, and *in vivo* (35, 81, 82). Based on the preliminary data our two-wavelength polarimetric system presents the capability to compensate for birefringence in the presence of motion artifact both *in vitro*, *ex vivo*, and *in vivo* in rabbits (35, 81, 82). However, the system is currently relatively large and will need reduction in size to a cart based system for human testing.

Birefringence is a material property where the atoms of the material are oriented such that they form a regular repetitive array. A material is said to be birefringent if the repetitive arrangement of molecules results in the material being optically anisotropic, meaning the materials optical properties, including refractive index, differ depending on the direction of the propagation of light through the material (157, 158). The fast axis is defined by the direction of propagation that results in the lower value of refractive index and the difference between the principle refractive indices is a measure of the amount of birefringence. Due to their birefringent (materials with two indices of refraction) nature, some transparent tapes produce brilliant colors when viewed between polarizing filters. When a ray of un-polarized light enters a birefringent material, it divides into two rays. The two rays have different speeds and are polarized at right angles to each other, meaning that two different colors can be seen depending on the orientation of the polarizers (157, 158).

The *in vivo* performance of polarimetry for anterior chamber glucose measurements is limited primarily by the time varying birefringence of cornea due to motion artifact making it difficult to discern the optical rotation due to glucose. The cornea changes the state of polarization of light transmitted through it due to the structure of the corneal stroma being primarily composed of collagen lamellae that constitutes almost 90% of the cornea (159-162). Each individual lamella exhibit intrinsic birefringence and can therefore be considered as a linear retarder with the fast axis oriented perpendicular to the fibril orientation. In humans, the lamellae that lie in parallel to the surface of the cornea are composed of about 200 stacked lamellae (163). Thus, the total corneal birefringence manifests itself as form birefringence, and can be considered as the sum of the individual lamella birefringence (157, 158, 164).

2.1.6. Single Wavelength Polarimeter

Because of this rotation, caused by the optically active sample, some light will pass through the analyzer, measurable with an optical detector.

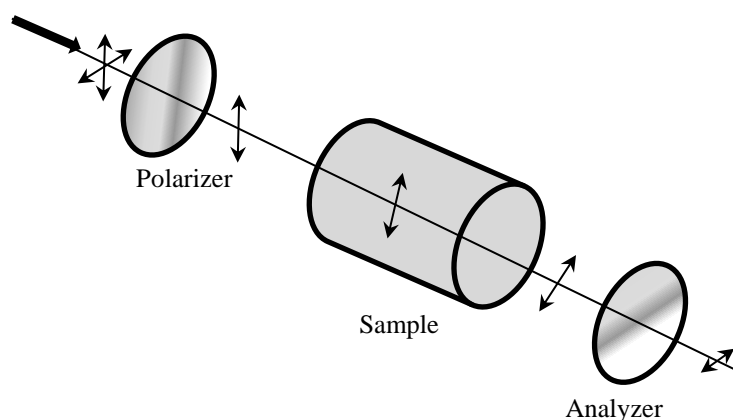


Figure 2.3: Illustration of optical rotation of plane-polarized light.

This simply described polarimetric method is employed in quality control, process control, and research in the pharmaceutical, chemical, essential oil, flavor and food industries. It is so well established that the United States Pharmacopoeia and the Food & Drug Administration include polarimetric specifications for numerous substances (165). Since the late 1800s, one of the earliest applications of polarimetry has been the development of bench-top polarimeters, known as saccharimeters, designed solely for the estimation of starch and sugar in foods and beverage manufacturing and in the sugar industry (145). For this agricultural industry application, in which the concentrations and pathlengths are high, commercial bench-top units similar to the system depicted in Figure 2.3 are adequate. However, for the low glucose concentrations found in cell culture systems and *in vivo* much more sophisticated polarimetry systems are required to monitor the glucose.

One of the difficulties associated with polarimetric glucose through the eye is the corneal birefringence coupled with motion artifact. Time varying birefringence is the most significant source of noise for attempting polarimetric glucose sensing in the

anterior chamber of the eye, wherein it confounds the signature of the optical activity of glucose by contributing a significant change in the state of polarization of the probing light (1). Our group has previously quantified the effect of corneal birefringence on glucose sensing through the eye both theoretically and experimentally (35, 156). We reported that the perceived change in optical rotation due to time varying corneal birefringence is two to three orders of magnitude larger than the rotation due to glucose in the aqueous humor. Therefore, it is important to account for time varying corneal birefringence, due to motion artifact, in order for accurate prediction of glucose concentration in the aqueous humor of the eye.

To date, the two mechanisms that are being researched to address the noise due to time varying corneal birefringence in polarimetric glucose sensing are use of a dedicated birefringence compensator (36, 166), and a dual wavelength polarimeter (35, 81, 82). Specifically, Cameron and Anumula utilized a dedicated birefringence compensator to attempt to account for the corneal birefringence (166). Their system includes a variable retarder, which has the potential to compensate the birefringence by negating the contribution of sample birefringence. Our group has utilized dual wavelength polarimetry, which is effectively a scaled subtraction of the two wavelengths using multiple linear regression analysis to nullify the contribution of birefringence to the total rotation of the state of polarization yet be sensitive to a change in rotation due glucose (35, 81, 82). This results in reduction in the effect of time-varying corneal birefringence, which manifests as sample noise for both the wavelengths.

Other embodiments of polarimetric glucose sensing through the eye include reflection of light from the intraocular lens (IOL). Rawer et al. utilized an open-loop system to measure the rotation of plane of polarization of light by glucose in the aqueous humor (AH) of the eye (167, 168). The eye phantom used an artificial cornea and an artificial IOL to enhance the reflectance at the AH-IOL interface, which otherwise is lower than 0.5%. The system was tested in the glucose concentration range of 0 to 40 g/dL with the smallest glucose concentration of 10 g/dL, more than 1,000 times the physiologic range. Although, the authors discuss the effect eye movements can have on

the system they conclude that further system optimization is needed to allow for high-speed compensation of eye motion. A similar but more advanced system was proposed by Ansari et al., which exploited the reflection at AH-IOL interface at the Brewster's angle, wherein, a plano-convex lens was used as an artificial IOL but this too does not have the capability to overcome changes in the signal due to motion artifact (169). More recently, Purvinis et al. used an open-loop, single wavelength, polarimeter to measure the glucose concentration in the eye *in vivo* (36). Therein, the motion artifact reduction and effective elimination occurred by limiting animal motion, and the authors concluded that corneal birefringence compensation along with closed-loop control could provide measurements that are more robust.

2.1.7. Dual-wavelength Polarimeter

Based on earlier system results we anticipate that the time varying corneal birefringence will be significantly reduced utilizing a dual-wavelength polarimeter *in vivo*. The optical setup illustration in the form of a computer-aided design for this system is present below, Figure 2.4. The system components are the same as described recently by our group and described in further detail later in Chapter III and IV (35, 81, 82). In brief, the optical setup consists of two platforms: the source (left) and detection (right) sides with the sample placed in between the two platforms via an eye-coupling device. The source side of the system consists of two lasers of different colors (one red and one green), as shown on the left in Figure 2.4. The light emitted from the two lasers combines and the combined beam modulates using a series of electro-optical components. The beam of light then passes through the sample via the eye-coupling device, separates into respective colors, and then collects by the two detectors shown on the collection side of the optical setup. The sample causes the signal at the detector to change, which includes information about both the amount of glucose present in the sample (aqueous humor) and the noise associated with the signal (such as birefringence). The relationship between the noises, present in the two respective signals remains constant and, therefore, minimization using a multiple linear regression (MLR) analysis of the signals. A MLR analysis is essentially a scaled subtraction of the two signals

wherein it removes the common noise and detects the signal variation caused by the change in glucose concentration only.

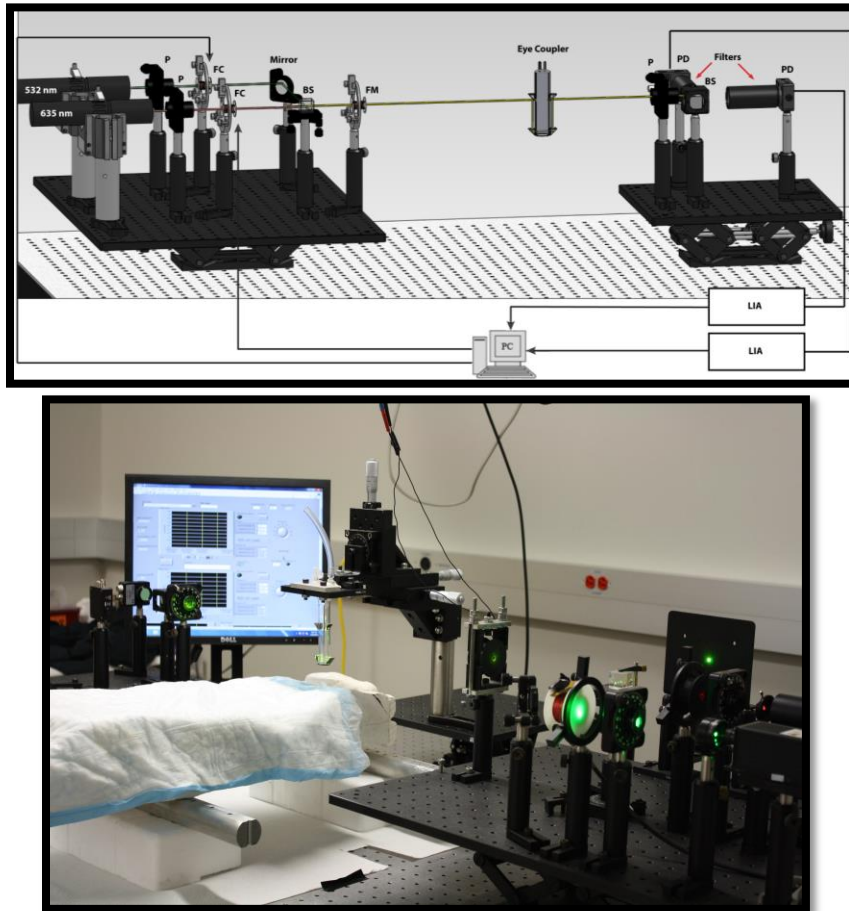


Figure 2.4: CAD model of the *in vivo* dual-wavelength polarimetric glucose detection system. Note that the rabbit's eye was coupled to the system via the refractive index matching eye coupling device shown after the Faraday modulator (FM). The two ports on the top of the eye coupling device are used to fill in the device with PBS solution in order to achieve index matching between the air and cornea. P, polarizer; FC, Faraday compensator; BS, beam-splitter; FM, Faraday modulator; PD, photodetector; LIA, lock-in amplifiers.

2.1.8. Polarimetric Faraday Rotation

Common electro-optic (EO) and magneto-optic (MO) techniques for rotating the plane of polarization employ nonlinear optical approaches such as Kerr effect, Pockel

effect, or Faraday Effect (158, 170, 171). The majority of magneto-optic Faraday rotator (MOFR) devices used in polarimetric sensing applications use an air-core solenoid inductor approach (82, 170-173). Optical modulators used for high frequency applications such as a Pockels cell, liquid crystal rotators, or other electro-optic designs typically sacrifice the precision of the rotation since they are applied for large modulation angles (modulation depths of up to 90 degrees). Conversely, air-core optical techniques that are commonly used for fine rotation (modulation depths of ± 1 degree) of the polarization plane have been limited primarily to direct current (DC) and low frequency alternating current (AC) modulation applications (82, 171-174). Specifically, the design of air-core solenoid modulator devices have several limitations when used as Faraday rotators (FRs) where a magnetic field density (MFD) on the order of 1 mT up to 30 mT is typically required at frequencies greater than 1 kHz. Faraday modulators have been used in previous polarimetric glucose sensing systems, dating all the way back to the original work of Rabinovich (29) but are bulky and prone to yield a large amount of electromagnetic cross talk due to the large size from the bulky coils used. This requires separation of the coils by large distances from each other and the detectors to avoid cross talk and thus makes miniaturization of the system problematic.

To address some of the limitations of air-core designs, our group recently reported on a novel high permeability ferrite based air gapped magneto-optic (MO) polarized light modulator (MOPLM) design. The key advantages of the high permeability MOPLM over established Faraday based AC modulation designs are namely; given a smaller overall device size, higher AC modulation can be achieved while still providing a higher magnetic field density (MFD) for a given driving power (172, 173, 175). The ferrite device is capable of optical modulation in the state of polarization at high frequency with lower power requirements, a smaller footprint, and increased energy storage density capabilities compared to current air-core techniques (175).

2.1.9. Electric Field Derivation of Experimental Polarimetric Setup

Now let us consider the entire optical train from the light source to the photodetector. The equation for the electric field at the detector can be derived using the Jones vector

calculus (35). For any given wavelength, the optical system can be modeled as a linear polarizer, followed by two Faraday rotators, the sample, and finally the analyzer, as shown in Figure 2.4. The sample can be represented as a general linear retarder, which would change both the azimuth angle and the ellipticity of the state of polarization. However, as shown above, for the limited range of motion observed *in vivo*, the sample corneal birefringence for our case effects the azimuth angle only and, hence, the change in ellipticity of the state of polarization for this case can be ignored. Therefore, the phantom can be represented as an optical rotator. The resulting matrix representation is,

$$V_{system} = \begin{matrix} \text{Analyzer} & \text{Glucose sample} & \text{Eye phantom} & \text{Faraday modulator} \\ \begin{bmatrix} 1 & 0 \\ 0 & 0 \end{bmatrix} & \begin{bmatrix} \cos \phi_g & -\sin \phi_g \\ \sin \phi_g & \cos \phi_g \end{bmatrix} & \begin{bmatrix} \cos \phi_b & -\sin \phi_b \\ \sin \phi_b & \cos \phi_b \end{bmatrix} & \begin{bmatrix} \cos(\theta_m \sin(\omega_m t)) & -\sin(\theta_m \sin(\omega_m t)) \\ \sin(\theta_m \sin(\omega_m t)) & \cos(\theta_m \sin(\omega_m t)) \end{bmatrix} \\ \begin{bmatrix} \cos \phi_f & -\sin \phi_f \\ \sin \phi_f & \cos \phi_f \end{bmatrix} & \begin{bmatrix} 0 & 0 \\ 0 & 1 \end{bmatrix} & & \\ \text{Faraday compensator} & \text{Polarizer} & & \end{matrix} \quad (2.3)$$

Where V_{system} is the system equivalent Jones matrix, ϕ_g , ϕ_b and ϕ_f represent optical rotations due to glucose, corneal birefringence, and the Faraday compensator, respectively, θ_m is the modulation depth, and ω_m is the modulation frequency. The resultant system matrix is,

$$V_{system} = \begin{bmatrix} 0 & -\sin(\theta_m \sin(\omega_m t) + \phi_g + \phi_b + \phi_f) \\ 0 & 0 \end{bmatrix} \quad (2.4)$$

Therefore, the final signal intensity, I , at the detector is,

$$I \propto \sin^2 \{ \phi + \theta_m \sin(\omega_m t) \} \quad (2.5)$$

Where $\phi = \phi_g + \phi_b + \phi_f$

Using several trigonometric and Bessel function identities [19], it follows that,

$$I \propto E^2 = \left(\phi^2 + \frac{\theta_m^2}{2} \right) + 2\phi\theta_m \sin(\omega_m t) - \frac{\theta_m^2}{2} \cos(2\omega_m t) \quad (2.6)$$

DC offset 1.09 kHz, ω_m 2.18 kHz, $2\omega_m$

Using phase-sensitive detection, our system can lock-in to the single-frequency

component represented by the middle term in Equation 2.6. For a dual-wavelengths system, the single-frequency components for the two signals at the respective photodetectors can be represented as,

$$\begin{aligned} I_{\lambda_1} &\propto 2(\phi_{g\lambda_1} + \phi_{b\lambda_1} + \phi_f)\theta_m \\ I_{\lambda_2} &\propto 2(\phi_{g\lambda_2} + \phi_{b\lambda_2} + \phi_f)\theta_m \end{aligned} \quad (2.7)$$

Where I_{λ_1} and I_{λ_2} are the detected intensities, $\phi_{g\lambda_1}$ and $\phi_{g\lambda_2}$ are rotations due to glucose, and $\phi_{b\lambda_1}$ and $\phi_{b\lambda_2}$ are rotations due to the sample birefringence. The optical rotation due to the Faraday compensator, ϕ_f , is known as a function of wavelength and so is easily removed. The phase shift, ϕ_b , introduced due to cornea is given by,

$$\phi_b = \frac{2\pi}{\lambda} \Delta n L \quad (2.8)$$

Where λ is the wavelength, $\Delta n = |n_e - n_o|$ is the corneal birefringence, and L is the path length through the cornea. It is obvious that the optical retardation for a birefringent sample is a function of both the wavelength and the birefringence $|n_e - n_o|$. In case of the cornea, the birefringence quantity $|n_e - n_o|$ is known to be constant with wavelength, a behavior attributed to the *form* birefringence of the cornea (32, 156, 176, 177). However, the rotation due to glucose is wavelength dependent. With Δn and L constant, the product of λ and ϕ_b is fixed. Specifically, $\phi_{b\lambda_1}$ and $\phi_{b\lambda_2}$ can be calculated as long as the wavelengths are known (635 nm and 532 nm in this case). Thus, the relationship between $\phi_{b\lambda_1}$ and $\phi_{b\lambda_2}$ is easily determined. Using the MLR methodology, the scaled change in rotation due to the birefringence can be accounted for with respect to wavelength and, further, MLR can be used to extract the glucose concentration as shown in Equation 2.9.

$$MLR_{signal} \propto (I_{\lambda_1} - I_{\lambda_2}) \propto (\phi_{b\lambda_1} - \phi_{b\lambda_2}) + (\phi_{g\lambda_1} - \phi_{g\lambda_2}) \quad (2.9)$$

The first term on the right hand side is a constant and the second term varies as function of glucose concentration. Thus, Equation 2.9 can be represented as,

$$\begin{aligned} &\propto C + (m_1 C_g - m_2 C_g) \\ &\propto C + (m_1 - m_2) C_g \end{aligned} \quad (2.10)$$

$$\begin{aligned}
MLR_{signal} &\propto K_1 + (K_2 C_g - K_3 C_g) \\
&\propto K_1 + (K_2 - K_3) C_g
\end{aligned}$$

Where $C = \lambda_1 * \phi_{b\lambda_1} - \lambda_2 * \phi_{b\lambda_2}$, $K_1 = \phi_{b\lambda_1} - \phi_{b\lambda_2}$, $\phi_{g\lambda_1} = K_2 C_g$ and $\phi_{g\lambda_2} = K_3 C_g$ and C_g is the glucose concentration. The MLR analysis accommodates the offset C due to birefringence and normalizes for the slopes m_1 and m_2 as a function of wavelength for a given glucose concentration.

2.2. Polarimetric System Design

2.2.1. In Vivo Dual-wavelength Polarimeter

More specifically for *in vivo* testing, the optical sources used in the system consists of two laser diodes: a 635 nm wavelength module (Power Technology, Inc., Little Rock, AR) emitting at 7 mW and a 532 nm wavelength diode-pumped solid state module (Aixiz LLC, Houston, TX) emitting at 10 mW. Glan-Thompson linear polarizers (Newport, Irvine, CA) convert the beams from an un-polarized to horizontally linearly polarized state. The individual beams then pass through respective Faraday rotators that operate as rotational compensators in order to achieve closed-loop feedback control of the system. The Faraday rotators consist of inductive solenoid coils with a Terbium Gallium Garnet (TGG) optical crystal rod wrapped within the center. The TGG crystals (Deltronic Crystals Inc., Dover, NJ) have a high Verdet constant designed to achieve the desired optical rotation for the magnetic field generated. The Faraday compensation coils are driven by current amplifiers to create a magnetic field required to produce the necessary compensation in optical rotation. The two beams are then overlaid on top of each other using a beam-splitter/combiner (Optosigma Corp., Santa Ana, CA). The combined beam then passes through a Faraday rotator set to modulate at 1.09 kHz with a modulation depth of approximately ± 1 degree, which modulates the direction of linear polarization. The combined light beams are then passed through the aqueous humor of a New Zealand White (NZW) rabbit using a custom built index matched eye coupling device shown in Figure 2.5 and shown being coupled to a rabbit in Figure 2.6. A linear polarizer is positioned perpendicularly to the initial polarizers to act as an analyzer to the optical beam. The beam then passes through a 50/50 beam-splitter. The beams are then

separated using bandpass filters at each of the wavelengths (635 nm and 532 nm) before being converted into electronic signals using two PIN photodiodes (Thorlabs, Newton, NJ). The signal from each of the diodes then passes through wide-bandwidth current amplifiers (CVI Melles Griot, Albuquerque, NM). Noise reduction in the output signal from the amplifiers is accomplished through the utilization of lock-in amplifiers (Stanford Research Systems, Sunnyvale, CA) to minimize the noise from outside the frequency band of interest.

2.2.2. Control System and Signal Acquisition

The lock-in amplifiers then produce DC signals that serve as inputs to a PID controller programmed in LabVIEW 8.9 (National Instruments, Austin, TX). The outputs of this controller are then passed through a driver circuit that in turn is used to drive the two compensating Faraday rotators. Real-time response of the system is essential in order to overcome motion artifacts. The respiratory cycle (~ 1.5 Hz) and the cardiac cycle (~ 3.4 Hz) are the primary contributors to motion induced corneal birefringence artifact *in vivo* (84). To date our current PID control feedback mechanism reaches stability in about 100 ms, in this study, which is sufficient for analyte detection in the presence of motion artifacts in the eye, caused primarily by respiratory and cardiac cycles. As previously reported the dual wavelength polarimetric system described above can achieve an accuracy of less than 0.4 millidegrees, which corresponds to glucose measurements of less than 10 mg/dL (81). For the initial polarimetric system described in this chapter a PID controller was designed in LabVIEW and optimized to provide fast compensation closed-loop feedback control in the polarimetric system. Once the system incorporated the improved frequency ferrite core modulator designs, the PID controller was converted from a LabVIEW VI to a LabVIEW FPGA VI allowing the control application to be embedded on a cRio chassis providing significantly improved PID control speed allowing for faster settling and closed-loop data acquisition. The FPGA VI is described in detail in Appendix G.

2.2.3. Faraday Rotators

To address some of the limitations of air-core designs, our group recently reported on a novel high permeability ferrite based air gapped magneto-optic (MO) polarized light modulator (MOPLM) design. The key advantages of the high permeability MOPLM over established Faraday based AC modulation designs are namely; given a smaller overall device size, higher AC modulation can be achieved while still providing a higher magnetic field density (MFD) for a given driving power (172, 173, 175). The ferrite device is capable of optical modulation in the state of polarization at high frequency with lower power requirements, a smaller footprint, and increased energy storage density capabilities compared to current air-core techniques (175).

The air-core MOFR device was constructed of an air-core inductive solenoid coil of AWG #26 magnetic wire (MWS wire, Westlake Village, CA) wrapped around a custom machined Delrin® bobbin. The Delrin® bobbin was 20 mm long, had a diameter of 25.5 mm, and a thru hole at the center with a diameter of 5.5 mm, shown in Figure 2.7a. A 3-D CAD rendering of the device is shown in Figure 2.7b. A Terbium Gallium Garnet (TGG) optical crystal rod (Deltronic Crystals Inc., Dover, NJ) was placed within the center of the solenoid bobbin. TGG rods are commonly used in Faraday rotator applications because the material offers one of the largest Verdet constants ($\sim -134 \text{ rad/T}\cdot\text{m}$) of any commercially available crystal rod while also maintaining a high percentage of optical transmission across the visible range (178). By applying a current to the conductive wire, a magnetic field is produced throughout the center hole in parallel to the optical propagation direction. This magnetic field allows the magneto-optic material to rotate the angle of polarization (β) of linearly polarized light. The magnetic field density (B) produced is proportional to the number of turns of the conductive wire (N), permeability of material (μ), applied current (i), and the overall length (l) of the core (175)

$$B = ((\mu \times N \times i))/l \quad (2.11)$$

With the air-core MOFR design, thousands of turns of wire are typically needed to produce relatively small magnetic fields (<20 mT). Thus, these devices are size limited

and can have low associated inductances (L) leading to lower energy storage density. The inductance value in the coil increases with an N^2 relationship and often causes the need to create resonant circuits to achieve modulation even at relatively low frequencies (~ 1 kHz). Further, to generate significant magnetic fields for the purpose of optical rotation (>20 mT), these designs often require a large number of windings to generate the required inductance leading to high DC and AC resistances along with increases in eddy current and proximity effects. Thus, overall there are common tradeoffs in the design of these devices including between the required driving power and the DC coil resistance from the large number of turns as well as the operating frequency range with respect to the self-resonant frequency (SRF) of the device and the measured inductance.

2.2.4. Eye Coupling Mechanism

The eye is ideally suited to coupling light to the back of the retina for vision. The index mismatch between the cornea and air is partially responsible for the beam bending toward the retina and, although good for vision, this complicates our ability to couple the light across the anterior chamber of the eye. As shown in Figure 2.5, we have built an eye-coupling device that performs the requisite index matching for anesthetized rabbit studies and this worked great for developing our dual wavelength system for overcoming birefringence but is clearly not a long-term solution for human subject studies. Although building on this idea and miniaturizing an index matching device such as a scleral or contact lens for human use is possible and would likely work (as listed in the alternatives section below), the primary optical approach described below that does not require an index matching device would be preferred in terms patient acceptance since no device that directly contacts the eye would be needed.

Using the old coupling method, and the new one as it is developed, we also need to develop better within and between animal calibration algorithms that will provide better within subject, absolute, glucose concentrations across days relative to blood glucose as well as potentially develop an across subject universal calibration. In order to predict glucose accurately *in vivo* on a given day, we need to insure that the approach is accurate within a subject across days and, although not required for a viable sensor, it would be

ideal to have a universal calibration that is accurate across subjects. Thus, using *in vivo* data, focus was geared towards developing these coupling methods and algorithms *in vivo* using animals (rabbits) and then adjusting them as appropriate for both humans and as the new hardware and software is developed and available. An eye-coupling device that overcomes the index mismatch and allows us to take data *in vivo* with NZW rabbits with our dual-wavelength polarization system was designed, built, and tested.

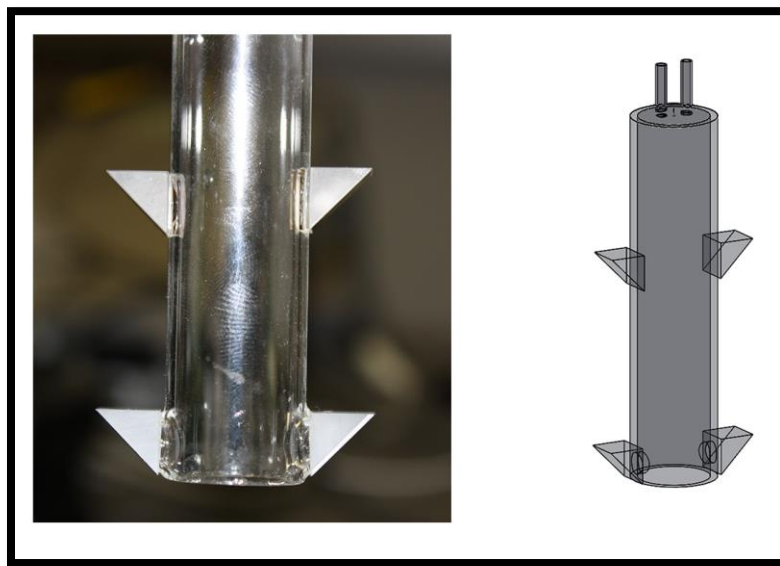


Figure 2.5: Photograph (left) and CAD model (right) of the eye-coupling device. The glass test tube is filled with PBS solution to allow for index-matched coupling with isolated corneas clamped on the artificial phantom and *in vivo*.

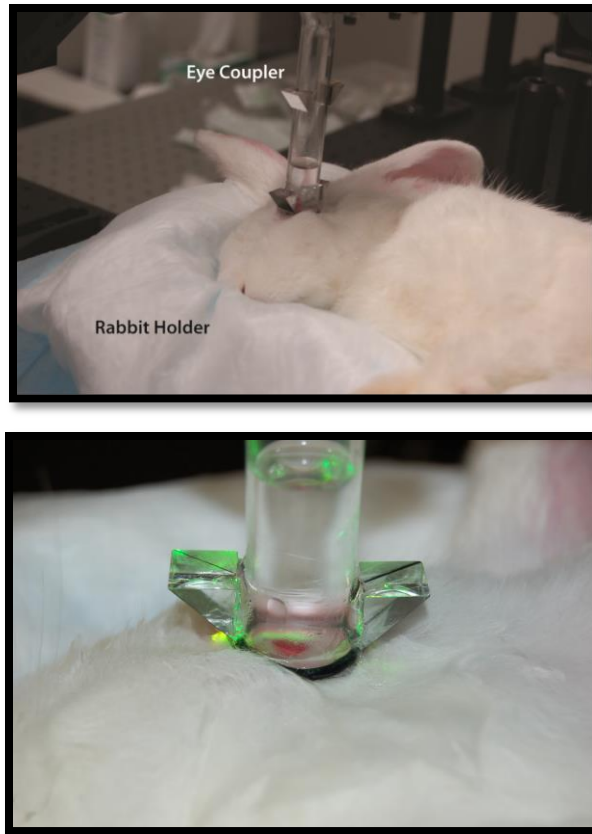


Figure 2.6: Photograph of eye coupling device used during in vivo NZW rabbit experiments. The rabbit's eye was coupled to the system via the eye-coupling device; the glass test tube was filled with PBS solution to accomplish refractive index matching. The rabbits were placed into a custom-built rabbit holder to provide comfort and rabbit orientation that allowed for repeatable positioning of the rabbit to achieve eye coupling.

2.2.5. Theoretical Description of Overcoming Corneal Birefringence in the Presence of Motion Using Dual-wavelength Optical Polarimetry

The post processing for our current dual-wavelength system starts with the voltage collected on the detectors as depicted in Figure 2.4, since this voltage is proportional to the glucose concentration for each wavelength. Mathematically, the operation of the single wavelength system is based on Equation 2.6, where θ_m is the depth of the Faraday modulation, ω_m is the modulation frequency, and ϕ represents the rotation due to the optically active sample. From Equation 2.6, it is evident that the signal from our single wavelength polarimeter is based on three terms; a DC term, a fundamental frequency term, and a double frequency term. It is the second, fundamental frequency term, that

contains the glucose information, ϕ . Without an optically active sample and with the DC term removed, the detected signal only consists of the double modulation frequency ($2\omega_m$) term since the rotation, ϕ , due to glucose is zero. However, when an optically active sample is present, such as glucose, the detected signal then becomes an asymmetric sinusoid, which contains both the fundamental (ω_m) and the $2\omega_m$ modulation frequency terms. By locking into this fundamental term, the signal is proportional to glucose.

In equation 2.6, it is assumed that the rotation, ϕ , is due to glucose only, which is valid when there is no motion artifact or faraday compensation. However, in the dual-wavelength system with an *in vivo* sample both faraday compensation and motion artifact exist. In a recent publication it has been shown that when birefringence is added and faraday compensation, for the limited range of motion observed *in vivo*, it affects the azimuth angle only. Hence, the change in ellipticity of the state of polarization for this case can be ignored and the signal can be represented as a sum of terms, namely $\phi = \phi_g$, ϕ_b and ϕ_f represent optical rotations due to glucose, corneal birefringence, and the Faraday compensator, respectively. For the dual-wavelength system, the single-frequency components for the two signals at the respective photodetectors represented, as shown in Equation 2.7.

Where $I_{\lambda 1}$ and $I_{\lambda 2}$ are the detected intensities, $\phi_{g\lambda 1}$ and $\phi_{g\lambda 2}$ are rotations due to glucose, and $\phi_{b\lambda 1}$ and $\phi_{b\lambda 2}$ are rotations due to the sample birefringence. The optical rotation due to the Faraday compensator, ϕ_f , is known so it can be easily removed. The optical retardation for a birefringent sample is a function of both the wavelength and the birefringence $|n_o - n_e|$. In case of the cornea, the birefringence quantity $|n_o - n_e|$ is known to be constant with wavelength, a behavior attributed to the *form* birefringence of the cornea (176, 179, 180). However, both the rotation due to glucose and rotation due to the birefringence are wavelength dependent, but the relationship between $\phi_{b\lambda 1}$ and $\phi_{b\lambda 2}$ is fixed as long as the wavelengths are known (635 nm and 532 nm in the case of our preliminary results). Using the MLR scaled subtraction methodology, the known scaled change in rotation due to the birefringence can be accounted for with respect to

wavelength and, further, MLR can be used to extract the glucose concentration as shown in Equation 2.10. The MLR analysis accommodates the offset K_1 due to birefringence and normalizes for the slopes K_2 and K_3 as a function of wavelength for a given glucose concentration (35).

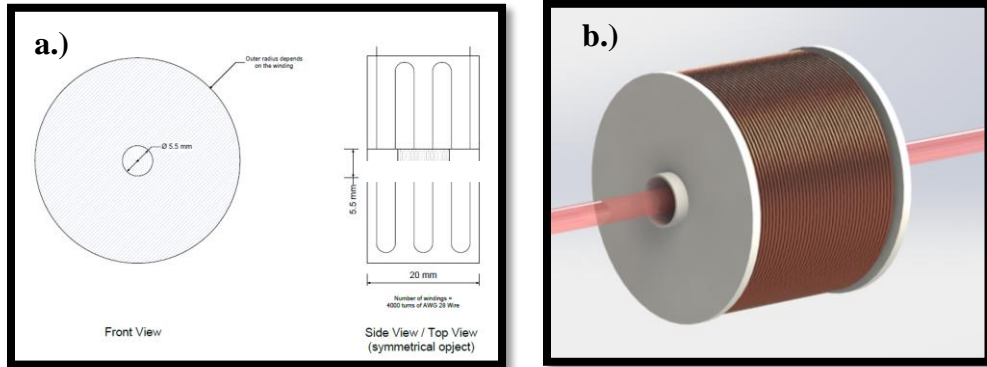


Figure 2.7: (a) CAD dimensions of air-core solenoid modulator and (b) CAD rendering of air-core solenoid device with eight rows of 26 AWG wire wound.

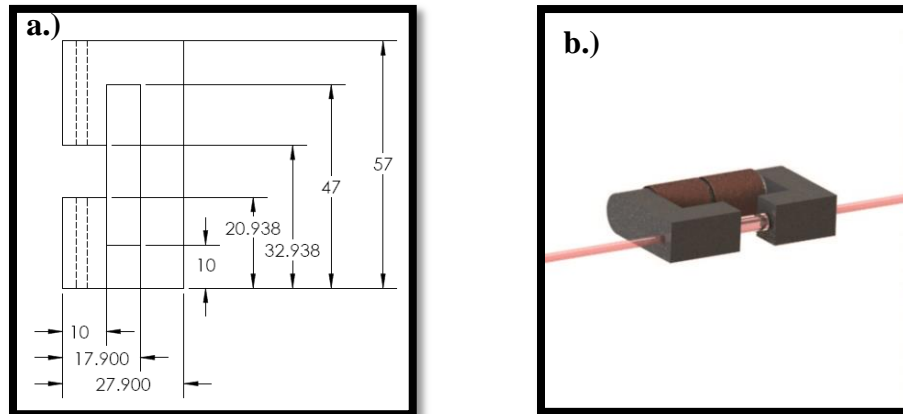


Figure 2.8: (a) CAD schematic showing dimensions of the custom-machined ferrite modulator with a C core geometry and (b) CAD rendering of air gapped high permeability rotator design.

2.3. Required Components and Modeling Time Delay for Clinical Use

2.3.1. In Vivo Experiments in Rabbits

The main goal of this study focuses on acquiring *in vivo* rabbit data to determine if the correlation exists between blood and aqueous glucose concentrations. With the

collected data a model and validation of the dual-wavelength polarimetric signal to determine if, the system is capable of overcoming time-varying birefringence *in vivo*. An accurate mathematical model of the current optical train of the polarimetric system including a representative eye model is critically important toward understanding the overall effect of this noise source compared to other changes in the signal and can aid in anticipated changes in the design of the polarimetric system. To this end, an accurate mathematical model of the current optical system was generated, utilized previously for the *in vitro* and *ex vivo* testing, in order to simulate the system output results. A Multiple Linear Regression (MLR) method, in MATLAB, using values for corneal birefringence and glucose concentration from the experimental models (*in vivo* trials and excised rabbit corneas) were developed to compensate for birefringence in the presence of motion. The simulation assesses different glucose concentrations and explicit demonstration of the MLR technique.

This simulation was used to validate recent *in vitro*, *ex vivo*, and *in vivo* experimental findings and the current dual-wavelength system architecture. Additionally, variations in net retardance and the effect it may have on the system performance were evaluated and compared to experimental findings. Three NZW rabbits will be utilized over three studies per rabbit. The protocol utilized was AUP #2010-5 approved by TAMU IACUC on 4-2-2010, full protocol attached as Appendix A & B. During each *in vivo* rabbit trial the output voltages from the lock-in amplifiers and compensation voltages required to null the system, for each wavelength, were collected at a sample rate of 5 ms over the duration of the trial via the LabVIEW VI on the PC shown in Figure 2.4. The compensation voltage data for each wavelength was then averaged over a minute around the time of each blood drawl and the calculated values were used for both the individual linear regression analysis and the dual wavelength MLR analysis. A glucose prediction model was created for each individual rabbit trial. The known glucose concentration was determined from the collected blood samples using an YSI 2300 STAT Plus™ Biochemistry Analyzer (YSI Life Sciences, Yellow Springs, OH) at the time of each study. For the individual regression models, the predicted glucose concentrations were

calculated using an equation of the form $\text{Glucose}_{\text{pred}}=m*[V(t)]+b$ where $V(t)$ is the averaged compensation voltage signal for the individual wavelengths and m and b are calibration coefficients calculated by the regression models. The MLR predicted concentrations for each individual rabbit were determined from models of the form $\text{Glucose}_{\text{pred}}=m_2*[V_2(t)]+ m_1*[V_1(t)]+b$ where $V_1(t)$ and $V_2(t)$ are the time averaged compensation voltages required to null the system for each individual wavelength and b , m_1 and m_2 are calibration coefficients calculated by the multiple linear regression model. The predictive measurements utilized in the individual rabbit trials were calculated without accounting for the time delay associated with the glucose concentration of aqueous humor. Due to the variability in the position of the entrance beam on the cornea between rabbit trials, the regression analyses used for predicting glucose concentration were calculated individually for each rabbit trial. Due to the changes in light coupling between rabbit trials, quantitative real-time glucose measurements were not calculated. Rather, all predicted glucose measurements were calculated retrospectively during post processing of the data.

2.3.2. Design, Build, and Characterize a High Permeability Ferromagnetic, Air Gapped Magneto-Optic Faraday Rotator

For this portion of the study, improvements for design of a pre-clinical cart-based dual-wavelength system were identified and evaluated. Mainly alternative approaches for Faraday rotators and compensators were explored in addition to methods for reducing the electromagnetic cross talk between the multiple existing coils when placed in close proximity. Additionally, a novel high permeability ferrite based air gapped magneto-optical polarized light modulator (MOPLM) design is put forward that overcomes several of the limitations of the air-core solenoid design used in the current polarimeter. The design and characterization of the device were evaluated to verify the key advantages of the high permeability MOPLM device over established Faraday based AC modulation designs namely, that with a smaller overall device size, higher AC modulation frequencies can be achieved while still providing a higher MFD for a given driving power. A magnetic core design can enormously concentrate the strength and

increase the effect of magnetic fields that can be produced by electric currents (172, 175, 178, 181).

Specifically, a ferrite core allows for a reduction in the number of turns of wire required to achieve similar AC modulation compared to air-core designs, which leads to significantly lower DC resistance values. The combination of a high permeability, low DC resistance, and tunable inductive response in the design using ferrite cores allows higher frequency modulation to be achieved without reducing the maximum generated MFD. This allows for significant advantages in terms of overall device size and power compared to traditional air-core Faraday based optical modulators (175). Theoretically, if an optimized winding type is used such as litz wire, modulation up to the rated material limit of 200 kHz should be achievable. This allows for faster data collection (in the 10 microsecond range) providing better signal-to-noise ratio and more data points per unit time for post processing. The current solenoid devices used require a high current source, impedance matching, and modulation at 1 kHz (or rather one millisecond).

The new design will be characterized using both AC and DC power and compared to theoretical values calculated based on a generated model for the high permeability, C core design, shown in Figure 2.8.

2.4. Materials and Method

2.4.1. In Vivo Animal Protocol

Three NZW rabbits weighing between 2.2-3.8 kg were utilized during the *in vivo* experiments. Each rabbit was tested 3 times over a period of 5 months. The rabbits were anesthetized using an intramuscular injection of ketamine, xylazine, acepromazine, and saline solution combination. The combination resulted in a 21 cc cocktail consisting of 42.9 mg/ml of ketamine, 8.6 mg/ml of xylazine, 1.4 mg/ml of acepromazine, and 7.2 ml of saline solution. The cocktail was administered at a dose of 1 ml/ 1.5 kg body weight intramuscularly. Once the rabbit was anesthetized, it was placed into a custom built rabbit mold and the eye coupling mechanism was coupled to the eye as shown in Figure 2.6. Saline solution was added to the eye coupling device to act as an index matching

solution. Data was obtained from the system and blood was collected from the animal throughout the experiment. Approximately 1 ml of blood was collected every 10 minutes and placed into a heparin (Beckton Dickinson (BD), Sparks, MD) and a fluoride (Beckton Dickinson (BD), Sparks, MD) blood collection tube to prevent the blood from clotting. After each blood draw a combination of 1 ml of heparin saline was used to flush through the catheter tubing in order to reduce the risk of clotting. The heparin saline syringe and blood collection syringes were connected to a 19-21 gauge SURFLO® Winged Infusion set (Terumo, Somerset, NJ), that was inserted into the central auricular artery of the rabbits left ear for blood collection via a standard bore 3-way stopcock (Baxter®, Deerfield, IL). Glucose induction was achieved via two methods. Initially, blood glucose was elevated using the xylazine in the anesthetic cocktail. Xylazine has been shown to block the pancreatic insulin release via stimulation of parasympathetic receptors (182, 183). The resulting effect creates a temporary rise in the blood glucose level and also in the aqueous humor of the eye (182, 183). This side effect is beneficial in our particular case because it provided for large changes in glucose without having to induce diabetes in the animal. Blood samples were collected from the rabbits using a 19 gauge needle and syringe every 10 minutes until the anesthetic began to wear off, approximately 45 minutes. A second method to increase glucose levels utilized bolus injections of 25% glucose solution. The glucose solution was administered using a 22-24 gauge IV catheter (Terumo, Somerset, NJ) inserted into one of the marginal ear veins on the rabbit's left ear. After blood collection, the blood glucose was measured using AlphaTRAK (Abbott, Abbott Park, IL) and Aviva ACCU-CHEK (Roche, Switzerland) handheld meters along with a YSI 2300 STAT Plus™ Biochemistry Analyzer (YSI Life Sciences, Yellow Springs, OH) for comparison to the acquired signal. The blood glucose level ranged from 70 mg/dL to an upper limit near 320 mg/dL based on the measurements obtained using the YSI analyzer. Note that most commercially available hand-held glucose monitors are made to work within this range of glucose concentrations with target accuracy of within 20% of a laboratory standard measurement (184, 185).

2.4.2. Improved Faraday Modulator Design

A method was developed to modulate the plane of polarized light using a high permeability ferrite core design. A proof-of-principal, optical Faraday Effect device has been constructed and tested. Magnetic fields were generated to provide up to 1 degree of rotation at frequencies of DC up to 10 kHz using a terbium gallium garnet (TGG) crystal rod. Optical modulators used for high frequency (HF) applications such as a Pockels cell, liquid crystal rotators, or other electro-optic (EO) designs typically sacrifice the precision of the rotation since they are used for large modulation angles (depths of up to 90°). Conversely, air-core optical techniques that are commonly used for fine rotation (depths of $\pm 1^\circ$) of the polarization plane have been limited primarily to direct current (DC) and low frequency alternating current (AC) applications (35, 82, 158, 171, 175).

In this study, a proof-of-principal high permeability ferrite based air gapped magneto-optic (MO) polarized light modulator (MOPLM) is put forward that overcomes some of the limitations of air-core designs. The device characterization and preliminary results are presented to show key advantages of the high permeability MOPLM over established Faraday based AC modulation designs, namely; given a smaller overall device size, higher AC modulation can be achieved while still providing a higher magnetic field density (MFD) for a given driving power (173-175).

As shown in Figure 2.8, the ferrite MOPLM was constructed with an inductive coil wrapped around a ferromagnetic core with an air gap and a through hole to serve as an optical path. One major advantage of using a ferrite design is that through the proper selection of the core material, geometry, dimensions, and length of the air gap, design parameters can be adjusted to optimize both performance and MFD generation for a large range of operating frequencies (35, 171, 173). A photograph of the designed MOPLM is shown in Figure 2.09b. An optical rod is placed inside the air gap, as shown in Figure 2.09a, with the facets aligned with the thru hole in the core. As a current is supplied to the conductive coil, a proportional magneto-motive force (MMF) is produced in the ferrite core. This magnetic field (MF) propagates through the core and creates a relatively uniform MFD across the air gap.

Faraday effect dictates that by producing a MF parallel to the direction of propagation of light through a magneto-optic material, the amount of rotation in the plane of polarization (β) of light traveling through the MO material is found to equal the product of the applied magnetic flux, the Verdet constant (V), and the length of the MO crystal (L).

$$\beta = V \times B \times L \quad (2.12)$$

Excitation of the coiled wire with an AC current allows the plane of polarization of the incident light to modulate at a given frequency, with a modulation depth of $\pm \beta$. Polarimetric modulation techniques are commonly used for determining concentration information of chiral molecules (158, 175). Theoretical magnetic flux generated in a given core can be calculated using Equation 2.13.

$$B = \frac{N \times i}{A_{\text{gap}}} \times \frac{1}{\left(\frac{l_{\text{core}}}{\mu_r \times \mu_0 \times A_{\text{core}}} + \frac{l_{\text{gap}}}{\mu_0 \times A_{\text{gap}}} \right)} \quad (2.13)$$

Where (B) is MFD, (A_{gap}) and (A_{core}) are the areas of the air gap and core respectively, (i) is the current supplied to the wire, (N) is the number of turns of wire, (μ_r) is relative permeability of the core, (l_{gap}) and (l_{core}) are the length of the air gap and magnetic core, and (μ_0) is the permeability in a vacuum.

The optical setup used to measure the AC modulation depth is illustrated in Figure 2.09a. The optical source used was a 635 nm diode laser. The beam was passed through a Glan-Thompson linear polarizer, (P), to convert it to horizontally linearly polarized light. This linear polarized beam passed through the MOPLM device. Separate MOPLM devices were designed to modulate at frequencies between 1.09 kHz-10 kHz. The MO material utilized in this design was a terbium gallium garnet (TGG) rod (178). TGG is used in Faraday applications because it offers a large Verdet constants ($\sim -134 \text{ rad/ T} \cdot \text{m}$) (178, 186). The ferromagnetic material selected for the core design was a soft ferrite known as M25 (a composition of manganese and zinc, MnZn). Selection of the ferrous material resulted after careful evaluation of trade-offs between saturation flux density, energy loss and cost of several available magnetic materials. The material, M25 offers ideal magnetic and low loss properties is designed for high magnetic flux capabilities and is intended for applications involving HF's, up to 200 kHz (174, 181). The MOPLM M25 cores were custom-machined, by ELNA Magnetics, into a gapped C core geometry. Additionally, the core permeability is known to vary with changes in frequency (181).

Three cores were wound with different numbers of turns. Two ferrite cores were individually wrapped with 26 AWG magnetic wire and the third core was wrapped with 30 AWG wire. The first coil was wrapped with 324 turns, the second with 91, and third with 170 turns. An air-core solenoid, with 3364 turns, was also tested in place of the MOPLM device for comparison.

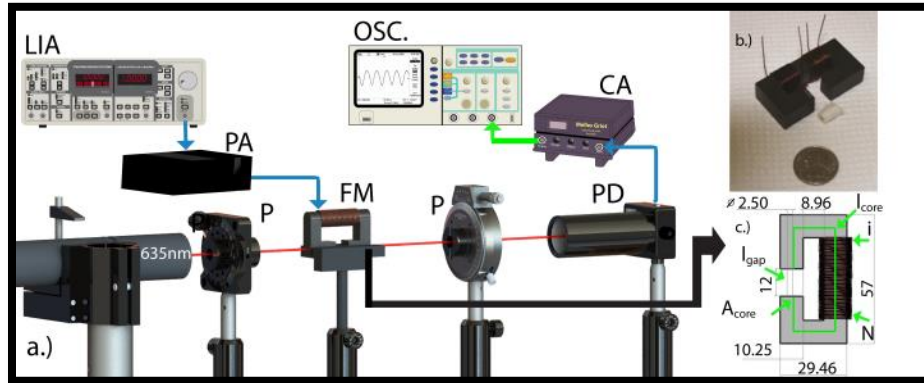


Figure 2.9: (a) CAD rendering of setup used to measure the polarization rotation; (b) photograph of MOPLM; and (c) dimensional schematic of the ferrite modulator in millimeters.

The MOPLM devices were driven with a sinusoidal signal generated by a lock-in amplifier (LIA) after being passed through a high gain audio amplifier (PA). After the light beam exited the MOPLM device, it passed through an analyzer, positioned perpendicular to the initial polarizer. The beam was converted into an electronic signal using a PIN photodiode (PD). The signal was amplified utilizing a wide-bandwidth current amplifier (CA) and analyzed using an oscilloscope. The resulting modulation depth in the plane of polarization was measured for each of the devices. Determining the degree of optical rotation was accomplished by carefully rotating the analyzer using a high precision optical rotation stage and evaluating the voltage and frequency response on the oscilloscope. The MFD required across the TGG rod to produce the rotation in the plane of polarization, equivalent to the angle measured from the polarimeter setup, was calculated using Equation 2.12. The measured change in polarization for each power setting was then compared to the theoretical values calculated using a combination of Equations 2.12 and 2.13.

Magnetic flux calculations and optical rotation measurements were determined with each device driven by DC power supplied with currents ranging from 0A to 1A. The optical setup

used for DC measurements was similar to the polarimetric setup utilized in acquiring the AC measurements; however, for DC testing the modulators were driven by a DC power supply in constant current mode. Additionally, a commercial PAX-series-polarimeter was used to measure the polarization rotation. Thus, for DC testing, the optical elements after the MOFR, namely the analyzer and PIN photodiode, were removed and replaced with the PAX. Change in the azimuth angle was measured over a range of voltages and currents for each of the rotator designs. Using the rotation from the polarimeter and Equation 2.12, the MFD was determined utilizing and compared to the theoretical MFD calculated using Equation 2.13. For each device, testing over the range of currents was conducted by increasing the current from 0 A to 1 A and then decreasing it from 1 A to 0 A.

The inductance, magnitude impedance (AC resistance), and Q values were measured for DC, 100 Hz, 1 kHz, and 10 kHz for each of the designs. The AC resistance values increased with frequency for all four designs but the amount of increase was two orders of magnitude less for the 324 turn ferrite core design and three orders of magnitude less for the 91 and 170 turn designs. Similar to traditional inductor design theory, using a ferrite core allows for fewer turns of wire (because of the higher material permeability) resulting in a lower resistance and decreased insertion loss with respect to an air-core design. The increased core permeability allows for an increase in inductance for a given number of turns. As the number of turns are increased the inductance of the modulator increased respectively from 1.29 mH for the 91 turn ferrite to 154.27 mH for the 3364 turn air-core design.

2.5. Results and Discussion

2.5.1. In Vivo Experiments in Rabbits

The results of the dual-wavelength polarimetric system for determining glucose concentration inside the anterior chamber of the NZW rabbits are shown in Figures 2.09-2.12 below. After a series of initial tests to establish the procedure for blood collection and eye coupling, the experiments were repeated 9 times using 3 NZW rabbits (n=3) across multiple days. For each rabbit trial, data was collected continuously over a period of approximately 45 minutes, which allowed for maximum change in the glucose concentration due to the anesthesia (182, 183). For analysis of the data, the voltage

required to null the compensating faraday rotators within the system for each of the individual wavelengths was averaged over a one minute period around the time of the blood collection. The red line in Figures 2.09-2.123 represent the ideal result where predicted glucose concentration is the same as the actual glucose concentration over the ranges measured in the animal trials.

2.5.1.1. Results Within a Rabbit: On a Single Day

As illustrated in Figure 2.10a and 2.10b the individual glucose predictions are depicted within one rabbit on a single day for the 532 nm (left) and 635 nm (right) wavelengths using a standard linear regression analysis. As shown the mean absolute relative difference (MARD) within a rabbit on a single day was calculated to be 12% (32.7 mg/dL standard error) and 14.7% (40.4 mg/dL standard error). In addition, the correlation coefficients for the 532 nm and 635 nm wavelength data respectively were 0.853 and 0.776 using a linear regression approach. As shown, the single wavelength data is unable too accurately predict the glucose concentration *in vivo* in the presence of birefringence with motion. Although the data from each wavelength had large errors, those errors showed a trend with each other (i.e. common mode noise at each wavelength due to motion) and thus, by using the two wavelengths with a multiple linear regression (MLR) model, the accuracy improved tremendously to a MARD of 5.4% (19.9 mg/dL standard error). In addition, the data had an improved linearity with a correlation coefficient of 0.959 and, when plotted on a Clarke error grid, showed 100% in zones A+B as depicted in Figure 2.10c. The time profile for the predicted glucose concentration and measured glucose concentration of an individual rabbit trial is depicted in Figure 2.11.

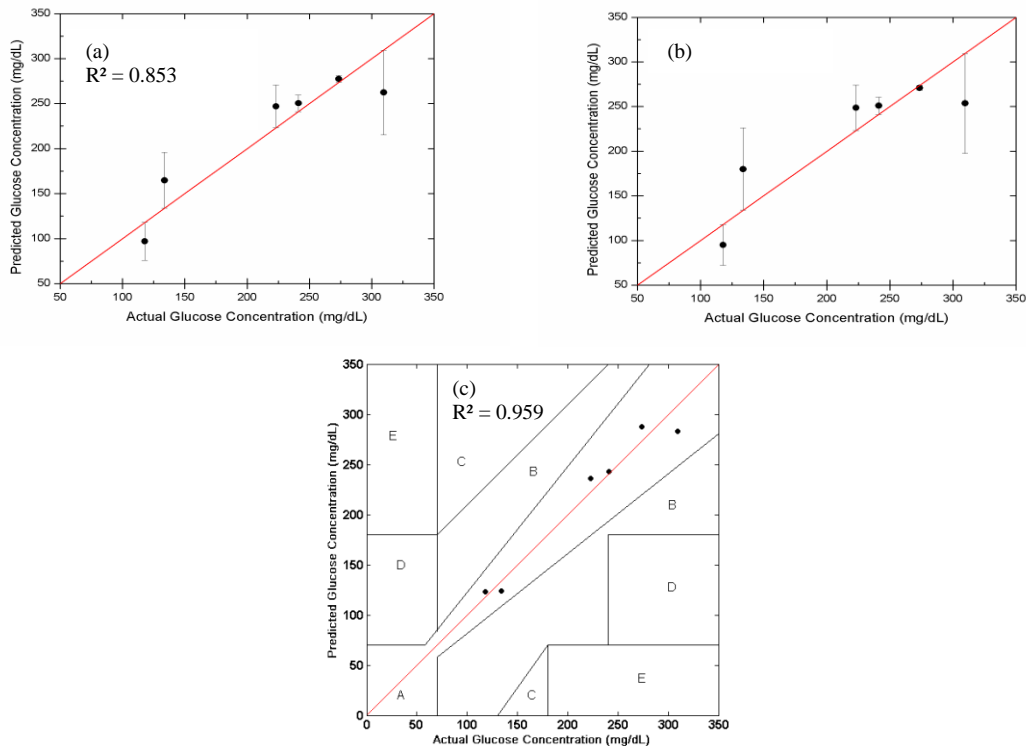


Figure 2.10: *In vivo* glucose estimation for a single day using a linear regression model for (a) the individual 532 nm laser, (b) the individual 635 nm laser, and (c) the combined laser wavelengths shown on a Clarke error grid. Note the large error (above 30 mg/dL) and MARD (above 10%) for each of the individual wavelengths because of the motion, due to cardiac cycle and respiration, but that the error and MARD are significantly reduced (20 mg/dL and 5.4%) relative to the individual wavelength models when both wavelengths are used.

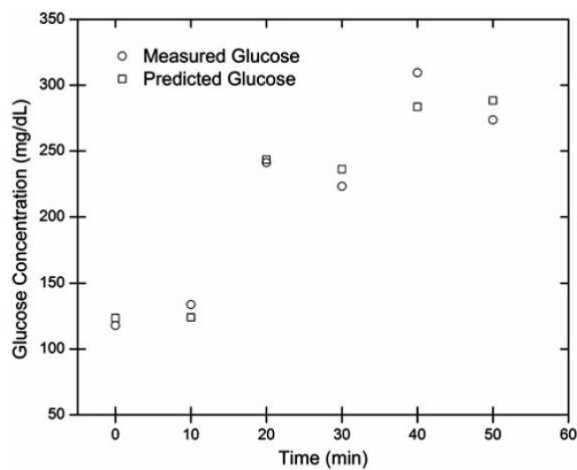


Figure 2.11: *In vivo* time profile of measured and predicted glucose concentrations for an individual rabbit trial.

To determine the frequency or source of the motion artifact in the individual studies a portion of the feedback signal provided to the system as a function of was broken into the individual frequency component responses using a fast Fourier transform (FFT). In an ideal case for the lock-in amplifier output, which is a DC value proportional to the signal of interest, would produce a DC value only. The resulting frequency domain signal for each of the individual wavelengths for two separate in vivo runs are shown in Figures 2.12 below. In both studies and each wavelength below the FFT resulted in the largest component peak other than at DC occurring in the range near 1.0 – 1.1 Hz. The frequency component variation in the signal here is believed to be due to the motion artifact caused by respiratory cycle. The respiratory cycle in breaths per minute for NZW rabbit's under anesthesia using ketamine/xylazine/acepromazine has been reported to vary between 40 to 90 breaths per minute. The overall rate varies somewhat due to time of administration of the anesthesia (182, 183). Other sources of motion artifact at around 3 Hz observed in previous studies were not observed in this study.

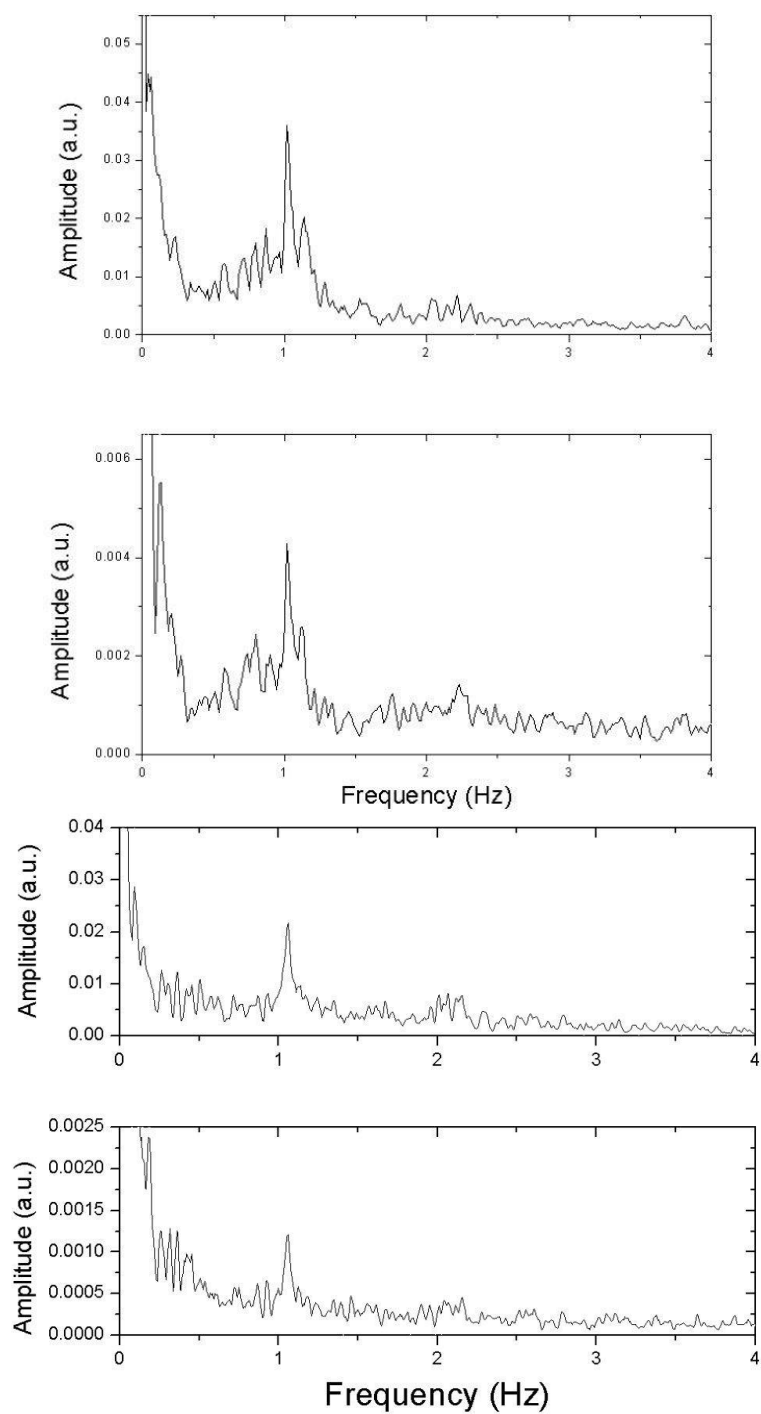


Figure 2.12 (A) Spectral analysis of the time-based polarimetric feedback signal – Run 1; top: 635-nm feedback, bottom: 532-nm feedback. (B) Run 2; top: 635-nm feedback, bottom: 532-nm feedback.

2.5.1.2. Results Within Each Rabbit: Across Multiple Days

The results within a rabbit ($n=3$) across three days are shown in Figure 5 for Rabbit_1, Rabbit_2, and Rabbit_3. For this comparison the regression models were again formed using the data collected for each individual trial separately and then the overall standard error in estimation was calculated for the individual rabbits ($n=3$). Rabbit_1 resulted in MARDs of 16.95% and 8.53% (33.08 mg/dL and 22.06 mg/dL standard errors) for the individual wavelength regression models of the 532 nm and 635 nm wavelengths respectively. Using dual wavelengths and the MLR analysis provided a MARD of 4.08% (9.35 mg/dL standard error). The MARDs for Rabbit_2 were 10.32% and 10.47% (35.26 mg/dL and 35.78 mg/dL standard error) for the 532nm and 635 nm individual wavelength models. The dual wavelength MLR model resulted in a reduction in the MARD to 3.58% (14.14 mg/dL standard error). For Rabbit_3, the MARDs using individual 532 nm and 635 nm wavelengths were 8.50% and 11.73% respectively (20.58 mg/dL and 25.31 mg/dL standard errors). The dual wavelength MLR approach for Rabbit_3 resulted in a reduction of the MARD to 5.13% (11.34 mg/dL standard error) which is at the accuracy limit of the system. Note that the dual wavelength data in Figure 2.13c was placed on a Clarke error grid and showed 100% of the data within the A+B zone for all three rabbits (Rabbit_1, Rabbit_2, and Rabbit_3) across days. All three rabbits showed 100% of data within zone A.

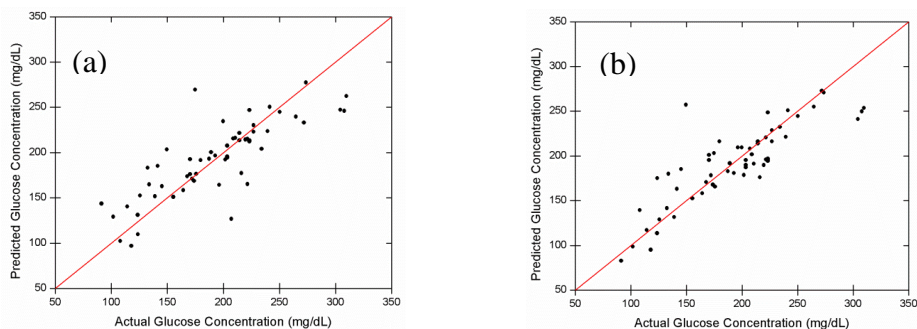


Figure 2.13: *In vivo* glucose estimation using linear regression (a) with 532 nm wavelength and (b) 635 nm wavelength as well the (c) dual wavelength MLR glucose estimation for all 9 rabbit studies (3 rabbits across 3 separate days) shown on a Clarke error grid. Note the large error (above 25 mg/dL) and MARD (above 10%) for each single wavelength because of the motion but that the error and MARD are significantly reduced (11.66 mg/dL) and MARD (4.49%) relative to the single wavelength models when both wavelengths are used.

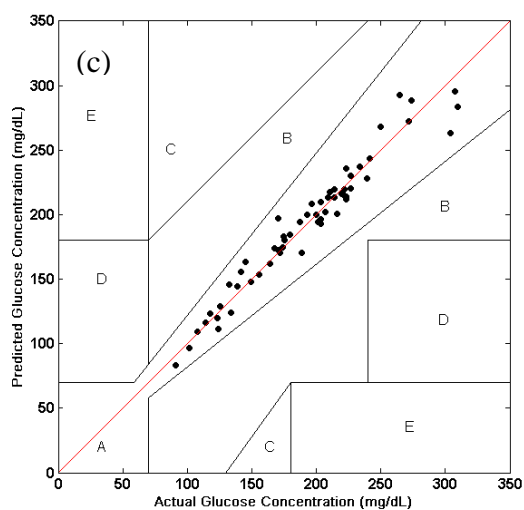


Figure 2.13 Continued

2.5.1.3. Results for All 3 Rabbits: Across Multiple Days

The linear regression analysis for the individual 532 nm and 635 nm wavelengths for all nine trials are represented in Figure 2.13a and 2.13b respectively. The MARDs for the 532 nm and 635 nm single wavelength models were calculated to be 12.05% and 10.47% (29.87 mg/dL and 27.34 mg/dL standard error), respectively, over all trials. Using individual dual wavelength MLR analysis for each trial and then comparing MARD across all the trials produced a MARD of 4.49% (11.66 mg/dL standard error) as depicted in Figure 2.13c. As shown in Figure 2.14a and 2.14b the individual wavelength linear regression models appear too once again present a poor prediction model around the actual glucose measurement line shown in red. The MLR analysis for all nine studies is illustrated below in Figure 2.14c. The data demonstrates that dual wavelength polarimetry can effectively predict glucose concentrations within the aqueous humor in the presence of motion induced corneal birefringence given the position of the beam remains relatively the same. In Figure 2.14c, it is clear that the combined MLR analysis provides a much tighter grouping of predicted glucose concentrations with respect to the actual glucose concentrations over the entire rabbit study with an MARD of 4.49% (11.66 mg/dL standard error). In addition, as depicted in 2.14c, when plotted on a Clarke error grid, 100% of the points were in zone A+B with 100% of the hits falling in zone A.

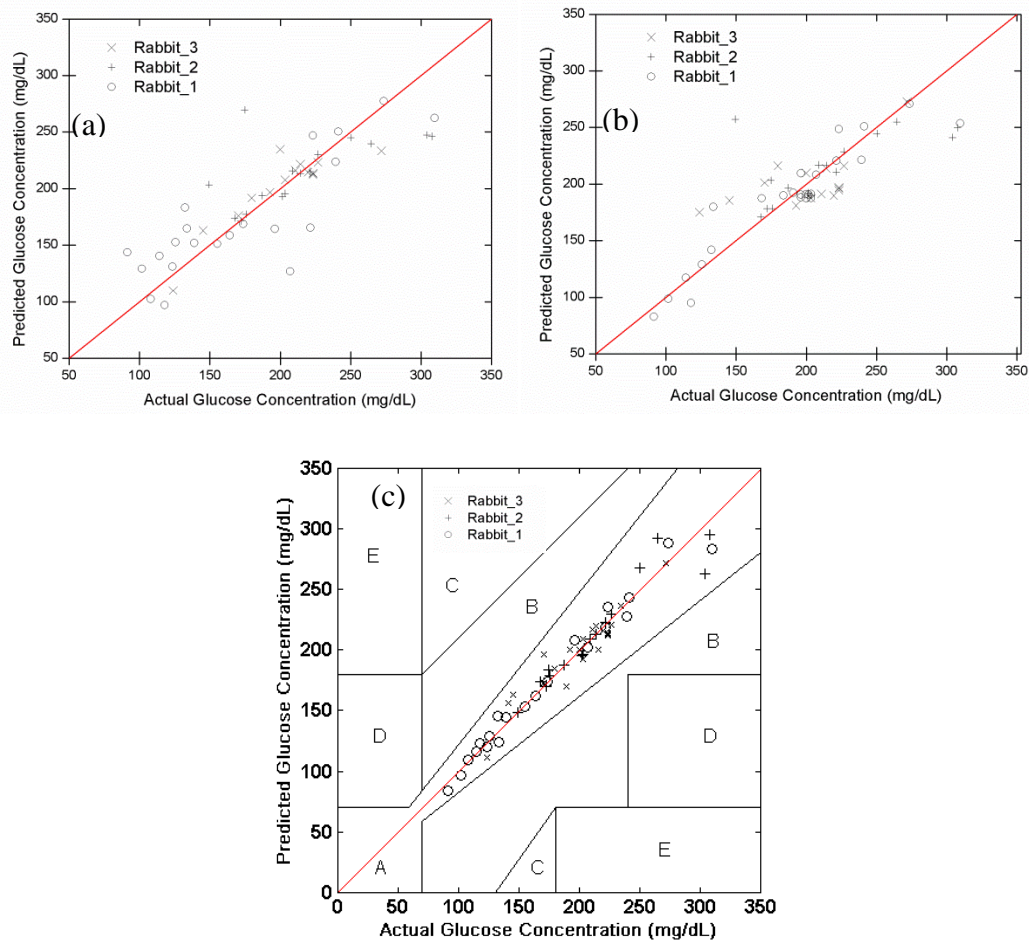


Figure 2.14: *In vivo* glucose prediction within rabbits across multiple days using linear regression model for individual wavelengths (a) 532 nm and (b) 635 nm as well as the (c) dual wavelength data using MLR shown on a Clarke error grid. Note the large errors within rabbit (20-35 mg/dL) for each single wavelength because of the motion but that the error is reduced (9-14 mg/dL) relative to the single wavelength models when both wavelengths are used.

2.5.2. Faraday Device Magnetic Field Measurements

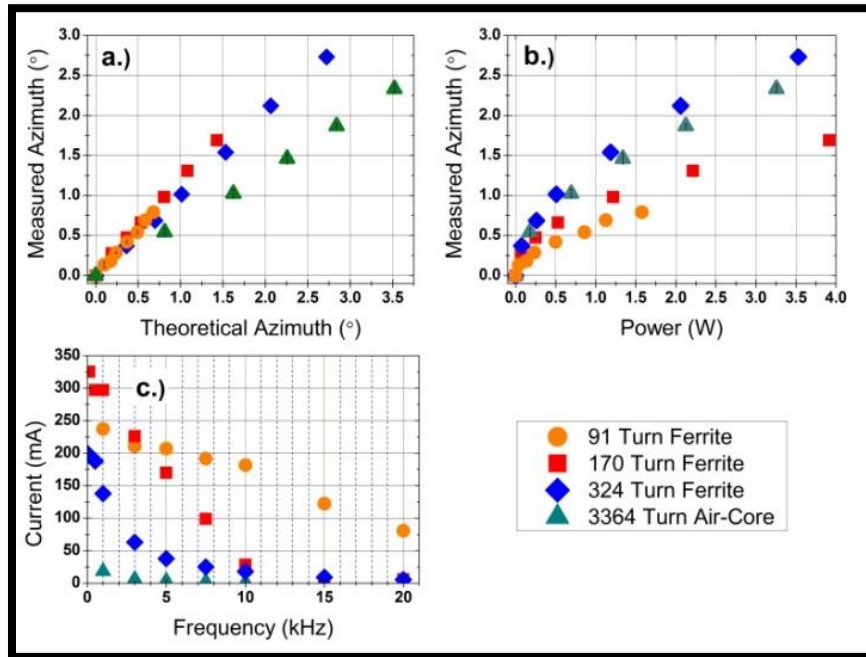


Figure 2.15: Mean value of each device comparing (a) measured and theoretical change in DC rotation; (b) DC power with rotation; and (c) change in current with frequency.

The measured versus theoretical azimuth angle for the DC signal is shown in Figure 2.15a. The measured azimuth versus power is shown in Figure 2.15b. Using the measured voltage and current, the power required to supply rotation was calculated. The rotation was measured twice and the Azimuth values were effectively the same. The increased energy storage capability of the ferrite design allowed for increased magnetic field strengths to be generated with a design of fewer turns of wire, resulting in a reduction in the resistance of the device. This provided a more efficient design with a higher percentage of supplied power converted into magnetic field across the air gap. The 324-turn ferrite device provided equivalent rotation with approximately 26.7% less power than the 3364 comparable air-core design as shown in Figure 2.15b. The DC measurements in the azimuth angle change with respect to current change for the 324, 91, and 170 turn coils confirmed that rotation of the plane of polarization was achievable using this technique. This showed the change in rotation increases linearly with increase in current. The

measured change in azimuth corresponds very well with the theoretical calculations for each coil, as shown in Figure 2.15a. This can be used for optimization of the coil to provide maximum change in polarization with minimum power at HFs. Specifically, reducing the insertion loss into the coil and lowering the resistance increases the amount of supplied power converted into MF strength across the TGG rod.

The measured changes in current with respect to frequency (Figure 2.15c) were taken to determine if the ferrite design could provide modulated rotation in the degree of polarization from 1 kHz to 10 kHz, with and without impedance matching. For AC testing, the 3364 turn air-core device was used for comparison. While the 3364 and 324 turn devices share a similar profile with respect to change in current and frequency, the current for the ferrite based design is significantly higher at frequencies below 5 kHz. The measured current through the 91 and 170 turn devices decreased at a much slower rate producing a more prolonged profile with respect to frequency. The reduced change in current with frequency can likely be attributed to the lower number of turns of wire and layers of wire stacked together. Both added turns and multiple layers of wire greatly increase the effect of resistance with frequency of the device. As multiple layers of conductor carrying AC current are packed closely in a small region, proximity effects can greatly increase the resistance of adjacent rows within a device as compared to the measured DC resistance.

Impedance matching was not required to achieve 1 kHz modulation for the 324 and 91-turn ferrite MOPLMs. At 1 kHz, the 324-turn device generated a modulation depth of $\pm 0.719^\circ$ in the plane of polarization when a current of $192.33 \text{ mA}_{\text{pk-pk}}$ was supplied. This is over 100X higher than the air-core device without impedance matching. Additionally, lower voltage and power could be used to provide an equivalent degree of rotation in the 324-turn ferrite in comparison to the 3364-turn air-core coil. This is likely a result of the impedance within the 324-turn coil being considerably lower for HFs than the air-core device and, therefore, the equivalent power could achieve a larger degree of rotation than that of the air-core. Without impedance matching circuitry, a 2f signal at 1 kHz and above with the 3364-turn air-core device was virtually nonexistent, making it hard to obtain any meaningful measurements for the device. The current also decreases rapidly for the 324-turn ferrite coil, less rapidly for the 170-turn ferrite,

and only slightly for the 91-turn ferrite device. Further, as the frequency of the supplied signal was increased, the impedance of the devices began to increase, causing the signal for all four devices to decrease. Results were obtained for the 1f and 2f signal of the 324-turn ferrite modulating at a 1f frequency of ~ 1 kHz. The addition of a capacitor measuring 65.6nF in series with the 324-turn device created a resonant circuit tuned to 5.03 kHz, which allowed for the generation of a measured modulation depth of $\pm 0.875^\circ$ with 231.51mA_{pk-pk} of current supplied. Similarly, an impedance matched circuit (using a 15nF capacitor) at a frequency of 9.23 kHz provided modulation of $\pm 0.5^\circ$. This shows that through use of impedance matching, HF modulation is achievable with this design. However, even with the added impedance matching the 3364-turn air-core produced un-measurable rotation above 1 kHz.

The ferrite devices demonstrated that modulated Faraday rotation is achievable with lower power consumption. Using the 324-turn ferrite core design, modulation in the degree of polarization was achieved at HFs, however, the device required impedance matching to achieve modulation of greater than a half degree at frequencies up to 10kHz. Figures 2.15b and 2.15c illustrate that with the ferrite design, the device could be optimized to achieve more power or to have less turns allowing a HF response. This is displayed for the 91 turn coil in Figure 2.15c and the low power option such as the 324-turn. However, the 324-turn design sacrifices HF functionality unless impedance matching is utilized. For each design, no heating issues were observed with the ferrite core. However, as operating frequency is further increased and hence more power required, heating of the core over time will need to be further characterized.

3. MODELING OF CORNEAL BIREFRINGENCE*

3.1. Introduction

For polarimetry to be used as a noninvasive technique for blood glucose monitoring, the polarized light signal must be able to pass from the source, through the body, and to a detector without total depolarization of the beam. Since most tissues, including the skin, possess high scattering coefficients, maintaining polarization information in a beam passing through a thick piece of tissue (i.e. 1 cm), which includes skin, would not be feasible. Even tissue thicknesses of less than 4 mm incur 95% depolarization of the light due to scattering from the tissue. In addition, in these highly scattering tissues there are a large amount of proteins and other chiral substances that have a much stronger rotation than that due to glucose making it very difficult to measure the millidegree rotations required for physiologic glucose concentrations. Thus, due to the lack of scatter, the aqueous humor of the eye as a site for detection of *in vivo* glucose concentrations has been suggested as an alternative to transmitting light through the skin (28-42). For the polarimetric approach, the cornea and fluid contained in the anterior chamber and the aqueous humor not only provide a low scattering window into the body but since the aqueous humor is virtually devoid of proteins, the main optically chiral molecule is glucose.

Unlike on-line processing systems that measure relatively high sugar concentrations (grams) and allow for longer path lengths (10 cm), the *in vivo* glucose concentration is smaller and, if the eye is to be used as the sensing site, the pathlength in an adult human eye measures between 1-1.2 cm with a volume of approximately 250 μL (187). Advances in polarimetric instrumentation have only recently made it possible to measure the small rotations due to glucose at physiological levels. For example, at a wavelength

* Part of this chapter is reprinted from Pirnstill, C.W., Cummins, B., Coté, G.L., and McNichols, R.J., (2014). Glucose Monitoring. Biomedical Photonics Handbook, Second Edition, CRC Press: 47-76 with kind permission of CRC press.

Part of this chapter is reprinted from Pirnstill, C.W., Malik, B.H., Gresham V.C., and Coté, G.L. "In Vivo Glucose Monitoring Using Dual-Wavelength Polarimetry to Overcome Corneal Birefringence in the Presence of Motion," *Diabetes Technol. Thera.* 14(9), (2012), with kind permission of Mary Ann Liebert, Incorporated.

Part of this chapter is reprinted from Malik, B.H., Pirnstill, C.W., and Coté, G.L., "Dual Wavelength Polarimetric Glucose Sensing in the Presence of Birefringence and Motion Artifact Using Anterior Chamber of the Eye Phantoms," *J. Biomed. Opt.* 18(1), 037012 (2013), with kind permission of SPIE.

Part of this chapter is reprinted from Pirnstill, C.W., Yu, Z.F., and Coté, G.L., "Modeling the optical coupling across the anterior chamber of the eye towards polarimetric glucose sensing," *J. Biomed. Opt.* (2015), with kind permission of SPIE.

of 670 nm (red), glucose will rotate the linear polarization of a light beam by approximately 0.4 millidegree per 10 mg/dl for a 1 cm sample pathlength. In order to measure such small rotations, a very sensitive and stable polarimeter must be employed. Throughout the past few decades, many researchers have investigated the development of such sensitive devices (30-42). The primary approaches being investigated today include a light source (typically low powered lasers), a means of modulating the plane of polarization (photoelastic modulator, Faraday rotator, etc.), and a means of detecting and demodulating the signal, typically by using a lock-in amplifier or some means of heterodyne detection.

The eye as a sensing site for polarimetric glucose monitoring, however, is not without its share of problems that need to be overcome. Although the eye is great at coupling light into the body for the purpose of vision, it provides a couple of challenging problems when it is desired to couple the light into and back out of the anterior chamber of the eye as required for glucose monitoring. In particular, for polarimetric monitoring, the light must travel across the anterior chamber of the eye but, due to its curvature and change in the refractive index, the eye naturally tries to focus all the light impinging on it toward the retina. In addition, the cornea is birefringent, which means it can change the state of polarization of the light (i.e. somewhat like a quartz crystal) and this change is variable in the presence of eye motion, which can confound the polarization signal due to glucose. Using a lock-in amplifier the amplitude of the second harmonic or twice the modulation frequency of the signal can be monitored continuously over the course of an experiment. In an ideal situation where no motion is present, the value observed should be constant represented in the form of a straight line. However, Figure 3.1 shows the spectral components of *in vivo* rabbit data corresponding to the time varying motion induced signal. The two dominant components appear at 1.4 Hz and 3.4 Hz corresponding to the respiration and cardiac cycle of the rabbit. Therefore, the key issues that need to be addressed for this approach to be feasible in monitoring glucose include building an instrument that can accommodate for the large birefringence of the cornea,

particularly in the presence of motion artifact, and to develop an instrument that can safely and simply couple the light source across the anterior chamber of the eye.

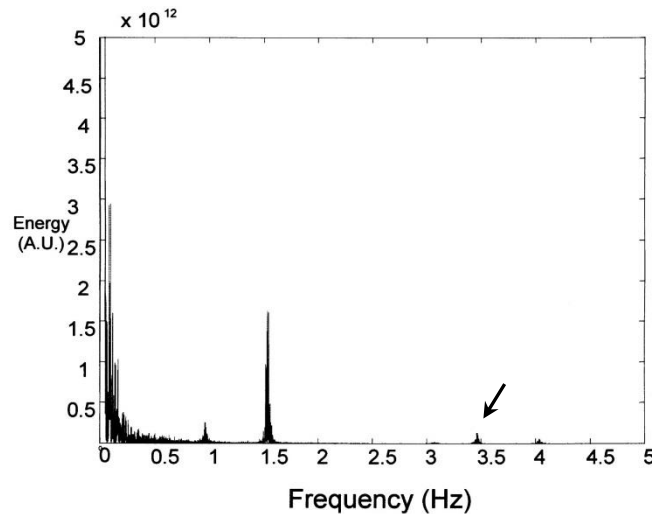


Figure 3.1: Frequency analysis indicating the common sources of motion artifact caused by the cardiac (3.4 HZ) and respiratory (1.6 Hz) cycles (1) –Reproduced by permission of the author.

Over the past decade, research in polarimetric glucose sensing has focused on methods to overcome motion induced time varying corneal birefringence and the coupling of light across the anterior chamber of the eye (33-36, 156). Two primary techniques have been suggested to account for this motion artifact which include the use of a phase sensitive element to compensate for the corneal birefringence (166) and the use of a dual-wavelength polarimeter which, with a multiple linear regression signal processing approach, accounts for the time varying birefringence (33-35, 156). To couple light through the anterior chamber of the eye an index matched coupling device has been used for the *in vivo* New Zealand White rabbit studies (36, 41, 42, 188). Although index matching for coupling of light across the cornea is useful for experimental testing of polarimetric systems in animals and could potentially be done using a scleral lens in humans, solutions for coupling light through the anterior chamber (e.g. light incidence at a grazing angle) are also currently being researched (189).

3.1.1. Anterior Chamber of the Eye

To date, research on the use of optical polarimetry towards noninvasively monitoring glucose levels in the aqueous humor have focused on overcoming time varying corneal birefringence, one major limiting factor of the technique. However, in these studies an index coupling device was utilized to overcome the index mismatch between the air-aqueous humor barriers (35, 81, 82, 189). It is well known through the process of vision that the eye is ideally suited to couple light to the back of the retina. While this approach is useful in removing the index mismatch limitation from experimental testing for evaluating different polarimetric system configurations to monitor glucose in the presence of motion induced birefringence, it is not a practical approach for a final device design. Previous success in measuring aqueous glucose levels over physiologically relevant ranges using polarimetry were obtained in a cuvette or utilizing index matched coupling devices to overcome the index mismatch of the air-cornea interface. Thus, a major limitation that needs to be overcome toward feasibility of polarimetric glucose monitoring is the ability to couple polarized light across the anterior chamber of the eye without the use of a coupling device.

Several research groups have modeled the optical bending of light as it passes through the anterior chamber (156, 190, 191). Malik et al. produced optical simulations and calculations utilizing CODE V optical design software (Optical Research Associates, Pasadena, CA) and MATLAB (The MathWorks, Natick, MA) (156). The results produced in the optical simulations indicated that light could be coupled through the anterior chamber over a narrow range in input angles of the incident light relative to the entrance corneal surface. Previous models have indicated that light could be coupled through the anterior chamber of the eye and out of the adjacent corneal surface with the input beam becoming a divergent “fanning” beam shape at the exiting corneal surface.

In this chapter, further modeling of light coupling through the anterior chamber of the eye in an unmatched index environment and evaluated the addition of incoming and outgoing optics to provide a collimated beam both at the entrance corneal surface and at the detection optics in a polarimetric setup. Utilizing the model previously published by

our group, a computer aided drawing (CAD) rendering in Figure 3.2 below shows that by using glancing angles with a round mirror at 45 degrees (a small mirror at the nose and a larger off-axis parabolic collecting mirror at the outside of the skull) we can potentially overcome the index mismatch and propagate polarized light across the anterior chamber of the eye. All parameters for the eye were obtained from the literature (156, 190, 192, 193).

3.1.2. Cornea Description

Our group has proposed optical polarimetry through the anterior chamber of the eye for noninvasive monitoring of glucose, which can potentially serve as a tool to improve management of diabetes. One of the main challenges with using polarimetry for glucose sensing *in vivo* is that most of the biological tissues are optically turbid. Polarimetric sensing of glucose in such media thus becomes challenging due to the presence of relatively high concentrations of chiral components such as albumin, and multiple scattering events, which can significantly confound the state of polarization of the reflected or transmitted light (46). Thus, one possible way to overcome these problems is by propagating polarized light through the anterior chamber of the eye including the cornea and aqueous humor, where the absorption and scattering effects are minimal and glucose is the principal chiral component (1).

The cornea, in particular, not only serves as the gateway into the eye for vision but also for potential optical monitoring of analytes such as glucose. It is the major refractive structure along with the ocular lens, focusing light onto the retina. The fibrous collagen of the cornea is responsible for its mechanical strength and aids in maintaining the ocular contour but also is a source of its optical birefringence (163). These collagen fibers are primarily present in the stromal region, which constitutes more than 90% of the cornea. The regular arrangement and uniformity of these fibers plays a major role in maintaining corneal transparency (162). Any disturbance in such an arrangement can result in significant scattering of the transmitted light and, therefore, adversely affect optical clarity of the cornea (194).

As mentioned, the fibrous structure of the stroma makes the cornea birefringent,

which varies spatially across the surface of the cornea (32, 156, 195). Birefringence in structured materials such as linear retarders is characterized by $\Delta n = (n_e - n_o)$, which is the difference between the extraordinary and ordinary refractive indices i.e. n_e and n_o , respectively (158). In the case of the cornea, individual constituent collagen fibrils can be regarded as linear retarders with the direction of the fast axis oriented perpendicular to the fibril orientation (196). When such birefringent layers are arranged on top of each other with different orientations of their fast axes, the overall composition exhibits a type of birefringence known as *form* birefringence (164). Several models have been proposed to explain this behavior of corneal birefringence (32, 163, 195, 197-200). Most of these models agree that birefringence is minimum at the center of the cornea, and increases monotonically towards the peripheral regions of the cornea. These models also indicate that the effective birefringence increases as the angle of incidence with respect to the surface normal of the cornea increases.

3.1.3. Eye Model Parameters

In order to understand how the effect of time varying corneal birefringence is minimized using a dual-wavelength polarimetric approach, we utilize the eye model described in detail previously (156, 189). The input beam diameter was fixed at 1 mm. The polarization vector was chosen to be at 45 degrees with the vertical axis to experience maximum change in the state of polarization, and hence the worst-case condition. In principle, the dual-wavelength method should be applicable regardless of the state of polarization of the input light. This being said, in the actual optical setup, the state of polarization was kept horizontal-linearly polarized in order to minimize parasitic polarization effects of optical elements such as prisms and beam splitters. The values used for n_o and n_e are 1.3760 and 1.3744 i.e. $|\Delta n| = 1.6 \times 10^{-3}$. As seen in Figure 3.2, this model consists of four interfaces. The interfaces are numbered 1 through 4 in order of the direction of light propagation. The polarization properties of each surface can be identified with a Jones matrix. The properties assigned to a surface correspond to the following layer. For instance, in the eye model presented, the surface properties defined for surface 1 actually define the optical properties of the corneal layer present between

surfaces 1 and 2. The relationship between output and input Jones vectors is then given by the following equation:

$$\begin{bmatrix} a_4 & b_4 \\ c_4 & d_4 \end{bmatrix} \begin{bmatrix} a_3 & b_3 \\ c_3 & d_3 \end{bmatrix} \begin{bmatrix} a_2 & b_2 \\ c_2 & d_2 \end{bmatrix} \begin{bmatrix} a_1 & b_1 \\ c_1 & d_1 \end{bmatrix} \begin{bmatrix} A_x e^{i\phi_x} \\ A_y e^{i\phi_y} \end{bmatrix} = \begin{bmatrix} B_x e^{i\phi'_x} \\ B_y e^{i\phi'_y} \end{bmatrix} = \begin{bmatrix} B_x e^{i\Delta\phi} \\ B_y \end{bmatrix} \quad (3.1)$$

Where the 2×2 matrices represent the Jones matrices for the four surfaces, A_x and A_y are the electric field components of the input beam at a given wavelength, ϕ_x and ϕ_y are the respective phase components, B_x and B_y are the electric field components of the output beam, ϕ'_x and ϕ'_y are the respective phase components of the output field components, and $\Delta\phi$ represents the net phase difference i.e. $\phi'_x - \phi'_y$ between the electric field components of the output beam. By introducing the net phase term, the relative phase of both ϕ'_x and ϕ'_y is incorporated.

It has been modeled previously that the effect of motion artifact is minimized in the region near the midpoint between the corneal apex and limbus (i.e. 1.5 mm below the apex) (156). Therefore, this point was chosen as the center point in the range of motion. The beam position was then changed from 1.48 mm to 1.52 mm below the apex in steps of 10 μm . The output Jones vectors for each of these positions are noted in for 635-nm and 532-nm models, respectively. For the range of motion considered in this model, the change in the ellipticity of the beam is insignificant as indicated by the elements of the Jones vectors (which remain unchanged up to third decimal place), and the change in corneal birefringence manifests itself as a change in the net phase difference $\Delta\phi$, which varies as a function of beam position for both the wavelengths, as shown in Figure 3.2. Within a short range of motion, such as what is expected *in vivo*, the variation in the phase difference is a highly linear function with respect to the beam position. The change in the major axis of the output beam's state of polarization is mainly dictated by the net phase difference. As a result, the perceived angle of rotation also varies linearly with a correlation coefficient of 0.999 for each of the single wavelength models.

For the dual-wavelength model, multiple-linear regression (MLR) analysis results in a correlation coefficient of one, indicating true linear behavior. Such an analysis combines the information of the two independent single-wavelength data sets to improve

upon the correlation of single predictor model, thereby, providing a merged model with higher correlation between the dependent and independent variables.

As indicated in our previous publications (35, 82), the general idea is to use MLR analysis to predict the contribution of birefringence to the rotation of major axis of the state of polarization. The respective data points for both wavelengths are used to calculate optimal weights, which then serve as coefficients for scaled subtraction. Specifically, the single-wavelength models are of the form $[\text{Glucose}]_{\lambda} = m.V_{\lambda} + c$, where $[\text{Glucose}]$ is the glucose concentration, V_{λ} is the corresponding voltage signal applied to the Faraday compensator for the respective wavelength via the PID controller, and m and c are calibration coefficients. The sample noise can then be removed by subtracting the scaled data sets. The dual-wavelength model generated by MLR analysis is of the form $[\text{Glucose}] = m_1.V_{\lambda_1} + m_2.V_{\lambda_2} + c$, where V_{λ_1} and V_{λ_2} are voltage signals applied to the Faraday compensators by the PID controller to null the system for the corresponding two single-wavelength models, and m_1 , m_2 and c are calibration coefficients which serve as weights for scaled subtraction. In this manner, the use of a second wavelength allows for removal of the noise due to linear changes in birefringence induced with motion. With the noise removed using the dual wavelength approach, accurate monitoring of optical activity due to glucose can be calculated in the presence of time varying corneal birefringence. The relationship between the compensation voltages for each of the single wavelength models and the observed optical rotation is shown from the resulting matrix representation,

$$\begin{bmatrix} V_{\lambda_1} \\ V_{\lambda_2} \end{bmatrix} = \begin{bmatrix} a_1 & b_1 \\ a_2 & b_2 \end{bmatrix} \begin{bmatrix} \text{Glucose} \\ \text{Birefringence} \end{bmatrix} + \begin{bmatrix} C_1 \\ C_2 \end{bmatrix} \quad (3.2)$$

Previous work in characterizing the cornea and AH provide enough information to compute physiological values for glucose concentration, linear birefringence, and diattenuation, with each variable used as inputs to the MATLAB simulation. The eye model, corneal dimensions and other eye parameters were chosen to be the same values as reported previously by Malik et al. (156). Parameters to define the eye model size and refractive index properties are listed in Table 3.1 below. The anterior (Anter.) and posterior (Post.) sides of the cornea were modeled as two spheres with radii of 6.8 mm

and 7.7 mm, respectively each centered about the optical axis of the eye. The thickness of the cornea at the center was 0.5 mm, monotonically increasing in thickness (as a conicoidal function) to 1.97 mm at 6 mm from center (191). The cornea posterior surface will behave similar to a polished optical lens due to the formation of a tear film in liquid form, which defines the smoothness of the cornea (192). At the center, the height of the aqueous chamber was 3 mm. The refractive index on the outside of the corneal surfaces was assumed to be air ($n=1$) and the cornea and aqueous humor refractive index were 1.376 and 1.336, respectively. The input beam diameter of each wavelength of light, fixed at 1 mm. The ordinary (n_o) and extraordinary (n_e) refractive index values were 1.376 and 1.3744, respectively producing a birefringence $|\Delta n| = 1.6 \times 10^{-3}$.

<u>Anter.Surface radius</u>	6.8 mm
<u>Post. Surface radius</u>	7.7 mm
<u>Thickness cornea (center)</u>	0.5 mm
<u>Height Aq chamber</u>	3 mm
<u>Path Length Aqueous</u>	10 mm
<u>n</u>	1
<u>n_{cornea}</u>	1.376
<u>n_{aqueous}</u>	1.336

As indicated in simulation produced by Malik et al. motion artifact is minimal near the midpoint between the corneal apex and limbus, which is approximately 1.5 mm below the apex (156). Additionally, previous modeling has indicated that in an index-unmatched configuration a glancing angle of approximately 16 degrees allows for a fanned beam to exit the cornea after traversing the anterior chamber (156). For modeling purposes, the two optical paths were set to wavelengths of 635 nm and 532 nm, respectively. These wavelengths were chosen for the modeling and simulation because these wavelengths are what we have previously used in *ex vivo* and *in vivo* testing with a dual-wavelength polarimetric system. For the optical component design a total of four or

more mirrors were considered for steering the non-index matched beams into the cornea from the source side of the polarimeter, through the AC, and out of the cornea at a controlled glancing angle and position on the initial corneal surface through the detection optical components onto an optical detector. Corneal retardance values were examined over three cases in the simulations were variations in the corneal shape were considered at two extreme cases and one with an “average” eye model shape “Navarro eye model” (190). The values for the extreme corneal shape cases were taken from corneal shape extremes reported in measurements *in vivo* of 176 human subjects reported by Kiely et al. (190, 201) and later utilized by Winkler et al. (190). Surface face and other parameters for each of the three eye models were reported by Winkler et al. and are shown below in Table 3.2. Surfaces for each model are defined by asphericity parameter (Q) and the radius of curvature (R). As described by Van Blokland et al. and Winkler et al. the definition of corneal birefringence defining in the xz plane is independent from the XZ plane where the surface is defined by a quadratic equation of the form displayed in Equation 3.3:

$$X^2+(1+Q)Z^2-2RZ=0 \quad (3.3)$$

From the surface incidence and exitance angles in relation to the surface normal and refractive indices before and after the surface a diattenuation value can be calculated. Diattenuation can be calculated from the definition in Equation 3.4:

$$D=(T_{\max}-T_{\min})/(T_{\max}+T_{\min}) \quad (3.4)$$

Maximum transmittance (T_{\max}) is the transmittance value for the most attenuated polarization state at the surface. The attenuation can occur via absorption or reflection. As described by Winkler et al., at an interface, the maximum transmittance is the Fresnel coefficient for p-polarized light and the minimum transmittance (T_{\min}) is the Fresnel coefficient for s-polarized light.

<u>Surface</u>	<u>Radius (mm)</u>	<u>Q</u>	<u>Medium</u>	<u>Δz (mm)</u>	<u>n</u>
Navarro Model					
Anterior Cornea	7.72	-0.26	Cornea	0.55	1.3760
Posterior Cornea	6.50	0	Aqueous	3.05	1.3374
Extreme 1					
Anterior Cornea	7	0.5	Cornea	0.55	1.376
Posterior Cornea	6.5	0	Aqueous	3.05	1.3374
Extreme 2					
Anterior Cornea	8.7	-0.8	Cornea	0.55	1.3760
Posterior Cornea	6.5	0	Aqueous	3.05	1.3374

<u>Medium</u>	<u>γ (deg)</u>	<u>L (mm)</u>	<u>ΔnL (μm)</u>
Navarro Model			
Cornea, Entrance	-38.58- -42.69	1.11-1.27	0.62-0.67
Cornea, Exit	37.92-43.32	1.16-1.22	0.55-0.75
Extreme 1			
Cornea, Entrance	-17.9- -33.05	0.057-0.5	$1.2e^{-3}$ - 0.17
Cornea, Exit	20.55-30.16	0.23-0.32	0.016-0.088
Extreme 2			
Cornea, Entrance	-43.89- -49.43	1.92-2.23	1.42-1.51
Cornea, Exit	44.48-48.92	1.82-2.35	1.41-1.53

<u>Surface</u>	<u>γ_1 (deg)</u>	<u>γ_2 (deg)</u>	<u>n_1</u>	<u>n_2</u>	<u>D</u>
Navarro Model					
Anterior Cornea	-59.11- -68.91	-38.58- -42.69	1	1.376	0.066-0.108
Posterior Cornea	-34.60- -41.55	-35.75- -43.03	1.376	1.3374	$2e^{-4}$ - $3.4e^{-4}$
Posterior Cornea	35.75-43.03	34.60-41.55	1.3374	1.376	$2e^{-4}$ - $3.4e^{-4}$
Anterior Cornea	37.92-43.32	57.74-70.73	1.376	1	0.061-0.119
Extreme 1					
Anterior Cornea	-25.02- -48.63	-17.9- -33.05	1	1.376	$7.7e^{-3}$ - 0.037
Posterior Cornea	-33.93- -43.13	-35.05- -44.7	1.376	1.3374	$1.9e^{-4}$ - $3.8e^{-4}$
Posterior Cornea	35.05-44.7	33.93-43.13	1.3374	1.376	$1.9e^{-4}$ - $3.8e^{-4}$
Anterior Cornea	20.55-30.16	28.89-43.74	1.376	1	0.23-0.32
Extreme 2					
Anterior Cornea	-59.11- -68.91	-38.58- -42.69	1	1.376	0.066-0.108
Posterior Cornea	-29.05- -40.41	-29.92- -41.83	1.376	1.3374	$1.3e^{-4}$ - $3.1e^{-4}$
Posterior Cornea	29.97-41.83	29.05-40.41	1.3374	1.376	$1.3e^{-4}$ - $3.1e^{-4}$
Anterior Cornea	37.92-43.32	57.74-70.73	1.376	1	0.061-0.119

3.2. Non-index Coupling Design Tasks

3.2.1. Develop a Birefringent Eye Model for Non-index Matched Light Coupling Design

The propagation of the light, including the birefringence, with no coupling apparatus was modeled. This modeling is used as the starting point in re-designing the optical system to eliminate or reduce the size of the current coupling device. This will be followed by polarimetric measurements in excised New Zealand White (NZW) rabbits' corneas. Beyond corneal birefringence, the next hurdle toward feasibility of this polarimetric glucose monitoring approach is the ability to couple the dual wavelength polarized light across the anterior chamber of the eye. The eye is ideally suited to coupling light to the back of the retina for vision. The index mismatch between the cornea and air is partially responsible for the beam bending toward the retina and, although good for vision, complicating our ability to couple the light across the anterior chamber of the eye.

Our group has previously performed optical simulations and calculations in CODE V optical design software (Optical Research Associates, Pasadena, CA) and MATLAB (The MathWorks, Natick, MA) of the optical path through the cornea without the use of an index matching solution. The CODE V software employs a polarization ray tracing method to solve for the optical path through the optical system (i.e., the cornea). The corneal parameters and dimensions utilized in the model were taken from reference (156). Utilizing our existing model we will evaluate various commercial optical designs employing a glancing angle and determine the optimal design to allow for non-index matched coupling of light through the aqueous humor.

Using existing eye models developed by our group (156) we will explore the difference between reflective and transmissive optical coupling without an index matching medium using various commercial optics. The models were developed utilizing various optical ray tracing software packages such as Zemax, Code V, and OptiCAD. The resulting models and capabilities of each software package were weighed in choosing the optimal final design choice. The combination of the models developed in

Zemax and OptiCAD were utilized for determining the placement of the commercial optics due to their ease of implementing commercial optical geometries and material parameters. Additionally these models were used to evaluate the optical beam displacement between the two wavelengths of light. Once the optimal optical components were chosen, Code V was then used in addition to MATLAB to evaluate the polarization parameters of these optical element choices. The combination of these models were used to guide in the proposed design (Figure 3.2b), where we replaced the output mirror with a 90° concave mirror for collecting the light in order to re-collimate the light output from the cornea, which is critical for the light to travel through the receiving optics and to the detector. The resulting polarized light ray tracing models was used for evaluating and optimizing various optical coupling designs that allow for non-index matched light coupling across the aqueous humor. The ray tracing models developed evaluate refraction, diattenuation, reflection, and polarization changes at each optical interface within the setup.

Integration of this coupling method with the overall opto-electronic system design is shown. Ideally, the final design consists of reflective optics, as they reduce the amount of variation in the optical path location of the two wavelengths of light as they travel through the optical surfaces.

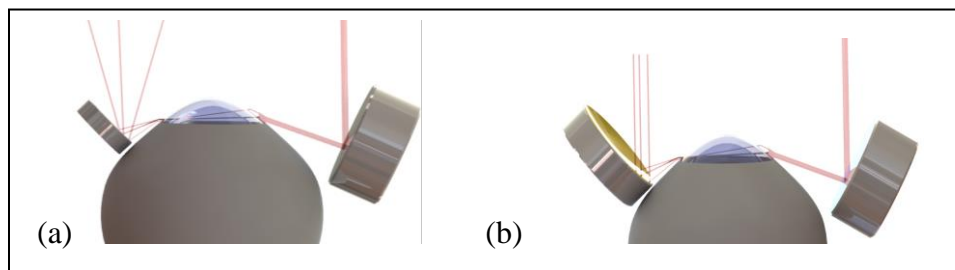


Figure 3.2: Modeling of the optical path through the anterior chamber of the eye for unmatched refractive indices. There is no visible difference (on the current scale) between the optical paths taken (through the eye) by the two beams at different wavelengths, and hence, a single beam path is shown. (a) This design illustrates the need for coupling optics that allows the beam output from the cornea to be re-collimated. However, the output beam is not collimated due to index of refraction mismatch. (b) This design places a 90° concave mirror on the output to re-collimate the fanned beam exiting the eye. The angle of incidence, α , is measured from the horizontal. Note that light has to be incident at a relative glancing angle with respect to the posterior corneal surface in order for the beam to exit the anterior chamber through the cornea. However, the output beam is now collimated, which is critical for transmission through the detection optics.

After the modeling confirmed the approach is achievable, we built the non-index matched eye coupling mechanism and tested the approach. The proposed non-index matched eye coupling design (Figure 3.2b) should provide a feasible noninvasive coupling approach according to the modeling. Specifically, to assess the design we measure the effect of birefringence on the major axis of the state of polarization of the output beam as a function of the wavelength, beam position, and angle of incidence on the posterior corneal surface for the models. The most significant difference in this coupling mechanism compared to index-matched mechanism is that incident light has to enter the eye at a relative glancing angle with respect to the posterior corneal surface, as illustrated in Figure 3.2, in order to be coupled out of the anterior chamber. Utilizing the modeled schemes. Devices were constructed and the components purchased for *in vitro* experiments.

3.2.2. *Test the Eye-Coupling Device*

The final task in this chapter is to perform a series of *in vitro* studies to test the new coupling mechanism. Initially, using the existing bench top system and then transition to the miniaturized system described in Chapter 4. Our group had previously discussed coupling light across the anterior chamber utilizing a 90 degree concave mirror and glancing angle configuration in addition the use of a scleral lens. We will utilize similar schemes to build separate devices for *in vitro* experiments.

To assess the design the effect of birefringence on the major axis of the state of polarization of the output beam as a function of beam position and angle of incidence on the posterior corneal surface for both models was measured. Utilizing the modeled scheme two separate devices were constructed and the components purchased for *in vitro* experiments.

3.2.3. *If Needed Develop Alternative Modeling Utilizing Scleral Lens Coupling Approach*

If the glancing angle or reflection based approach shown above did not work and an appropriate angle could not be easily found during testing or, if after testing the design

with phantoms, the approach is found to be not accurate enough according to the defined target milestones, then the alternative approach is to use an index matching sclera contact lens. The approach, although still noninvasive, requires an index matching contact lens to be inserted. A model was generated and evaluated utilizing commercial scleral lens variables for an index matched solution. In the past, our group has developed a coupling mechanism to index match the eye and allow light to pass across the anterior chamber of the eye (154). The setup we modeled utilized a scleral lens, for index matching, between air and cornea in order to provide a straight path across the anterior chamber with no coupling of light through the pupil. The method is described for this model in the next section. However, the results are displayed in the Appendix E because the design of this method was not needed based on the results from the index-unmatched design model.

3.3. Materials and Methods

3.3.1. Modeling Index-unmatched Coupling of Light

To evaluate a non-index matched optical coupling scheme, models were designed and verified using Code V, an optical modeling software package, evaluating various coupling schemes and optical component variations. For the eye model, the corneal parameters and dimensions utilized in this report were the same as described in detail previously by Malik et al. (156). In the final design, shown below, we use a 90 degree off-axis parabolic mirror to collect and re-collimate the light beam after exiting the cornea. The parabolic mirror is needed because the beam shapes, after traveling through the aqueous humor, will fan out as shown in Figure 3.3; thus, the beams need to be re-collimated in order for it to travel through the receiving optics and arrive onto the detectors. As depicted in Figures 3.4-3.6, we have developed a CAD rendering of the model similar to that shown in Figure 3.3 in which all the optical simulations performed in CODE V optical design software (Optical Research Associates, Pasadena, CA). The initial variables adjusted were the input mirror angle and entry point of the beam as well as the output parabolic mirror angle and distance. Optimization of the model was then achieved by adjusting the coupling optics position and angle in three dimensions to

ensure the two optical beams undergo roughly the same optical path as they pass through the polarimetric system. An additional 90 degree off-axis parabolic mirror was added after the first parabolic mirror at the output of the eye to help ensure collimation of the beam before entering the detection optics. The posterior and anterior corneal surfaces were modeled as spheres centered on the optic axis of the eye with radii of 7.7 mm and 6.8 mm, respectively. The central thickness of the cornea was set to be 0.5 mm and the thickness increased monotonically (as a conicoidal function) to 1.97 mm at 6 mm away from the center (191). The index of refraction at the outside of the cornea was assumed to be that of air ($n=1.00$). The refractive indices of cornea and aqueous humor were set to values of 1.376 and 1.336, respectively (i.e. $|\Delta n|=1.6 \times 10^{-3}$). The smoothness of cornea is defined by the formation of a liquid tear film over the posterior surface, which makes the cornea behave similar to a polished optical lens (192). As indicated in the optical simulation produced by Malik et al. the effect of motion artifact can be minimized when the beam is positioned in the region of the entrance near the midpoint of the corneal apex and limbus (i.e. 1.5 mm below the apex) (156). For optical ray tracing of each wavelength, the beam diameter was chosen as fixed at a diameter of 1 mm to be consistent with the model utilized previously by our group (156). The CODE V software package allows for a polarization ray tracing method to be employed, which solves for the path/surface interactions through the optical system for each wavelength, further details of which have been described elsewhere (193). CODE V has the ability to divide the optical surface into a rectangular or circular grid like pattern. The user then has the ability to define the birefringence parameters such as the direction of fast axis and the birefringence (n_e-n_o , where n_e and n_o are the extraordinary and ordinary refractive indices, respectively) for each individual grid section (35).

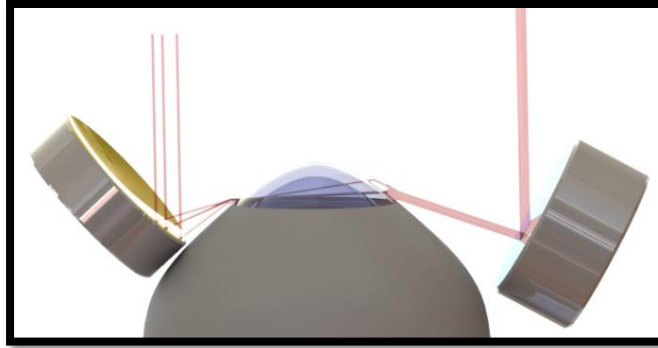


Figure 3.3: Modeling of the optical path through the anterior chamber of the eye using the new optical coupling method. Note that light still has to be incident at a relatively glancing angle with respect to the posterior corneal surface and there is no visible difference (on the current scale) between the optical paths taken by the two beams at different wavelengths. However, the output beam is now collimated, which is critical for transmission through the detection optics.

In the dual-wavelength polarimetric system design, two optical coupling schemes were explored utilizing reflective based systems. In the reflective based optical coupling setup that offered the best results, a 90 degree off-axis parabolic mirror was placed at the output of the cornea to collect the fanning output beams of each of the wavelengths in the system. The off-axis parabolic mirror reflected the beam back into the system towards the collection optics while collimating the fanned beam. Additionally, a second off-axis parabolic mirror was placed after the first too further collimate the overlapping wavelengths in the system prior to directing the beams through the analyzer onto the detector.

Commercial optics were evaluated from multiple vendors and an optical coupling scheme was constructed and evaluated in modeling software utilizing reflective based optical components. In the final design, a round mirror was employed for guiding the entrance beam into the eye at a glancing angle and two 90 degree off-axis silver coated parabolic mirrors were utilized to couple the light for both wavelengths out of the cornea and then providing a relatively collimated beam onto the detection optics. For the optical ray trace simulation, CAD models were downloaded from the THORLABS (Newton, NJ) website for each optical component and the listed specifications for the products were input into CODE V to simulate the use of commercial optical mirrors. The 90 degree off-axis parabolic mirror item #: MPD127075-90-P01 (THORLABS, Newton,

NJ) was chosen for collimating the output beam in the coupling model because it offered the most optimal parameters for the specified design. Utilizing two off-axis parabolic mirrors it was expected that the design would re-collimate the output beam accounting for the expected beam divergence at the output of the cornea as described by Malik et al. (156). The off-axis parabolic mirror listed above was chosen because it provided the shortest reflected focal length (RFL), diameter, and parent focal length of any 90 degree parabolic mirror commercially available from several optical device vendors. The diameter of the parabolic mirror is 12.7 mm, the RFL is 15 mm, and the parent focal length was listed as 7.5 mm for the parabolic mirror listed above. Additionally, a round protected silver mirror was determined to be optimal for providing the input beam into the cornea at a glancing angle. In the modeling software, the specifications for the round mirror were obtained from THORLABS for item #: PF03-03-P01. The specified mirror had a diameter of 7 mm and a thickness of 2 mm.

Utilizing the CODE V optical modeling software, a model was constructed as illustrated Figure 3.4 to evaluate the possibility of passing a beam of light through the eye without the use of an index matching device. In the model, a glancing angle for the entrance beam of 16 degrees was utilized. Evaluating the beam position of the two wavelengths at the detector and the appearance of the two beam ray traces the x, y, and z position of the two 90 degree off-axis parabolic mirrors was varied until optimal results were obtained maximizing the overlap between the wavelengths and minimizing the change in the optical signal observed on the detector over multiple simulations. The parameters specified by THORLABS were utilized in designing the mirrors in CODE V. Utilizing the eye model presented by our group previously (156) the mirrors were added to the model and the ray trace results were simulated and evaluated. After the parameters were entered for each optical component the position of the optical elements were modified until the results indicated an optimal ray trace of the overlapping wavelengths providing the most visually collimated output product, as shown in Figure 3.4 below. Along with CODE V, Zemax was utilized to evaluate the non-polarized ray trace in the proposed design. The Zemax files for each of the mirrors were downloaded

from THORLABS and imported into a Zemax non-sequential design shown in Appendix E.

3.3.1.1. Anatomical Constraint Analysis

After the optimal position was determined for each element a CAD rendering of the ray trace starting with the entrance beam up to the beams onto the detection optics were output in STL format. Then utilizing SolidWorks a 3D model was generated of the respective ray traces for the individual wavelengths with the exported file as a reference. Using the CODE V output ray traces and CAD models for the optical elements, a human eye (190), and a rendering of a human face obtained via scanning a face into a 3D representation it was possible to evaluate the placement of the optical elements and beam path as shown by the models in Figure 3.5 below. Using the exported models specified in CODE V the model was then evaluated with respect to anatomical features on the human face such as the nose and corneal/sclera surface to determine if the optical model would be feasible with anatomical constraints. Figures 3.5a and 3.5b illustrate the compiled 3D model of the optical simulation provided from CODE V via multiple different viewing angles. As illustrated in Figures 3.5a and 3.5b it appears the proposed non-index matched optical coupling scheme is feasible from an anatomical and optical standpoint.

3.3.1.2. Polarization Analysis of Dual-wavelength System

In addition to ray tracing analysis to determine the feasibility of coupling light through the aqueous humor a polarization analysis was performed on the optical system to determine the change in the multiple wavelengths' polarization state as they pass through the optical train. It is important to note that in regards to evaluating polarization behavior of an optical design, there is not one perfect analytical method. However, there are general methods that can be followed in analyzing an optical system. In this system polarization analysis, the following method was utilized: First, the requirements and specifications of the optical system were examined and the polarization behavior was determined to be explicitly important. Then, the highly polarizing optical elements of the

system were identified (polarizers, Faraday modulator, Faraday compensators, eye, and analyzer). For each element identified, the range of use was examined with respect to the wavelengths utilized in the system, angles of incidence, and various other parameters that could vary the polarization performance. For each polarization dependent element, the vendor specifications were consulted to identify key parameters utilized in the optical model. Following the element specifications it was determined that the light will remain polarized through the system. Then the entire optical system was identified as highly critical in terms of polarization behavior. For each wavelength, the optical system was modeled as a linear polarizer, followed by two Faraday rotators (compensator and modulator), the eye, and finally an analyzer. More details on the specific information and theoretical system analysis can be found elsewhere (35, 82). As illustrated previously by our group and Winkler et al., the eye can be represented as a series of an optical rotator, diattenuators, and linear retarders (35, 176, 190). Thus, the Jones matrix formulation of the eye phantom shown in Equation 3.6 is presented as an optical rotator placed between two linear retarders of equal retardation (35, 176, 190). The resulting eye model varies with respect to both the angle of azimuth and the ellipticity of the state of polarization. Further, the ellipticity is primarily affected by retardation, where time varying retardation $\delta(t)$ introduced due to the cornea can be described as shown in Equation 3.5 by,

$$\delta(t) = \frac{2\pi}{\lambda} \Delta n L(t) \quad (3.5)$$

In this equation λ is the wavelength, the corneal birefringence is $\Delta n = |n_e - n_o|$, and $L(t)$ is the path length through the cornea changing as a function of time. As described by Malik et al. the effects of corneal birefringence can be minimized through alignment of the linear polarization vector near the fast axis of the cornea. The net perceived optical rotation due to both birefringence and glucose is assumed to remain under ± 1 degree of rotation, the maximum modulation depth of the faraday modulator utilized in polarimetric glucose detection schemes (35, 82). If the rotation were above this value, the compensation component in the system proposed by our group would not be capable of providing adequate feedback to null the device. The initial polarizers were assumed as

aligned with the fast axis; the resulting system matrix representation is shown in Equation 3.6 below.

$$\begin{aligned}
 V_{system} = & \begin{pmatrix} \text{Analyzer} \\ 1 & 0 \\ 0 & 0 \end{pmatrix} \begin{pmatrix} \text{Eye Model} \\ \cos(\phi_g)e^{-i\frac{\delta_1(t)+\delta_2(t)}{2}} & \sin(\phi_g)e^{i\frac{\Delta\delta(t)}{2}} \\ -\sin(\phi_g)e^{-i\frac{\Delta\delta(t)}{2}} & \cos(\phi_g)e^{i\frac{\delta_1(t)+\delta_2(t)}{2}} \end{pmatrix} \begin{pmatrix} \text{Faraday Modulator} \\ \cos(\theta_m \sin(\omega_m t)) & -\sin(\theta_m \sin(\omega_m t)) \\ \sin(\theta_m \sin(\omega_m t)) & \cos(\theta_m \sin(\omega_m t)) \end{pmatrix} \\
 & \begin{pmatrix} \cos(\phi_f) & \sin(\phi_f) \\ -\sin(\phi_f) & \cos(\phi_f) \end{pmatrix} \begin{pmatrix} \text{Faraday Compensator} & \text{Polarizer} \\ 0 & 0 \\ 0 & 1 \end{pmatrix}
 \end{aligned} \tag{3.6}$$

Where the system equivalent Jones matrix is V_{system} , changes in optical rotation due to glucose and optical rotation from the Faraday compensator are ϕ_g and ϕ_f , respectively, $\delta_1(t)$ and $\delta_2(t)$ represent the amount of retardation from the light entering and exiting the cornea as a function of time, $\Delta\delta(t)$ is the difference between the two surface retardations, θ_m represents the modulation depth for the Faraday modulator, and ω_m is the modulation frequency. The primary relationship in system voltage that contributes to the net optical rotation is the matrix representing the eye, shown in Equation 3.6.

For the polarization ray tracing model designed in MATLAB a glucose concentration was varied from 0 to 500 mg/dL in increments of 10 mg/dL under randomly generated birefringence values ranging between 0 and 3×10^{-4} . The compensation voltage and predicted glucose concentration as a function of actual glucose concentration for a single wavelength model at 635 nm and 532 nm were calculated and the results are shown in Figure 3.7 below. This data was generated utilizing Jones matrix mathematics solving for Equations 3.6 above. The millidegree rotation generated for the respective wavelengths and shown in Figure 3.7 were calculated based on the “random” function in MATLAB that arbitrarily assigns a value for birefringence at each glucose concentration, from a specified range. Following verification of the system model, an additional time-varying model was generated with the birefringence values randomly ranging between zero and 3×10^{-4} using the random function in MATLAB. The thickness of each corneal surface was assigned a thickness of 0.35 mm and the path length through the aqueous humor was assumed 8.5 mm. Diattenuation was included into the eye model

using the values presented in the Navarro model (190). For the first surface the diattenuation values were a matrix $D = [0.108 \ 0.00034 \ 0.00034 \ 0.119]$ and the exiting surface diattenuation values were assigned a matrix value of $D2 = [.066 \ 0.0002 \ .0002 \ 0.061]$.

In the model, a modulation frequency of 1.09 kHz was chosen with a modulation depth of +/-1 degree because the majority of published polarimetric schemes used for glucose detection operate at this frequency. Thus, there are reference values available to compare the simulated data with at the specified frequency. The glucose concentration was evaluated between 0 to 500 mg/dL at 10 mg/dL increments. Utilizing the model parameters described above the theoretical signal at the detector in mg/dL utilizing the optical train was calculated as shown in Equation 3.6. The time varying birefringence simulation was calculated for both 635 nm and 532 nm wavelengths over a range of random values. Using the calculated rotation the predicted glucose concentration was then calculated and plotted with respect to actual glucose concentration for both wavelengths as shown in Figure 3.7. Utilizing the reduced matrix method described by Savenkov et al. (193), the predicted glucose concentration in mg/dL were calculated for both wavelengths and compared to the system equation results in addition to the actual glucose concentration results.

$$\begin{aligned}
 & \text{Diattn} \\
 = T_{ave} & \begin{bmatrix} (1 + D) \cos^2 \theta + (1 - D) \sin^2 \theta & (1 + D) \cos \theta \sin \theta - (1 - D) \cos \theta \sin \theta \\ (1 + D) \cos \theta \sin \theta - (1 - D) \cos \theta \sin \theta & (1 - D) \cos^2 \theta + (1 + D) \sin^2 \theta \end{bmatrix}
 \end{aligned}
 \tag{3.7}$$

$$\begin{aligned}
 \text{Eye} = & \text{antDiattn2} * \text{linRtd2} * \text{postDiattn2} * \text{optRot} * \text{postDiattn1} * \text{linRtd1} \\
 & * \text{antDiattn1}
 \end{aligned}$$

Table 3.5: Corneal Diattenuation Parameters	
Corneal Surface	Diattenuation (Diatten. (D))
Anterior #1	0.66-0.108
Posterior #1	0.0002-0.00034
Posterior #2	0.0002-0.00034
Anterior #2	0.061-0.119

3.3.2. *Modeling Scleral Index-matched Coupling of Light*

The non-contact eye coupling design shown above should provide a feasible noninvasive coupling approach according to the modeling but, it is anticipated that each final unit would ultimately need to be aligned by a physician per patient and that not all patients will have an appropriate eye geometry to allow for easy alignment. In these cases, if the glancing angle or reflection based approach shown above does not work and an appropriate angle cannot be easily found by a trained physician or, if after testing the design with both phantoms and *in vivo* in rabbits, we find the approach is not accurate enough according to the defined target milestones, then the alternative approach would be to use an index matching sclera contact lens. The approach, although still noninvasive, would require an index matching contact lens to be inserted. The ideal lens would not need to cover the cornea but rather could be a doughnut shaped lens inserted at the cornea/sclera interface. This lens would be similar to current contact lenses in terms of pliability and ability to be inserted but due to its doughnut shape would not affect the vision. Initially a commercial lens such as the one from Danker Labs (<http://www.dankerlabs.com/lenses.html>) can be used. Although the lens may not be a perfect match to the cornea, which has an index of 1.376, our CAD modeling depicted that they would be good enough to allow translation across the anterior chamber without the need for a glancing angle and should provide accurate results similar to our existing eye-coupling device.

3.4. Results and Discussion

3.4.1. *Modeling Index-unmatched Coupling of Light Ray Trace Analysis*

Optical models for non-index matched coupling of light entering the cornea at a glancing angle were observed utilizing two different software packages. The three different optical modeling software packages helped to validate the results produced by the respective software. Additionally each software offered unique features that were beneficial in overall modeling the coupling scheme proposed above. For example, CODE V is great for exporting the beam profile of the ray trace into 3D CAD software

for anatomical consideration in the coupling design. However, in CODE V importing existing commercial models available is not possible in their existing formats. Thus, Zemax is great in incorporating the optical elements from THORLABS because the models are provided for Zemax by THORLABS including the optical properties and CAD dimensions of the elements. However, the version of Zemax utilized was not capable of performing advanced polarization related modeling such as the birefringence profile of the cornea.

The proposed non-index coupling scheme including the input beam entering the eye at a glancing angle and 90 degree off-axis parabolic mirrors placed at the exit point of the eye was modeled in the various software packages and the ray trace for 635 nm and 532 nm wavelengths of the respective models are shown in Figures 3.4 through 3.6 below. For each optical model, the beam diameter was chosen to be circular with a diameter of approximately 1mm. This is representative of the beam diameter utilized in the system designed by our group. Additionally, a glancing angle of approximately 16 degrees was introduced between the input beam and the entrance corneal surface of the eye.

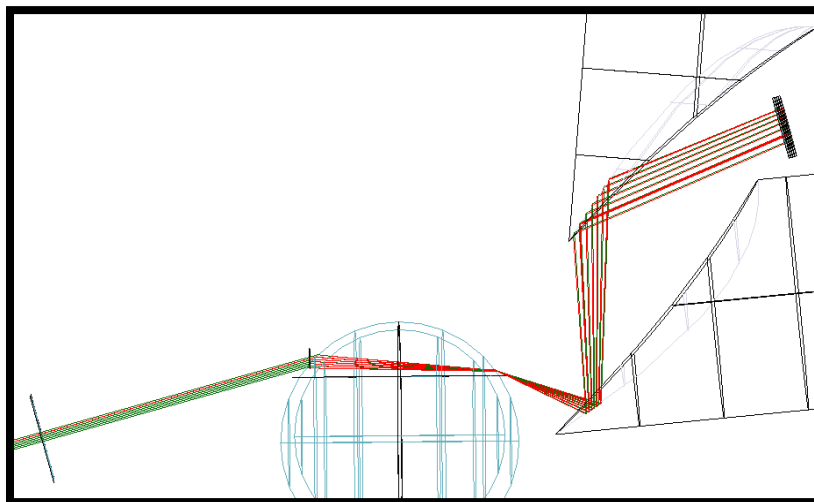


Figure 3.4: CODE V simulation of proposed non-index matched eye-coupling scheme utilizing two 90 degree off-axis parabolic mirrors re-collimating the beam exiting the cornea in addition to a round mirror guiding the entrance beam into the cornea at a specified glancing angle

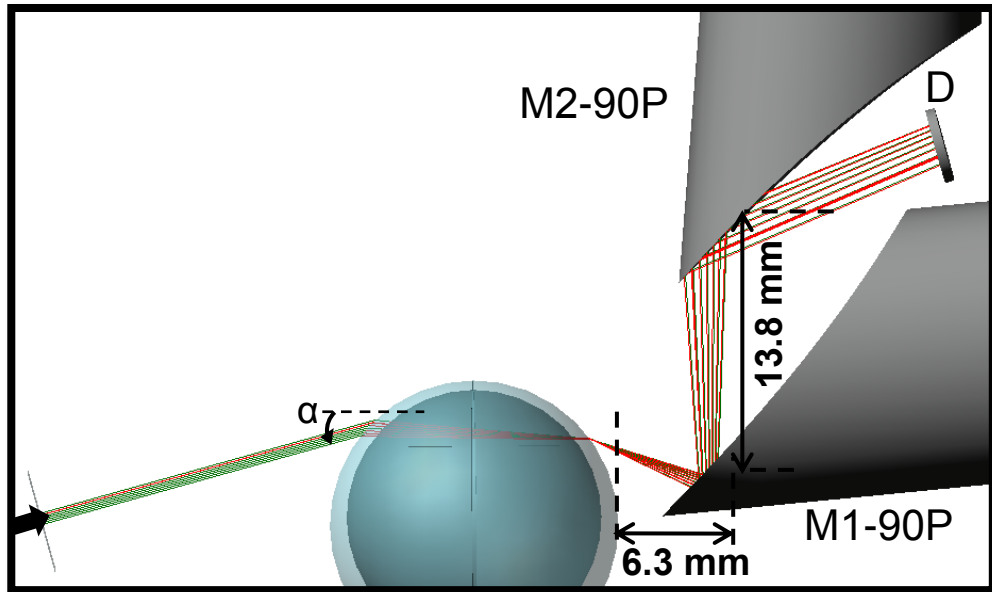


Figure 3.5: CODE V simulation of proposed non-index matched eye-coupling scheme utilizing two 90 degree off-axis parabolic mirrors re-collimating the beam exiting the cornea in addition to a round mirror guiding the entrance beam into the cornea at a specified glancing angle with solid fill.

Glancing angle (α): 16°
Beam Width (mm): 1 x 1
Wavelengths (nm): 635 & 532
of rays: 5 x 5
Detector (mm): 3 x 3

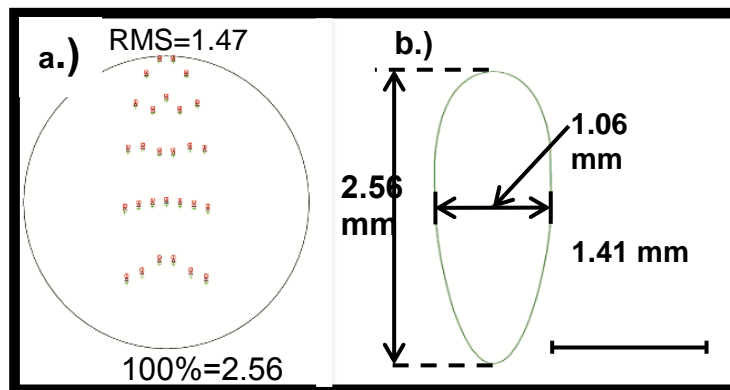


Figure 3.6: CODE V simulation, detector beam profile at the detector for model shown in Figure 3.4 and Figure 3.5

3.4.1.1. Anatomical Boundary Analysis

This model shows that by using glancing angles with a round mirror at 45 degrees (a small mirror at the nose and larger off-axis parabolic collecting mirror at the outside of the skull) the index mismatch can be overcome and polarized light can be propagated across the anterior chamber.

Based on the results illustrated in Figures 3.8a and 3.8b it appears that the proposed non-index matched coupling scheme could be achieved without being limited anatomically by the facial structure. From the modeled CAD results, it appears significant room is available to modify the position of the input and output mirrors for varying anthropometric requirements that exist between people. This model also helped to observe if the exiting beam could pass out of the cornea or would be blocked by the sclera. Due to limited design ability in the ray tracing software the cornea was constructed as two concentric circles. However, in reality the shape is actually similar to the eye model shown in Figure 3.3 above. The main difference in the two geometries does not affect the optical properties but could act to further constrain the range of exiting beam angles that would allow the beam to exit the eye and propagate to the collimating optics in the system. As indicated by the ray tracing results produced from each of the optical software packages it appears the proposed scheme when optimized with respect to optical element position is capable of providing the desired output of relatively collimated overlapping beams. Additionally, the simulations indicate very little fluctuation in the detector beam profile for each of the modeled designs.

3.4.1.2. Polarization Ray Tracing (MATLAB)

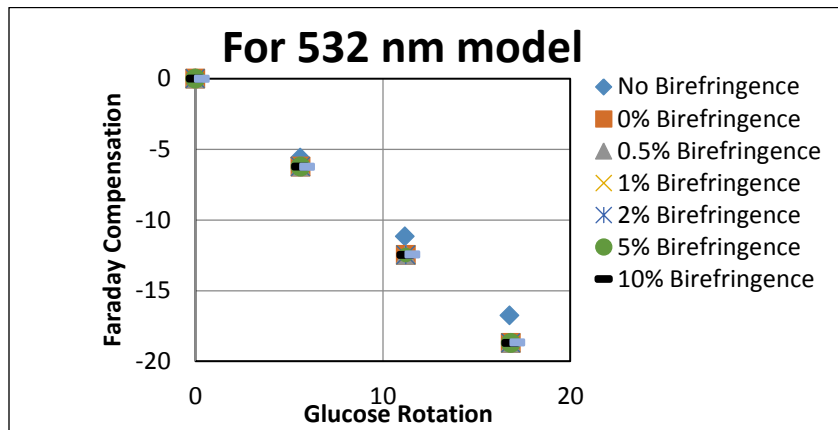
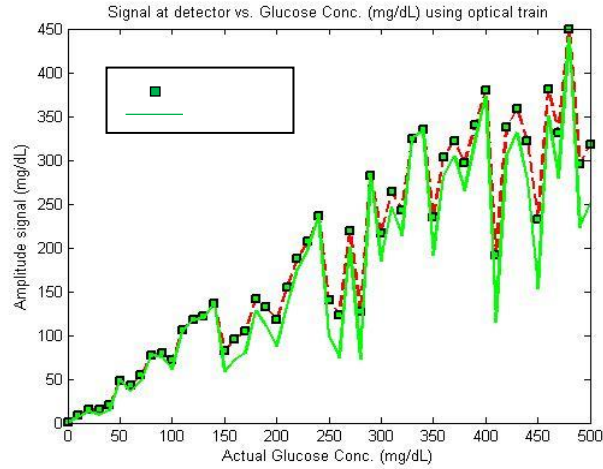


Figure 3.7: Theoretical polarization rotation results for a simulated dual-wavelength polarimeter passing through an eye model with parameters comparable to recorded in vivo data. The data provided indicates the predicted vs. actual glucose concentration for 635 nm and 532 nm wavelengths over a range of 0-500 mg/dL of glucose with simulate motion induced into the system.

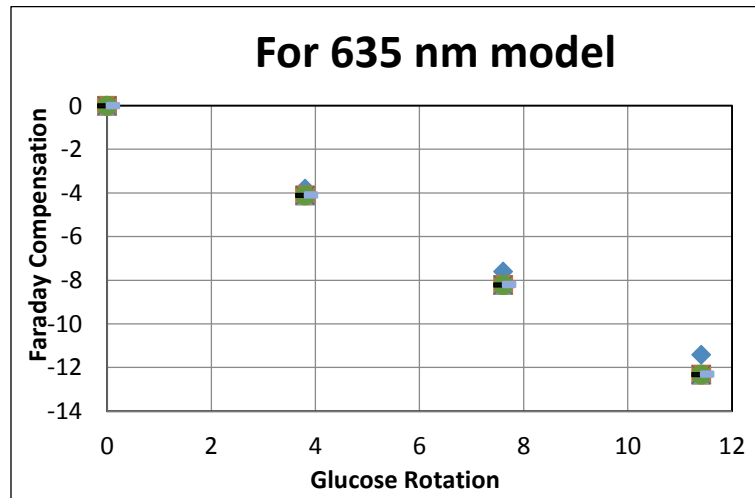
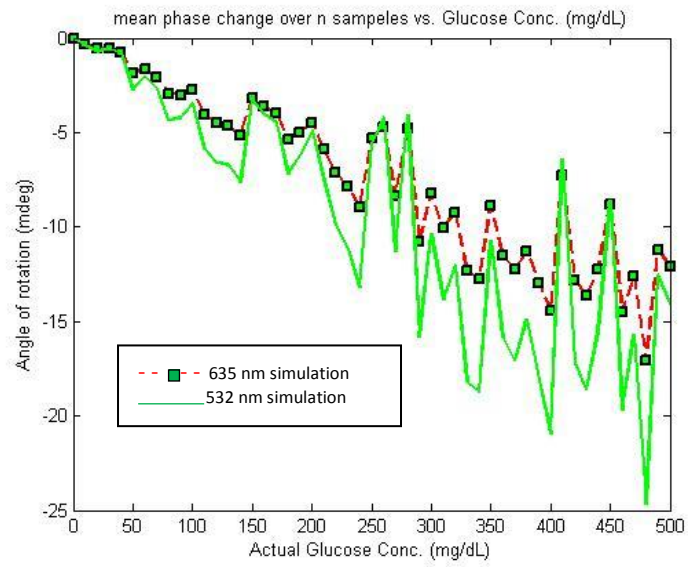


Figure 3.7 Continued

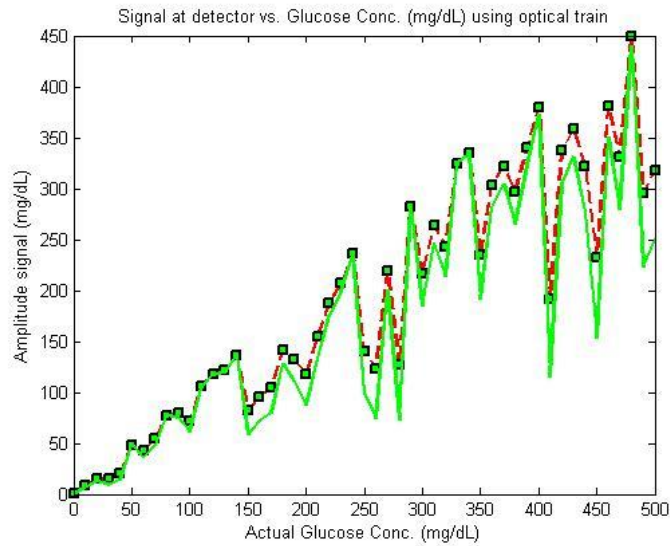


Figure 3.7 Continued

The results presented in Figure 3.7 illustrate that slight variations exist between the different wavelengths as calculated with the theoretical system model. This is expected as shown in Equation 3.5 due to the wavelength dependence of birefringence. The main thing to note is that in the theoretical model of the system response for both wavelengths change in the same direction over the 500 different sample concentrations simulated over the range of 0 to 500 mg/dL of glucose. Thus, multiple linear regression (MLR) can be utilized to eliminate the birefringence that is present on the glucose signal to determine more accurately the glucose concentration of the dual-wavelength polarimetric system. The combination of the theoretical polarized system model can be utilized in combination with the dual-wavelength ray tracing models presented in this report to evaluate the system response over the physiologic range of known parameters for the eye. These ray tracing models generated with CODE V, Zemax, and Solidworks in addition to the polarimetric analysis performed in MATLAB illustrate that a non-index matched coupling scheme can be implemented utilizing existing commercial optical elements. In addition, the results indicated the expected polarization variation with such a non-index matched coupling scheme can theoretically be accounted for by

using multiple linear regression analysis of the two signals when collected in a dual-wavelength polarimetric system.

Table 3.6: Polarization Model Analysis 635nm Wavelength						
		Actual	Predicted	Savenkov	1f to 2f	Mean change
<u>% Change Linear Retar.</u>	<u>Gluc. Conc. mg/dL</u>	<u>Gluc. Rotation mdeg (635 nm)</u>	<u>Faraday Comp. mdeg (635 nm)</u>	<u>Faraday Comp. mdeg (635 nm)</u>	<u>Faraday Comp. mdeg (635 nm)</u>	<u>Faraday Comp. mdeg (635 nm)</u>
No Bire.	0.00	0.00	0.00	0.00	0.00	0.00
No Bire.	100.00	3.81	-3.75	-3.81	-3.86	-3.27
No Bire.	200.00	7.61	-7.50	-7.61	-7.72	-6.53
No Bire.	300.00	11.42	-11.24	-11.42	-11.58	-9.79
0.00%	0.00	0.00	0.00	0.00	0.00	0.00
0.00%	100.00	3.81	-3.03	-4.71	-3.12	-2.64
0.00%	200.00	7.61	-6.06	-9.41	-6.24	-5.28
0.00%	300.00	11.42	-9.09	-14.12	-9.37	-7.91
0.50%	0.00	0.00	0.00	0.00	0.00	0.00
0.50%	100.00	3.81	-3.02	-4.71	-3.11	-2.64
0.50%	200.00	7.61	-6.05	-9.42	-6.23	-5.26
0.50%	300.00	11.42	-9.07	-14.14	-9.34	-7.90
1.00%	0.00	0.00	0.00	0.00	0.00	0.00
1.00%	100.00	3.81	-3.02	-4.72	-3.11	-2.63
1.00%	200.00	7.61	-6.03	-9.44	-6.21	-5.25
1.00%	300.00	11.42	-9.05	-14.15	-9.32	-7.88
2.00%	0.00	0.00	0.00	0.00	-0.01	-0.13
2.00%	100.00	3.81	-3.00	-4.73	-3.09	-2.62
2.00%	200.00	7.61	-6.00	-9.46	-6.19	-5.23
2.00%	300.00	11.42	-9.01	-14.19	-9.28	-7.84
5.00%	0.00	0.00	0.00	0.00	-0.01	-0.13
5.00%	100.00	3.81	-2.96	-4.76	-3.05	-2.58
5.00%	200.00	7.61	-5.92	-9.52	-6.10	-5.15
5.00%	300.00	11.42	-8.88	-14.28	-9.14	-7.73
10.00%	0.00	0.00	0.00	0.00	-0.01	-0.13
10.00%	100.00	3.81	-2.89	-4.82	-2.97	-2.51
10.00%	200.00	7.61	-5.77	-9.63	-5.94	-5.02
10.00%	300.00	11.42	-8.66	-14.45	-8.92	-7.54
30.00%	0.00	0.00	0.00	0.00	-0.01	-0.13
30.00%	100.00	3.81	-2.56	-5.06	-2.64	-2.23
30.00%	200.00	7.61	-5.12	-10.11	-5.28	-4.46
30.00%	300.00	11.42	-7.69	-15.17	-7.92	-6.69

The glucose concentration was varied from 0 to 500 mg/dL in increments of 100 mg/dL under randomly generated birefringence values ranging between 0 and 3×10^{-4} randomly selected. Figures. 3.10a-d show the compensation voltage and predicted glucose concentration as a function of actual glucose concentration for a single wavelength model at 635 nm and 532 nm respectively. This data was generated utilizing Jones matrix mathematics solving for Equations 3.6 and 3.7 above. The millidegree rotation generated for the respective wavelengths based on percent change in linear retardance at glucose concentrations between 0 and 300 mg/dL in steps of 100 mg/dL are listed in Tables 3.6 and 3.7 below for 635 nm and 532 nm wavelengths respectively. For the initial polarization compensation model (values in Tables 3.6 and 3.7 below) the cornea length was assumed to be 400 microns, aqueous path 0.85 dm, Nasal retardance and temporal retardance were varied from 0 with no birefringence, 1.59×10^{-4} with 0 percent birefringence then varied up to 2.067×10^{-4} to represent a 30 percent change in the linear retardance. In the model, the initial surface retardance remained at 1.59×10^{-4} and the second surface was varied by the corresponding percentage change to evaluate the system performance with respect to changes in birefringence. Following verification of the system model, an additional time-varying model was generated with the birefringence values randomly ranging between zero and 3×10^{-4} using the random function in MATLAB. The thickness of each corneal surface was assigned a thickness of 0.35 mm and the path length through the aqueous humor was assumed 8.5 mm. Diattenuation was included into the eye model using the values presented in the Navarro model (190). For the first surface the diattenuation values were a matrix $D = [0.108 \ 0.00034 \ 0.00034 \ 0.119]$ and the exiting surface diattenuation values were assigned a matrix value of $D2 = [.066 \ 0.0002 \ .0002 \ 0.061]$.

In the models, data generated a modulation frequency of 1.09 kHz was chosen with a modulation depth of +/-1 degree because the majority of published polarimetric schemes used for glucose detection operate at this frequency. Thus, there are reference values available to compare the simulated data with at the specified frequency. The glucose concentration was evaluated between 0 to 500 mg/dL at 10 mg/dL increments.

Table 3.7: Polarization Model Analysis 532nm Wavelength						
		Actual	Predicted	Savenkov	1f to 2f	Mean change
<u>% Change Linear Retard.</u>	<u>Glucose Conc. mg/dL</u>	<u>Glucose Rotation mdeg (532 nm)</u>	<u>Faraday Comp. mdeg (532 nm)</u>	<u>Faraday Comp. mdeg (532 nm)</u>	<u>Faraday Comp. mdeg (532 nm)</u>	<u>Faraday Comp. mdeg (532 nm)</u>
No Bire.	0.00	0.00	0.00	0.00	0.00	0.00
No Bire.	100.00	5.59	-5.53	-5.61	-5.69	-4.81
No Bire.	200.00	11.18	-11.05	-11.22	-11.39	-9.62
No Bire.	300.00	16.76	-16.58	-16.83	-17.08	-14.43
0.00%	0.00	0.00	0.00	0.00	0.00	0.00
0.00%	100.00	5.61	-4.04	-7.68	-4.16	-3.89
0.00%	200.00	11.22	-8.08	-15.35	-8.32	-7.78
0.00%	300.00	16.83	-12.12	-23.03	-12.48	-11.67
0.50%	0.00	0.00	0.00	0.00	0.00	0.00
0.50%	100.00	5.61	-4.03	-7.69	-4.15	-3.88
0.50%	200.00	11.22	-8.05	-15.38	-8.29	-7.76
0.50%	300.00	16.83	-12.08	-23.07	-12.44	-11.64
1.00%	0.00	0.00	0.00	0.00	0.00	0.00
1.00%	100.00	5.61	-4.01	-7.70	-4.13	-3.87
1.00%	200.00	11.22	-8.02	-15.41	-8.26	-7.74
1.00%	300.00	16.83	-12.03	-23.11	-12.40	-11.61
2.00%	0.00	0.00	0.00	0.00	-0.01	-0.13
2.00%	100.00	5.61	-3.98	-7.73	-4.10	-3.86
2.00%	200.00	11.22	-7.96	-15.46	-8.20	-7.71
2.00%	300.00	16.83	-11.95	-23.19	-12.31	-11.56
5.00%	0.00	0.00	0.00	0.00	-0.01	-0.13
5.00%	100.00	5.61	-3.89	-7.81	-4.01	-3.80
5.00%	200.00	11.22	-7.79	-15.63	-8.02	-7.60
5.00%	300.00	16.83	-11.68	-23.44	-12.04	-11.39
10.00%	0.00	0.00	0.00	0.00	-0.01	-0.13
10.00%	100.00	5.61	-3.75	-7.96	-3.86	-3.71
10.00%	200.00	11.22	-7.49	-15.91	-7.72	-7.41
10.00%	300.00	16.83	-11.24	-23.87	-11.57	-11.11
30.00%	0.00	0.00	0.00	0.00	-0.01	-0.13
30.00%	100.00	5.61	-3.09	-8.58	-3.19	-3.29
30.00%	200.00	11.22	-6.19	-17.17	-6.38	-6.58
30.00%	300.00	16.83	-9.28	-25.75	-9.56	-9.87

Utilizing the model parameters described above the theoretical signal at the detector in mg/dL utilizing the optical train shown in Equation 3.6 was utilized. The time varying results are plotted with respect to actual glucose concentration for both wavelengths in Figure 3.9a. Utilizing the reduced matrix method described by Savenkov et al. (193), the

predicted glucose concentration in mg/dL were calculated for both wavelengths and compared to the system equation results in addition to the actual glucose concentration results. A plot of the results produced using the Savenkov method are shown in Figure 3.9b below. An additional calculation was made for each wavelength evaluating the theoretical angle of rotation generated using the ratio of the 1f and 2f signals multiplied by the modulation depth divided by four, as shown in Figure 3.9c. The phase change in each wavelength signal was then evaluated of 10 samples as shown in Figure 3.9d.

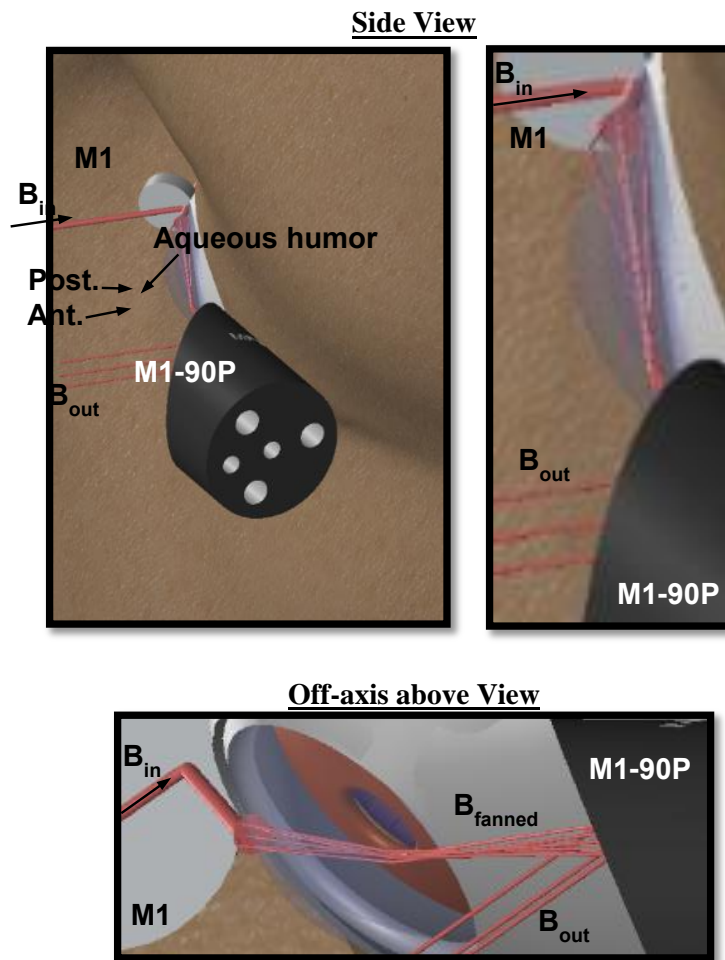


Figure 3.8: 3D anatomical analysis for proposed non-index matched design configuration utilizing CODE V ray trace exported in CAD format. (a) Side view 3D rendering of proposed design for eye coupling, (b) additional zoomed side view illustrating ray trace as beam passes through cornea, and (c) 3D rendering top view of proposed design coupled to eye with facial anatomy included and (b) additional side view of proposed setup illustrating the collimated beam profile for input and output beams.

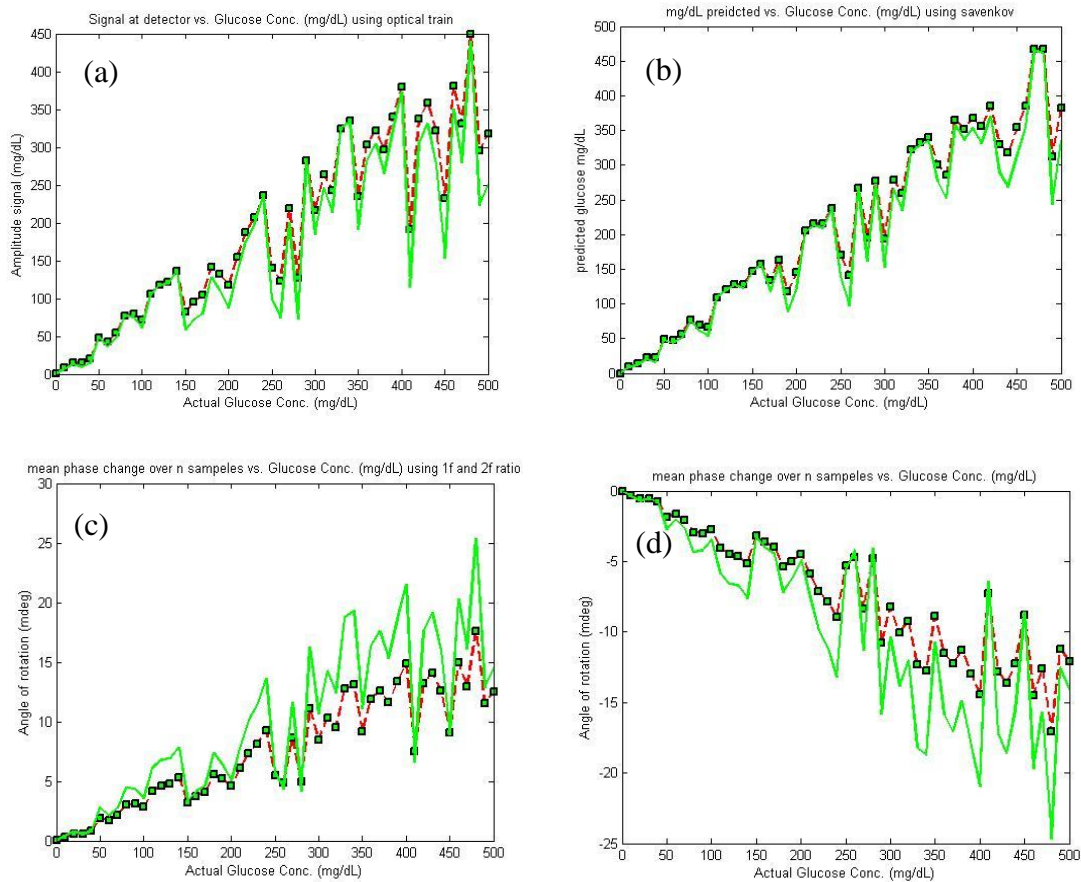


Figure 3.9: Theoretical polarization rotation results for a simulated dual-wavelength polarimeter passing through an eye model with parameters comparable to recorded in vivo data. (a) represents the predicted vs. actual glucose concentration for 635 nm and 532 nm wavelengths over a range of 0-500 mg/dL of glucose with simulate motion induced into the system, (b) represents the same information calculated using the Savenkov method described by Equation 3.7 above, (c) value of rotation for the two respective wavelengths calculated using a ratio relationship between the 1f and 2f signals, and (d) the predicted angle of rotation observed under simulated motion utilizing the mean phase change over 10 samples to determine the theoretical rotation in millidegrees.

The results presented in Tables 3.6 and 3.7 and plotted in Figure 3.9a-d illustrate that slight variations exist between the different theoretical model utilized, which is most likely due to the assumptions that were made in forming each of the simplified polarimetric system models shown in Figure 3.9a-d. The main thing to note is that in all the theoretical models both wavelengths change in the same direction over the 500 sample concentrations tested thus, multiple linear regression (MLR) can be utilized to eliminate the birefringence that is present on the glucose signal to determine more accurately the glucose concentration of the dual-wavelength polarimetric system. The

combination of the theoretical polarized system model can be utilized in combination with the dual-wavelength ray tracing models presented in this report to evaluate the system response over the physiologic range of known parameters for the eye. These models combined illustrate that a non-index matched coupling scheme appears to be achievable utilizing existing commercial optics and the expected polarization changes generated with such a coupling scheme can theoretically be accounted for utilizing a dual wavelength MLR polarimetric system.

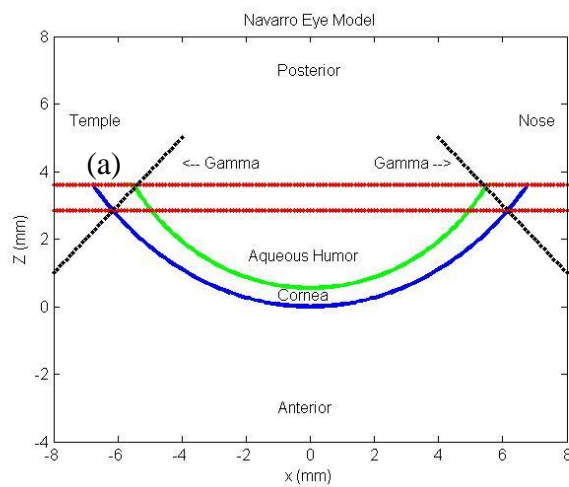


Figure 3.10: Theoretical eye dimensions for the Navarro model and the two extreme cases reported by Winkler et. al (a) represents the size and spacing of the average eye parameters based on the model produced by Navarro, (b) represents the first extreme case where the two corneal surfaces meet near the temple and nose and, (c) the case discussed by Winkler regarding a large separation between corneal layers at the base of the eye near the temple and nose.

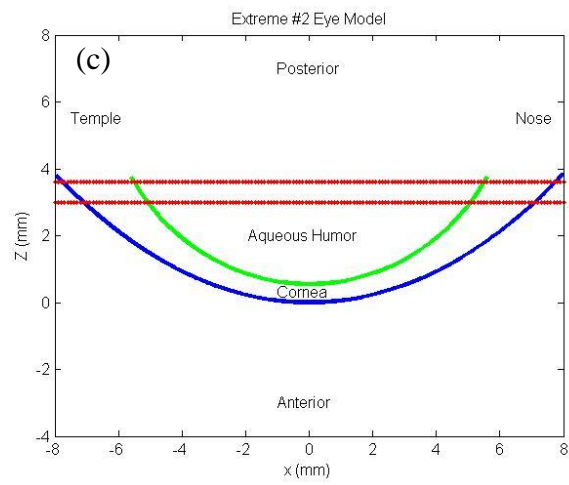
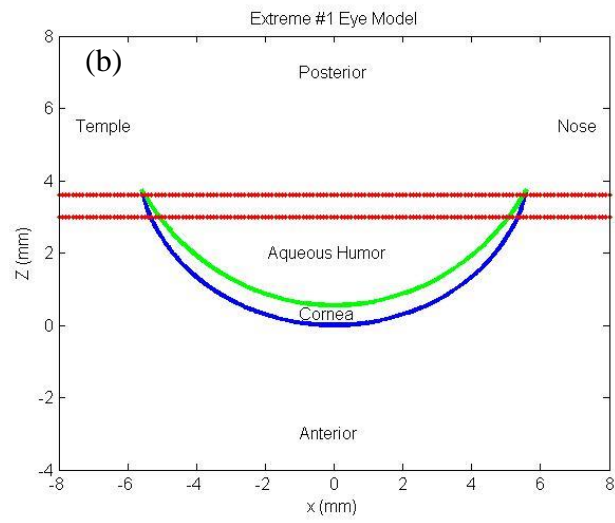


Figure 3.10 Continued

4. DUAL-WAVELENGTH POLARIMETER SYSTEM MINIATURIZATION^{*}

The focuses of the research discussed in this Chapter are studies on the design, building, and testing of a cart-based, non-index matched, dual-wavelength polarimetric system. The current system previously was a large bench top unit that is clearly not ready for the clinic and will thus need to be reduced in size to a cart based system for clinical testing. Additionally, improved compensation speed is preferred about ~100 kHz to allow for improved SNR of the system. Both the optics and the electronics for this system will be re-designed with a focus on enhancing performance with a reduction in overall size. Thus, the optical miniaturization will be accomplished using small laser diodes, miniaturized mirrors, polarizers, and faraday rotators. The reduction is needed primarily to allow for the miniaturized unit, a practical clinical device, as depicted in Figure 4.1. The focus in this specific aim will be designing, building, and testing a miniaturized cart based optical dual-wavelength polarimeter employing an index un-matched eye coupling approach.

The largest sources of noise and speed limiting component in the system are the bulky Faraday rotators. These units are inductive solenoids, typically have multiple windings (over 3,000 turns stacked in multiple layers), and thus require large amounts of current to get even 1 kHz modulation. With a 1 kHz modulation rate, we were able to achieve millisecond sampling. Nonetheless, to progress well above the noise floor and allow for microsecond sampling, we require modulation in the plane of polarization within the 100 kHz range. This range is simply not possible with the current Faraday rotator devices. Additionally, because of potential inductive cross-talk in the magnetic fields between the bulky coil designs, the current Faraday rotators need to be physically separated by a certain distance. However, since we want to miniaturize the system footprint, the distance required to offset the cross-talk is not ideal. Further, the large number of windings causes thermal noise as the coils heat up. Thus, in addition to

^{*} Part of this chapter is reprinted from Pirstill, C.W., Malik, B.H., Thomas E. III, and Coté, G.L. "Design and Characterization of a Ferromagnetic, Air Gapped Magneto-Optic Faraday Rotator," *Opt. Letters*. 30(8), (2013), with kind permission of Optical Society of America.

Part of this chapter is reprinted from Pirstill, C.W., Grunden, D., and Coté, G.L. "Polarimetric Glucose Sensing *in vitro*: a high frequency approach," *Proc. SPIE*. (2013), with kind permission of SPIE.

system miniaturization alternative approaches for Faraday rotators and compensators will be investigated.

4.1. System Miniaturization Tasks

4.1.1. Design and Build Cart Based Miniaturized Dual-wavelength Polarimetric System

Using developed SolidWorks CAD models of the proposed system based on commercially available optical components, as depicted in Figure 4.1, the system was assembled. The system components build on the design described in the previous chapter. Utilizing this model a compact, cart-based optical system that included a small, high frequency laser diodes and a rail system on a ramp platform for easy alignment and coupling to the human subject was constructed. In the approach, two lasers and two feedback rotators were used along with a modulation rotator. The optical sources used in the new design had a smaller footprint. Laser diodes that are 532 and 635 nm offering temperature and power control were purchased. The diodes will be followed by Glan-Thompson linear polarizers (Newport, Irvine, CA) that provide strong horizontal linearly polarized states. The individual beams pass through the newly designed magneto-optic Faraday rotator design that that could potentially operate as both modulators and rotational compensators in order to achieve closed-loop feedback control. After modulation, the two beams are overlaid using a beamsplitter/combiner (Optosigma Corp., Santa Ana, CA). The combined light beams are passed through the (1) adjustable mirror, (2) the eye at a glancing angle, and (3) collected by a concave mirror. The beams, after collimation by the concave mirror, are coupled through a linear polarizer positioned perpendicularly to the initial polarizers to act as an analyzer to the optical beams. The beams are coupled to the detectors and converted into electronic signals using the PIN photodiode (Thorlabs, Newton, NJ).

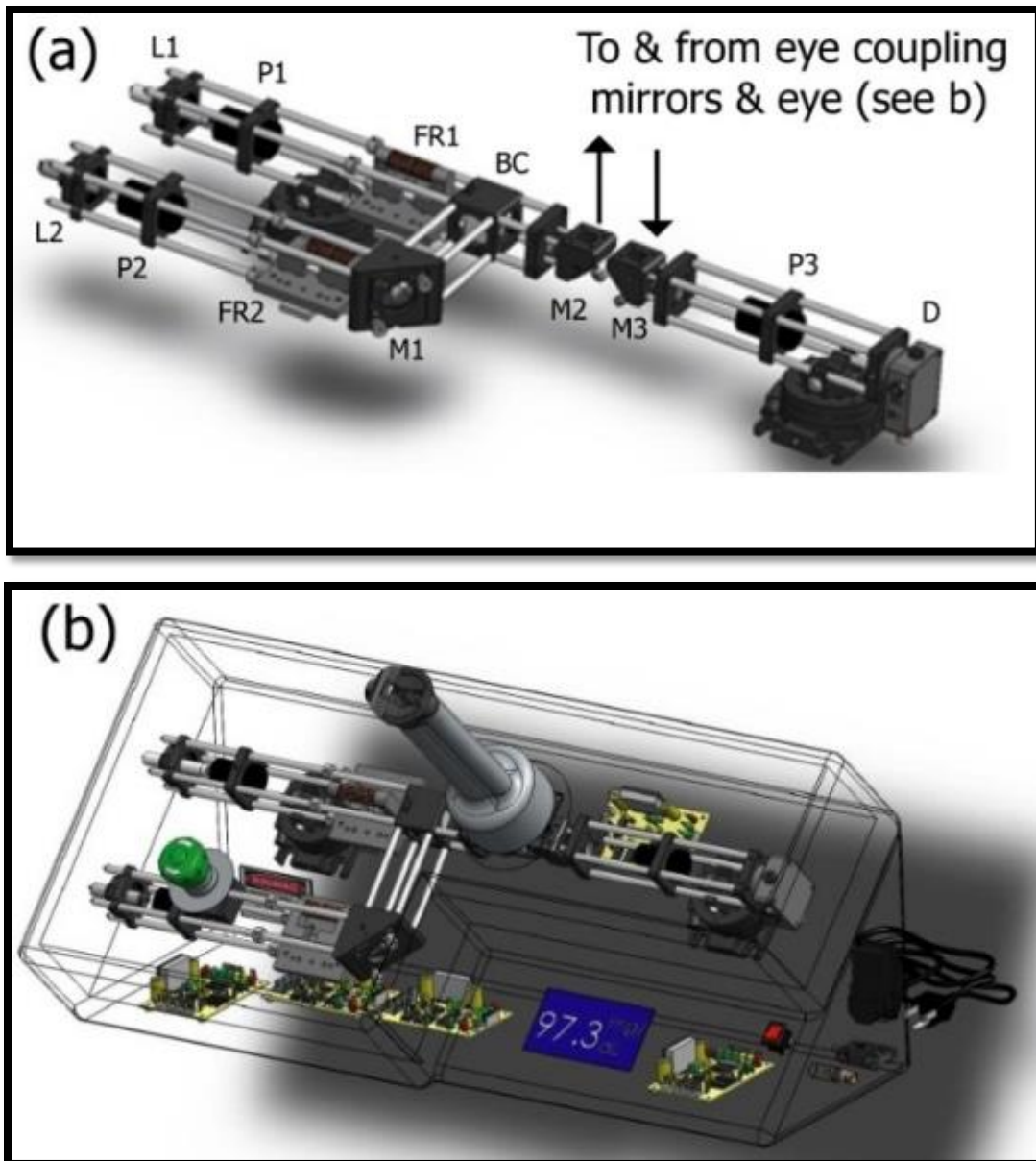


Figure 4.1: (a) SolidWorks model of the caged optical system; left to right are the two lasers (L1 & L2), two polarizers (P1 & P2), two faraday rotators (FR1 & FR2), mirror (M1) and beam combiner (BC), mirror (M2) up to the eye and mirror (M3) to the detection system including crossed polarizer (P3) and detector (D), (b) transparent view of the system with optics, electronics, and eye coupling extension.

The electronic signals pass through wide-bandwidth current amplifiers (CVI Melles Griot, Albuquerque, NM) and signal separation as well as noise reduction of the output from the amplifier is accomplished through the same electronics described in Chapter 2. The electronic outputs of the two lock-in chips will produce DC signals, which serve as

inputs to the laptop computer running a PID controller programmed in LabVIEW 8.9 (National Instruments, Austin, TX). The outputs of this controller are proportional to the glucose concentration and are thus recorded and then used to drive the DC coils on the two Faraday rotators. The data collected was processed using the algorithms defined to provide a real-time glucose response, essential for overcoming motion artifacts and providing a user friendly device with minimal data collection time.

4.1.2. *Perform In Vitro Testing Using a Birefringent Plastic Cuvette*

To test the miniaturized high frequency system a series of *in vitro* (phantom plastic eye) studies were performed. *In vitro* studies were performed with the miniaturized system replacing the current system and new eye coupling design (Figures 4.1 and 3.3). The initial variables examined were optical alignment, optical cross talk, and optimization of the new magneto-optic Faraday rotator design (number of turns, coil length, gap distance, and number of coil layers). The focus was on minimizing the cross talk between the modulators and the electronics and minimizing noise in the system. The milestones was modulation depth of +/- 1 degree, modulation frequency of >10 kHz, and resolution of the overall polarimeter at each wavelength of 0.4 millidegrees (comparable to 10 mg/dL glucose) without motion artifact. Once a sufficient system design and optimal integration with the coupling testing of the accuracy and precision of the approach by conducting *in vitro* glucose studies with the new coupling mechanism over the physiologic range (0-500 mg/dL), with and without motion artifact was performed. Multiple linear regression analysis was utilized. The target milestones were to obtain a mean absolute relative difference (MARD) of less than 15% error in glucose levels across the physiologic range (202).

4.2. **Materials and Methods**

4.2.1. *High Frequency Modulation with Improved Faraday Rotator Design*

The high permeability ferrite core modulator was constructed with an inductive coil wrapped around a ferromagnetic core, designed with an air gap and a through hole designed as an optical path, as shown in Figure 2.8. The core was wrapped with 102

turns of type 100 stranded 38 gauge AWG wires (SPNSN 100/38 served) litz wire (MWS Industries). The magneto-optic material utilized in this design was a Terbium Gallium Garnet (TGG) rod (Deltronic Crystals Inc., Dover, NJ). A soft ferrite high permeability core design allows for a reduction in the overall number of turns of conductive wire required to achieve AC modulation as compared to traditional air-core designs which leads to significantly lower DC coil resistance. The combination of a high permeability, low DC coil resistance coupled with the tunable inductive response in the ferrite cores allows higher frequency modulation to be achieved without suffering from any reduction in the maximum MFD that can be generated by the device. Thus, significant increases in overall device size, or increasing the input power driving the device in comparison to traditional air-core Faraday based optical modulation devices is not required with this design (175).

The components utilized in the single-wavelength polarimeter have been described in detail elsewhere as part of a dual-wavelength polarimetric system (81). The major change to the previously described system is the use of a new Faraday modulator/compensator, as described above. As illustrated in Figure 4.2, the system utilizes a 635nm laser diode emitting at seven mW (Power Technology Inc., Little Rock, AR). The optical beam was passed through a 100,000:1 Glan-Thompson linear polarizer (Newport, Irvine, CA) followed by a magneto-optic ferrite based Faraday rotator, that was driven by both an AC and DC signal. The light beam then travelled through an optical cuvette containing varied concentrations of glucose. The beam exiting the cuvette was then passed through another linear polarizer, the analyzer. The optical train ends at a P-i-N photodetector (Thorlabs, Newton, NJ) that is connected through a wide-bandwidth amplifier (CVI Melles Griot, Albuquerque, NM) to a lock-in amplifier (Stanford Research Systems, Sunnyvale, CA). The output from the lock-in amplifier served as the input to a PID controller, operating on a field-programmable gate array (FPGA), to determine the compensation voltages required to null the system.

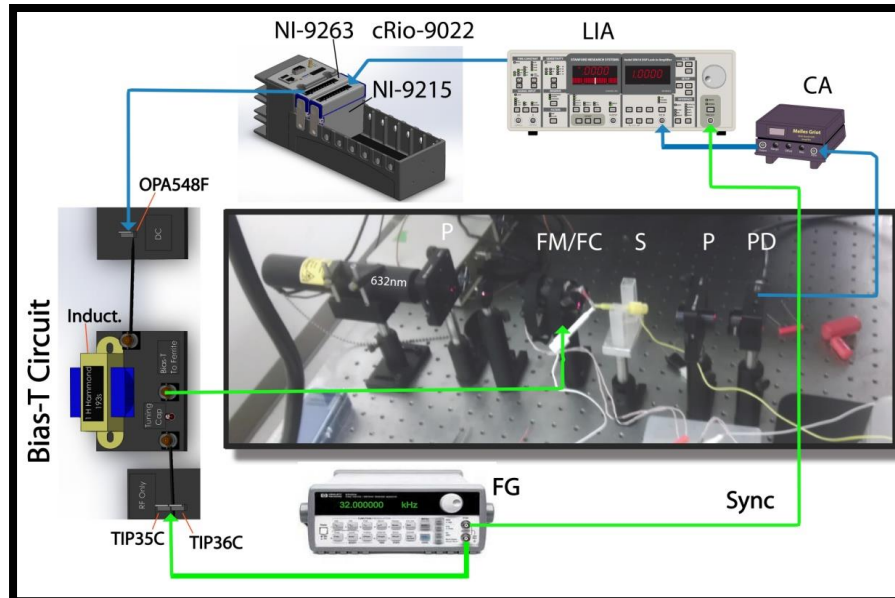


Figure 4.2: Computer-aided design of the single-wavelength polarimetric glucose detection system. P, polarizer; FG, function generator; FM/FC, Faraday modulator/compensator; S, sample cuvette; PD, photodetector; CA, wideband current amplifier; LIA, lock-in amplifier; cRio-9022, compact Rio Real-time FPGA controller, and on the left side is a bias-T circuit used to combine DC and AC signals before supplying the optical modulator. Sync indicates the function of synchronizing the signal generated with the FG with the LIA signal.

The combined AC and DC signal were provided to the Faraday device through the implementation of a Bias-T circuit. The AC signal was generated using a function generator set to provide a 32 kHz sinusoidal waveform with 20 V_{pk-pk} amplitude. The signal was supplied to the Faraday rotators after passing through the combination of a push pull current amplifier constructed from two power transistors (TIP36C and TIP 35C) and a capacitor placed in series with the device. The capacitor was implemented for tuning the device to modulate at the same frequency as the provided signal. This resulted in an AC magnetic field of approximately 53.7 mT produced in the air gap of the rotator, generating a modulation depth of approximately ± 1 degree in the plane of polarization. The DC signal was generated by an analog output module, NI-9263 (National Instruments, Austin, TX) configured into a reprogrammable input/output, compact Rio (cRIO-9022), chassis (National Instruments, Austin, TX). The amplitude of the signal produced by the analog module was provided via the PID controller. The output module was then connected with the input of an OPA548F operational amplifier

used to amplify the DC signal, provided from the PID controller. The amplified DC compensation signal then passed through a one Henry inductor (Hammond 193S) placed in series, with the device and DC driver circuit, before traveling into the Faraday device. The series inductor was added to block the AC signal from traveling into the DC source. This approach provided the capability to drive the Faraday rotator with a combined AC signal and DC offset. More information on the design and implementation of a Bias-T circuit into a polarimeter is available [18].

The PID controller was programmed in LabVIEW 8.9 (National Instruments, Austin, TX), implemented on the cRio-9022 Real-time controller equipped with an onboard FPGA. The Real-Time controller was additionally equipped with two expansion modules to provide analog input and analog output capability to the device. The signal from the lock in amplifier was supplied to the real-time controller chassis via the 4-channel analog input module, NI-9215 (National Instruments, Austin, TX). Using the 4-channel analog output module, NI-9263, feedback was provided to the Faraday compensation/modulation device. The voltage output from the NI-9263 module changing in amplitude at ($<200 \mu\text{sec}$ per iteration), based on the PID determined value, was sent to the OPA548F operational amplifier, part of the Bias-T driver circuit, and in turn used to drive the Faraday compensation on the modulator/compensator device.

4.2.2. Miniaturized Optical Polarimeter For Human Use

Utilizing the cage based system described previously; SolidWorks CAD models of the proposed system based on commercially available optical components as depicted in Figure 4.1 were constructed. The system components build on the design described in Chapter 3 for achieving non-index matched coupling through the anterior chamber. Utilizing this model a compact, cart-based optical system that will include small, high frequency laser diodes and a rail system on a ramp platform for easy alignment and coupling to the human subject was constructed. In the approach, two lasers and two feedback rotators were used along with a modulation rotator. The optical sources used in the new design have a smaller footprint. Laser diodes that are 532 and 635 nm offering temperature and power control were purchased from power technologies. The diodes

were followed by Glan Thompson linear polarizers (Newport, Irvine, CA) that provides a strong horizontal linearly polarized state. The individual beams then pass through the newly designed magneto-optic Faraday rotator design that can operate as both modulators and rotational compensators in order to achieve closed-loop feedback control. After modulation, the two beams are overlaid using a beamsplitter/combiner (Optosigma Corp., Santa Ana, CA). The combined light beams are passed through the (1) adjustable mirror, (2) the eye at a glancing angle, and (3) collected by a concave mirror as described in Chapter 3. The beams, after collimation by the concave mirror, are coupled through a linear polarizer positioned perpendicularly to the initial polarizers to act as an analyzer to the optical beams. The beams are coupled to the detectors and converted into electronic signals using the PIN photodiode (Thorlabs, Newton, NJ).

The electronic signals pass through wide-bandwidth current amplifiers (CVI Melles Griot, Albuquerque, NM) and signal separation as well as noise reduction of the output from the amplifier is accomplished through newly designed electronics. The electronic outputs of the two lock-in chips will produce DC signals, which serve as inputs to the laptop computer running a PID controller programmed in LabVIEW 8.9 (National Instruments, Austin, TX). The outputs of this controller are proportional to the glucose concentration and are thus recorded and then used to drive the DC coils on the two Faraday rotators. The data collected was processed using the algorithms defined in the second Chapter to provide a real-time glucose response, essential for overcoming motion artifacts and providing a user friendly device with minimal data collection time.

To test the new system a series of *in vitro* (plastic cuvette) was examined. The *in vitro* studies were conducted after the current system was replaced with the miniaturized system and new eye coupling design (Figures 4.1 and 3.3). The initial variables examined are optical alignment, optical cross talk, and optimization of the new magneto-optic Faraday rotator design (number of turns, coil length, gap distance, and number of coil layers).

4.3. Results and Discussion

4.3.1. In Vitro Experiments Using Glucose in Cuvette High Frequency

The glucose concentration was varied from 0 to 600 mg/dL in increments of 100 mg/dL over multiple runs. Figures 4.3 and 4.4 show the compensation voltage and predicted glucose concentration as a function of actual glucose concentration for a single wavelength model at 635 nm. This data was analyzed using a simple linear regression model. The standard error in prediction for each data set in addition to the standard error for the average of each data set are shown in Table 4.1. The standard error in prediction of glucose ranged from 9.19 mg/dL to 21.18 mg/dL and 10.08 mg/dL to 19.64 mg/dL for the first and second data run of the 635 nm single wavelength model, respectively.

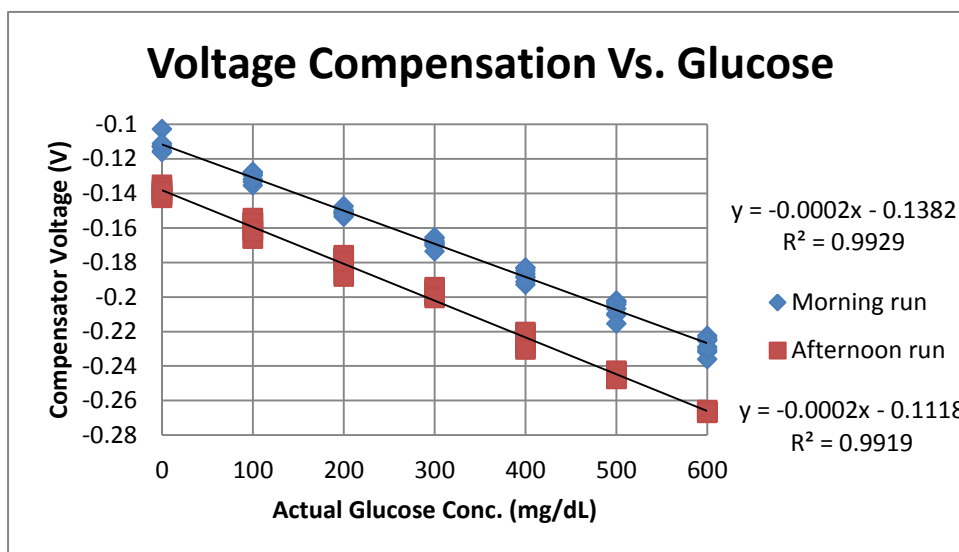


Figure 4.3: Compensation voltage as a function of actual glucose concentration for 635nm single-wavelength model from 0 mg/dL–600 mg/dL in increments of 100 mg/dL, first data set for multiple runs over 2 repeated tests collected at different times.

When taking the average of four runs repeatedly for the first data set and two runs repeatedly for the second data set the standard error was significantly reduced in each of the separate data sets as shown in Table 4.1 below. This illustrates that with faster modulation/compensation achievable with the Faraday modulator/compensator

described herein, it is possible to improve the standard error through obtaining more data over a shorter time span used to average for a more accurate and repeatable standard error. The system produced a standard error of less than 18.5 mg/dL and a MARD of less than 6.66% over the physiologic glucose range in this configuration. The closed-loop system was capable of optical modulation at a frequency of 32 kHz utilizing the ferrite based Faraday modulator device. As shown in Figure 4.3, the two data sets were offset with respect to the starting compensation voltage required in the absence of glucose. Although the voltages were offset between the two runs, the slope for each of the two data sets is the same as shown by the regression line equations in Figure 4.3. Both sets of compensation voltage data sets had a slope of -0.0002. Although the intercepts were different, the overall values were very close together. The first data run “Morning run” consisted of three runs from 0-600 mg/dL with four voltage measurements acquired per concentration change. The result was 12 data points for each glucose concentration. The second data run “Afternoon run” consisted of four runs from 0-600 mg/dL with three voltage measurements acquired per concentration change. The result was 12 data points for each glucose concentration.

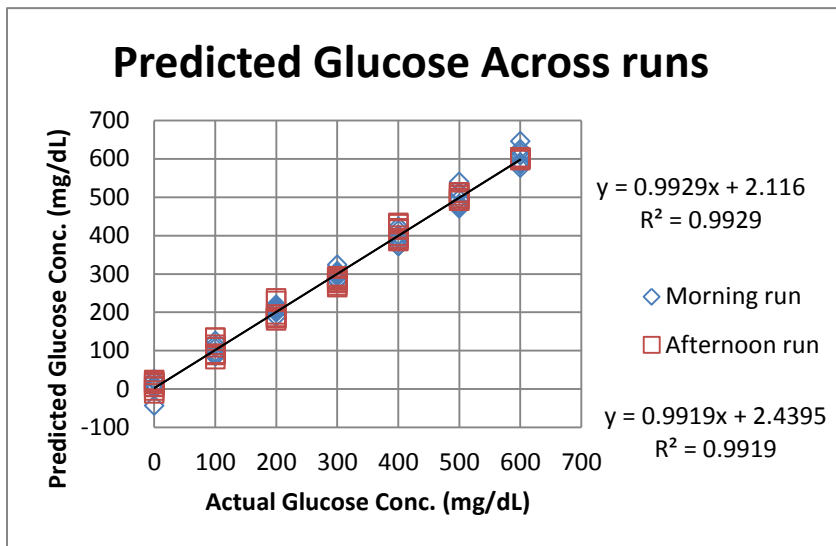


Figure 4.4: Predicted glucose concentration as a function of actual glucose concentration for 635nm single-wavelength model from 0 mg/dL–600 mg/dL in increments of 100 mg/dL, model for multiple runs over 2 repeated tests collected at different times.

Using the data in Figure 4.3 above, a single-wavelength glucose prediction model was created using one of the data sets over the entire morning session and another model for the entire afternoon session using a single data set. Using this model the predicted glucose concentration for each voltage compensation measurement was calculated, as shown in Figure 4.4. Using the predicted glucose concentrations from this linear regression model in addition to the regression model within each data run the mean absolute relative difference (MARD) for each data set was evaluated over a single run and within runs in the morning and afternoon and across runs. In the morning data run a MARD of 2.40% was produced and in the afternoon it was calculated to be 2.06%. The MARD within runs during the morning was 5.33%, within runs in the afternoon produced a MARD of 6.65%, and a MARD of 27.13% was calculated across both data sets. When taking the average of four runs repeatedly for the first data set and two runs repeatedly for the second data the standard error was reduced in each of the separate data sets as shown in Table 4.1 below. This illustrates that with faster modulation/compensation achievable using the Faraday modulator/comp. described herein, it is possible to procure a more accurate and repeatable standard error by obtaining more data over a shorter time span. Using the average voltage over the samples acquired at each individual glucose concentration the standard errors were reduced to between 6.47 to 7.52 mg/dL and 10.75 to 18.17 mg/dL for the morning and afternoon sessions respectively. Due to the offset that occurred between the two data collection sessions, an across morning and afternoon analysis was not evaluated for the data. The offset occurred due to a change in the modulated signal amplitude used for driving the modulation of the device at 32 kHz. The data for the morning and afternoon sessions showed good correlation within the session with calculated R^2 coefficients of 0.992 and 0.993 for the sessions, respectively.

Table 4.1: Standard Error for Each Run and Averaged Runs in mg/dL					
Data Set 1					
Data Set	Run 1-1	Run 1-2	Run 1-3	Run 1-4	Run 1-Average
Standard Error	10.69	11.06	10.78	8.99	7.32
Data Set	Run 2-1	Run 2-2	Run 2-3	Run 2-4	Run 2-Average
Standard Error	12.58	9.19	14.71	15.14	6.47
Data Set	Run 3-1	Run 3-2	Run 3-3	Run 3-4	Run 3-Average
Standard Error	15.20	9.71	16.82	21.18	7.52
Data Set 2					
Data Set	Run 1-1	Run 1-2	Run 1-average		
Standard Error	19.64	16.97	18.17		
Data Set	Run 2-1	Run 2-2	Run 2-average		
Standard Error	15.33	15.37	15.29		
Data Set	Run 3-1	Run 3-2	Run 3-average		
Standard Error	10.10	12.79	10.75		
Data Set	Run 4-1	Run 4-2	Run 4-average		
Standard Error	17.29	14.73	15.86		

Table 4.2: Standard Error for Each Data Set in mg/dL		
Data Set	Morning	Afternoon
Standard Error	18.37	17.10

4.3.2. *PID Closed-Loop Control Design*

4.3.2.1. LabVIEW FPGA PID Configuration and Stabilization Testing

The Proportional-Integral-Derivative (PID) control was programmed in LabVIEW 8.9 (National Instruments, Austin, TX) and implemented utilizing the cRio-9022 real-time controller equipped with an onboard FPGA. In addition to the FPGA chip, the Real-Time controller was also equipped with two expansion modules to provide analog input and output capability to the device. The signal from the lock-in amplifier was supplied to the real-time controller chassis via the 4-channel analog input module, NI-9215

(National Instruments, Austin, TX). Using the 4-channel analog output module, NI-9263, feedback was provided to the Faraday compensation/modulation device. The voltage output from the NI-9263 module, changing in amplitude at ($<200 \mu\text{sec}$ per iteration) based on the PID determined value, was sent to the OPA548F operational amplifier, part of the Bias-T driver circuit, and in turn used to drive the Faraday compensation on the modulator/compensator device. Improved system speed was achieved via utilization of a cRio FPGA DAQ device for the closed-loop control of the polarimetric device. Utilizing the closed-loop system with the ferrite core modulator allowed for optical modulation at 32 kHz with the PID control system reaching stability in less than 10 ms.

4.3.3. Miniaturized Optical Polarimeter Design

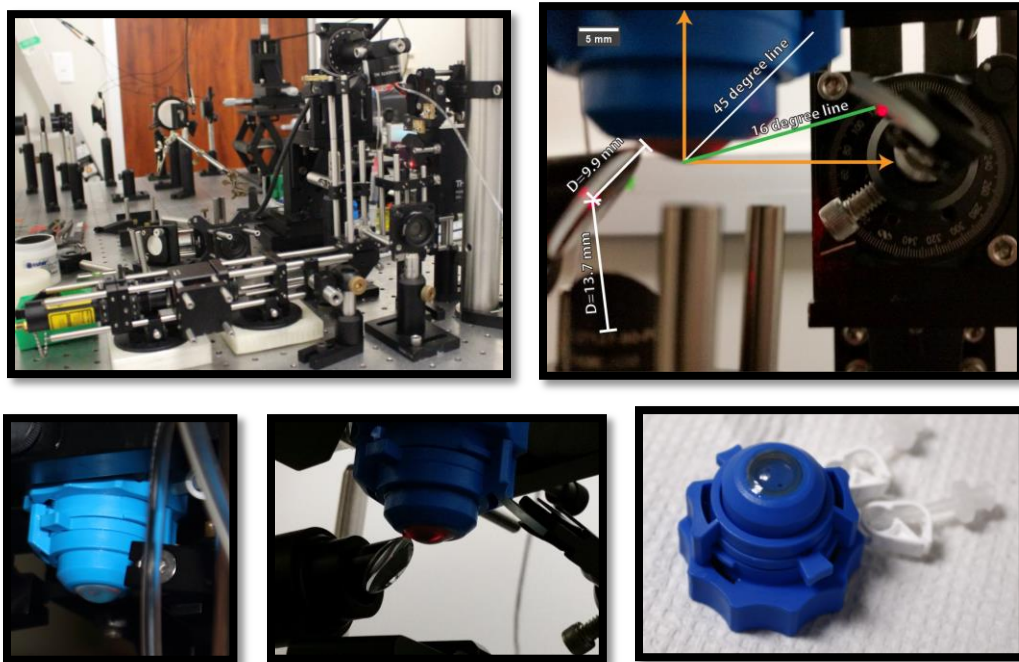


Figure 4.5: (A) Optics of miniaturized dual-wavelength polarimeter on a mount to hold the device steady in envisioned case. (B) Zoomed view of the non-indexed eye coupling in miniaturized system

Using the miniaturized system the eye model illustrated in Chapter 3 was constructed using commercial parts as shown in Figure 4.5(B) and the entire cage system for a single

wavelength was constructed as shown in Figure 4.5(A). Using this system cornea's from three human subjects were mounted onto the eye mount chamber shown in Figure 4.5(B) and polarization measurements were acquired with a Thorlabs polarimeter prior to and after the coupling through the eye. Using the acquired measurements the azimuth, ellipticity, and power measurements were examined at three varying angles (14 degrees, 16 degrees, and 17 degrees) with respect to the optical axis. For these tests, a 632 nm laser diode was used with a laser spot size of approximately 2 mm. The power before the eye was set to around 420 microwatts and the cornea pressure was fixed at 16 mmHg with the anterior glucose solution consisting of a 100 mg/dL solution of glucose.

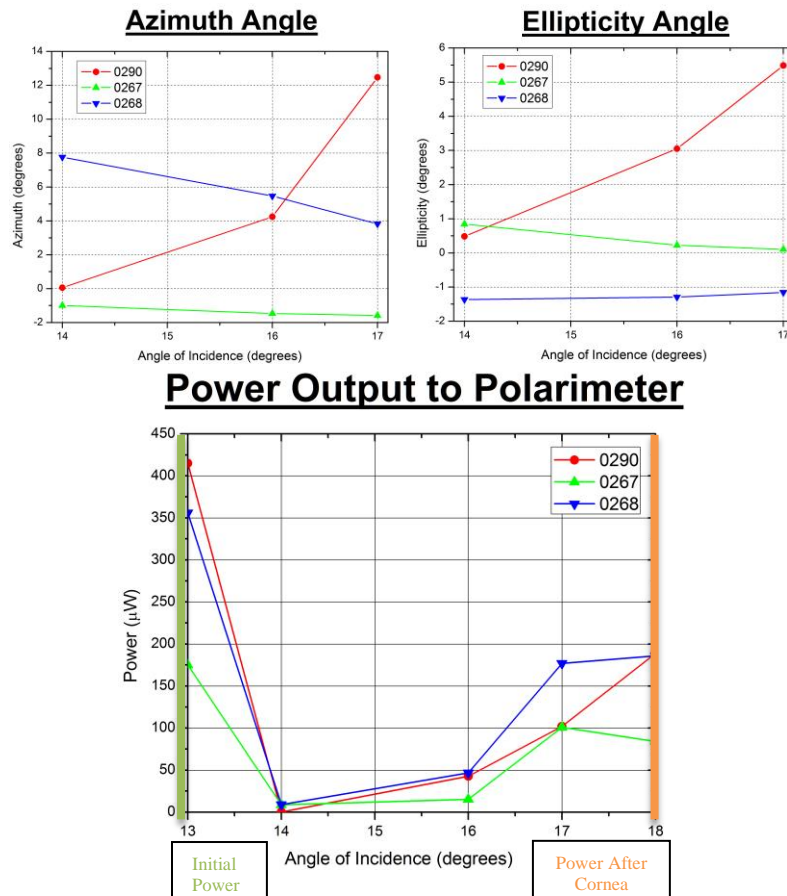


Figure 4.6: (A) Azimuth angle measured across three different human corneas mounted for three angles of incidence. (B) Resultant ellipticity measurement for the same setup and (C) the power output measured at the end of the optical train for each configuration.

5. POLARIZED MICROSCOPY FOR CELL-PHONE BASED MALARIA DIAGNOSIS^{*}

This Chapter describes the design, building, and testing of a low cost, high quality, cellphone based polarimetric imaging system to aid in improved diagnosis of disease. Malaria remains a major global health burden and new methods for, low-cost, high-sensitivity diagnosis of malaria are needed particularly in remote low-resource areas throughout the world. Here, a cost effective optical cell-phone based transmission polarized light microscope system is presented utilized for imaging the malaria pigment known as hemozoin, produced as a by-product of malarial parasitic metabolism during the consumption of hemoglobin that occurs within malaria infected. It can be difficult to determine the presence of the pigment from background and other artifacts even for skilled microscopy technicians using conventional white light microscopy. The pigment is much easier to observe using polarized light microscopy. However, implementation of polarized microscopy lacks widespread adoption because the existing devices have complicated designs, require sophisticated maintenance, tend to be bulky, can be expensive, and would require re-training to existing microscopy technicians. For these reasons, it has not completely translated into the clinic or in developing countries, specifically in remote areas. To this end we present, a high fidelity and high optical resolution cell-phone based polarized light microscopy system, comparable to larger bench-top polarized microscopy systems but at much lower cost and complexity. The detection of malaria infected fixed and stained blood smears are presented using both, a conventional polarized microscope and our cell-phone based system. Although presented over a small sample set, the cell-phone based polarimetric microscopy design described shows the potential to have both the resolution and specificity to detect malaria in a low-cost, easy-to-use, modular platform.

For looking at blood smears for the detection of malaria in addition to histological stained slides it is ideal to have the capability to transmit polarized white light through the sample slide and then collect images with the analyzer oriented at both 45 degrees

^{*} Part of this chapter is reprinted from Pirstill, C.W. and Coté, G.L. "Malaria Diagnosis Using a Mobile Phone Polarized Microscope," Scientific Reports. (2015), with kind permission of Nature Publishing Group.

and 90 degrees with respect to the initial light source polarization. We propose to have a snap on cartridge that allows for transmission mode polarized microscopy as shown in the CAD rendering in Figure 5.2.

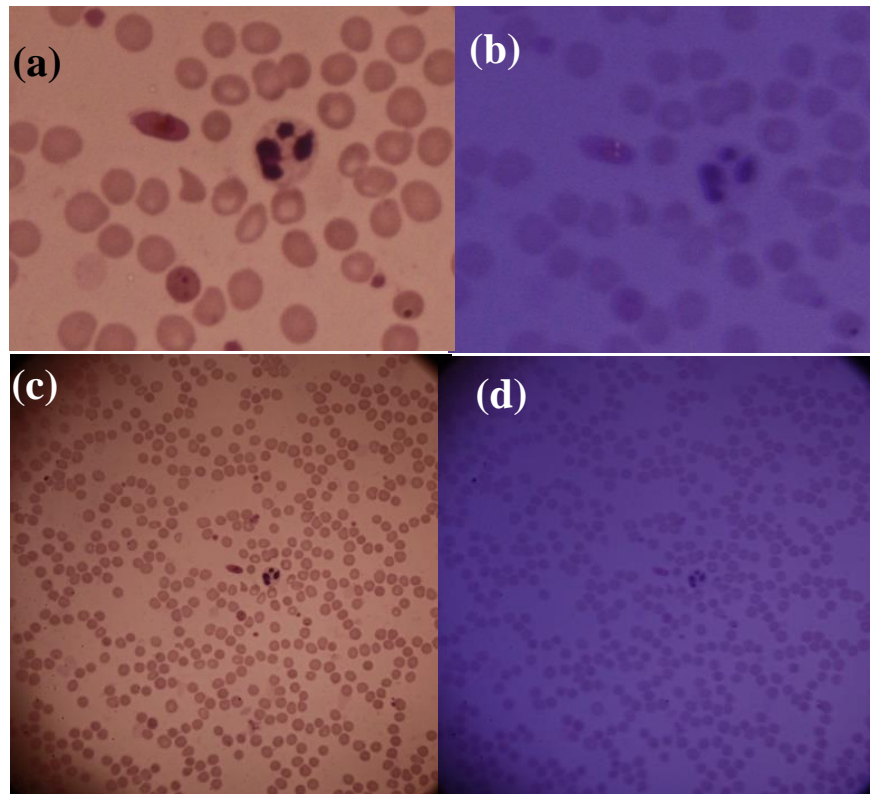


Figure 5.1: Plasmodium falciparum malaria pigment on a thick blood film from a patient with malaria (a) the image was taken using conventional light microscopy (b) image was taken using polarized light microscopy. Similar Giemsa staining as shown in the conventional microscopy severe malaria image and polarized light image over larger FOV for (c) and (d) respectively.

The transmission based cartridge setup will consist of low power surface mount white light LEDs for transmissive illumination. The LEDs will be connected via the 1/4" headphone jack into the cell phone for power. Following the LEDs a polarizer is placed in the optical train generating linearly polarized light prior to transmission through the sample. The opening in Figure 5.2, labeled slide rack is the location where the blood smear or histological slide may be inserted into the optical train. This slit will be located such that the sample is optimally positioned at the focal length of the imaging system.

Utilizing a multi-position insert the slide can be manually moved past the camera from left to right in incremental steps that will be determined during the design process. Using these step incremental movements through the slide will allow the end user the possibility of a mosaic image of the entire slide or an individual image of a specific region within the slide. Following the slide rack opening a polarizer oriented 45 degrees with respect to the light source is placed into the optical path. This polarizer will be movable into and out of the optical path of the imaging train utilizing a slide groove design. However, to eliminate the possibility of losing components the polarizers will be connected using a track design that doesn't allow the component to easily be removed from the overall system. Following this component, positioned a distance relative to the focal length of the lens combination utilized in the setup, will be a lens combination as described above. The final component prior to the cellular phone is another polarizer sheet that will be oriented 90 degrees with respect to the initial polarizer and will be placed just prior to the camera phone. Again this polarizer will be movable into and out of the optical path of the imaging train utilizing a slide groove design.

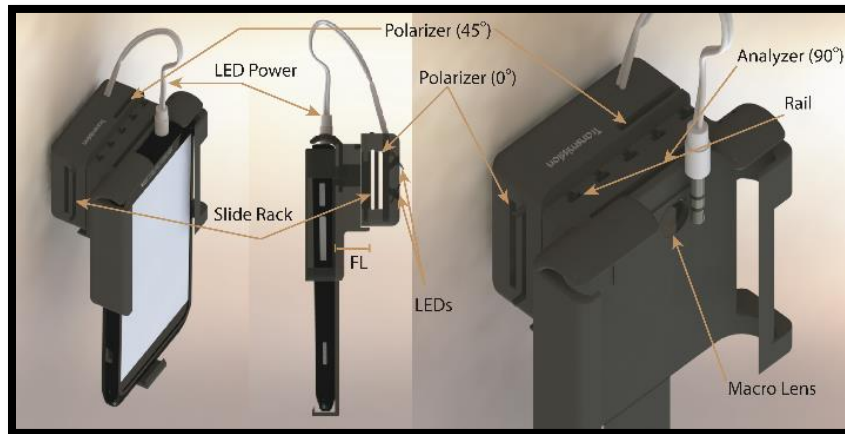


Figure 5.2: CAD prototype of the single-lens on-chip polarized biosensor (left) off axis view of the system with optics, cellphone mount for slide based transmission microscopy applications, (middle) side view illustrating LEDs and compartments for polarizers and (right) additional off axis view of the design illustrating the slots for the polarizer sheets.

5.1. Introduction

Malaria is a life-threatening disease caused by parasites that most often infect a subject via transmission from a mosquito bite. Following infection, the parasite begins invading the host red blood cells and liver cells, modifying the biochemistry and structural properties of the cells. According to the World Health Organization (WHO), an estimated 584,000 deaths were caused by malaria in 2013 with an estimated 198 million new cases in the span of time (85). Worldwide, the mortality rates associated with the disease have fallen, however, a significant portion of deaths still primarily affect African children (85).

In this study, we describe the design of a low-cost, lightweight, high quality mobile-optical-polarization imaging device (MOPID) with similar resolution and field-of-view (FOV) compared to larger bench-top polarized microscopy systems for point-of-care (POC) diagnosis of malaria. The device characterization and preliminary results presented illustrate these key advantages of a MOPID for malaria diagnosis over established detection modalities. In addition to providing advantages such as improved contrast of images containing malaria-infected blood, the technique presented also allows for a reduction in time a skilled professional would need to examine a test slide for determining the presence of an infection.

5.1.1. Design, Build, and Characterize a Mobile Phone Based Transmission Polarized Imaging Microscope

To design, build, and test a low-cost, cellphone based, polarimetric biosensor to aid the medical health professional in improved diagnosis of disease in the clinic and low resource settings. To begin SolidWorks CAD models of the proposed system based on commercially available optical components was developed, as depicted based on preliminary data the multi-wavelength polarimetric approach provides sufficient magnification for the intended applications. Several research groups have previously reported on cell phone based microscopes. Thus, we expect the addition of the polarizers should not change overall functionality of the proven techniques. Additionally, since many of the proposed improvements in diagnosis have already been validated on

commercial polarized microscopy systems the largest remaining challenge will be acquiring images with enough resolution and quality to provide similar diagnostic results. However, since the system is intended to be low-cost the quality will likely be less than commercial polarized microscopy systems. Therefore, validation testing of the optical resolution required to provide similar disease diagnosis to commercial systems will be conducted and the optimal design will be utilized in addition to image processing to improve the diagnosis capability.

5.1.2. Comparison of Design with Traditional Polarized Microscope Using Blood Smears Infected with Malaria

The final step before *in vivo* field-testing of the device is comparison of images to gold standard images from a polarized white light laboratory grade microscope. Testing will evaluate and compare the mobile phone based approach to commercial polarized microscope system based on the following criteria against an air-force target and malaria stained slides.

- **Resolution**
- **Field of View (FOV)**
- **Magnification**
- **Illumination quality**

The milestone for the technique is when it provides similar diagnostic results as the use of polarized microscopy on a lab microscope. Once diagnostic quality is achieved, the design will be tested utilizing malaria infected slides. During the optical ray tracing simulation depth of focus, illumination beam path quality, and divergence angle will be analyzed. The effect these parameters have on the field-of-view, which is in focus for each design, was calculated. Additionally, the predicted system magnification was calculated for each lens combination. Similarly the numerical aperture of the system was calculated and compared to the reported data. Using this number, the diffraction limited resolution is then calculated for each setup configuration. Utilizing each variation of the hardware configuration and different lens combinations United States Air-force (USAF) resolution target images were acquired in addition to many samples on microscope slides

of biological and plant specimens. Utilizing the USAF resolution target in addition to a software package known as imagej the conversion of pixel length to distance in microns on an image can be calculated based on the known size of one of the rectangular bars on the USAF resolution target. Using the known camera settings for focal length, pixel spacing, number of pixels, and f number theoretical limits of the imaging system were calculated. Using these values and known size images the magnification, field of view, and resolution were calculated. Then utilizing a transition between a dark and light rectangle on the air force target a resolution can be calculated based on the full-width-half-max of the derivative of the line passing over the edge between a dark and light.

5.2. Materials and Methods

5.2.1. Polarized Light Systems

In this chapter, a commercial non-inverted polarized Leica DMLM microscope (Leica, Germany) utilized as the reference (Figure 5.3a). The system was equipped with a 20X and/or 40X objective coupled to a commercial Cannon Rebel T3i digital SLR camera (Cannon, Melville, NY), as shown in Figure 5.3a. For the MOPID system the optical setup and components (Figure 5.3b) consisted of a commercial cellular phone, customized attachable mount, two polarizer sheets, low-power high efficiency white light emitting diodes (LEDs), and a plastic lens assembly configuration allowing for appropriate magnification, resolution, and FOV for diagnosing the presence of the malaria parasite.

The Apple (iPhone 5s) camera-enabled cell-phone was used as the base unit. The iPhone 5s employs an 8-Megapixel iSight camera with a CMOS Back-illuminated sensor (BSI). The camera has a physical sensor size of 1/3" or 8.47 mm, with pixel dimensions of 3264×2448 composed of 1.5 μm pixels. The camera also features an autofocus lens and consists of a 5-element plastic lens combination with an aperture size of f/2.2 on top of a sensor.

The designed system utilizes a low-cost plastic lens assembly adjustable to achieve different magnification, resolution, and FOV parameters depending on the desired system and sample specifications. Following the iPhone, an inexpensive microscope

plastic lens assembly (GadgetZone, U.S.), with adjustable focus and zoom between 160X-200X, attached at the focal point just past the camera on the back of the iPhone. The microscope assembly is fitted to the iPhone 5s using a modified plastic phone case (CARSON Optical®, Ronkonkoma, NY) with an open port available to attach the microscope lens assembly positioned at the camera face on the back of the iPhone device. To achieve the range of magnification specified for the product digital zoom implementation using the mobile phone in combination with the optical zoom of the constructed MOPID becomes required.

Following the adjustable multiple lens microscope assembly in the MOPID design, a snap on 3D-printed cartridge constructed to allow for transmission mode polarized microscopy via compartments for individual optical components. The cell-phone 3D-printed cartridge attachment designed consisted of PLA plastic constructed using a Fused Deposition Modeling 3D-printer (MakerBot Industries, New York NY). The attachment included slotted areas to insert the sample microscope slide, a rotatable polarizer sheet, Titanium dioxide, TiO_2 , chip diffuser plate (RTP Company, Winona, MN), and white LEDs (COAST, Portland, OR) to illuminate the sample. The ability to rotate the analyzer, varying the degree of polarization, allows both conventional histology to be utilized in addition to using the birefringence present from the hemozoin crystal for additional contrast in determining the presence of malaria in a blood smear sample for malaria diagnosis.

Utilizing the portable commercial microscope lens assembly, which consisted of two separate plastic lens modules and had a numerical aperture (NA) value of 0.65, utilizing known sample images acquired with the system calculation to determine the NA in addition to other system values. The MOPID design incorporated white light LEDs placed at a distance from the sample, attempting to achieve approximately collimated illumination across the FOV of the microscope. The individual LEDs chosen because of their low-cost, low power, durability, and long lifetime, all characteristics ideally suited for use low-resource settings (89, 97, 203, 204). In the designed system, the white light LED total power was ~66 lumens, and the light passes through a TiO_2 diffuser plate. The

diffuser plate is utilized to allow for homogenous illumination across the sample and was followed by a polarizer sheet generating linearly polarized light prior to transmission through the sample. The opening in Figure 5.3b, labeled slide rack is the location where the blood smear or histological slide is inserted into the optical train. This slit is located such that the sample is optimally positioned at approximately the focal length of the imaging system. Utilizing a multi-position insert the slide can be manually moved past the camera from left to right in incremental steps. Following the slide rack opening, positioned a distance relative to the focal length of the compound element camera lens configuration within the cellular phone (~4 mm from surface of phone), a combination of lenses as described above were inserted to allow for the appropriate magnification and resolution to achieve malaria detection at the individual RBCs level. The final component prior to the mobile phone surface in the optical path is a second polarizer, an analyzer, capable of being oriented either at 45 and/or 90 degrees with respect to the initial polarizer orientation.

Utilizing this illumination geometry the design provided sufficient illumination in non-polarized and cross polarized system configurations to evaluate single red blood cell (RBC) resolution of stained samples and evaluate the birefringence in the sample from the hemozoin crystals.

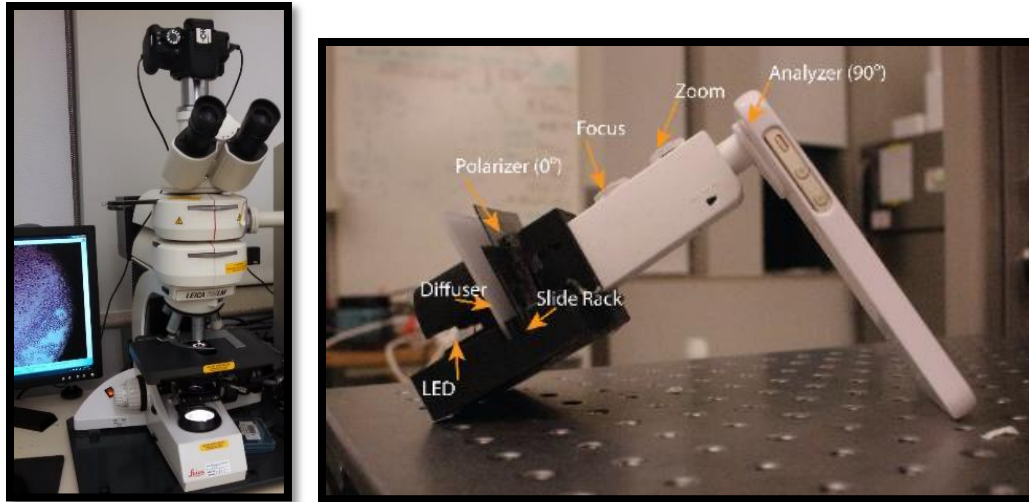


Figure 5.3: (left) Leica DMLM polarized white light microscope used as reference for comparison in this study; and (right) A microscope lens combination implemented into a 3D-printed fitting to allow similar function to a traditional polarized laboratory microscope. MOPID configured in transmission mode with a magnification designed for 40X when using a mobile phone camera. An iPhone 5s used with polarizer sheets added and a 3D-printed fitting to hold the light source, diffuser, sample slide, and microscope attachment.

5.2.2. Blood Smear Sample Preparation

Sample blood smear slides were prepared by collecting a single drop of blood obtained from BALB T cell receptor (TCR) transgenic mice infected with the *Plasmodium chabaudi* malaria parasite. The mice were infected and the blood smear samples collected on day 8 of the infection. The drop of blood acquired from the mice generated the blood smears. To prepare the smear each drop placed onto a glass microscopy slide and smeared with a second glass microscope slide positioned on an edge, dragged across the initial slide generating a wedge-shaped smear of blood across the slide. Prior to acquiring images from the blood sample, the glass slides undergo fixation with methanol and Giemsa-staining. If the malaria parasite is present once the sample is Giemsa-stained the virus becomes visible, a purple ring forms in the RBCs when present, observed via microscopy by carefully trained personal.

5.2.3. Method for Polarized Light Microscopy Imaging

Polarized images acquired with the MOPID and Leica microscope setups described above allowed for comparison between the two systems. The system comparative

evaluation based on the following criteria against a USAF target and blood smear malaria-infected Giemsa-stained slides.

The optical system comparative image analysis to determine if the MOPID provided similar diagnostic accuracy as compared to the Leica reference polarized microscope were conducted. The effect of depth of focus, illumination beam path quality, and divergence angle on the FOV, which is in focus for each design, was calculated. Additionally, the predicted system magnification was determined for the MOPID combination. Similarly the NA of the system was calculated and compared to the reported data. Using this number, the diffraction limited resolution was then calculated for each setup configuration both the MOPID and reference design described above. Utilizing each hardware configuration and the different lens combinations USAF resolution target images were acquired in addition to many prepared samples on microscope slides. Utilizing the USAF target images acquired from the designed MOPIDs in addition to freely-available image analysis software package, ImageJ, the pixel number of each image was converted to distance (μm) based on the known size of the rectangular bar Elements of each Group on the USAF target. Using the recorded camera settings for focal length, pixel spacing, number of pixels, and f-number the theoretical limits of the imaging systems were calculated. With these calculated values and the USAF target images with converted size dimensions, the overall system magnification, FOV, and resolution were calculated for each configuration. Then evaluating the transition between a dark and light rectangle on the smallest resolvable Group and Element number on the USAF target image, a system resolution is calculated based on the FWHM of the derivative of the value of pixel intensity for a line passing over the edge boundary between a dark and light region on the USAF target Element.

5.2.4. Image Analysis

To determine the resolution, FOV, and other optical parameters of each image acquired between the two systems both the ImageJ Fiji plugin and Origins Pro (version 8) statistical software utilized. Initial images acquired from the two respective systems each then opened in ImageJ for processing and analysis of the individual images. To

convert the measurement area of each photograph into micrometer units for FOV calculations and resolution measurements utilizing the Set Scale command in ImageJ. Following this for each image captured a straight line manually placed over the image corresponding to a known distance in the microscope stage image. Using the constructed line and known distance a unit of measurement entered into the Set scale command dialog for conversion allows for transforming pixels to distance. ImageJ then auto populated the distance in pixels field based on the length of the line drawn (110). Following the conversion of length to calculate the resolution, the following sequence of analysis occurred. First, starting with a known Group and Element number on each air-force target a constructed line placed vertically from the black background across the white bar edge of a known length is examined. Using the plot values command in the analyzed pull-down the line x and y values were listed. Using the values a plot generated in Origins from analyzing the shape of the output profile at the edge between the dark and light boundary. Additionally, manual insertion of a scale bar on each image using the ImageJ software occurred followed by saving the images as jpeg extension and utilizing them in this report.

In Origins Pro, after plotting the graph of the boundary, a fit sigmoid function utilized from the analysis pull-down using a Boltzmann function relationship. Using the generated sigmoid fit function, a plot consisting of the derivative of the sigmoid function resulted in a new plot. Then, from the derivative curve plot, a non-linear fit function utilized with a Gaussian fit to the derivative generated curve. From this fit, a FWHM of the spatial resolution generated for each imaging system results. For each USAF target image, multiple Groups and Elements combinations averaged over all FWHM values to develop an approximate resolution value. Averaging reduces the chance of error that can occur in using a single calculation.

5.3. Results and Discussion

A Leica microscope was used as the gold standard and compared to the designed brightfield and polarized brightfield optical instruments that were attached to the iPhone 5s cell-phone as described in the experimental methods section as shown in Figure 5.3.

5.3.1. Performance Testing

Acquisition of individual United States Air-Force (USAF) resolution target images, Figure 5.4 below, using the reference microscope and constructed MOPID device each equipped for transmission mode imaging. The approximate magnification achievable by the MOPID at the camera face was determined to range from ~40X to ~100X depending on the sample, illumination settings, and the FOV for individual images acquired with the mobile phone camera. The overall full-width half maximum (FWHM) was calculated by averaging over the total number of FWHM values individually determined for the sample based on different Group and Element measurements for each image.

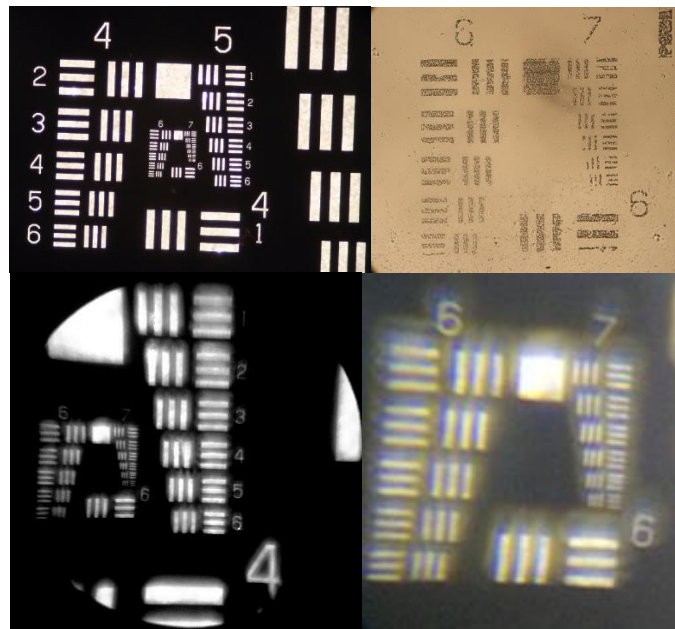


Figure 5.4: USAF resolution target images utilized to determine FOV, resolution, in addition to other optical system parameters with a reference Leica microscope using A.) 20x magnification; and B.) 40x magnification Images. The Air-force target images on bottom acquired using the polarized mobile platform C.) Full zoom with microscope attachment for cell-phone on iPhone 5s and D.) Additional image of target from mobile-phone polarized microscope used to determine the same parameters.

Using Group 7 Element 6, the smallest group on the USAF resolution target, without using the devices digital zoom function FOV for each configuration was determined. From the acquired images, shown in Figure 5.4a-5.4d and Figure 5.5, the FOVs were calculated to be 1.97 mm x 1.10 mm for the reference microscope and 0.78 mm x 0.79

mm for the MOPID configuration shown in Figure 5.3b attached to an iPhone 5s cellular phone. Using the USAF resolution target (Edmund Optics, Barrington, NJ) the highest resolvable Group (Group 7 for iPhone 5s configuration) the systems spatial (lateral) resolution was determined to be $\sim 1.05 \mu\text{m}$. Calculations for spatial resolution resulted from the FWHM measurement of a fit function for the derivative of the boundary line intensity, value between light and dark regions on the USAF target. Calculating the total effective system magnification occurred after careful interpretation of acquired USAF target image features with known distance measurements. This magnification varied from the approximate magnification value at the camera face because of digital enlargement capabilities of the acquired image via the camera software settings on the iPhone 5s before capturing the photograph.

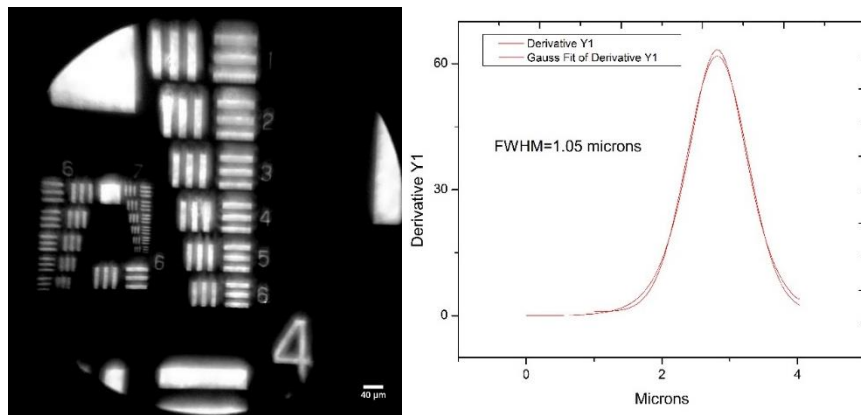


Figure 5.5: iPhone 5s (left) configuration USAF target image and (right) the calculated derivative for a line spread across Group 7 Element 6. FOV was 0.778 mm x 0.792 mm.

The system's lateral resolution measured to be $\sim 1.05 \mu\text{m}$ based on the FWHM of the derivative of USAF line intensity plot. The measured resolution is a factor of 2.6 larger than the nominal Rayleigh resolution limit of $0.4 \mu\text{m}$ for the portable system. An expected increase in measured resolution as compared to nominal Rayleigh resolution limit occurs because the optical components utilized in the construction of the MOPID consist of low-cost plastic lenses. Poor lens selection results in improper correction for field of curvature and additional aberrations that are present in the system, resulting in

reduced resolution away from the field radius of best focus. In addition to the plastic microscope lens components, the mobile phone camera lens assembly also contributes to reduced system resolution observed, resulting in non-diffraction limited performance.

However, as previously reported with many brightfield cell-phone microscope designs (89, 127, 130), the system limitations did not hinder the mobile phone camera from being able to capture high-definition (HD) images of malaria infected blood smear samples and additional non-malaria samples allowing for useful diagnosis and comparison between reference images utilizing a commercially available laboratory microscope.

5.3.2. *Non-Malaria Polarized Light Comparative Sample Images*

Prior to characterizing the MOPID towards the clinically relevant malaria application, non-polarized and cross-polarized images were evaluated from the same area of a slide containing wheat starch using the reference polarized microscope, as shown in Figure 5.3a, and the MOPID, as depicted in Figure 5.3b. The resolution of the images acquired with each system were compared in addition to evaluating if the classic Maltese cross could be depicted from the polarization changes as light transmits through the wheat starch molecules. Indeed, in Figure 5.6b and 5.6c the starch molecules exhibit a Maltese cross configuration. Additionally, using a 40X objective with an NA of 0.65 on the Leica microscope achieved comparable FOV and resolution, with respect to the MOPID images acquired over the same area.

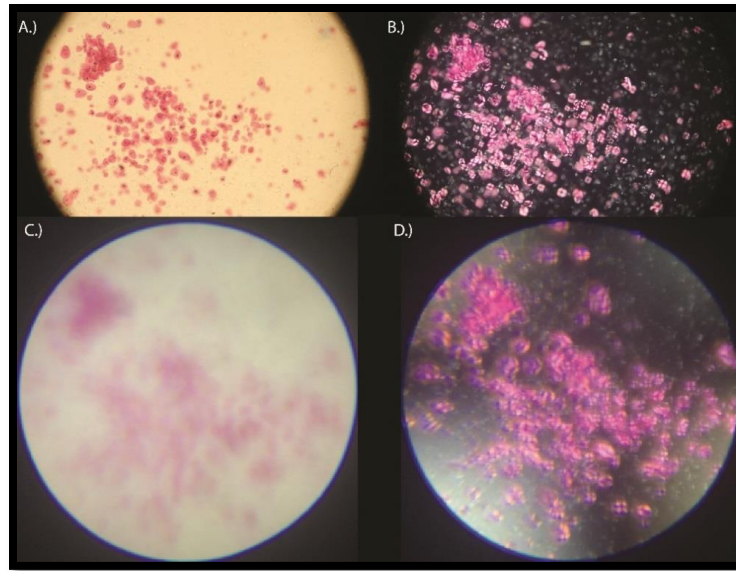


Figure 5.6: Images of a microscope slide coated with wheat starch acquired using a Leica microscope with a 40X objective with a.) No polarizers present in the imaging plane and b.) With a polarizer and analyzer crossed at 90 degrees in the imaging plane. For comparison, the reference an iPhone 5s utilized to acquire images of the same location on the wheat starch slide with c.) Non-polarized; and d.) Polarized with polarizer and analyzer crossed at 90 degrees. In both setups, the polarized images illustrate the presence of a Maltese cross for each starch molecule as expected.

5.3.3. *Brightfield and Polarized Imaging of Malaria*

Comparative brightfield images acquired to analyze a specific zoomed in section on the infected thin blood smear with the reference microscope in non-polarized transmission mode and the MOPID in non-polarized mode, shown in Figure 5.7a-5.7b below. To compare the respective images acquired from each system further illustrating the minimal resolvability of single cell characteristics utilizing the MOPID system, each image acquired in Figure 5.7a-5.7b was enlarged and cropped, as shown with the respective images above Figure 5.7a-5.7b. To represent a smaller region within the image for evaluating individual RBC boundary resolution of less than 1 micron. Figure 5.7 illustrates <2 micron resolution that is capable of being achieved with the low-cost, high resolution MOPID, illustrated in Figure 5.3b below.

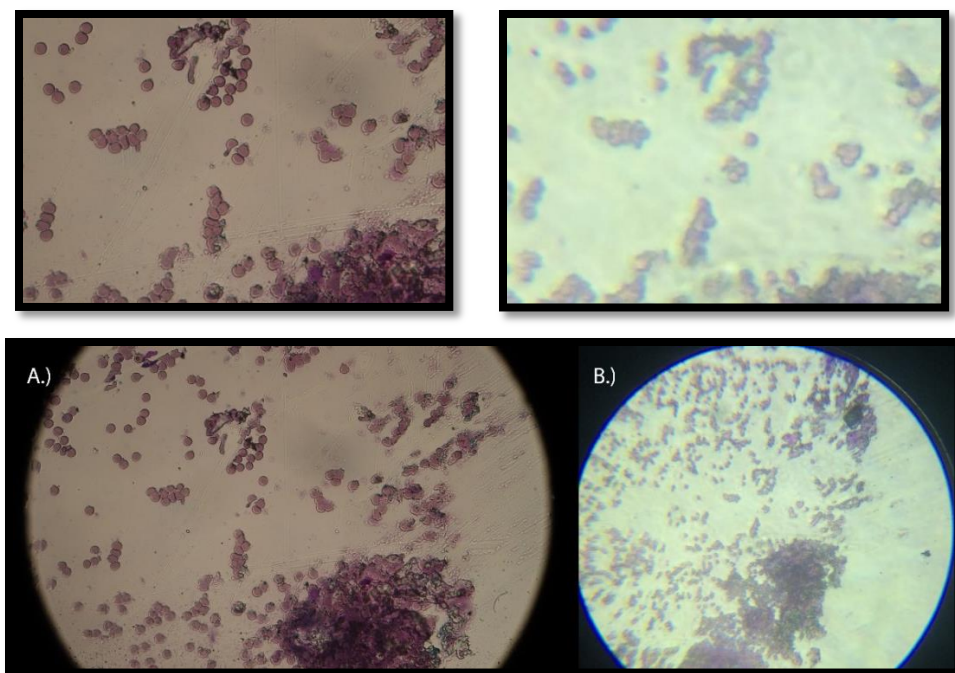


Figure 5.7: Images acquired of mouse malaria strain blood smear using (A) a Leica microscope in non-polarized transmission mode with a 40X magnification objective and (B) the same area of the slide imaged utilizing the iPhone 5s mobile phone based design shown in Figure 5.3b. Above each of the respective images is a zoomed in image of the same region for each photo to better illustrate the comparable resolution of the two microscopes.

The images acquired and displayed in Figure 5.7 for the representative zoomed regions illustrate that while the MOPID cannot resolve each individual blood cell in the FOV, it is capable of resolving single RBC boundaries in many cases where overlap of the RBCs does not occur. Although, this could potentially be a problem in traditional histological examination of the malaria-infected blood smears, it is not an issue in the current setup because of the fact that enhanced contrast achieved when examining the cross-polarized images for the presence of any birefringent variation caused by the hemozoin present in the sample. Following this, evaluation of the constructed MOPID against the reference system in capturing brightfield illumination high-resolution non-polarized and cross-polarized images of thin smears of *Plasmodium chabaudi* malaria-infected blood samples occurred (Figure 5.8).

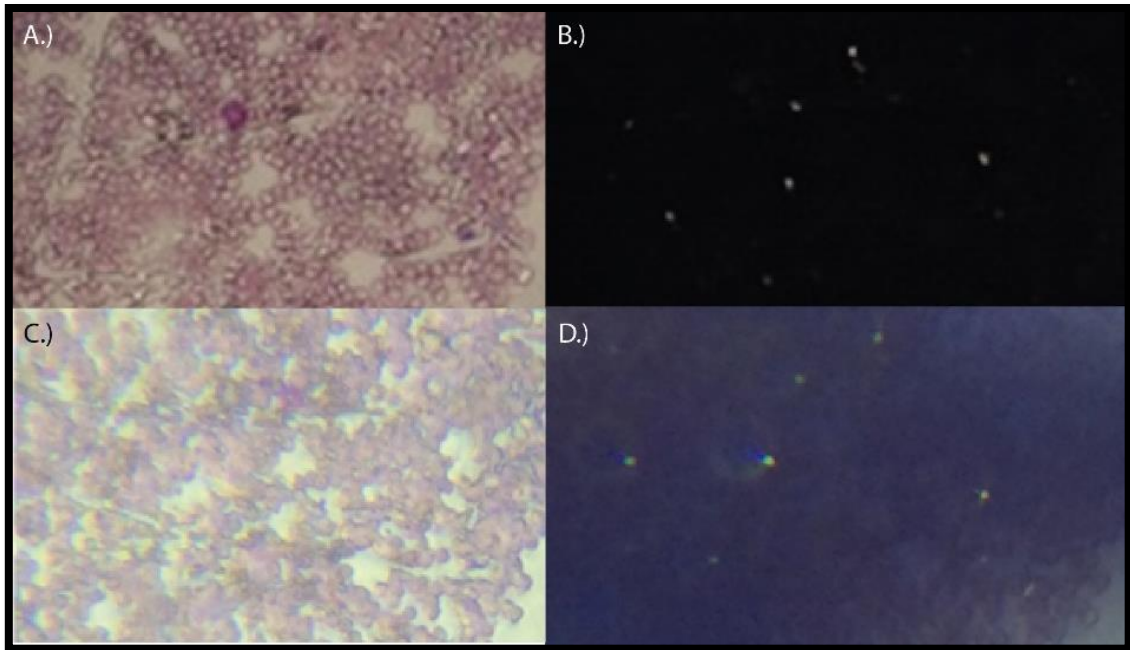


Figure 5.8: Images of a Giemsa stained mouse blood smear using a Leica microscope with a 40X objective and A.) No-polarizers present in the image plane and B.) With a polarizer and analyzer crossed at 90 degrees in the image plane. The iPhone 5s utilized to acquire images of the same location on the prepared microscope slide with C.) The mobile phone polarized microscope system having no polarizers in the system and D.) Including a polarizer and analyzer crossed at 90 degrees in the image plane.

Figures 5.8a and 5.8b show color images, obtained via a digital SLR camera mounted onto a Leica DMLM polarized microscope, of brightfield non-polarized and polarized thin Giemsa-stained blood smear samples of malaria-infected RBCs at 40X magnification. As indicated by the presence of birefringent changes in the polarized reference image, Figure 5.8a, the sample had positive infected areas with the malaria-parasite. The presence of hemozoin particles in the sample cause the polarized transmitted illumination light to vary in intensity and wavelength due to variation in the light as it transmits through the birefringent hemozoin particles. The results of this change, shown in Figure 5.8b, are represented by seven bright white dots that appear in the cross-polarized reference image. As described by Maude et al. in addition to others, the use of polarized microscopy in observing the presence of malaria-infected RBCs has shown to improve diagnostic capability two fold in some instances (91, 110). Following the acquisition of the two reference images, two additional images, a non-polarized and

polarized image were capture employing the same malaria-infected sample and sample region on the blood smear with the MOPID setup and are shown in Figure 5.8c and 5.8d above. It is clear from the non-polarized images that the mobile platform has a reduced system resolution as compared to the reference microscope in polarized mode. However, in examining the polarized images from both systems it is clear that the presence of birefringence appears at the same spots within the sample as the polarized reference image of the sample. This indicates that the results obtained with the MOPID are capable of determining the presence of malaria, potentially more accurately, with lower system resolution, and with less user focus than traditional microscopy requires. The quality of the malaria images could be improved on the MOPID utilizing any one of several methods recently reported in the literature (89, 124, 127-131, 205, 206), such as using improved optical lens designs, using holography techniques, or by employing software image processing techniques to the acquired images. It does not appear necessary, with the current images already providing enough resolution to illustrate the potential improved diagnostic utility of the MOPID system compared to the reference microscope.

The main advantages of the system described in this report are the reduction in cost and complexity associated with conducting polarized microscopy for malaria detection on a mobile platform as well as a reduction in focus and time required by the trained microscopy expert in diagnosing the presence of malaria in a blood smear sample. This significantly increases the potential applications for the approach in addition to increasing the likelihood of adoption of the technique in developing countries where cost and complexity can often prohibit the use of a polarized microscopy technique when traditional laboratory microscopes exist as the standard of diagnosis.

6. CONCLUSIONS AND FUTURE WORK*

6.1. Noninvasive Polarimetric Glucose Monitoring Conclusions

6.1.1. *Conclusions In Vivo*

In summary, we have presented, for the first time, that dual wavelength polarimetry can be used *in vivo* with NZW rabbits to significantly reduce the noise due to corneal birefringence in the presence of motion and provide accurate glucose concentration predictions. The results show MARDs with the dual wavelength system of less than 4.49% across animals and across days and that we can plot the data on a Clarke error grid and obtain 100% within the A+B zones which is within the range of current commercial glucose meters. Although the results presented show, dual-wavelength polarimetry has the ability to measure glucose concentration within the aqueous humor in the presence of motion induced time varying birefringence there are still limitations to this optical approach that will need to be overcome prior to use in pre-clinical trials. One limitation in the *in vivo* data presented was that, although the prediction analysis could be done across animals and across days, it required that within individual trial calibrations be done due to changes in the location of the entrance and exit beam on the cornea across days. Thus, the results are not based on a universal calibration because the current eye-coupling device does not allow a means to determine beam entrance location on the cornea, which imposes offset constraints within and across rabbits. Future work will focus on the development of a better coupling system to allow for the creation of a universal calibration model that works at least within a subject across days and possibly across subjects over several days.

6.1.2. *Conclusions Ferrite Core*

In summary, we present a modulation approach for real-time polarimetry that is capable of glucose monitoring *in vitro* at optical modulation frequencies of tens of kHz and includes the DC-compensation in a single device. Such higher frequency modulation has the potential benefit of improving the signal-to-noise ratio of the system in the presence of motion artifacts. In comparison to previous single and dual wavelength

* Part of this chapter is reprinted from Pimstill, C.W. and Coté, G.L. "Malaria Diagnosis Using a Mobile Phone Polarized Microscope," Scientific Reports. (2015). with kind permission of Nature Publishing Group.

models, the increased frequency response and ability for high frequency modulation and DC compensation on a single device allows for the potential of improved signal-to-noise in addition to decreased system size. The result if employed in a dual-wavelength model provides the potential for improved sensitivity *in vivo*. Future work will focus on the implementation of this design into a dual-wavelength system to test the ability of the device to improve to signal-to-noise ratio utilizing a higher frequency averaging approach in the presence of motion artifact and the development of index unmatched coupling mechanism and the application of this approach *in vivo*.

6.1.3. *Conclusions Eye Modeling*

In summary, we have developed and modeled an index unmatched optical coupling scheme using a reflective based approach capable of evaluating the potential for coupling light into and out of the cornea without the use of index matching between the air-cornea interface. Models were generated in CODE V to evaluate the feasibility of a non-index matched coupling approach consisting of only commercially available optical elements. A reflective optical configuration for each wavelength was modeled. The results produced from the optical modeling indicate the use of a reflective based non-index matched eye-coupling design, such as the one described in this report has the potential to provide polarimetric glucose detection without the use of index matching. The model indicated that with the right commercial optics it is possible to maintain a collimated beam through the optical coupling into and out of the eye if a glancing angle is used to input the beam into the eye and off-axis parabolic mirrors are used to re-collimate the fanned beam exiting the cornea. The CODE V software was shown to work great for exporting the beam profile of the ray trace into 3D CAD software for anatomical consideration in the coupling design. However, in CODE V importing existing commercial models available is not possible in their existing formats. Thus, a modeling program such as Zemax would potentially be better at incorporating the optical elements from THORLABS because the models are provided for Zemax by THORLABS including the optical properties and CAD dimensions of the elements. Further, we presented the development of index unmatched coupling scheme evaluating

optical coupling of light into and out of the cornea via optical ray tracing software. Additionally, we explored reflective optical configurations as well as changes in the polarization signal due to motion for each wavelength. The result indicate with the right commercial optics it is possible to maintain a collimated beam through the optical coupling into and out of the eye if a glancing angle is used to input the beam into the eye and off-axis parabolic mirrors are used to re-collimate the fanned beam exiting the cornea. Future work will focus on the implementation of this design into a dual-wavelength system to test the ability of the optical components utilized in this model to provide results similar to previously reported index matched systems designed by our group.

6.2. Noninvasive Polarimetric Glucose Monitoring Future Work

Further work will focus on developing an algorithm for quantitative real-time glucose measurements as opposed to the retrospective calibrations used in this study. In addition, animals induced with diabetes will be used to enable larger dynamic glucose ranges from 50-600 mg/dL followed by excised human cornea data measurements using the non-index matched system then pre-clinical trials with the newly optimized miniaturized system.

6.3. Polarization Histopathology of Malaria Blood Smears Conclusions

In summary, a polarized microscope platform design was demonstrated using a cell-phone with add on polarization and lens optics that was shown for the first time to be capable of detecting birefringence in histological specimens from the malaria parasite. The MOPID consists of a simple, low-cost, design capable of easily being adapted to multiple mobile device platforms. Device resolution was determined to be sufficient for observing birefringence from hemozoin crystals. Based on the USAF resolution target images acquired with the designed system using the iPhone 5s, a resolution calculated to be 1.05 μm with a system magnification at $\sim 50\text{X}$ and a FOV of 0.78 mm x 0.79 mm. While the non-polarized RBC images are difficult to diagnose, the cross-polarized image clearly indicates the presence of hemozoin in the sample with resolution comparable to polarized imaging using a Leica DMLM polarized microscope. Future work will focus

on further examination of the designed system including more extensive data evaluation using human strains of malaria in addition to the construction of a more compact device, improving durability for *in vivo* field-testing in Rwanda, Africa.

6.4. Polarization Histopathology of Malaria Blood Smears Future Work

Future work on this project will focus on developing an improved form factor possibly using a PDMS based magnification lens reducing the size of the overall optical attachment followed by the design of an automated staining microfluidic channel cartridge to replace the microscopy slides. This would allow repeatable smear data to enhance the automation capabilities of this type of malaria diagnostic technique. Once the final design is optimized and an automated blood smear fluidic design is created the device will be tested in the field in Rwanda to validate the portable durability of such a design in remote areas.

REFERENCES

1. B. D. Cameron, "The Application of Polarized Light to Biomedical Diagnostics and Monitoring," in *Biomedical Engineering*, Texas A&M, Texas A&M (2000).
2. Centers_for_Disease_and_Prevention_(CDC), "National Diabetes Statistics Report: Estimates of Diabetes and Its Burden in the United States, 2014," US Department of Health and Human Services, Atlanta, GA (2014).
3. WHO, "Diabetes Fact Sheet, 2014," (2014)
4. W. Morgan, *Diabetes Mellitus: Its History, Chemistry, Anatomy, Pathology, Physiology, and Treatment*, The Homeopathic Publishing Company, United Kingdom (1877).
5. R. Bilous and R. Donnelly, *Handbook of Diabetes*, John Wiley & Sons, United Kingdom (2010).
6. N. S. Papaspyros, *The History of Diabetes Mellitus*, Georg Thieme Verlag, Stuttgart (1964).
7. D. D. Cunningham and J. A. Stenken, Eds., *In Vivo Glucose Sensing*, John Wiley & Sons, Hoboken, New Jersey (2010).
8. J. L. Smith, *The Pursuit of Noninvasive Glucose: "Hunting the Deceitful Turkey"* (2011).

9. R. Phillips, McGarraugh, G., Jurik , F. A., and Underwood, R. D., Whole blood glucose test strip. Patent #: US 5563042A, (1996).
10. B. G. Osbourne and T. Fearn, *Near Infrared Spectroscopy in Food Analysis*, Longman Scientific and Technical, Harlow, Essex, England (1986).
11. "Intensive Diabetes Treatment and Cardiovascular Disease in Patients with Type 1 Diabetes," *New England Journal of Medicine* 353(25), 2643-2653 (2005)
12. "The effect of intensive treatment of diabetes on the development and progression of long-term complications in insulin-dependent diabetes mellitus. The Diabetes Control and Complications Trial Research Group," *The New England Journal Of Medicine* 329(14), 977-986 (1993)
13. Y. Suzuki, K. Maruo, A. W. Zhang, K. Shimogaki, H. Ogawa and F. Hirayama, "Preliminary evaluation of optical glucose sensing in red cell concentrations using near-infrared diffuse-reflectance spectroscopy," *Journal of Biomedical Optics* 17(1), 017004-017008 (2012)
14. Z.-h. Huang, C.-n. Hao, L.-l. Zhang, Y.-c. Huang, Y.-q. Shi, G.-r. Jiang and J.-l. Duan, "Noninvasive blood glucose sensing on human body with near-infrared reflection spectroscopy," J. J. Puschell, J. Chu, H. Gong and J. Lu, Eds., pp. 81931O-81910, SPIE, Beijing, China (2011).
15. J. J. Burmeister, M. A. Arnold and G. W. Small, "Noninvasive Blood Glucose Measurements by Near-Infrared Transmission Spectroscopy Across Human Tongues," *Diabetes Technology & Therapeutics* 2(1), 5-16 (2000)

16. L. A. Marquardt, M. A. Arnold and G. W. Small, "Near-infrared spectroscopic measurement of glucose in a protein matrix," *Analytical Chemistry* 65(22), 3271-3278 (1993)
17. M. R. Robinson, R. P. Eaton, D. M. Haaland, G. W. Koepp, E. V. Thomas, B. R. Stallard and P. L. Robinson, "Noninvasive glucose monitoring in diabetic patients: A preliminary evaluation," *Clinical Chemistry* 38(9), 1618-1622 (1992)
18. N. Dingari, I. Barman, G. Singh, J. Kang, R. Dasari and M. Feld, "Investigation of the specificity of Raman spectroscopy in non-invasive blood glucose measurements," *Analytical and Bioanalytical Chemistry* 400(9), 2871-2880 (2011)
19. K. Ma, J. M. Yuen, N. C. Shah, J. T. Walsh, M. R. Glucksberg and R. P. Van Duyne, "In Vivo, Transcutaneous Glucose Sensing Using Surface-Enhanced Spatially Offset Raman Spectroscopy: Multiple Rats, Improved Hypoglycemic Accuracy, Low Incident Power, and Continuous Monitoring for Greater than 17 Days," *Analytical Chemistry* 83(23), 9146-9152 (2011)
20. J. M. Yuen, N. C. Shah, J. T. Walsh Jr, M. R. Glucksberg and R. P. Van Duyne, "Transcutaneous glucose sensing by surface-enhanced spatially offset Raman spectroscopy in a rat model," *Analytical Chemistry* 82(20), 8382-8385 (2010)
21. R. Weiss, Y. Yegorchikov, A. Shusterman and I. Raz, "Noninvasive continuous glucose monitoring using photoacoustic technology - Results from the first 62 subjects," *Diabetes Technology & Therapeutics* 9(1), 68-74 (2007)

22. L. Zeng, G. Liu, D. Yang, Z. Ren and Z. Huang, "In Design of a portable noninvasive photoacoustic glucose monitoring system integrated laser diode excitation with annular array detection," in *Prog. Biomed. Optics Imag.- Proc. SPIE* (2009).
23. N. Sudheendran, M. Mohamed, M. G. Ghosn, V. V. Tuchin and K. V. Larin, *Assessment of Tissue Optical Clearing As a Function Of Glucose Concentration Using Optical Coherence Tomography* (2010).
24. K. Larin, I. Larina, M. Motamedi, V. Gelikonov, R. Kuranov and R. Esenaliev, "Potential application of optical coherence tomography for non-invasive monitoring of glucose concentration," in *Prog. Biomed. Optics Imag.- Proc. SPIE* pp. 83-90 (2001).
25. K. V. Larin, M. S. Eledrisi, M. Motamedi and R. O. Esenaliev, "Noninvasive Blood Glucose Monitoring With Optical Coherence Tomography," *Diabetes Care* 25(12), 2263-2267 (2002)
26. K. V. Larin, J. D. Morrisett, M. G. Ghosn and V. V. Tuchin, "Noninvasive functional imaging of tissue abnormalities using optical coherence tomography," in *Sensors, 2010 IEEE*, pp. 2283-2286 (2010).
27. K. V. Larin, M. Motamedi, T. V. Ashitkov and R. O. Esenaliev, "Specificity of noninvasive blood glucose sensing using optical coherence tomography technique: a pilot study," *Phys. Med. Biol.* 48(1371-1390 (2003)

28. W. F. March, B. Rabinovitch and R. L. Adams, "Noninvasive Glucose Monitoring of the Aqueous Humor of the Eye: Part II. Animal Studies and the Scleral Lens," *Diabetes Care* 5(3), 259-265 (1982)
29. B. Rabinovitch, W. F. March and R. L. Adams, "Noninvasive glucose monitoring of the aqueous humor of the eye: Part I. Measurement of very small optical rotations," *Diabetes Care* 5(3), 254-258 (1982)
30. B. D. Cameron, H. W. Gorde, B. Satheesan and G. L. Coté, "The Use of Polarized Laser Light Through the Eye for Noninvasive Glucose Monitoring," *Diabetes Technology & Therapeutics* 1(2), 135-143 (1999)
31. T. W. King, G. L. Cote, R. J. McNichols and M. J. Goetz, "Multispectral polarimetric glucose detection using a single Pockels cell," *Optical Engineering* 33(8), 2746-1753 (1994)
32. R. W. Knighton, X. R. Huang and L. A. Cavuoto, "Corneal birefringence mapped by scanning laser polarimetry," *Opt. Express* 16(18), 13738-13751 (2008)
33. B. H. Malik and G. L. Coté, "Real-time, closed-loop dual-wavelength optical polarimetry for glucose monitoring," *Journal of Biomedical Optics* 15(1), 017002 (2010)
34. B. H. Malik, C. W. Pirstill and G. L. Cote, "Polarimetric glucose sensing in an artificial eye anterior chamber," in *SPIE Photonics West* R. J. Nordstrom and G. L. Cote, Eds., pp. 82290O-82290O-82296, SPIE, San Francisco, CA (2012).

35. B. H. Malik, C. W. Pirnstill and G. L. Cote, "Dual wavelength polarimetric glucose sensing in the presence of birefringence and motion artifact using anterior chamber of the eye phantoms," pp. 1-27, *Journal of Biomedical Optics* (2012).
36. G. Purvinis, B. D. Cameron and D. M. Altrogge, "Noninvasive polarimetric-based glucose monitoring: an in vivo study," *J Diabetes Sci Technol* 5(2), 380-387 (2011)
37. Q. Wan, G. L. Coté and J. B. Dixon, "Dual-wavelength polarimetry for monitoring glucose in the presence of varying birefringence," *Journal of Biomedical Optics* 10(2), 024029 (2005)
38. G. L. Cote, M. D. Fox and R. B. Northrop, "Noninvasive optical polarimetric glucose sensing using a true phase measurement technique," *Biomedical Engineering, IEEE Transactions on* 39(7), 752-756 (1992)
39. B. D. Cameron and G. L. Cote, "Noninvasive glucose sensing utilizing a digital closed-loop polarimetric approach," *Biomedical Engineering, IEEE Transactions on* 44(12), 1221-1227 (1997)
40. C. Chou, C.-Y. Han, W.-C. Kuo, Y.-C. Huang, C.-M. Feng and J.-C. Shyu, "Noninvasive Glucose Monitoring in Vivo with an Optical Heterodyne Polarimeter," *Appl. Opt.* 37(16), 3553-3557 (1998)
41. B. D. Cameron, J. S. Baba and G. L. Coté, "Measurement of the Glucose Transport Time Delay Between the Blood and Aqueous Humor of the Eye for

the Eventual Development of a Noninvasive Glucose Sensor," *Diabetes Technology & Therapeutics* 3(2), 201-207 (2001)

42. A. J. Webb and B. D. Cameron, "The use of optical polarimetry as a noninvasive in vivo physiological glucose monitor," R. J. Nordstrom and G. L. Cote, Eds., pp. 79060E-79065, SPIE, San Francisco, California, USA (2011).
43. R. J. McNichols and G. L. Cote, "Optical glucose sensing in biological fluids: an overview," *Journal of Biomedical Optics* 5(1), 5-16 (2000)
44. A. Tura, A. Maran and G. Pacini, "Non-invasive glucose monitoring: Assessment of technologies and devices according to quantitative criteria," *Diabetes research and clinical practice* 77(1), 16-40 (2007)
45. N. S. Oliver, C. Toumazou, A. E. G. Cass and D. G. Johnston, "Glucose sensors: a review of current and emerging technology," *Diabetic Medicine* 26(3), 197-210 (2009)
46. V. V. Tuchin, Ed., *Handbook of Optical Glucose in Biological Fluids and Tissues*, Taylor and Francis Group, Boca Raton, FL (2009).
47. A. C. Guyton and J. E. Hall, *Textbook of Medical Physiology*, Saunders (2005).
48. V. Kumar, A. K. Abbas, N. Fausto and J. Aster, *Robbins & Cotran Pathologic Basis of Disease, 8th edition*, Saunders Elsevier, Philadelphia, PA (2010).

49. D. G. Marrero, "The Prevention of Type 2 Diabetes: An Overview," *J. Diabetes Sci. Technol.* 3(4), 756-760 (2009)
50. G. G. Harrigan and R. Goodacre, Eds., *Metabolic profiling: its role in biomarker discovery and gene function analysis*, Kluwer Academic Publishers (2003).
51. S. Y. Wang, C. E. Hasty, P. A. Watson, J. P. Wicksted, R. D. Stith and W. F. March, "Analysis of metabolites in aqueous solutions by using laser Raman spectroscopy," *Applied optics* 32(6), 925-929 (1993)
52. M. J. Goetz Jr, G. L. Cote, R. Erckens, W. March and M. Motamedi, "Application of a multivariate technique to Raman spectra for quantification of body chemicals," *IEEE Transactions on Biomedical Engineering* 42(7), 728-731 (1995)
53. X. Dou, Y. Yamaguchi, H. Yamamoto, H. Uenoyama and Y. Ozaki, "Biological applications of anti-Stokes Raman spectroscopy: Quantitative analysis of glucose in plasma and serum by a highly sensitive multichannel Raman spectrometer," *Applied Spectroscopy* 50(10), 1301-1306 (1996)
54. A. J. Berger, I. Itzkan and M. S. Feld, "Feasibility of measuring blood glucose concentration by near-infrared Raman spectroscopy," *Spectrochimica Acta - Part A Molecular Spectroscopy* 53(2), 287-292 (1997)
55. T. W. Koo, A. J. Berger, I. Itzkan, G. Horowitz and M. S. Feld, "Reagentless blood analysis by near-infrared Raman spectroscopy," *Diabetes technology & therapeutics* 1(2), 153-157 (1999)

56. M. S. Borchert, M. C. Storrie-Lombardi and J. L. Lambert, "A noninvasive glucose monitor: preliminary results in rabbits," *Diabetes technology & therapeutics* 1(2), 145-151 (1999)
57. R. V. Tarr and P. G. Steffes, "Non-invasive blood glucose measurement system and method using stimulated Raman spectroscopy," (1993).
58. J. P. Wicksted, R. J. Erckens, M. Motamedi and W. F. March, "Raman Spectroscopy Studies of Metabolic Concentrations in Aqueous Solutions and Aqueous Humor Specimens," *Appl. Spectrosc.* 49(7), 987-993 (1995)
59. N. C. Dingari, I. Barman, J. W. Kang, C.-R. Kong, R. R. Dasari and M. S. Feld, "Wavelength selection-based nonlinear calibration for transcutaneous blood glucose sensing using Raman spectroscopy," *Journal of Biomedical Optics* 16(8), 087009-087010 (2011)
60. B. Shim, H. Oh, J. Oh, Y. Yang, Y. Ku, M. Kim, D. Kim, H. Eum, S. Cho and D. R. Miller, "An investigation of the effect of in vivo interferences on Raman glucose measurements," R. J. Nordstrom and G. L. Cote, Eds., pp. 79060Z-79067, SPIE, San Francisco, California, USA (2011).
61. N. C. Dingari, I. Barman, G. P. Singh, J. W. Kang, R. R. Dasari and M. S. Feld, "Investigation of the specificity of Raman spectroscopy in non-invasive blood glucose measurements," *Analytical and Bioanalytical Chemistry* 400(9), 2871-2880 (2011)
62. M. Moskovits, "Surface-enhanced spectroscopy," *Reviews of Modern Physics* 57(3), 783-826 (1985)

63. R. K. Chang and T. E. Furtak, *Surface Enhanced Raman Scattering*, Plenum Press, New York (1982).
64. K. Kneipp, H. Kneipp, I. Itzkan, R. R. Dasari and M. S. Feld, "Surface-enhanced Raman scattering: A new tool for biomedical spectroscopy," *Current Science* 77(7), 915-924 (1999)
65. T. Vo-Dinh, D. L. Stokes, G. D. Griffin, M. Volkan, U. J. Kim and M. I. Simon, "Surface-enhanced Raman Scattering (SERS) method and instrumentation for genomics and biomedical analysis," *Journal of Raman Spectroscopy* 30(9), 785-793 (1999)
66. T. Vo-Dinh, "Surface-enhanced Raman spectroscopy using metallic nanostructures," *TrAC - Trends in Analytical Chemistry* 17(8-9), 557-582 (1998)
67. P. Matousek, I. P. Clark, E. R. C. Draper, M. D. Morris, A. E. Goodship, N. Everall, M. Towrie, W. F. Finney and A. W. Parker, "Subsurface probing in diffusely scattering media using spatially offset Raman spectroscopys," *Applied Spectroscopy* 59(4), 393-400 (2005)
68. P. Matousek, M. D. Morris, N. Everall, I. P. Clark, M. Towrie, E. Draper, A. Goodship and A. W. Parker, "Numerical simulations of subsurface probing in diffusely scattering media using spatially offset Raman spectroscopy," *Applied Spectroscopy* 59(12), 1485-1492 (2005)

69. G. B. Christison and H. A. MacKenzie, "Laser photoacoustic determination of physiological glucose concentrations in human whole blood," *Medical and Biological Engineering and Computing* 31(3), 284-290 (1993)
70. K. M. Quan, G. B. Christison, H. A. MacKenzie and P. Hodgson, "Glucose determination by a pulsed photoacoustic technique: An experimental study using a gelatin-based tissue phantom," *Physics in Medicine and Biology* 38(12), 1911-1922 (1993)
71. M. Pleitez, H. von Lilienfeld-Toal and W. Mäntele, "Infrared spectroscopic analysis of human interstitial fluid in vitro and in vivo using FT-IR spectroscopy and pulsed quantum cascade lasers (QCL): Establishing a new approach to non invasive glucose measurement," *Spectrochimica Acta Part A: Molecular and Biomolecular Spectroscopy* 85(1), 61-65 (2012)
72. H. von Lilienfeld-Toal, M. Weidenmüller, A. Xhelaj and W. Mäntele, "A novel approach to non-invasive glucose measurement by mid-infrared spectroscopy: The combination of quantum cascade lasers (QCL) and photoacoustic detection," *Vibrational Spectroscopy* 38(1-2), 209-215 (2005)
73. S. Camou, Y. Ueno and E. Tamechika, "Towards non-invasive and continuous monitoring of blood glucose level based on CW photoacoustics: New concept for selective and sensitive measurements of aqueous glucose," in *Sensing Technology (ICST), 2011 Fifth International Conference on*, pp. 193-197 (2011).
74. J. Kottmann, J. M. Rey, J. Luginbühl, E. Reichmann and M. W. Sigrist, "Glucose sensing in human epidermis using mid-infrared photoacoustic detection," *Biomed. Opt. Express* 3(4), 667-680 (2012)

75. J. Solanki, P. Sen, J. T. Andrews and K. K. Thareja, "Cyclic Correlation of Diffuse Reflected Signal with Glucose Concentration and Scatterer Size," *Journal of Modern Physics* 3(64-68 (2012)
76. X. Guo, Z. Guo, H. Wei, H. Yang, Y. He, S. Xie, G. Wu, H. Zhong, L. Li and Q. Zhao, "In vivo quantification of propylene glycol, glucose and glycerol diffusion in human skin with optical coherence tomography," *Laser Physics* 20(9), 1849-1855 (2010)
77. A. Popov, A. Bykov, S. Toppari, M. Kinnunen, A. Priezhev and R. Myllyla, "Glucose sensing in flowing blood and Intralipid by laser pulse time-of-flight and optical coherence tomography techniques," *Selected Topics in Quantum Electronics, IEEE Journal of PP(99)*, 1-1 (2011)
78. Z. Li, H. Li, J. Li and X. Lin, "Feasibility of glucose monitoring based on Brownian dynamics in time-domain optical coherence tomography," *Laser Physics* 21(11), 1995-1998 (2011)
79. H. Ullah, A. Mariampillai, M. Ikram and I. Vitkin, "Can temporal analysis of optical coherence tomography statistics report on dextrorotatory-glucose levels in blood?," *Laser Physics* 21(11), 1962-1971 (2011)
80. R. Ballerstadt, A. Kholodnykh, C. Evans, A. Boretsky, M. Motamedi, A. Gowda and R. McNichols, "Affinity-Based Turbidity Sensor for Glucose Monitoring by Optical Coherence Tomography: Toward the Development of an Implantable Sensor," *Analytical Chemistry* 79(18), 6965-6974 (2007)

81. B. H. Malik and G. L. Cote, "Real-time, closed-loop dual-wavelength optical polarimetry for glucose monitoring," *Journal of Biomedical Optics* 15(1), 017002-017006 (2010)
82. C. W. Pirnstill, B. H. Malik, V. C. Gresham and G. L. Coté, "In Vivo Glucose Monitoring Using Dual-Wavelength Polarimetry to Overcome Corneal Birefringence in the Presence of Motion," *Diabetes Technology & Therapeutics* 14(9), 819-827 (2012)
83. B. D. Cameron, J. S. Baba and G. L. Cote, "Measurement of the glucose transport time delay between the blood and aqueous humor of the eye for the eventual development of a noninvasive glucose sensor," *Diabetes Technol Ther* 3(2), 201-207 (2001)
84. J. S. Baba, B. D. Cameron, S. Theru and G. L. Cote, "Effect of temperature, pH, and corneal birefringence on polarimetric glucose monitoring in the eye," *Journal of Biomedical Optics* 7(3), 321-328 (2002)
85. World-Health-Organization, "Malaria Factsheet 2013," (2013)
86. A. Butykai, A. Orbán, V. Kocsis, D. Szaller, S. Bordács, E. Tátrai-Szekeres, L. F. Kiss, A. Bóta, B. G. Vértessy, T. Zelles and I. Kézsmárki, "Malaria pigment crystals as magnetic micro-rotors: key for high-sensitivity diagnosis," *Sci. Rep.* 3((2013)
87. B. K. Wilson, M. R. Behrend, M. P. Horning and M. C. Hegg, "Detection of malarial byproduct hemozoin utilizing its unique scattering properties," *Opt. Express* 19(13), 12190-12196 (2011)

88. Who, *Malaria light microscopy: Creating a culture of quality. Report of the WHO WPRO-SEARO bi-regional workshop on quality assurance for malaria microscopy* (2005)
89. D. N. Breslauer, R. N. Maamari, N. A. Switz, W. A. Lam and D. A. Fletcher, "Mobile phone based clinical microscopy for global health applications," *PloS one* 4(7), e6320 (2009)
90. C. Wongsrichanalai, M. J. Barcus, S. Muth, A. Sutamihardja and W. H. Wernsdorfer, "A review of malaria diagnostic tools: microscopy and rapid diagnostic test (RDT)," *The American journal of tropical medicine and hygiene* 77(6 Suppl), 119-127 (2007)
91. R. J. Maude, W. Buapetch and K. Silamut, "A Simplified, Low-Cost Method for Polarized Light Microscopy," *The American journal of tropical medicine and hygiene* 81(5), 782-783 (2009)
92. W. S. U. M. O. S. T. Y. O. L. S. Bishara and A. Ozcan, "Handheld and lensless microscope identifies malaria parasites," *SPIE newsroom* (2011)
93. S. Mavandadi, S. Dimitrov, S. Feng, F. Yu, U. Sikora, O. Yaglidere, S. Padmanabhan, K. Nielsen and A. Ozcan, "Distributed medical image analysis and diagnosis through crowd-sourced games: a malaria case study," *PloS one* 7(5), e37245 (2012)
94. S. Mavandadi, S. Feng, F. Yu, S. Dimitrov, K. Nielsen-Saines, W. R. Prescott and A. Ozcan, "A mathematical framework for combining decisions of

multiple experts toward accurate and remote diagnosis of malaria using tele-microscopy," *PloS one* 7(10), e46192 (2012)

95. S. Mavandadi, S. Feng, F. Yu, S. Dimitrov, R. Yu and A. Ozcan, "BioGames: A Platform for Crowd-Sourced Biomedical Image Analysis and Telediagnosis," *Games for health journal* 1(5), 373-376 (2012)
96. K. R. Steingart, M. Henry, S. Laal, P. C. Hopewell, A. Ramsay, D. Menzies, J. Cunningham, K. Weldingh and M. Pai, "Commercial Serological Antibody Detection Tests for the Diagnosis of Pulmonary Tuberculosis: A Systematic Review," *PLoS Med* 4(6), e202 (2007)
97. K. R. Steingart, M. Henry, V. Ng, P. C. Hopewell, A. Ramsay, J. Cunningham, R. Urbanczik, M. Perkins, M. A. Aziz and M. Pai, "Fluorescence versus conventional sputum smear microscopy for tuberculosis: a systematic review," *The Lancet Infectious Diseases* 6(9), 570-581
98. M. H. Steinberg and J. G. I. Adams, "Laboratory Detection of Hemoglobinopathies and Thalassemias," in *Hematology: Basic Principles and Practice* R. Hollman, E. Benz, S. Shattil, B. Furie, H. Cohen, L. Silberstein and P. McGlave, Eds., pp. 2481-2491, Churchill Livingstone, Philadelphia, Pennsylvania (2000).
99. S. A. Boppart and R. Richards-Kortum, "Point-of-care and point-of-procedure optical imaging technologies for primary care and global health," *Science translational medicine* 6(253), 253rv252 (2014)

100. J. D. Maguire, E. R. Lederman, M. J. Barcus, W. A. O'Meara, R. G. Jordon, S. Duong, S. Muth, P. Sismadi, M. J. Bangs, W. R. Prescott, J. K. Baird and C. Wongsrichanalai, "Production and validation of durable, high quality standardized malaria microscopy slides for teaching, testing and quality assurance during an era of declining diagnostic proficiency," *Malar J* 5(92) (2006)
101. F. Who Tdr, *Methods Manual for Laboratory Quality Control Testing of Malaria Rapid Diagnostic Tests, Version Six* (2010)
102. D. Bell and R. W. Peeling, "Evaluation of rapid diagnostic tests: malaria," *Nat Rev Micro*
103. T. Endeshaw, T. Gebre, J. Ngondi, P. M. Graves, E. B. Shargie, Y. Ejigsemahu, B. Ayele, G. Yohannes, T. Teferi, A. Messele, M. Zerihun, A. Genet, A. W. Mosher, P. M. Emerson and F. O. Richards, "Evaluation of light microscopy and rapid diagnostic test for the detection of malaria under operational field conditions: a household survey in Ethiopia," *Malar J* 7(118) (2008)
104. P. T. Vo, "Novel Optical Detection of Synthesized Hemozoin Crystals for Malaria Diagnosis.pdf," York Suburban Senior High School, <http://web.mit.edu/vophong/www/Novel%20Optical%20Detection%20of%20Synthesized%20Hemozoin%20Crystals%20for%20Malaria%20Diagnosis.pdf> (2012).
105. W. H. Organization, "Malaria Rapid Diagnostic Test Performance," (Geneva, 2009)

106. W. H. Organization, "The role of laboratory diagnosis to support malaria disease management: Focus on the use of rapid diagnostic tests in the areas of high transmission," (2004)
107. D. M. Newman, J. Heptinstall, R. J. Matelon, L. Savage, M. L. Wears, J. Beddow, M. Cox, H. D. F. H. Schallig and P. F. Mens, "A Magneto-Optic Route toward the In Vivo Diagnosis of Malaria: Preliminary Results and Preclinical Trial Data," *Biophysical Journal* 95(2), 994-1000 (2008)
108. T. Leslie, A. Mikhail, I. Mayan, M. Anwar, S. Bakhtash, M. Nader, C. Chandler, C. J. M. Whitty and M. Rowland, "Overdiagnosis and mistreatment of malaria among febrile patients at primary healthcare level in Afghanistan: observational study," *BMJ* 345((2012)
109. S. Ashraf, A. Kao, C. Hugo, E. Christophel, B. Fatunmbi, J. Luchavez, K. Lilley and D. Bell, "Developing standards for malaria microscopy: external competency assessment for malaria microscopists in the Asia-Pacific," *Malaria Journal* 11(1), 352 (2012)
110. D. R. Rahardjo, N. Siti and Tur, "Haemozoin Detection in Mouse Liver Histology Using Simple Polarized Light Microscope," *Hayati Journal of Biosciences* 21(48-52 (2014)
111. C. Lawrence and J. A. Olson, "Birefringent hemozoin identifies malaria," *American journal of clinical pathology* 86(360-363 (1986)
112. C. Romagosa, C. Menendez, M. R. Ismail, L. Quinto, B. Ferrer, P. L. Alonso and J. Ordi, "Polarisation microscopy increases the sensitivity of hemozoin

and Plasmodium detection in the histological assessment of placental malaria," *Acta Trop* 90(3), 277-284 (2004)

- 113.B. V. Mendelow, C. Lyons, P. Nhlangothi, M. Tana, M. Munster, E. Wypkema, L. Liebowitz, L. Marshall, S. Scott and T. L. Coetzer, "Automated malaria detection by depolarization of laser light," *British Journal of Haematology* 104(3), 499-503 (1999)
- 114.A. K. Dharmadhikari, H. Basu, J. A. Dharmadhikari, S. Sharma and D. Mathur, "On the birefringence of healthy and malaria-infected red blood cells," *Journal of Biomedical Optics* 18(12), 125001-125001 (2013)
- 115.D. Payne, "Use and limitations of light microscopy for diagnosing malaria at the primary health care level," *Bulletin of the World Health Organization* 66(5), 621-626 (1988)
- 116.A. H. Kilian, W. G. Metzger, E. J. Mutschelknauss, G. Kabagambe, P. Langi, R. Korte and F. von Sonnenburg, "Reliability of malaria microscopy in epidemiological studies: results of quality control," *Trop Med Int Health* 5(3-8) (2000)
- 117.D. B. Klarkowski and J. D. Orozco, "Microscopy quality control in Medecins Sans Frontieres programs in resource-limited settings," *PLoS Med* 7(e1000206) (2010)
- 118.W. P. O'Meara, F. E. McKenzie, A. J. Magill, J. R. Forney, B. Permpnich, C. Lucas, R. A. Gasser and C. Wongsrichanalai, "Sources of variability in

determining malaria parasite density by microscopy," *AmJTrop Med Hyg* 73(593-598 (2005)

119.H. Zhu, S. Mavandadi, A. F. Coskun, O. Yaglidere and A. Ozcan, "Optofluidic fluorescent imaging cytometry on a cell phone," *Anal Chem* 83(17), 6641-6647 (2011)

120."International Telecommunication Union, Market Information and Statistics," (2011).

121.J. Sambira, "Texting your way to health: UN launches 'mHealth' initiative to fight diseases," in *Africa Renewal* (2013).

122.P. J., "Number of mobile phones to exceed world population by 2014," *Digital Trends* (2013).

123.A. Fitzpatrick, "75% of World Has Access to Mobile Phones [STUDY]," in *Mashable*, Mashable, Internet (2012).

124.H. Zhu, O. Yaglidere, T. W. Su, D. Tseng and A. Ozcan, "Cost-effective and compact wide-field fluorescent imaging on a cell-phone," *Lab Chip* 11(2), 315-322 (2011)

125.S. C. Hur, H. T. K. Tse and D. Di Carlo, "Sheathless inertial cell ordering for extreme throughput flow cytometry," *Lab on a Chip* 10(3), 274-280 (2010)

- 126.S. Seo, T. W. Su, D. K. Tseng, A. Erlinger and A. Ozcan, "Lensfree holographic imaging for on-chip cytometry and diagnostics," *Lab Chip* 9(6), 777-787 (2009)
- 127.Z. J. Smith, K. Chu, A. R. Espenson, M. Rahimzadeh, A. Gryshuk, M. Molinaro, D. M. Dwyre, S. Lane, D. Matthews and S. Wachsmann-Hogiu, "Cell-Phone-Based Platform for Biomedical Device Development and Education Applications," *PloS one* 6(3), e17150 (2011)
- 128.D. Tseng, O. Mudanyali, C. Oztoprak, S. O. Isikman, I. Sencan, O. Yaglidere and A. Ozcan, "Lensfree microscopy on a cellphone," *Lab Chip* 10(14), 1787-1792 (2010)
- 129.H. Zhu, O. Yaglidere, T. W. Su, D. Tseng and A. Ozcan, "Wide-field fluorescent microscopy on a cell-phone," *Conference proceedings : ... Annual International Conference of the IEEE Engineering in Medicine and Biology Society. IEEE Engineering in Medicine and Biology Society. Conference 2011*(6801-6804 (2011)
- 130.A. Arpa, G. Wetzstein, D. Lanman and R. Raskar, "Single lens off-chip cellphone microscopy," in *Computer Vision and Pattern Recognition Workshops (CVPRW), 2012 IEEE Computer Society Conference on*, pp. 23-28 (2012).
- 131.A. F. Coskun, I. Sencan, T. W. Su and A. Ozcan, "Lensless wide-field fluorescent imaging on a chip using compressive decoding of sparse objects," *Opt Express* 18(10), 10510-10523 (2010)

- 132.A. F. Coskun, T. W. Su, I. Sencan and A. Ozcan, "Lensless fluorescent microscopy on a chip," *Journal of visualized experiments : JoVE* 54), (2011)
- 133.S. O. Isikman, W. Bishara and A. Ozcan, "Lensfree on-chip tomographic microscopy employing multi-angle illumination and pixel super-resolution," *Journal of visualized experiments : JoVE* 66), e4161 (2012)
- 134.S. O. Isikman, W. Bishara, U. Sikora, O. Yaglidere, J. Yeah and A. Ozcan, "Field-portable lensfree tomographic microscope," *Lab Chip* 11(13), 2222-2230 (2011)
- 135.S. O. Isikman, A. Greenbaum, M. Lee, W. Bishara, O. Mudanyali, T. W. Su and A. Ozcan, "Lensfree Computational Microscopy Tools for Cell and Tissue Imaging at the Point-of-Care and in Low-Resource Settings," *Studies in health technology and informatics* 185(299-323 (2013)
- 136.M. Lee, O. Yaglidere and A. Ozcan, "Field-portable reflection and transmission microscopy based on lensless holography," *Biomed Opt Express* 2(9), 2721-2730 (2011)
- 137.H. Zhu and A. Ozcan, "Wide-field fluorescent microscopy and fluorescent imaging flow cytometry on a cell-phone," *Journal of visualized experiments : JoVE* 74), (2013)
- 138.Q. Wei, H. Qi, W. Luo, D. Tseng, S. J. Ki, Z. Wan, Z. Gorocs, L. A. Bentolila, T. T. Wu, R. Sun and A. Ozcan, "Fluorescent Imaging of Single Nanoparticles and Viruses on a Smart Phone," *ACS nano* (2013)

- 139.A. F. Coskun, I. Sencan, T. W. Su and A. Ozcan, "Lensfree fluorescent on-chip imaging of transgenic *Caenorhabditis elegans* over an ultra-wide field-of-view," *PloS one* 6(1), e15955 (2011)
- 140.A. F. Coskun, T. W. Su and A. Ozcan, "Wide field-of-view lens-free fluorescent imaging on a chip," *Lab Chip* 10(7), 824-827 (2010)
- 141.A. F. Coskun, T. W. Su, I. Sencan and A. Ozcan, "Lensfree Fluorescent On-Chip Imaging using Compressive Sampling," *Optics and photonics news* 21(12), 27 (2010)
- 142.S. A. Arpali, C. Arpali, A. F. Coskun, H. H. Chiang and A. Ozcan, "High-throughput screening of large volumes of whole blood using structured illumination and fluorescent on-chip imaging," *Lab Chip* 12(23), 4968-4971 (2012)
- 143.V. Oncescu, M. Mancuso and D. Erickson, "Cholesterol testing on a smartphone," *Lab on a Chip* 14(4), 759-763 (2014)
- 144.B. E. R. Newlands, *Sugar*, Spon & Chamberlain, New York (1909).
- 145.C. A. Browne and F. W. Zerban, *Physical and Chemical Methods for Sugar Analysis*, John Wiley & Sons, New York (1941).
- 146.G. L. Spencer, *A Handbook for Cane-Sugar Manufacturers*, John Wiley & Sons, New York (1917).

147. J. McMurry, *Organic Chemistry*, Brooks/Cole Publishing Company, Pacific Grove, CA (1992).
148. G. L. Cote, M. D. Fox and R. B. Northrop, "Noninvasive optical polarimetric glucose sensing using a true phase measurement technique," *IEEE Transactions on Biomedical Engineering* 39(7), 752-756 (1992)
149. Goetz M.J, Jr., "Microdegree Polarimetry for Glucose Detection," University of Connecticut, Storrs, CT 06269 (1992).
150. T. W. King, G. L. Cote, R. McNichols and M. J. Goetz Jr, "Multispectral polarimetric glucose detection using a single Pockels cell," *Optical Engineering* 33(8), 2746-2753 (1994)
151. B. D. Cameron and G. L. Cote, "Noninvasive glucose sensing utilizing a digital closed-loop polarimetric approach," *IEEE Transactions on Biomedical Engineering* 44(12), 1221-1227 (1997)
152. G. L. Cote, H. Gorde, J. Janda and B. D. Cameron, "Multispectral polarimetric system for glucose monitoring," in *Biomedical Sensing and Imaging Technologies*, pp. 36-40, SPIE, San Jose, CA, USA (1998).
153. B. D. Cameron and H. Anumula, "Development of a real-time corneal birefringence compensated glucose sensing polarimeter," *Diabetes Technology and Therapeutics* 8(2), 156-164 (2006)

154. B. D. Cameron, H. W. Gorde, B. Satheesan and G. L. Cote, "The Use of Polarized Laser Light Through the Eye for Noninvasive Glucose Monitoring," *Diabetes Technology & Therapeutics* 1(2), 135-143 (1999)
155. F. C. a. P. Salvadori, Ed., *Fundamental Aspects and Recent Developments in Optical Rotatory Dispersion and Circular Dichroism*, Heyden and Son Ltd, London (1973).
156. B. H. Malik and G. L. Coté, "Modeling the corneal birefringence of the eye toward the development of a polarimetric glucose sensor," *Journal of Biomedical Optics* 15(3), 037012 (2010)
157. D. H. Goldstein, *Polarized Light, Third Edition*, CRC Press (2010).
158. E. Hecht, *Optics, 4th Edition*, Addison-Wesley (2001).
159. D. J. Donohue, B. J. Stoyanov, R. L. McCally and R. A. Farrell, "Numerical modeling of the cornea's lamellar structure and birefringence properties," *J. Opt. Soc. Am. A* 12(7), 1425-1438 (1995)
160. M. Born and E. Wolf, *Principles of Optics*, Cambridge University Press, 1998 (1998).
161. R. A. Farrell, D. Rouseff and R. L. McCally, "Propagation of polarized light through two- and three-layer anisotropic stacks," *Journal of the Optical Society of America A: Optics and Image Science, and Vision* 22(9), 1981-1992 (2005)

- 162.J. H. Krachmer, M. J. Mannis and E. J. Holland, *Cornea*, Elsevier Mosby (2011).
- 163.D. J. Donohue, B. J. Stoyanov, R. L. McCally and R. A. Farrell, "Numerical modeling of the cornea's lamellar structure and birefringence properties," *Journal of Optical Society of America A* 1425-1438 (1995)
- 164.M. Born and E. Wolf, *Principles of Optics*, Cambridge University Press (1998).
- 165.R. R. Analytical, "Polarimetry Definitions," *Polarimetry Fundamentals*.
- 166.B. D. Cameron and H. Anumula, "Development of a real-time corneal birefringence compensated glucose sensing polarimeter," *Diabetes technology & therapeutics* 8(2), 156-164 (2006)
- 167.R. Rawer, W. Stork and K. D. Muller-Glaser, "Polarimetric methods for measurement of intra ocular glucose concentration," *Biomedizinische Technik. Biomedical engineering* 47 Suppl 1 Pt 1(186-188 (2002)
- 168.R. Rawer, W. Stork and C. F. Kreiner, "Non-invasive polarimetric measurement of glucose concentration in the anterior chamber of the eye," *Graefe's archive for clinical and experimental ophthalmology = Albrecht von Graefes Archiv fur klinische und experimentelle Ophthalmologie* 242(12), 1017-1023 (2004)
- 169.R. R. Ansari, S. Bockle and L. Rovati, "New optical scheme for a polarimetric-based glucose sensor," *J Biomed Opt* 9(1), 103-115 (2004)

170. T. D. Wolfenden, P. E. G. Baird, J. A. Deeny and M. Irie, "Use of a Faraday modulator in a laser polarimeter for optical forward-wave level-crossing experiments in atomic vapours," *Measurement Science and Technology* 1(10), 1060 (1990)
171. Y.-L. Lo and T.-C. Yu, "A polarimetric glucose sensor using a liquid-crystal polarization modulator driven by a sinusoidal signal," *Optics Communications* 259(1), 40-48 (2006)
172. C. W. Pirnstill, B. H. Malik, E. Thomas and G. L. Coté, "Design and characterization of a ferromagnetic, air gapped magneto-optic Faraday rotator," *Opt. Lett.* 38(8), 1298-1300 (2013)
173. M. M. P. Association, *Soft Ferrites: A User's Guide*, Magnetic Materials Producers Association (1997).
174. Magnetics, "Section 4. Power Design," in *Ferrite Cores*, Magnetics, Butler, PA (2000).
175. S. J. Chapman, *Electric Machinery Fundamentals*, McGraw-Hill Science/Engineering/Math, Boston (2004).
176. R. Knighton, "Spectral Dependence of Corneal Birefringence at Visible Wavelengths," *Invest. Ophthalmol. Vis. Sci.* 43(12), 152- (2002)
177. K. Irsch, B. Gramatikov, Y. K. Wu and D. Guyton, "Modeling and minimizing interference from corneal birefringence in retinal birefringence

scanning for foveal fixation detection," *Biomed Opt Express* 2(7), 1955-1968 (2011)

178.H. J. Reyher, B. Faust, B. Sugg, R. Rupp and L. Ackermann, "Optically detected magnetic resonance via the magnetic circular dichroism of absorption of cerium impurities in bulk paramagnetic terbium gallium garnet," *Journal of Physics: Condensed Matter* 9(42), 9065 (1997)

179.R. W. Knighton, X.-R. Huang and L. A. Cavuoto, "Corneal birefringence mapped by scanning laserpolarimetry," *Opt. Express* 16(18), 13738-13751 (2008)

180.K. Irsch, B. Gramatikov, Y.-K. Wu and D. Guyton, "Modeling and minimizing interference from corneal birefringence in retinal birefringence scanning for foveal fixation detection," *Biomed. Opt. Express* 2(7), 1955-1968

181.I. National Magnetics Group, "M25 Ferrite Material," I. National Magnetics Group, Ed., National Magnetics Group, INC., Bethlehem, PA (2010).

182.J. Arnbjerg and T. Eriksen, "Increased glucose content in the aqueous humour caused by the use of xylazine," *Ophthalmic research* 22(4), 265-268 (1990)

183.K. Chalabi, M. Schutte and M. Reim, "Alterations of glucose levels in the blood and the anterior eye segment of rabbits exposed to ketamine-xylazine anaesthesia," *Ophthalmic research* 19(5), 289-291 (1987)

184.M. Montagnana, M. Caputo, D. Giavarina and G. Lippi, "Overview on self-monitoring of blood glucose," *Clinica Chimica Acta* 402(1-2), 7-13 (2009)

- 185.D. D. Cunningham and J. A. Stenken, *In vivo glucose sensing*, Wiley, Hoboken, N.J.
- 186.N. Grumman, "Terbium Gallium Garnet-TGG," Synoptics, Charlotte, NC (2013).
- 187.J. H. Krachmer, M. J. Mannis and E. J. Holland, Eds., *FUNDAMENTALS, DIAGNOSIS, AND MANAGEMENT*, MOSBY ELSEVIER (2011).
- 188.J. S. Baba, B. D. Cameron, S. Theru and G. L. Coté, "Effect of temperature, pH, and corneal birefringence on polarimetric glucose monitoring in the eye," *Journal of Biomedical Optics* 7(3), 321 (2002)
- 189.B. H. Malik and G. L. Coté, "Characterizing dual wavelength polarimetry through the eye for monitoring glucose," *Biomed. Opt. Express* 1(5), 1247-1258 (2010)
- 190.A. M. Winkler, G. T. Bonnema and J. K. Barton, "Optical polarimetry for noninvasive glucose sensing enabled by Sagnac interferometry," *Applied optics* 50(17), 2719-2731 (2011)
- 191.H.-L. Liou and N. A. Brennan, "Anatomically accurate, finite model eye for optical modeling," *Journal of the Optical Society of America A* 14(8), 1684-1695 (1997)
- 192.D. MAURICE, "The Charles Prentice Award Lecture 1989: The Physiology of Tears," *Optometry & Vision Science* 67(6), 391-399 (1990)

- 193.E. Sokolova, B. Kruizinga and I. Golubenko, "Recording of concave diffraction gratings in a two-step process using spatially incoherent light," *Optical Engineering* 43(11), 2613-2622 (2004)
- 194.H. F. Edelhauser, "The balance between corneal transparency and edema: the Proctor Lecture," *Investigative ophthalmology & visual science* 47(5), 1754-1767 (2006)
- 195.G. J. Van Blokland and S. C. Verhelst, "Corneal polarization in the living human eye explained with a biaxial model," *J. Opt. Soc. Am. A* 4(1), 82-90 (1987)
- 196.R. A. Farrell, D. Rouseff and R. L. McCally, "Propagation of polarized light through two- and three-layer anisotropic stacks," *Journal of the Optical Society of America. A, Optics, image science, and vision* 22(9), 1981-1992 (2005)
- 197.R. W. Knighton and X. R. Huang, "Linear birefringence of the central human cornea," *Investigative ophthalmology & visual science* 43(1), 82-86 (2002)
- 198.W. A. Christens-Barry, W. J. Green, P. J. Connolly, R. A. Farrell and R. L. McCally, "Spatial mapping of polarized light transmission in the central rabbit cornea," *Experimental eye research* 62(6), 651-662 (1996)
- 199.R. H. Andreo and R. A. Farrell, "Corneal small-angle light-scattering theory: wavy fibril models," *Journal of the Optical Society of America* 72(11), 1479-1492 (1982)

- 200.E. P. Chang, D. A. Keedy and J. C. Chien, "Ultrastructures of rabbit corneal stroma: mapping of optical and morphological anisotropies," *Biochim Biophys Acta* 343(3), 615-626 (1974)
- 201.P. M. Kiely, G. Smith and L. G. Carney, "Meridional variations of corneal shape," *American journal of optometry and physiological optics* 61(10), 619-626 (1984)
- 202.B. Kovatchev, S. Anderson, L. Heinemann and W. Clarke, "Comparison of the numerical and clinical accuracy of four continuous glucose monitors," *Diabetes Care* 31(6), 1160-1164 (2008)
- 203.N. Van Hung, D. N. Sy, R. M. Anthony, F. G. J. Cobelens and D. van Soolingen, "Fluorescence microscopy for tuberculosis diagnosis," *The Lancet Infectious Diseases* 7(4), 238-239
- 204.D. Jones, J. Nyalwidhe, L. Tetley and M. P. Barrett, "McArthur revisited: fluorescence microscopes for field diagnostics," in *Trends Parasitol*, pp. 468-469, England (2007).
- 205.Z. Gorocs and A. Ozcan, "On-chip biomedical imaging," *IEEE reviews in biomedical engineering* 6(29-46) (2013)
- 206.H. Zhu, I. Sencan, J. Wong, S. Dimitrov, D. Tseng, K. Nagashima and A. Ozcan, "Cost-effective and rapid blood analysis on a cell-phone," *Lab Chip* 13(7), 1282-1288 (2013)

APPENDIX A

ANIMAL STUDY PROTOCOL

TEXAS A&M UNIVERSITY

DIVISION OF RESEARCH AND GRADUATE STUDIES—OFFICE OF RESEARCH COMPLIANCE
1186 TAMU 979.458.1467
College Station, TX 77845-1186 FAX 979.862.3176
750 Agronomy Road <http://researchcompliance.tamu.edu>

Institutional Animal Care and Use Committee

Institutional Review Board

April 2, 2010

MEMORANDUM

TO: Dr. Gerard L. Cote
Industrial Engineering
MS 3120

FROM: Institutional Animal Care and Use Committee SACC

SUBJECT: Approval of AUP 2010-5
"Glucose monitoring using polarized light"
Funding Source: NIH
AUP Approval Date: 4/2/2010
AUP Expiration Date: 4/1/2013

This AUP has been approved by the IACUC for a period of 3 years. It is the responsibility of the principal investigator to assure all animal work is conducted in accordance with this AUP.

To allow for Committee review and approval of continuing work on this project, **Annual Reviews are due on the 1st day of the month preceding the month of anniversary.** If an Annual Review is not received, or not approved, your AUP will be deactivated on the anniversary date, no animal work will be permitted and all animals must be transferred or otherwise disposed of.

If you have indicated that you will be performing post procedural monitoring of animals at specific intervals, please provide documentation of your observations in the medical record or by using "Animal Observation" cards that are available through the Comparative Medicine Program.

A copy of this approval will be sent to the housing facility. **You must consult with the housing facility manager prior to ordering animals to ensure that space is available.**

Pc: Routing Agency: TEES
Housing Facility: LARR Main
Attending Veterinarian
IACUC

Funding Source: NIH
Routing Agency: TEES

Protocol Number: 2010-005 (Assigned by IACUC)
Version 10/05

TEXAS A&M UNIVERSITY
Research/Teaching Proposals Involving Animal Subjects

Research investigators and class instructors are entrusted with an essential role in assuring the humane care and use of animals. In activities you conduct or that are conducted under your supervision, you have a direct and continuing responsibility to ensure that animals are adequately cared for and used in a humane fashion. Investigators and instructors must ensure that discomfort, pain or injury to the animals is avoided or minimized, consistent with sound experimental/teaching design; that no more animals are used than are necessary to reach sound scientific conclusions or to teach the class; and that, when appropriate, animals are painlessly sacrificed in accordance with methods of euthanasia approved by the Panel on Euthanasia of the American Veterinary Medical Association. Forms and requirements for approval by the Institutional Biosafety Committee (IBC) can be accessed through the IACUC web page (<http://animal.tamu.edu>).

Please check below if your research/teaching protocol involves any of the following:

- Decapitation or cervical dislocation without anesthesia [Provide rationale in Section II.E]
- Death (without appropriate euthanasia) as an experimental endpoint [Complete Section III.D.4]
- More than momentary pain and distress not relieved by anesthesia and/or analgesics
- Surgery [Complete Attachment 1: Surgical Procedures]
- Multiple major survival surgery [Provide rationale in Attachment 1]
- Use of adjuvants or antibody production [Complete Attachment 2: Antibody Production]
- Use of hazardous chemicals (including chemical carcinogens) or radioactive materials [Complete Attachment 3 for each]
- Use of recombinant DNA or genetically altered materials [Provide IBC Approval]
- Use of agents infectious for personnel [Provide IBC Approval]
- Use of a select agent or biological toxin [See Appendix 2 of IBC permit form for list]
- Use of non-commercial genetically modified animals [Provide IBC Approval]
- Captured wild animals or field studies [Complete Attachment 4: Field Studies]

Complete the Information Below:

Investigator/Instructor Name: Gerard L. Coté Department: Biomedical Engineering Mail Stop: 3120

Project/Class Title: Glucose monitoring using polarized light

Is this AUP intended for continued work on a funded grant? (i.e. AUP was approved before grant?)

- No
 Yes (Previous AUP # 2007-32)

Is this AUP intended to replace another approved AUP?

- No (Effectively replaces AUP #2001-254 which expired due to lack of funding)
 Yes (Replace AUP # 2007-32)



FOR COMMITTEE ACTION ONLY

Animal usage (pertains to project design, not to species):

- Experiments involving food or fiber research or production (IAACUC)
- Experiments of a biomedical nature (IACUC)
- Client-Owned Animals (CVM CRRC)
- Experiment Station (PHS or USDA Regulated Species, IACUC)

TEN DAY REVIEW
JAN 06 2010

Pain Stress Category Assigned: I II III IV
USDA Category Assigned: N/A C D E

Returned for modification
 Approved by IACUC Date: 3/10/10 Signature: Duane C. Kraemer

INVESTIGATOR'S/INSTRUCTOR'S ASSURANCE

Texas A&M University (TAMU) recognizes the importance of the use of animals in its research, teaching, and testing programs, and is committed to maintaining high standards for the care and use of animals in research, teaching, and testing. TAMU has adopted the "U.S. Government's Principles for the Utilization and Care of Vertebrate Animals Used in Testing, Research and Training" and complies with all applicable portions of the Animal Welfare Act, the Public Health Service Policy for the Humane Care and Use of Laboratory Animals, and all other federal, state, and local laws which impact the care and use of animals. TAMU investigators, teachers, staff, and students accept responsibility for determining that research, teaching, and testing involving the use of animals fulfills these principles, policies, and regulations. To assure compliance:

•APPROVAL OF AUPS Approval of an Animal Use Protocol (AUP), by the appropriate Institutional Animal Care and Use Committee, is required for all vertebrate animal use. All vertebrate animals must be covered by an active AUP, even after termination of a project.

•DURATION OF APPROVAL AUPs are approved for a three-year period and require two annual reviews. The first annual and second annual reviews are due on the anniversary of the date the IACUC approved the protocol. A new AUP approval is required for continuation beyond the three-year period.

•AMENDMENTS TO AUPS Any proposed change in personnel, species usage, animal procedures, anesthesia, post-operative care, or biohazard procedures to the animal portion of a study must be reported in writing to the IACUC for approval. Committee approval of the proposed amendment is required prior to proceeding with the revised animal procedures.

•INFECTIOUS BIOHAZARDS, RECOMBINANT DNA All animal research projects involving infectious biohazards and recombinant DNA, including procedures such as introduction of recombinant organisms into animals and generation of transgenic or knockout animals, must be registered and approved by the TAMU Institutional Biosafety Committee (IBC).

•TRAINING OF PERSONNEL All personnel working with animals, from the animal care staff to the persons doing the experiments/teaching must be qualified by training and/or experience to do so. Such training and/or experience should be documented in the AUP. All personnel working with animals must be informed of the TAMU Occupational Health and Safety Program for Animal Care and Use Facilities, and have the opportunity to participate fully in the program.

•PROGRAM EVALUATIONS All approved animal housing locations will be inspected twice annually. Unannounced inspections and observations of animal quarters and/or experimental or teaching procedures may be performed by the attending veterinary staff. Where procedures are causing severe distress to an animal and the pain cannot be relieved, veterinarians are authorized to humanely destroy that animal. Institutional Veterinarians will make a concerted effort to discuss these situations with investigators/instructors prior to initiating such action. The Committee is authorized to suspend research/teaching which does not conform to approved procedures outlined in the AUP.

Signature certifies that the Principal Investigator/Instructor:

1. Understands the requirements of the Public Health Service Policy for the Humane Care and Use of Laboratory Animals, applicable portions of the Animal Welfare Regulations (Animal Welfare Act), and the Institution's policies governing the use of vertebrate animals for research, testing, teaching, or demonstration purposes.
2. Will conduct the project/course in full compliance with the aforementioned requirements.
3. Will assure that personnel are appropriately trained and will conduct all procedures as described in this AUP.
4. Assures that this AUP accurately reflects the research/teaching described in any accompanying grant proposal.
5. Assures that the proposed work does not unnecessarily duplicate previous experiments.
6. Understands that work with animals is limited specifically to what is approved in this document.

Gerard L. Coté
Typed Name of Investigator/Instructor

Gerard L. Coté
Signature of Principal Investigator/Instructor

01/04/2010
Date

Typed Name of Graduate Student (If applicable)

Signature of Graduate Student



INVESTIGATORS MAY DESIGNATE UP TO BUT NO MORE THAN TWO PERSONS TO ACT ON THEIR BEHALF TO REVISE AND AMEND PROTOCOLS AND SUBMIT TRANSFERS AND ANNUAL REVIEWS. THE INVESTIGATOR REMAINS SOLELY RESPONSIBLE FOR THE CONTENT OF THE AUP AND THE CONDUCT OF THE ANIMAL WORK.

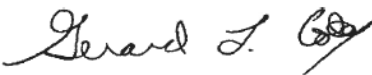
Designee name(s):

Certification of ALL Participants in Research/Teaching Procedures
(Anyone whose name appears in the AUP)

Signature certifies that the participant:

1. Understands the requirements of the Public Health Service Policy for the Humane Care and Use of Laboratory Animals, applicable portions of the Animal Welfare Regulations (Animal Welfare Act), and the Institution's policies governing the use of vertebrate animals for research, testing, teaching and for demonstration purposes.
2. Will conduct the project/class in full compliance with the aforementioned requirements.
3. Understands his/her role in the AUP, agrees to perform it and assures that he/she has the appropriate skills to do so.
4. Further understands that work with animals is limited specifically to what is approved in this document.

Typed Name of Participant	Signature	Date
---------------------------	-----------	------

Gerard L. Coté		01/04/2010
_____	_____	_____
_____	_____	_____
_____	_____	_____
_____	_____	_____

Please add as many lines as necessary.



ANIMAL USE PROTOCOL (AUP)
(For Institutional Review Only)

Instructions to Investigators: All questions must be answered even if not applicable (N/A). **This form must be type written.** PLEASE USE AS MUCH SPACE AS NECESSARY TO COMPLETELY ANSWER EACH QUESTION.

SECTION I. PROJECT/CLASS IDENTIFICATION

A. Investigator/Instructor Name: Gerard L. Coté Dept: BMEN Mail Stop: 3120

Work Phone: 979-845-4196

Emergency Phone: 979-574-6053

E-mail: gcote@tamu.edu

B. Title of Project/Class: Glucose monitoring using polarized light

Funding Source: NIH-RO1
(e.g., NIH, USDA, AHA, Teaching, Internal)

Campus Routing Office: TEES
(e.g., RF, TAES, TEES, none)

C. Project Animal-Care Contact Person *[Who is to be contacted in case of an animal emergency]:*

Gerard L. Coté

Work Phone: 979-845-4196

Emergency Phone: 979-574-6053

E-mail: gcote@tamu.edu

D. Abstract: Please provide a brief statement, in LAY TERMINOLOGY, understandable by someone with a high school education, with no acronyms or scientific jargon, outlining the purpose of the experimental/teaching procedures of this protocol. *[Why you are doing this experiment/class and what you propose to learn/teach.]*

A noninvasive glucose or sugar sensor using the eye as a sensing site is being developed for in-home use by diabetics. Specifically, the sensor measures glucose levels by measuring how glucose changes polarized light as it is passed through the aqueous humor or front part of the eye. One of the obstacles that this approach faces is that the eye itself, and in particular the cornea, also changes polarized light. Therefore, one of the stages for this sensor's development involves studying the manner in which polarized light is affected (via birefringence) by the cornea. A second area of interest is how the polarized light is changed as it is reflected off the lens of the eye. A third area of interest is how the glucose levels in the eye (specifically the aqueous humor) correspond to blood glucose levels.

E. Animal Procedures: These protocols are available to, and may be read by, the lay public. Describe in narrative form, using LAY TERMINOLOGY, understandable by someone with a high school education, no acronyms or scientific jargon, the experimental procedures and manipulation or teaching protocol that will be performed on the animals (not scientific rationale). *[Be brief and specific in describing the animal procedures. However, it is not necessary to go into detail (in this section) regarding surgical procedures—that information should be addressed on the Surgical Procedures Attachment I.]*

Two sets of rabbits will be used in these experiments, normal and those made diabetic. The rabbits that are made diabetic are first anesthetized using a solution of drugs (xylazine and ketamine) and then diabetes is induced by injecting alloxan monohydrate dissolved in saline into an ear vein. Glucose concentration will be measured in these rabbits using a standard glucose measurement system and, to avoid death from ketoacidosis, it will be necessary to administer small daily subcutaneous doses of insulin to most of the diabetic rabbits. In both sets of animals, after the rabbit is anesthetized using a solution of drugs

REVISED
via email



(ketamine and xylazine), a low intensity polarized light beam will be passed across the front (aqueous humor) part of the eye and collected through some optics by an optical power meter. The light information will be correlated with blood sugar information that is obtained via periodic blood draws through an ear vein. The animals do not need to be euthanized after the measurements and could be transferred to another study.

- F. Justify why you chose to use this (these) species in your research/class. *[Describe characteristics of the animal model that make it appropriate for use in your studies/teaching*. Body size, comparative data from prior studies or unique physiological features may be considered in justification of species. Cost alone is not an acceptable justification for selection of the animal model.]*

* If this is a teaching protocol please justify the use of live animals to achieve your teaching objectives.

The selection of species was primarily based on the comparable size of NZW rabbit eyes to that of human eyes as well as the comparable use of this species in the literature for both diabetes induction and glucose measurement.

G. Experimental Design/Teaching Protocol

1. Describe the number of animals per experiment/class, including a breakdown within experiments/lessons of animals per treatment condition *[Including number of replications and relevant controls.]* If the project involves breeding animals, indicate how many breeder stock will be required and how many offspring will be used for the studies. If the project utilizes a colony or herd which will be maintained for the purpose of supplying animals to other approved protocols, please contact the Chair of the IACUC for information on procedures for documenting colony numbers.

A CHART OR TABLE PROVIDING EXPERIMENTAL TREATMENT/TEACHING LABORATORY AND NUMBER OF ANIMALS PER TREATMENT/TEACHING LABORATORY WILL HELP EXPEDITE REVIEW.

The animal subject experimentation will involve two sets of experiments and a total of 30 NZW rabbits. The first short-term experiment will require the use of 10 NZW rabbits while second animal experiment will be a longer term experiment which will be performed on twenty rabbits (10 normal and 10 diabetic).

The short-term experiment will be used to determine the relationships between the delivery/collection system and the polarization effect *in vivo*. This will be used to verify the geometry of coupling across the rabbit eye and the ability to accommodate for eye motion artifact. Each rabbit will be tested no more than three times in a period of three weeks. After a 12 hour fasting period the rabbit will be anesthetized, the eye coupling device placed on the cornea, and three 10 minute runs of the laser polarization measurement determination of glucose done. The blood glucose level will be taken three times during each 10 minute run to insure it does not vary significantly. The results will be analyzed to assess baseline drifts in the instrument and the algorithms modified if required to accommodate such shifts to allow for meeting the milestone of less than 15% error in baseline glucose levels.

The second animal experiment will be a longer term experiment which will be performed on twenty rabbits (10 normal and 10 diabetic) in order to measure the *in vivo* equilibration time delay between blood and aqueous humor glucose levels. In addition, the repeatability, accuracy, and specificity of the noninvasive optical polarization technique to changes in blood glucose will be evaluated. The stability of the relationship across days will need to be assessed which will effect the necessity for continued calibration. The twenty rabbits will be randomly separated into two groups. One group will be made diabetic with alloxan injection while the other group will remain healthy. Under anesthesia, the rabbits will be given a bolus injection of glucose intravenously to obtain the nonlinear transfer function between aqueous humor and blood glucose. Blood samples and noninvasive optical polarization readings will be taken at 2-minute intervals for the first 10 minutes and 5-minute intervals thereafter up to 45 minutes. Each rabbit will be tested in this manner, at least three times, on three separate days over no more than three weeks. We will use the repetitions to study within and between animal variability and the

need for individual calibration. The lag time is defined as the difference between the time when the blood glucose reaches a maximum and when the aqueous humor glucose level reaches a maximum. Once this has been determined, the two curves will be used to determine the calibration for each rabbit. The rabbits will be followed over a the three separate day period to assess the stability of the calibration model over a normal dietary regimen. For each rabbit, the choice of the left or the right eye will be randomized to reduce bias. These experiments will allow us to study two areas of interest. First, we can verify the fasting aqueous glucose to blood glucose relationship results of previous papers and determine the constancy of that ratio under non-fasting situations. Second, we can use the results to study the variability of the polarization rotators, total protein and acids, under natural conditions.

2. Explain WHY you chose a certain number of animals per treatment/teaching laboratory condition. *[Taking into account known variation of the dependent variable, subject losses, etc. Statements such as "this number is required for statistical significance", without an indication of how you know this, are not adequate answers. Numbers of animals required to obtain enough tissue to adequately quantify parameters may be important, but PI must supply indicators of expected tissue content and assay parameters.]* The following URL is used for Statistical Calculations: Number of Animals Needed: <http://www.stat.uiowa.edu/~Rlenth/Power/index.html>.

Thirty rabbits will be used in this experiment. Originally, in consultation with Dr. Spiegelman within the Statistics department, 30 rabbits are needed based on power calculations using type I error set at 0.05 and type II error set at 0.10. The null hypothesis is that there is no correlation between rabbit blood glucose levels and the data provided by the optical system.

SECTION II. ANIMAL PROCUREMENT/MAINTENANCE INFORMATION

- A. List the total number of animals used, by species, for the duration of the project:

SPECIES	TOTAL NUMBER FOR DURATION OF AUP
Male NZW Rabbit	30

If the project involves breeding animals, please also complete the table below. These numbers, for the duration of the project, should be included in the overall Total above.

SPECIES	TOTAL NUMBER OF ADULT BREEDERS NEEDED	ESTIMATED TOTAL NUMBER OF OFFSPRING TO BE PRODUCED

- B. Where will you obtain the animals? *[If wild-caught by you, please describe applicable permits, method of capture and evaluation of health risks to personnel. Please provide a copy of permit approvals (Please contact the chairperson of IACUC if this presents a problem). Complete Field Studies Form, Attachment 4, for wild capture studies.]*

LARR

C. HOUSING (*It is the investigators responsibility to assure availability of housing with the facility.*)

1. Where will you house animals? LARR Bldg. #
 2. Is it IACUC approved?

Yes

No (*Please contact the IACUC office at 845-1828 to schedule a facility evaluation.*)

3. Describe any special housing, caging, diet, environment or other requirements necessary for this study/class (example: grid floors, special diets, food/water deprivation, identification of genetically modified animals).

For the first 24 hours after the rabbits are made diabetic via alloxan injection they will receive 10% glucose in drinking water. Nonfasting serum glucose concentration will be measured in unanesthetized rabbits 2-3 days after alloxan injection using a standard glucose measurement system and periodically thereafter, including weekly during the first 2-3 months. To avoid death from ketoacidosis it will be necessary to administer small daily subcutaneous doses of PZI insulin (1-2 U/day) to most of the diabetic rabbits. Insulin will begin 2-3 days after alloxan injection to eliminate serum ketones, as measured with Acetest tablets.

- D. Who will provide veterinary medical care for the animals? LARR Staff

- E. What will happen to the animals after you complete the experiment/class? [*If you plan to transfer the animals at the end of your study, please complete an Animal Transfer Form prior to such a transfer. This form is available on the IACUC website. If the animals are to be euthanized, please describe the agent and method employed. Decapitation or cervical dislocation without anesthesia requires written justification below.*]

Animal Transfer:

Internal to another AUP (requires IACUC approval)

External (outside agency, slaughter, adoption, etc.)

If adopting animals to private homes, please provide your laboratory procedures and guidelines. Transfer to a private destination requires prior approval. Assure appropriate drug withdrawal times if applicable.

Even when euthanasia is not an integral part of the AUP, please provide an adequate protocol for euthanasia in case there is an unexpected event.

Euthanasia (This section must be completed on all AUP's. *Exceptions must be clearly explained (e.g. protected species).)

Method: Sodium Pentobarbital

Agent: Sleepaway

Dose: 1 ml Route: IV (87 mg/ml concentration with 120 mg/Kg dose)

Justification of decapitation / cervical dislocation without anesthesia, if employed:

F. Name(s) of individuals(s) administering euthanasia. [*Note: Other than CMP or Vet Med Park staff, only the persons listed below will be authorized to perform the euthanasia procedure.*]
Gerard L. Coté, trained graduate student or trained LARR Staff

G. Specify the education, training and experience which qualifies each person named in Section IIF to perform euthanasia.

Dr. Coté has been and the trained graduate student will have completed the Texas A&M Rabbit Handling Course before the research begins. During this course, both Dr. Coté has and the student will have practiced the proposed anesthetic and euthanasia regimen. The LARR staff are well trained in this area.

SECTION III. ANIMAL PROCEDURES

A. Where will you conduct animal procedural/teaching work? [*List Bldg. and Room # for each procedure to be done*]:

All optical procedures and comparative blood draws will be performed in a LARR procedure room.

B. Briefly indicate below any non-surgical procedures to be used. Identify each species involved [*If more than one*]:

1. Method & duration of restraint: For these experiments, the rabbit will not need restraint since it will be anesthetized. The rabbit will rest on a table within a mold to support its body and head for approximately 45 minutes during the glucose testing procedure.

2. Method of obtaining blood or other tissues: [*Indicate the technique to be used, the volume to be collected, the frequency of collection, and the interval between collections. Terminal blood collections require use of a suitable anesthetic.*]

To examine glucose blood levels, blood will be drawn from the left or right marginal ear vein. 0.5cc will be drawn for each glucose measurement (eight will be drawn per rabbit in equally spaced intervals of the course of one hour each time). The rabbits will be used no more than 10 times for this procedure.

3. Agents to be administered (other than anesthetics/adjuvants), including dose, volume, route, & frequency:

Induction of diabetes mellitus in 10 animals will be done using the following protocol. Adult male NZW rabbits are anesthetized using 5 mg/kg Xylazine IM and 25 mg/kg Ketamine IM. Diabetes is induced with 140-150 mg/ml of alloxan monohydrate dissolved in 0.9% saline at 21-23 °C via an ear vein. It is injected over a seven-minute period. The rabbits are awakened with yohimbine 0.2 mg/kg IV. For the first 24 hours after the injection the rabbits will receive 10% glucose in drinking water. Nonfasting serum glucose concentration will be measured in unanesthetized rabbits 2-3 days after alloxan injection using a standard glucose measurement system and periodically thereafter. Only animals with serum glucose concentrations exceeding 300 mg/dl will be considered diabetic. All rabbits will chow and water ad libitum. To avoid death from ketoacidosis it will be necessary to administer small daily subcutaneous doses of PZI insulin (1-2 U/day) to most of the diabetic rabbits. Insulin will begin 2-3 days after alloxan injection to eliminate serum ketones, as measured with Acetest tablets or Ketostix.

4. Other procedures such as food or water deprivation, administration of noxious stimuli or substances and procedures which might induce clinical illness.

(see #3 above)

5. Names and qualifications of personnel to perform the specified procedures (Include training and experience in the techniques listed above):

Gerard Coté, graduate student to be named, Texas A&M University Rabbit Handling Course

C. Anesthesia/Analgesia

1. If anesthesia is necessary, please describe the agent to be used, dosage and route of administration for each species. *[Also indicate any other pre-anesthetic procedures, such as duration of fasting from food and water. Repeat for each species and/or surgical procedure if different.]*

Preanesthetic:	N/A	Dosage:		Route:	
Anesthetic:	Ketamine	Dosage:	25mg/kg	Route:	IM
	Xylazine		5 mg/kg		IM
Analgesics:	N/A	Dosage:		Route:	

2. Identify each person who will administer/monitor anesthesia and their qualifications. *[Indicate previous experience, education, and specific training for this specie and with this anesthetic agent. A listing of academic degrees is not an adequate response to this question. Anesthesia training is available; for information on training, visit the IACUC website, <http://animal.tamu.edu/training.html>. In teaching activities, students under the direct supervision of qualified personnel may be appropriate.]:*

Gerard Coté, graduate student to be named, Texas A&M University Rabbit Handling Course

D. Assessment of Pain and Distress

1. Does the project/class exercise involve the use of painful procedures or paralytic drugs without the benefit of anesthetics or analgesics? Yes ___ No X
IF YES, justify why anesthetics/analgesics are inappropriate for your experiments:
2. Could the procedures or outcome of this project/class cause more than slight or momentary pain or distress to animal subjects? **Be advised that the USDA has ruled that any surgical procedure has the potential for pain and/or distress.** (Please see the IACUC Website at <http://animal.tamu.edu/p&d.html> for examples of procedures which may cause pain or distress.)

NO _____

YES X (Complete below)

A. X As described in Section III.D.1. any potential pain or distress to these procedures will be relieved through use of anesthetics and analgesics and alternatives to these procedures are not available. **COMPLETE THE SECTION ON ALTERNATIVES BELOW**

B. ___ But as described in Section III.D.1., anesthetics and analgesics are inappropriate for these procedures. Alternatives to these procedures are not available. **COMPLETE THE SECTION ON ALTERNATIVES BELOW**

Describe the methods and sources you used to determine that alternatives to these procedures are not available. These might include computerized database searches (BIOSYS, Current Contents, Medline, PubMed, AgriCola). Be advised that database searches are not the only source of alternatives.

Databases searched: PubMed & Medscape

Dates searched (inclusive): 1975-2010

Keywords: polarized light, glucose detection, aqueous humor eye

A narrative of the results of alternatives search, addressing **Refinement** (new anesthetics, new analgesics, new surgical techniques, etc.) **Reduction** (please feel free to include reduction in numbers that have occurred during your career), **Replacement** (non-animal techniques) and a justification as to why these options were not used is required:

A search of using the keywords listed above in the phrase, "polarized light for glucose detection in the aqueous humor of the eye" yielded no references in PubMed from 1975 to 2010 and yielded 20 references in MEDSCAPE with no time limit (although the oldest article was 1983). Adding to the search the words, "animal use alternatives" using Boolean connector "and", produced zero results in the Medscape search.

3. Is there a possibility of any illness in the animals as a result of experimental/teaching procedures? Please include any clinically significant side effects that may occur in genetically modified animals.
No Yes if yes answer a-d below:

A. describe those effects and explain at what point and by what objective criteria (such as clinical condition) the animals may be euthanized or permanently removed from the study/class:

As described in III.B.3. above, Diabetes is induced in 10 animals with 140-150 mg/ml of alloxan monohydrate dissolved in 0.9% saline at 21-23 °C via an ear vein. It should be noted that after this diabetogenic dose of alloxan is given a massive necrosis of the beta cells in the islets of Langerhans is observed. This effect of alloxan is so specific that besides slight and mostly reversible changes in the kidney and possibly adrenal medulla no other histological changes are encountered. Thus, the potential side effects to alloxan injection include those of the Diabetes disease itself.

Apparent alloxan toxicity can be manifested by lethargy, weakness, ketosis, hyperglycemia, hypoglycemia, and acidosis. The disease can be effectively managed as described below. However, the criteria for euthanasia include severe hypoglycemic to the point of coma, severe ketosis, or 20% weight loss by the animal.

- B. describe the frequency per day that you or your staff will observe the animals after treatment administration:

At least 5 times within the first 24 hours and at least three times per day after the first 24 hours.

- C. describe the monitoring and recording procedures for determining physiological or behavioral abnormalities:

To examine glucose blood levels, blood will be drawn from the left or right marginal ear vein. 0.5cc will be drawn and a standard glucose meter used to make the measurement and, as indicated below, Acetest tablets or Ketostix will be used to assess ketoacidosis.

- D. State what measures will be taken to minimize or alleviate problems associated with experimental/teaching procedures:

Within 24 hours of initial alloxan injection some rabbits can become severely hypoglycemic and thus all animals must be closely monitored with standard blood glucose measurements within this time period. Also, after 2-3 days, to avoid death from ketoacidosis, it will be necessary to administer small daily subcutaneous doses of PZI insulin (1-2 U/day) to most of the diabetic rabbits. Insulin will begin 2-3 days after alloxan injection to eliminate serum ketones, as measured with Acetest tablets or Ketostix.

4. Is death (without euthanasia) an endpoint of the study? Yes ___ No X
IF YES, justify why an earlier end point is not acceptable:

APPENDIX B

AMENDMENTS ANIMAL STUDY PROTOCOL

TEXAS A&M UNIVERSITY

DIVISION OF RESEARCH - OFFICE OF RESEARCH COMPLIANCE

1186 TAMU
College Station, TX 77845-1186
750 Agronomy Road

979.458.1467
FAX 979.862.3176
<http://researchcompliance.tamu.edu>

Institutional Animal Care and Use Committee

Institutional Review Board

August 4, 2011

MEMORANDUM

TO: Dr. Gerard L. Cote
Industrial Engineering
MS 3120

FROM: Institutional Animal Care and Use Committee SACC

SUBJECT: Approval of Amendment to Animal Use Protocol #2010-5
Title: "Glucose monitoring using polarized light"
Funding Source: NIH
AUP Approval Date: 4/2/2010
Expiration Date: 4/1/2013

This is to inform you that the IACUC has approved the attached amendment. Your copy should be retained for future reference.

The Committee thanks you for your efforts to keep the IACUC informed of any changes to your protocol. If we can be of any further assistance, please contact the IACUC office at 979-845-1828.

Best of success in your research endeavors.

Pc: Routing Agency: TEES
Housing Facility: LARR Main
Attending Veterinarian
IACUC

TEXAS A&M UNIVERSITY **Amendment A**
INSTITUTIONAL ANIMAL CARE AND USE COMMITTEE

PROTOCOL AMENDMENT FORM

Date: 07-15-2011

Investigator: Dr. Gerard L. Coté

Department: Biomedical Engineering

Mail Stop: 3120

AUP#: 2010-5

Title: Glucose monitoring using polarized light



1. **CHANGES REQUESTED.** Please select all that apply. Provide the additional information requested in Section 2.

- Personnel** (designate personnel to act on behalf of PI to submit Amendments, Annual Reviews, and Transfers or to add personnel to AUP) Complete Amendment Signature Form at end of this form.
- Additional Animals** (provide justification for numbers and planned procedures)
- Additional Species** (provide justification, numbers justification, and planned procedures)
- Animal Housing** (provide justification, new holding conditions, building and room number)
- Surgical Procedure** (provide justification and description, including postoperative care)
- Addition or Deletion of Procedure** (provide justification and description)
- Anesthesia or Analgesia** (provide justification and description)
- Method of Euthanasia** (provide justification and description)
- Time Frame of Project** (provide justification and description of new duration)
- Funding Source** (provide new source)
- Project Title** (provide new title)
- Final Disposition of Animals** (provide justification and description of new disposition)
- Other:**

2. **DESCRIPTION OF PROPOSED CHANGES.** Please provide a detailed description of the proposed changes, including justification. Provide the same level of detail requested in the original AUP. If adding personnel provide names, description of training/experience for procedures performed.

Personnel:

As indicated in the original AUP, the personnel involved in performing the specified procedures include graduate students to be named. These graduate students include Bilal Malik and Casey Pirstill. Both the students have attended and completed basic rabbit handling and restraint workshop and are certified in research animal care and use.

Ver. 1-05

Animal Housing:

We would like to change the procedure area from initially specified LARR facility to PI's lab space (Room 1049, Emerging Technologies building). The equipment required to perform the optical procedures on the rabbits is complex and heavy, and is unfeasible to transport back and forth to LARR facility.

Addition or Deletion of Procedure:

In the original protocol, the blood drawing site was proposed to be an ear vein. Due to the orientation of rabbit in the experimental setup, it may not be the most practical and convenient location to draw blood. Therefore, we propose addition of following blood collection sites: central ear artery, the lateral saphenous vein, and the cephalic vein.

Anesthesia or Analgesia:

After discussing our anesthesia protocol with Dr. Gresham, Clinical Veterinarian at LARR, we would like to add another anesthesia cocktail to our protocol in case we need to prolong the anesthesia.

The Cocktail is formulated by mixing the following drugs:

9 cc Ketamine (100mg/cc) = 900 mg
3 cc Acepromazine (10mg/ml = 30 mg
1.8 cc L.A. Rompun (100mg/cc) 180 mg
7.2 cc Saline solution.

The result is 21 cc of cocktail administered at the rate of 1 cc/ 1.5 kg BW IM.

This is the same standard combination currently being used by the LARR facility.

CMP will monitor use of the rabbits at the new facility until CMP staff is confident that PI's staff can perform the new anesthesia regime adequately and safely.

Ver. 1-05

PAIN AND DISTRESS.

Could the **proposed changes** reasonably be expected to cause more than slight or momentary pain or distress to animal subjects? (Please see the Institutional Animal Care and Use Committee Website at <http://researchcompliance.tamu.edu/iacuc/procedures/items/painanddistress> for examples of procedures which fall under these three categories.)

- NO
- YES, but any potential pain or distress will be relieved through use of anesthetics and analgesics, and alternatives are not available. **COMPLETE THE SECTION ON ALTERNATIVES BELOW**
- YES, but anesthetics and analgesics are inappropriate for these procedures, and alternatives are not available. **COMPLETE THE SECTION ON ALTERNATIVES BELOW**

IF YES, describe the methods and sources you used to determine that alternatives to these **procedures** are not available. These might include computerized database searches (give database, dates, keywords, and results). Also include the date ranges of your search.

4. *Gerard T. Robinson* 08/02/2011
 SIGNATURE - PRINCIPAL INVESTIGATOR DATE

FOR COMMITTEE ACTION ONLY

- Minor changes approved by Chair/Campus Veterinarian
- Ten Day Hold Committee Review Required
- Full Committee Review Required

Approval Signature *[Signature]* 8-4-11
Date

TEXAS A&M UNIVERSITY
IACUC

AUG 04 2011

APPROVED

Ver. 1-05

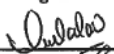
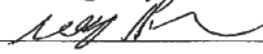
INVESTIGATORS MAY DESIGNATE UP TO BUT NO MORE THAN TWO PERSONS TO ACT ON THEIR BEHALF TO REVISE AND AMEND PROTOCOLS AND SUBMIT TRANSFERS AND ANNUAL REVIEWS. THE INVESTIGATOR REMAINS SOLELY RESPONSIBLE FOR THE CONTENT OF THE AUP AND THE CONDUCT OF THE ANIMAL WORK.

Designee name(s):

AMENDMENT SIGNATURE FORM
(Required when adding personnel to an approved AUP)

Signature certifies that the participant:

1. Understands the requirements of the Public Health Service Policy for the Humane Care and Use of Laboratory Animals, applicable portions of the Animal Welfare Regulations (Animal Welfare Act), and the Institution's policies governing the use of vertebrate animals for research, testing, teaching and for demonstration purposes.
2. Will conduct the project/class in full compliance with the aforementioned requirements.
3. Understands his/her role in the AUP, agrees to perform it and assures that he/she has the appropriate skills to do so.
4. Further understands that work with animals is limited specifically to what is approved in this document.

Typed Name of Participant	Signature	Date
Bilal Malik		08-02-2011
Casey Pirmstill		08-02-2011

Please add as many lines as necessary.

TEXAS A&M UNIVERSITY

DIVISION OF RESEARCH - OFFICE OF RESEARCH COMPLIANCE

1186 TAMU
College Station, TX 77845-1186
750 Agronomy Road

979.458.1467
FAX 979.862.3176
<http://researchcompliance.tamu.edu>

Institutional Animal Care and Use Committee

Institutional Review Board

October 26, 2011

MEMORANDUM

TO: Dr. Gerard L. Cote
Industrial Engineering
MS 3120

FROM: Institutional Animal Care and Use Committee I

SUBJECT: Approval of **Amendment B** to Animal Use Protocol #2010-5
Title: "Glucose monitoring using polarized light"
Funding Source: NIH
AUP Approval Date: 4/2/2010
Expiration Date: 4/1/2013

This is to inform you that the IACUC has approved the attached amendment. Your copy should be retained for future reference.

The Committee thanks you for your efforts to keep the IACUC informed of any changes to your protocol. If we can be of any further assistance, please contact the IACUC office at 979-845-1828.

Best of success in your research endeavors.

Pc: Routing Agency: TEES
Housing Facility: LARR Main
Attending Veterinarian
IACUC

TEXAS A&M UNIVERSITY
INSTITUTIONAL ANIMAL CARE AND USE COMMITTEE

PROTOCOL AMENDMENT FORM

Date: 07-15-2011

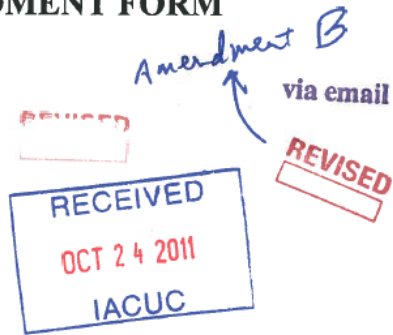
Investigator: Dr. Gerard L. Coté

Department: Biomedical Engineering

Mail Stop: 3120

AUP#: 2010-5

Title: Glucose monitoring using polarized light



1. **CHANGES REQUESTED.** Please select all that apply. Provide the additional information requested in Section 2.

- Personnel** (designate personnel to act on behalf of PI to submit Amendments, Annual Reviews, and Transfers or to add personnel to AUP) Complete Amendment Signature Form at end of this form.
- Additional Animals** (provide justification for numbers and planned procedures)
- Additional Species** (provide justification, numbers justification, and planned procedures)
- Animal Housing** (provide justification, new holding conditions, building and room number)
- Surgical Procedure** (provide justification and description, including postoperative care)
- Addition or Deletion of Procedure** (provide justification and description)
- Anesthesia or Analgesia** (provide justification and description)
- Method of Euthanasia** (provide justification and description)
- Time Frame of Project** (provide justification and description of new duration)
- Funding Source** (provide new source)
- Project Title** (provide new title)
- Final Disposition of Animals** (provide justification and description of new disposition)
- Other:**

2. **DESCRIPTION OF PROPOSED CHANGES.** Please provide a detailed description of the proposed changes, including justification. Provide the same level of detail requested in the original AUP. If adding personnel provide names, description of training/experience for procedures performed.

Addition or Deletion of Procedure:

This amendment proposes a procedure in addition to the original protocol. The proposed method will utilize multiple bolus injections of glucose, delivered intravenously, to elevate existing blood glucose levels, and non-invasively measure the response in the anterior chamber of the eye. An alternative method to elevate existing blood glucose level is to deliver a more dilute glucose solution at a fixed rate via a glucose drip. The volume of the boluses will be 2-3 ml (25% glucose) given at 10 -15 minute intervals with a targeted blood glucose range in excess of 400 mg/dl. Alternatively, 5% glucose will be given by continuous infusion (gravity drip up to 5 ml/minute) for a total of 125 ml. All

Ver. 1-05

injections will be given in the marginal ear vein. The implementation of this procedure can potentially serve as an alternative to raising blood glucose levels by induction of diabetes using Alloxan, as outlined in the original AUP.

Health related issues are not expected but there is the possibility of venous inflammation, more typical in bolus than CRI. This typically resolves within 3 days without treatment. If the inflammation were to create severe health related issues (necrosis of the ear margins) the animal would be euthanized. The blood sampling schedule will remain the same and does not exceed the single dose volume of 7.7ml/kg.

PAIN AND DISTRESS.

Could the **proposed changes** reasonably be expected to cause more than slight or momentary pain or distress to animal subjects? (Please see the Institutional Animal Care and Use Committee Website at <http://researchcompliance.tamu.edu/iacuc/procedures/items/paindistress> for examples of procedures which fall under these three categories.)

- NO
- YES, but any potential pain or distress will be relieved through use of anesthetics and analgesics, and alternatives are not available. **COMPLETE THE SECTION ON ALTERNATIVES BELOW**
- YES, but anesthetics and analgesics are inappropriate for these procedures, and alternatives are not available. **COMPLETE THE SECTION ON ALTERNATIVES BELOW**

IF YES, describe the methods and sources you used to determine that alternatives to these **procedures** are not available. These might include computerized database searches (give database, dates, keywords, and results). Also include the date ranges of your search.

Gerald L. Coy

4. SIGNATURE - PRINCIPAL INVESTIGATOR

10/23/2011
DATE

FOR COMMITTEE ACTION ONLY

- Minor changes approved by Chair/Campus Veterinarian
- Ten Day Hold Committee Review Required
- Full Committee Review Required

J. M. J. [Signature]
Approval Signature



10/26/11
Date

Revised 9/7/05

INVESTIGATORS MAY DESIGNATE UP TO BUT NO MORE THAN TWO PERSONS TO ACT ON THEIR BEHALF TO REVISE AND AMEND PROTOCOLS AND SUBMIT TRANSFERS AND ANNUAL REVIEWS. THE INVESTIGATOR REMAINS SOLELY RESPONSIBLE FOR THE CONTENT OF THE AUP AND THE CONDUCT OF THE ANIMAL WORK.

Designee name(s):

AMENDMENT SIGNATURE FORM
(Required when adding personnel to an approved AUP)

Signature certifies that the participant:

1. Understands the requirements of the Public Health Service Policy for the Humane Care and Use of Laboratory Animals, applicable portions of the Animal Welfare Regulations (Animal Welfare Act), and the Institution's policies governing the use of vertebrate animals for research, testing, teaching and for demonstration purposes.
2. Will conduct the project/class in full compliance with the aforementioned requirements.
3. Understands his/her role in the AUP, agrees to perform it and assures that he/she has the appropriate skills to do so.
4. Further understands that work with animals is limited specifically to what is approved in this document.

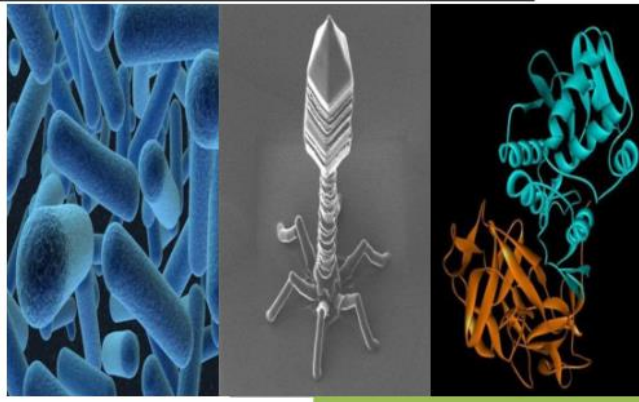
Typed Name of Participant Signature Date

Please add as many lines as necessary.

APPENDIX C

EXCISED CORNEA IBC PROTOCOL

Dr. Cote Biosafety Level 2 Manual



This lab-specific manual applies to the following BSL2 agents:

1. Human Corneas

0

Cote Laboratory
ETB 1049A

All lab personnel must read the contents of this manual and sign & date below. By signing this page, lab personnel agree to abide by the safety precautions and procedures discussed herein.

I have read, understand, and agree to adhere to the biosafety procedures contained within:

Principal Investigator:

Typed Name	Title	Signature	Date
Cote, Gerard Ph.D.	Principal Investigator		

Laboratory Staff:

Typed Name	Job/Student Title	Signature	Date
Grunden, Daniel	Research Assistant		
Pirnstill, Casey	Research Assistant		

Table of Contents

Lab Contacts and Training.....	3
Background	4
Exposure Risk	5
Inactivation and Surface Decontamination	6
Biosafety Requirements and Procedures.....	7
Safety SOPs for the <i>Gerard L Cote</i> Laboratory when using BSL2 Agents.....	11
Appendix II: Spill Response Cue Cards	16
Appendix III: BSL-2 Door Signage	19
Appendix IV: Training Certificates.....	21
Appendix V: Risk Assessments	22

Lab Contacts and Training

Principal Investigator:	Cote, Gerard
Lab Location:	1049A
Office Phone:	979-458-2331
24/7 contact (cell phone/pager):	979-574-6053
IBC Protocol #(s):	IBC2014-026
IACUC Protocol #(s) (if applicable):	NA

OHSU Research Training Courses. Courses required of all BSL2 researchers are indicated with asterisk. Other courses are research/work dependent. All courses are available on BigBrain (<https://bigbrain.ohsu.edu/>). Copies of completed training certificates should be included in Appendix IV.

Lab Personnel	Relevant Training Dates			
	Blood-borne Pathogens	Lab/Agent Specific	Biosafety Cabinet	BL2
Name				
Cote, Gerard				
Grunden, Daniel				
Pirnstill, Casey				

Cornea-specific Training. Laboratory personnel are not allowed to work with human corneas until they have been trained by the PI who supervises their work, or a designated technical expert. The worker should demonstrate good microbiological skills and an understanding of this SOP prior to being permitted to work with corneas.

Background

A noninvasive glucose sensor using the eye as a sensing site is being developed. Specifically, the sensor measures glucose levels by measuring how glucose changes polarized light as it is passed through the aqueous humor. One of the obstacles that this approach faces is that the cornea also changes polarized light. Therefore, one of the stages for this sensor's development involves studying the manner in which polarized light is affected (via birefringence) by the human cornea, and how light can be coupled through the cornea without index matching. A second area of interest is how a high-speed approach can decrease standard error in glucose readings. The isolated cornea will be mounted on an artificial anterior chamber, and the chamber will be fitted on a translation stage to induce motion artifact.

The major risks to be considered for research with human corneas include conjunctivitis, herpes zoster, and ocular herpes. Although each can be spread by touch, gloves and goggles should prevent exposure.

Exposure Risk

The most probable route of exposure for work with human corneas would be via touch.

Although conjunctivitis (Pink Eye) can be transmitted via touch, the virus or bacteria is only airborne when the infected individual coughs or sneezes. Therefore, there is a low health risk, because gloves and goggles can be worn to prevent spread. Symptoms can include burning, itching, discharge of thick, sticky mucus, and redness of the eye.

Herpes Zoster (shingles) can be spread via touch and can be prevented by wearing gloves and goggles. Most people already have the virus. Symptoms include headache, itching, tingling, or pain, dizziness, weakness, vision changes, and a rash. Luckily, the virus spreads only from rash fluid. The cornea does not include rashes.

Ocular herpes can be spread via touch. Symptoms include tearing, eye redness, blurry vision, and ocular discomfort.

Inactivation and Surface Decontamination

After both experiments, the corneas will be placed in a 10% bleach solution for 30 minutes. The corneas (along with the plastic bag and the parafilm) will then be disposed of in a heavy-duty leak proof biohazardous waste bucket that will be emptied for incineration within one week following the study. The Optisol preservation medium will be mixed with a 10% bleach solution for disinfectant inside the inner-transport container. After 30 minutes, the remaining solution will be poured down the drain. The inner-transport container will then be washed (while still wearing gloves, goggles, and lab coats) with soap and water followed by a wipe down with a Clorox disinfectant wipe. The forceps will soak in the 10% bleach solution created inside the inner-transport container. Afterwards, like the container, the forceps will be washed with soap and water followed by a wipe down with a Clorox disinfectant wipe. The outer-transport container (the portable ice chest) will be wiped down with a Clorox disinfectant wipe, and the inner-transport container and the forceps will dry on a towel. The towel will be cleaned at the end of the study.

***A note on bleach:** Household bleach is effective and inexpensive, but it is also volatile and corrosive. Bleach-soaked paper towels should not be autoclaved because autoclaving 1) releases chlorine, a chemical hazard, and 2) will corrode the autoclave over time. 10% (0.5% final concentration sodium hypochlorite) household bleach solutions should be prepared fresh prior to each work session, when needed. If 10% bleach is used to decontaminate a spill within the Biosafety Cabinet (BSC), once the spill has been absorbed on paper towels and disinfected with 10% bleach, the BSC should be wiped down with 70% ethanol (EtOH) in order to remove residual bleach.

Biosafety Requirements and Procedures

1. **Physical Containment.** All work with human corneas must be performed in a BSL-2 laboratory. When the corneas is/are present, a sign must be posted at the entrance to the lab. This sign must include the biosafety level (BSL-2), a biohazard symbol, the name of the agent(s) in use, the name and phone number of the PI or lab supervisor, and required procedures for entering and exiting the lab. (A sign that meets these requirements is available in Appendix III). Additionally, incubators and freezers must bear biohazard warning labels. (Please contact a Biosafety Officer/Specialist to request biohazard stickers). Doors to the laboratory should be lockable and self-closing. Laboratory windows that open to the outdoors must be fitted with fly screens.

2. **Personal Protective Equipment (PPE).** The following PPE must be worn when working with human corneas:

Please check appropriate boxes by double clicking and selecting "checked."

- | | | | |
|--|--|---|---|
| <input checked="" type="checkbox"/> Gloves | <input checked="" type="checkbox"/> Safety glasses | <input type="checkbox"/> N95 Respirator | <input type="checkbox"/> Shoe covers |
| <input checked="" type="checkbox"/> Latex | <input type="checkbox"/> Face shield | <input type="checkbox"/> Surgical mask | <input type="checkbox"/> Medical scrubs |
| <input type="checkbox"/> Nitrile | <input checked="" type="checkbox"/> Lab coat | <input type="checkbox"/> Hair net | |

Remove potentially contaminated gloves and replace them with new gloves before touching anything outside the BSC, such as the refrigerator, centrifuge, or incubator.

BSL-2 Personal Protective Equipment recommendations by agent

Bacteria: Gloves, Lab coat, Safety glasses when working with bacteria outside a BSC.

Viruses: Gloves, Lab coat, Safety glasses when working with virus outside a BSC.

Toxins: Gloves, Lab coat, Safety glasses when working with toxin outside a BSC or when using powder form of toxin.

3. **Spill Kit.** The lab must have a spill kit, or the components of such, readily accessible in the event of a spill. The spill kit should have:

- an easy-to-read outline of the spill response SOP,
- gloves,
- surgical masks,
- safety glasses or goggles,
- clean lab coat, disposable gown or clean scrubs and spare slip-on shoes (Crocs are not recommended because they do not fully enclose the feet) in case clothing not covered by lab coat becomes contaminated,
- paper towels to absorb contaminated liquids,
- disinfectant (e.g., 10% bleach),
- tongs or forceps to pick up broken glass,
- a biohazard waste container large enough to handle wet, contaminated paper towels.

4. **General Procedures for working with human corneas.** Standard BSL2 practices should be employed, conforming to the BMBL and TAMU Biosafety Manual including a prohibition of eating, drinking, food storage, handling of contact lenses, applying lipstick, cosmetics or lip balm, mouth pipetting, and a requirement of appropriate PPE.

Additional practices include the following recommendations:

- a. Whenever possible, work with human corneas during normal working hours, to enable adequate response to a severe adverse incident.

- b. Sharps should be avoided whenever possible in a BSL-2 laboratory. Plastic aspirating pipettes (e.g., Corning cat. # 4975; Falcon cat # 3575; Fisher Cat # 13-675-123) should be substituted for glass Pasteur pipettes. Needles with safety devices are recommended wherever possible. If conventional needles are required, they must *never* be re-capped, and must be disposed of in a rigid, red sharps waste container. *Never* reach into a sharps container to retrieve discarded items. Do not allow a sharps container to become more than $\frac{3}{4}$ full. Reminder: syringes without needles can be discarded in either a biohazard bag or a biohazardous sharps container, but must never be discarded in regular trash.
- c. Solid Waste: Everything that contacts human corneas or cornea preservation medium-containing solutions or vessels must be decontaminated or contained. Solid waste can be collected in a biohazard bag. Pipette tips can be collected in a disposable plastic box (e.g., an empty P-1000 box), and the box closed and deposited into the biohazard bag at the end of the work session. At the end of the work session, the biohazard bag must be closed, sprayed with 70% EtOH, and deposited into a biohazard waste container.
- d. Liquid Waste must be treated with disinfectant at the recommended final concentration, allowing a minimum time of 30 minutes to inactivate the agent. A simple 500 ml bottle containing disinfectant may be suitable to collect non-aspirated liquid waste.
- e. Storage: Human cornea stocks must be in leak-proof secondary containers in a -80° freezer clearly marked with a warning label to indicate that human cornea(s) is/are present.

5. **Accidents and spills**

a. Spills

- i. Small spills outside the BSC. A small spill, in this circumstance, is defined as a spill with low potential to aerosolize, presents no inhalational hazard, and no endangerment to people or the environment. As a practical consideration, volumes less than 10 ml fall into this category. First, ascertain the extent of the spill. Simply dropping a 150 mm dish contained inside a closed secondary container does not constitute a spill outside the BSC, since there is no breach of containment—as long as the secondary container stays closed. If other personnel are present, alert them immediately. Keep in mind: spills generate aerosols. Quickly check to ascertain the extent of the spill: Is PPE is contaminated? (Gloves, lab coat, pants cuffs, shoes?). Is bare skin is exposed? Has liquid splashed over a large area? If shoes are visibly contaminated, decontaminate them with appropriate disinfectant, then evacuate the room, closing the door. Remove gloves (or outer gloves, if double-gloved) before touching the door knob. Remove any potentially contaminated PPE, place it in a biohazard bag, wash hands and face thoroughly. Post a sign on the door warning personnel not to enter. Allow 30 min. for aerosols to settle. During this time, notify the PI and the campus Biosafety Officer/Specialist (see Appendix I for contact information). After hours, contact the TAMU Office of Biosafety for assistance (979-845-4311). After 20 min., don fresh PPE, re-enter the room, cover the spill with paper towels, then soak them with disinfectant starting at the periphery and moving inward toward the center. Be sure to check for and decontaminate small splashes beyond the main affected area. Leave the soaked towels in place for 20 min. to inactivate the agent. Leave the room during this time. After the 20 min. inactivation time, transfer soaked paper towels to biohazard waste. Wipe up the residual spill with more paper towels. Give the area a final wipe-down with paper towels using the appropriate disinfectant.
- ii. Large spills outside the BSC. A large spill, in this circumstance, is defined as a spill that spreads rapidly, presents an inhalational hazard, endangers people or the environment, and/or involves personal injury or rescue and should be handled as an emergency. In practical terms, this might be a spill of more than 10 ml splattering over a large area, thus

presenting the possibility of aerosolization and widespread contamination. If other personnel are present, alert them immediately. Keep in mind: spills generate aerosols. Ascertain the extent of the spill: possible overt exposure, splash on shoes or soles of shoes, contamination of PPE. If shoes are contaminated, disinfect them before evacuating the room (if shoes are extensively contaminated, you should remove them as you leave the room). After removing gloves (or outer gloves, if double-gloved), evacuate the room, closing the door as you leave. Remove PPE. Wash hands and face thoroughly. Post a sign on the door warning personnel not to enter. Allow 20 min. for aerosols to settle. During this time, notify the PI and the Biosafety Officer/Specialist (see Appendix I for contact information). If the spill is too difficult to manage alone, seek help from the Biosafety Officer. After 20 min. don fresh PPE, re-enter the room, cover the spill with paper towels, and soak the towels with appropriate disinfectant, working from the outside toward the center. Allow 20 min. for human corneas and cornea preservation medium to be inactivated. If there is any broken glass associated with the spill, pick it up with tongs or forceps, and transfer it to a biohazardous broken glass container. Pick up soaked paper towels, and transfer to a biohazard bag. Give the area a final wipe-down with paper towels using the appropriate disinfectant.

All Spills outside of the BSC that involve breach of containment, regardless of exposure, must be reported to a Biosafety Officer/Specialist.

b. Accidents

Accidents include the release of human corneas or cornea preservation medium due to equipment failure (e.g. tube failure in the centrifuge), needle-sticks, or other injuries concomitant with a breach of containment of human corneas or cornea preservation medium.

- i. Sharps should be avoided whenever possible for work with human corneas or cornea preservation medium manipulation, and delivery. However, if there is a needle-stick, briefly bleed the wound (squeeze it to produce a couple of drops of blood), then wash thoroughly with soap and water for 15 min. Report the incident to the PI and the Biosafety Officer.
- ii. Other accidents might include slips, falls, or collisions with other personnel, leading to spills of human corneas or cornea preservation medium. Additional help may be required in the event of personal injury, in which case assisting personnel must be made aware of the presence of uncontained agent(s) so that they can respond appropriately. In the event of a major spill involving serious personal injury or requiring rescue, call TAMU EHS (9-1111), a Biosafety Officer/Specialist (see Appendix I for contact information), and contact the PI.
- iii. Follow-up of exposures or injuries involving Human Corneas or Cornea Preservation Medium: Follow-up of laboratory injuries or documented, overt exposures to Human Corneas or Cornea Preservation Medium will be conducted through via the Supplemental Report of Injury Form: http://tees.tamu.edu/media/24971/supplemental_injury.pdf.

In the event of an exposure or injury the following steps should be followed:

- Determine the severity of the injury/exposure. If it is life-threatening, call Public Safety immediately (9-1111). They will help you decide whether to go directly to the ER or wait for emergency responders.
- If the injury/exposure is non-life-threatening, call TAMU Office of Biosafety (9-4311). Over the phone, they can help you with first-aid advice, and also help you decide whether to go to the ER or whether to come to Employee Health for follow-up treatment.

- If you are injured/exposed and need to leave the lab for treatment, delegate responsibility to a colleague for any clean-up or decontamination that may be necessary. Have the colleague document what happened.
- Monitoring after potential exposure to a potentially infectious agent (e.g., a needlestick with uncharacterized primary human cells or blood) can be conducted by Employee Health.
- Work-related injuries should be reported to Human Resources using their WCI forms: http://employees.tamu.edu/media/313101/569WC_FirstReportInstr.pdf
- In addition to the Risk Management Incident Report, above, the NIH/OBA independently requires notification (via the IBC) of overt exposures to BSL-2 agents, or spills outside the BSC. The following table presents the IBC reporting time-frame.

Type of spill or exposure	Reporting time frame
Spill of a BSL-2 agent outside the BSC	Incident Report Form must be submitted <u>to the IBC within 10 days.</u>
Documented exposure to a BSL-2 agent	Report <u>immediately</u> to the Biosafety Officer (preferably by phone call). Submit Incident Report Form to the IBC within 5 days.
Potential or documented exposure to a BSL-3 agent	
Spill of a BSL-3 agent outside the BSC	

Note:

Some incidents that do not require reporting to the EHS, such as a spill inside a BSC that is properly decontaminated, should nevertheless be reported to the PI/supervisor in order to review or revise SOPs so as to minimize recurrence of the event, or to prompt refresher training of personnel.

Safety SOPs for the Gerard L Cote Laboratory when using BSL2 Agents

The corneas will not be shipped. Instead, the sub-principal investigators will drive to the Lone Star Lions Eye Bank for cornea retrieval. The corneas will be transferred in the preservation medium, Optisol. Optisol contains dextran, 2.5% chondroitin sulfate, vitamins, and precursors of adenosine triphosphate (adenosine, inosine, and adenine). The corneas will be placed in a container sealed with parafilm. The container will then be placed in a heavy-duty sealable plastic bag. These bags will be placed in a handheld ice chest. The corneas will remain in the handheld ice chest until the experiment begins. The experiments will begin within 5 hours upon arrival since the corneas will begin to degrade immediately.

Before the corneas arrive, the optics and electronics will be turned on and allowed to warm up. Once the corneas arrive, lab coats, goggles, and gloves will be utilized to help prevent infection from possible pathogens. The cornea will be removed from the sealable plastic bag and the container sealed with parafilm. The isolated cornea will be mounted onto an artificial anterior chamber. After the cornea is mounted, ~1mW of linearly polarized light will shine through the cornea and measure glucose in the artificial anterior chamber. The artificial anterior chamber will first have fixed glucose concentrations at 100 mg/dl increments followed by a continuous flow of varying levels of glucose concentrations. Both the cornea and the artificial anterior chamber will be mounted on a translation stage to induce motion artifact. Following this first experiment, the cornea and the artificial anterior chamber will be moved to a second setup on the optics breadboard that will study how light can be coupled through the cornea without index matching. A polarimeter will be used to study the manner in which polarized light is affected by the human cornea. Both experiments will be performed 10 times using 10 different corneas. The sub-principal investigators will wear gloves, goggles, and lab coats at all times during the experiments when touching "dirty" objects like the corneas, forceps, syringe, bleach bottle, saline solution, and Clorox Wipes. The gloves will be removed when the computer mouse and keyboard, the door handle, the optics, and the electronics are touched. The local areas for the corneas in the optical setup will be covered with a replaceable absorbent pad to protect the optics breadboard.

After both experiments, the corneas will be placed in a 10% bleach solution for 30 minutes. The corneas (along with the plastic bag and the parafilm) will then be disposed of in a heavy-duty leak proof biohazardous waste bucket that will be emptied for incineration within one week following the study. The Optisol preservation medium will be mixed with a 10% bleach solution for disinfectant inside the inner-transport container. After 30 minutes, the remaining solution will be poured down the drain. The inner-transport container will then be washed (while still wearing gloves, goggles, and lab coats) with soap and water followed by a wipe down with a Clorox disinfectant wipe. The forceps will soak in the 10% bleach solution created inside the inner-transport container. Afterwards, like the container, the forceps will be washed with soap and water followed by a wipe down with a Clorox disinfectant wipe. The outer-transport container (the portable ice chest) will be wiped down with a Clorox disinfectant wipe, and the inner-transport container and the forceps will dry on a towel. The towel will be cleaned at the end of the study.

Due to possible pathogens inside the corneas, gloves, goggles, and lab coats will be worn at all times during the study, unless "clean" optics, electronics, and computers need to be used to prevent contamination. Possible non-contagious corneal diseases include dry eye, fuchs' dystrophy, iridocorneal endothelial syndrome, lattice dystrophy, map-dot-fingerprint dystrophy,

pterygium, and stevens-johnson syndrome. Conjunctivitis (Pink Eye) can be transmitted via touch, but the virus or bacteria is only airborne when the infected individual coughs or sneezes. Since we are dealing with only the corneas and not the entire individual, gloves and goggles can be worn to prevent infection. Herpes Zoster (shingles) provides low risk. Most people already have the Caricella-zoster (chickenpox) virus already, but the virus can be transferred via touch. Luckily, the virus spreads only from the rash fluid. Since the rash doesn't occur on the cornea, there is minimal risk for spread, but goggles and gloves will still be worn. Systemic diseases like Leber's congenital amaurosis, Ehlers-Danlos syndrome, Down syndrome, and osteogenesis imperfect can cause Keratoconus, an enlarged cornea. These diseases aren't contagious. Ocular herpes can be transferred via touch, but again, wearing gloves and goggles should prevent infection.

Appendix I: Contact Information

CENTRAL CAMPUS CONTACTS		RESEARCH COMPLIANCE AND BIOSAFETY CONTACTS	
<u>EMERGENCY</u>		<u>Biosafety</u>	
Emergency Services	911	Jennifer Biladeau	979-862-4688
TAMU EHS	979-862-1111	IBC Coordinator	979-845-7189
		Associate Biological Safety Officer	
<u>UNIVERSITY ASSISTANCE</u>		Frank Cox	979-845-7126
TAMU Office of Biosafety	979-845-4311	BL3 Laboratory Maintenance Manager	
(lead for BL2 incidents)		Kory Douglas	979-458-3525
TAMU EHS	979-862-1111	IBC Coordinator	979-862-4074
(lead for large blood spills)		High Containment Lab Manager	
TAMU Facilities Communication Center	979-845-4311	Ndingsa Fomukong	979-862-4011
University Police	979-845-2345	Project Manager	
		Susan Gater	979-458-3524
<u>EHS ASSISTANCE</u>		Associate Biological Safety Officer	
Debbie Adkins	979-862-8115	Lauren Horton	979-862-6455
Office of Safety and Security		Biosafety Occupational Health Specialist	
Johnny Contreras	979-458-3698	Sherri Koeppnick	979-845-6649
Hazardous Waste		Biosafety Occupational Health Coordinator	
Eric Falke	979-845-5844	Yan (Viola) Luo	979-458-1467
Fire and Life Safety		Project Manager	
Tassie Hermann	979-845-8761	Christine T. McFarland	979-845-6475
Environmental Compliance		Director, Biosafety	
Susan Karli	979-862-8114	Ruchira Mitra	979-862-6456
Administrative/Business		Associate Biological Safety Officer	

Appendix II: Spill Response Cue Cards



Cut out cue cards and post in a highly visible work area



SPILLS INSIDE THE BIOSAFETY CABINET

1. Make sure the cabinet continues to operate. Wait 5 min. to allow aerosols to be pulled through the HEPA filter.
2. Decontaminate the surfaces within the cabinet wearing protective clothing. Gently cover the spill with absorbent paper towels and apply the appropriate disinfectant starting at the perimeter and working towards the center.
* Note: Examine drain pan for contents of the spill. Disinfect if needed.
3. Discard soaked paper towels in a biohazard bag. Wipe up residual fluids. Wipe down surfaces with 70% EtOH, discarding towels in a biohazard bag.

SPILLS OUTSIDE THE BIOSAFETY CABINET

Small Spill (<10 mL, localized to small area)

1. Alert personnel in the vicinity.
2. Check for contaminated clothing, including shoes. Decontaminate if necessary.
3. Evacuate the room. Close door. Discard potentially contaminated PPE, remove and decontaminate any contaminated clothing. Wash hands.
4. Notify PI. Wait for 20 minutes to allow for room air exchanges to clear aerosols through room exhaust.
5. Don fresh PPE: lab coat or gown, gloves, mask, eye protection.
6. Cover spill with paper towels.
7. Soak paper towels with the appropriate disinfectant, from perimeter toward the center.
8. Allow 20 min. of contact time. Work can continue during contact time.
9. Discarded towels go in biohazard bags. Pick up sharps with tongs & place in sharps container.
10. Wipe down spill area one final time with appropriate disinfectant.

SPILLS OUTSIDE THE BSC

Major Spill (>10 mL, localized to small area)

1. Alert personnel in the vicinity.
2. Check for contaminated clothing, including shoes. Decontaminate if necessary.
3. Evacuate the room. Close door. Discard potentially contaminated PPE and remove any contaminated clothing. Wash hands thoroughly.
4. Post warning sign: "DO NOT ENTER: Biological spill!"
5. Wait 20 min. Meanwhile, notify PI and a Biosafety Officer/Specialist (9-3698, 9-5395).
6. If assistance is needed, discuss with Biosafety Officer.
7. Don fresh PPE: lab coat or gown, gloves, mask, eye protection.
8. Re-enter the room, cover spill with paper towels.
9. Soak paper towels with appropriate disinfectant, from perimeter toward the center.
10. Allow 20 min. of contact time. Work can continue during contact time.
11. Discarded towels go in biohazard bags. Pick up sharps with tongs & place in sharps container.
12. Wipe down spill area one final time with appropriate disinfectant.
13. With PI, write up a report and submit to the Biosafety Officer.

SPILLS INSIDE AN INCUBATOR

Decontaminate water pan via autoclave.

1. Alert personnel in the vicinity.
2. Evacuate the room. Close door. Discard potentially contaminated PPE and remove any contaminated clothing. Wash hands thoroughly.
3. Notify PI.
4. Don fresh PPE: lab coat or gown, gloves, mask, eye protection.
5. Cover spill with paper towels.
6. Soak paper towels with appropriate disinfectant, from perimeter toward the center.
7. Allow 20 min. of contact time.
8. Discarded towels go in biohazard bags. Pick up sharps with tongs & place in sharps container.
9. Wipe down spill area one final time with appropriate disinfectant.

SPILLS INSIDE A CENTRIFUGE

1. Open lid of centrifuge slowly.
2. If there has been no breach of containment, spray rotor with 70% EtOH.
3. If inside of rotor is contaminated, decontaminate in the BSC. As a precautionary measure, decontaminate the centrifuge chamber.
4. If rotor buckets are damaged, close centrifuge lid.
5. Alert personnel in the vicinity. Evacuate room.
7. Wait 30 min. Meanwhile, notify PI and a Biosafety Officer/Specialist (4-0655, 4-2580).
8. If assistance is needed, discuss with Biosafety Officer.
9. Open lid slowly and add paper towels.
10. Spray walls of chamber and rotor with 70% EtOH.
11. Close centrifuge lid for 20 min. contact time.
12. Finish centrifuge clean-up as for major spill outside the BSC. Transport rotor to BSC.
13. Open and decontaminate rotor/buckets in the BSC.
14. With PI, write up a report and submit to Biosafety Officer

Appendix III: BSL-2 Door Signage

Room No.: 1049A

BSL-2 Laboratory



Authorized Personnel Only

Biosafety Level 2 Biological Agents:	Human Corneas
Special Procedures, PPE, or Precautions for Entry/Exit:	Lab Coats Goggles Gloves

Principal Investigator		Emergency Contact	
Name	Phone	Name	Phone
Gerard L Cote, Ph.D.	979-845-4196	Andy Deuel	979-845-1581

20

Appendix IV: Training Certificates

Following this page, please insert copies of training certificates for each person who has completed a training course listed in the table on page 3.

Appendix V: Risk Assessments

If you have requested and received approval from the Biosafety Officer for a laboratory protocol that deviates from the BMBL, then add the protocol deviation(s) here:

Appendix VI: IBC Protocol and Approval

Following this page, please insert a copy of the IBC-approved Recombinant DNA Research Questionnaire (RDRQs) and/or Infectious Agent/Toxin Questionnaires (IAQs) related to this agent. Also include a copy of the IBC Approval Letter.

Please note: All work with your BSL2 agent(s) must be pre-approved by the IBC before experiments can begin.

Appendix VII: Disinfectant Table

Disinfectants	Practical Requirements		Inactivation Efficacy				Potential Application			Characteristics					
	Effective Dilution	Shelf Life (months)	Sink Disposal	Bactericidal	Virucidal	Fungicidal	Sporicidal	tuberculocidal	Skin disinfectant	hard surfaces	stainless steel	liquid for disposal	Leaves Residue	Inactivated by organic matter	Other
Appendix VIII: Disinfectant Chart															
Brand	1:100 (1,000 ppm)	1 yr													
Quatrol TB	N/A (2,100 ppm)		+	+	+	+	+	+	+	+	+			Parvocidal	
Quatrol FV	1:50 (1,750 ppm)		+	+	+	+	+	+	+	+	+			Parvocidal	
Quatrol	1:64 (750 ppm)	64 days	+	+	+	+	+	+	+	+	+				
Claykide II	1:64 (740 ppm)	2 years	+	+	+	+	+	+	+	+	+				
Lysol LC spray	N/A (1,000 ppm)	2 years	+	+	+	+	+	+	+	+	+				
Lysol LC Quat	1:256 (650 ppm)	2 years	+	+	+	+	+	+	+	+	+				
Masoxide-PD	N/A (300 ppm)		+	+	+	+	+	+	+	+	+				
Morning Mist	1:64 (750 ppm)		+	+	+	+	+	+	+	+	+				
Roccal	1:256 (320 ppm)		+	+	+	+	+	+	+	+	+				
	50,000 ppm A		+	+	+	+	+	+	+	+	+				
Appendix VIII: Disinfectant Chart															
Isopropyl	1:100 (1,000 ppm)	1 yr	+	+	+	+	+	+	+	+	+			corrosive metal	
	25-1500 ppm A	years	+	+	+	+	+	+	+	+	+			corrosive metal	
Wescoline	1:100 (125 ppm)	years	+	+	+	+	+	+	+	+	+			poor residual	
Bleachine		years	+	+	+	+	+	+	+	+	+			poor residual	
Iodine		years	+	+	+	+	+	+	+	+	+			Poor residual	
Phenolic Compounds															
Bleachcup	1.3-5.0% (10,000-50,000ppm)														
Amphyl	1:100 (125 ppm)														
Amphyl	5.0%														
Sporicidin	N/A (15,600 ppm)	6 mos													flammable
	70-85% (700,000-850,000 ppm)														
Alcohols															
Ethyl & Isopropyl	N/A (202,000 ppm)	2 years													
Eurocode	N/A (210,000 ppm)	years													
Opides3	N/A (700,000 ppm)	2 years													
	N/A (700,000 ppm)	2 years													
Aldehydes															
	0.2-0.6% (2,000-80,000 ppm)														
Citrykide G	1:16 (34,000 ppm)														
Mercide Plus 30	N/A (34,000 ppm)														
Cleav OPA	N/A (5,500 ppm)	2yr (14d)													
Cleav Plus 28	N/A (4-50,000 ppm)	(28d)													
Peroxide Compounds															
	5-6% (50,000-80,000 ppm)														
Hydrogen peroxide (L)															
Chlorhexidine															
	1:50 (600 ppm)	1 yr	+	+	+	+	+	+	+	+	+			non-toxic	

DIVISION OF RESEARCH

Office of Biosafety

May 28, 2014



MEMORANDUM

TO: Dr. Gerard Cote
Professor And Head
TEES - College Of Engineering - Biomedical Engineering

FROM: Kory Douglas Ph.D.
Biosafety Program

SUBJECT: *Approved Personnel for IBC Permit –IBC2014-026*

PERMIT EXPIRATION: 05/28/2017

Below is the current list of personnel authorized to work on your IBC Permit IBC2014-026. Please note this list only reflects those individuals that have met all protocol requirements.

Personnel	Date Added to IBC Permit
1. Gerard Cote	May 28, 2014
2. Daniel Grunden	May 28, 2014
3. Casey Pirstill	May 28, 2014
Additional Requirements/Notes:	
A) This approved personnel memo added Personnel 1 - 3 to the permit.	

Please note:

1. Any additional modifications in your personnel must be reviewed before individuals may begin work in the laboratory. Please note that the IBC must also be notified if you remove any personnel from your laboratory. All modifications to personnel may be submitted through the Amendment process.
2. Only personnel, who have met all training and occupational health requirements for this protocol and received written approval from the IBC, may conduct work listed in the permit.
3. If your project will involve direct work with vertebrate animals, please contact the Animal Welfare Assurance Program at <http://rcb.tamu.edu/animals>, if you have not already done so. Any work involving humans or human material, please contact the Human Subjects' Protection Program at <http://rcb.tamu.edu/humansubjects>.
4. Please forward copies to your campus routing agency coordinator for forwarding to your granting agency as applicable.

APPENDIX D

FARADAY ROTATOR DESIGN

D.1) Expanded Optical Rotation Experimental Setup

A more detailed description of the optical system described in the manuscript and shown in Figure 1a of the manuscript is as follows. The optical source used was a 635 nm wavelength laser diode module (Power Technology, Inc., Little Rock, AR) emitting at seven mW. The beam was initially passed through a 100,000:1 Glan-Thompson linear polarizer (Newport, Irvine, CA) to convert the beam to a horizontally linearly polarized state. The beam was then passed through the individual MOFR device, each of which was driven to modulate at frequencies between 1.09 kHz - 10 kHz. The magneto-optic material utilized in this design was a Terbium Gallium Garnet (TGG) rod (Deltronic Crystals Inc., Dover, NJ). The ferromagnetic material for the core design was custom-machined utilizing the M25 material into the air gapped C core geometry, shown on the left in FIG. S2a, and wound with three different numbers of wire turns as specified in the main text.

The device was driven by a lock-in amplifier (Stanford Research) coupled to a high gain audio amplifier (12-1971) (Optimus, Fort Worth, TX). The beam was converted into an electronic signal using a PIN photodiode (Thorlabs, Newton, NJ) and amplified utilizing a wide-bandwidth current amplifier (CVI Melles Griot, Albuquerque, NM). The output signal from the current amplifier was connected to an oscilloscope (Tektronix Inc., Beaverton, OR). Determining the degree of optical rotation was accomplished by carefully rotating the analyzer using a high precision optical rotation stage ARS301 (AeroTech Inc., Pittsburgh, PA) and evaluating the peak-to-peak voltage and frequency response of the optical signal on the oscilloscope.

For DC testing the Faraday modulators were driven by an HP triple output DC power supply in constant current mode (Hewlett Packard, Palo Alto, CA). Additionally, a commercial PAX-series-polarimeter model TXP-5004 (Thorlabs, Newton, NJ) was used to measure the rotation in the plane of polarization.

D.2) Expanded Description of the High Permeability Air Gapped Faraday Rotator

The high permeability core MOPLM devices were constructed with an inductive coil wrapped around a ferromagnetic core designed with an air gap and a through hole for use as an optical path as shown in Figure S2. The use of a high permeability core allows increased MFD to be produced, in a Faraday Effect device design, with fewer windings and lower power consumption than traditional air-core devices. As a result, a ferrite core design, compared to the standard air-core design, can produce an increased optical rotation for frequencies up to 1 kHz with an order of magnitude reduction in the number of turns in wire and without impedance matching circuitry. Additionally, a soft ferrite high permeability core design allows for a reduction in the overall number of turns of conductive wire required to achieve AC modulation as compared to traditional air-core designs which leads to significantly lower DC coil resistance values. A combination of high permeability, low DC coil resistance, and tunable inductive response in ferrite cores allows higher frequency modulation to be achieved in designs without it suffering from a reduced maximum generated MFD, requiring significant increases in overall device size, or increasing the input power driving the device in comparison to traditional air-core Faraday based optical modulation devices [1]. The ferromagnetic material selected for the core design was a soft ferrite known as M25 (National Magnetics Group INC., Bethlehem, PA) which is a composition of manganese and zinc (MnZn). The M25 material was purchased in the form of bars measuring 7.72" long X 1.1" wide X 0.55" thick. M25 was chosen because it offered ideal magnetic and low loss properties in addition to being designed for high magnetic flux capabilities intended for applications involving high frequencies [16, 10]. Specifically, it has a high initial magnetic permeability of $\mu_i=2500$ and a large operating frequency range of up to 200 kHz. The magneto-optic material utilized in this design was a Terbium Gallium Garnet (TGG) rod (Deltronic Crystals Inc., Dover, NJ).

D.3) Results and Discussion:

The inductance, magnitude impedance (AC resistance), and Q values were measured for DC, 100 Hz, 1 kHz, and 10 kHz for each of the designs. The recorded values for the two device designs with four different windings are listed in Table D3.1.

Table D3.1: RL Measurements of Faraday Modulation Devices						
	91 Turn Ferrite Core Coil			170 Turn Ferrite Core Coil		
Freq. (kHz)	Resistance (k Ω)	Induct. (mH)	Q	Resistance (k Ω)	Induct. (mH)	Q
DC	0.0016	-	1	0.0031	-	1
0.1	0.001654	1.29	1.49	0.00569	3.89	0.746
1	0.102	1.29	8.7	0.184	3.88	7.37
10	7.05	1.29	8.6	7.066	3.92	31.5
	324 Turn Ferrite Core Coil			3364 Turn Air-Core Coil		
Freq. (kHz)	Resistance (k Ω)	Induct. (mH)	Q	Resistance (k Ω)	Induct. (mH)	Q
DC	0.008	-	1	0.076	-	1
0.1	0.03814	15.23	2.68	0.2	150.52	1.39
1	3.717	15.20	26.6	13.403	151.21	13.5
10	25.9	15.52	62.9	2362	154.27	65.1

Specifically, a DC power supply (0-6 V, 0-3 A) was connected to the each of the MOFR devices and the change in azimuth angle was measured for supplied currents ranging between 0 A to 1.05 A. The supply was set to output a constant current, increased across this range in the first run, and decreased in the second run. The required voltage to supply the desired current was also measured. These measurements were then followed by AC measurements to see if the proposed design could provide modulated changes in the degree of polarization at varying frequencies without impedance matching components. For AC testing the 3364 air-core solenoid rotation device was used for comparative purposes. To verify modulation was possible at non-DC frequencies the devices were placed between two polarizers set at 0° and 90° and the optical signal was measured by a detector and observed on an oscilloscope. To determine the degree of change, the analyzer was rotated until the observed 1f signal was

converted to a $2f$ signal and the change in angle to achieve this was recorded. Using the optical rotation equation, the magnetic field created by the device was calculated. Results obtained from the oscilloscope for modulation of the 324 turn ferrite device at a $1f$ frequency of ~ 1 kHz and $2f$ frequency of ~ 2 kHz are shown in Figure D3.1.

Impedance matching circuitry was not required to achieve 1 kHz modulation of the 324 and 91 turn modulation devices. Impedance matching was required with the current 3364 turn air-core solenoid approach. Additional current was required to provide the equivalent degree of rotation however, the DC resistance of the 324 turn and 91 turn coils is lower such that the same supplied power can achieve a better degree of rotation than when provided to the 3364 air-core approach. Above ~ 1 kHz, the modulated signal starts to drop off for the 324 turn device. Also of note, the rotation measured experimentally from the 324 ferrite core was approximately 200 millidegrees more than predicted for the supplied current and number of turns. The increase could likely be attributed to variations in the actual permeability of the machined cores, the dimensions, or the material properties. The 200 millidegree change resulted in a difference of 2.86 mT between the theoretical and actual magnetic fields, indicating a lower current was required than originally anticipated to achieve the theoretically calculated degree of rotation.

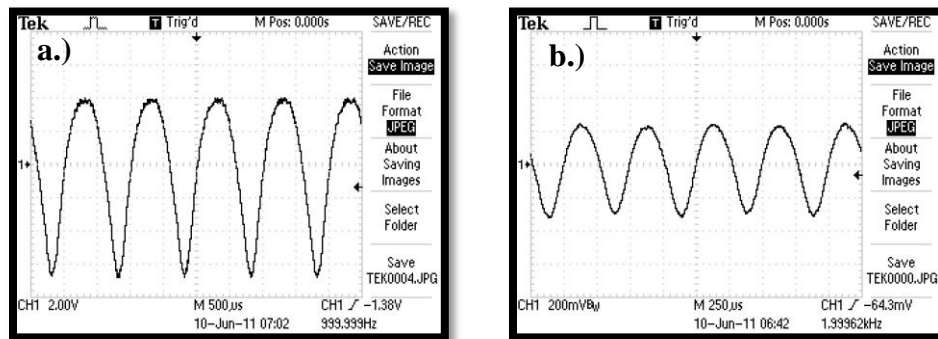


Figure D3.1: Oscilloscope recording of (a) ~ 1 kHz, $1f$, modulation signal of the 324 turn ferrite coil and (b) the $2f$ modulated signal.

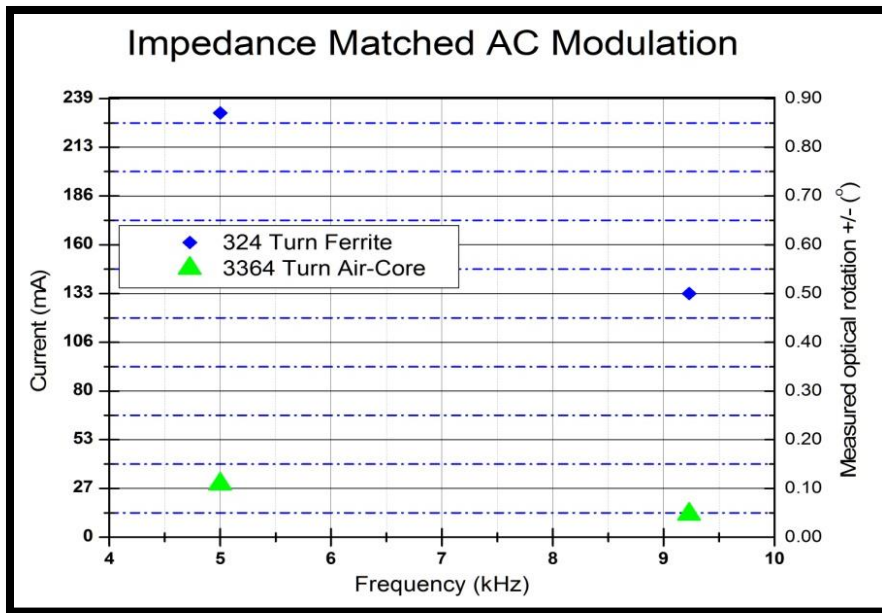


Figure D3.2: Impedance matched response with both the 324 turn ferrite and 3364 turn air-core using power amplifier polarimetric setup as described in polarized system description

APPENDIX E

PRELIMINARY EYE MODELING DATA

Utilizing CODE V, an optical model was constructed and ray trace simulations were evaluated for both 635 nm and 532 nm wavelengths, as illustrated Figure E1. In the model, a glancing angle of 16 degrees was utilized for the entrance beam. After the most suitable optical elements were determined to include in the reflective based optical coupling scheme, an optical ray trace model was constructed in Code V to evaluate the re-collimating capability of the proposed design. Initially the mirrors were placed arbitrarily in position with respect to an eye model. Then to optimize the performance of the coupling system the beam position for the individual wavelengths at the detector and the appearance of the ray traces for each wavelength were analyzed. To achieve suitable collimation of the beams at the detector the x, y, and z position and angles of the two 90 degree off-axis parabolic mirrors were varied until optimal results were obtained maximizing the overlap between the wavelengths and minimizing the change in the optical signal observed on the detector over multiple simulations. Additionally, after the optimal position parameters were determined and entered for each optical component the position of the optical elements were further modified until the results indicated an optimal ray trace of the overlapping wavelengths providing the most visually collimated output product, as shown in Figure E1 below. After the ray trace model was generated, as shown in Figure E1, the output beam profile and spot profile were evaluated over multiple runs. The sensor size was set to 3 mm x 3 mm for a 5x5 circular pattern of rays for both wavelengths. Then the beam overlay on the detector was plotted to determine if the beam shape would remain similar over multiple runs in order to fit on the surface area of commercially available optical detectors. As shown in Figures E2A and E2B the spot diagram analysis indicated the beam size remained within the 3 mm diameter detector area. Following the examination of the beam profile on the detector the optimal position was determined for each element and a CAD rendering of the ray trace starting with the entrance beam up to the rays onto the detection optics were output in STL

format. Utilizing SolidWorks a 3D model was generated of the respective ray traces for the individual wavelengths with the exported file as a reference for constructing the ray trace CAD models. Using the CODE V output ray traces and CAD models for the optical elements, a human eye model [20], and a rendering of a human face (obtained via scanning a face into a 3D representation) a model was re-constructed similar to the Code V model evaluating anthropometric constraints. Using this model it was possible to evaluate the placement of the optical elements and beam path as shown by the models in Figure 4 below. Using the exported ray traces generated in CODE V the model was then evaluated with respect to anatomical features on the human face such as the nose and corneal/sclera surface to determine if the optical model would be feasible with anatomical constraints. Figures E3A and E3B illustrate the compiled 3D model of the optical simulation provided from CODE V via multiple different viewing angles. As illustrated in Figures E3A and E3B it appears the proposed non-index matched optical coupling scheme is feasible from an anatomical and optical standpoint.

The proposed non-index coupling scheme including the input beam entering the eye at a glancing angle and 90 degree off-axis parabolic mirrors placed at the exit point of the eye were modeled in the CODE V and the ray trace for 635 nm and 532 nm wavelengths of the respective models are shown in Figures E1 through E3 below. For each optical model, the beam diameter was chosen to be circular with a diameter of approximately 1mm. This is representative of the beam diameter utilized in the system designed by our group. Additionally, a glancing angle of approximately 16 degrees was introduced between the input beam and the entrance corneal surface of the eye.

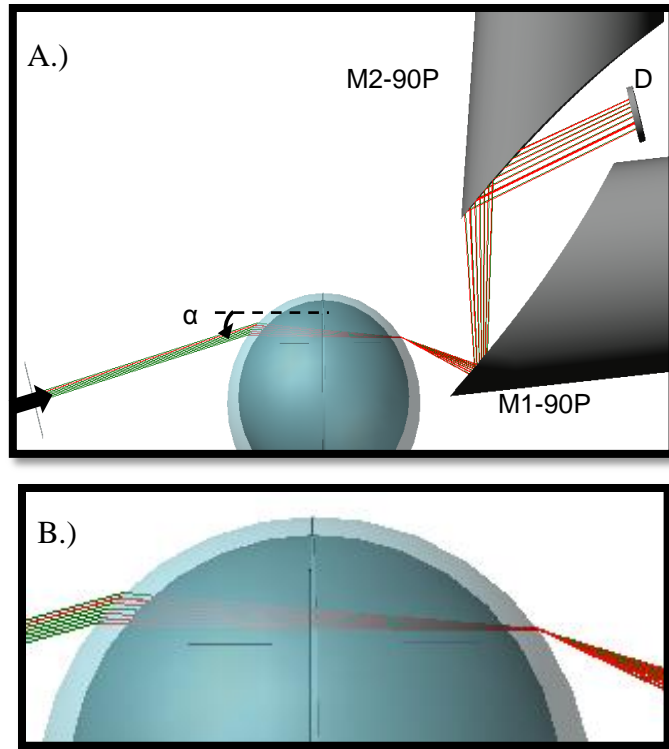


Figure E1: CODE V simulation of proposed non-index matched eye-coupling scheme (A) utilizing two 90 degree off-axis parabolic mirrors re-collimating the beam exiting the cornea in addition to a round mirror guiding the entrance beam into the cornea at a specified glancing angle and (B) close-up image of the model illustrating the ray trace change within the cornea and aqueous humor surfaces.

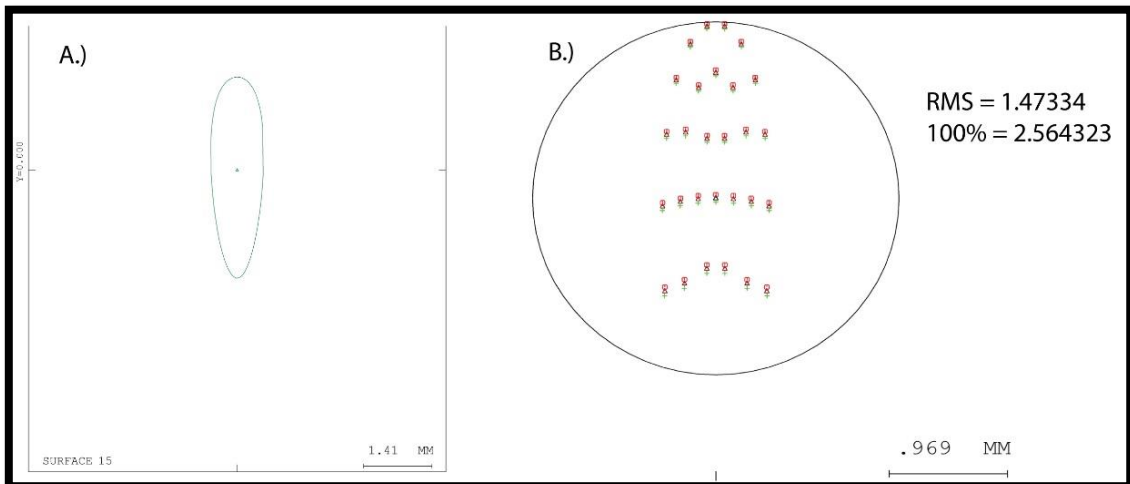


Figure E2: CODE V simulation spot ray trace simulation output at the detector for model shown in Figure D1 (A) profile showing repeatable beam shape under 3 mm x 3 mm which is the current size of the detector surface and (B) spot diagram using rays in circular pattern 5x5 rays of red and green beams with the total surface area set to 3 mm x 3 mm the detector area size.

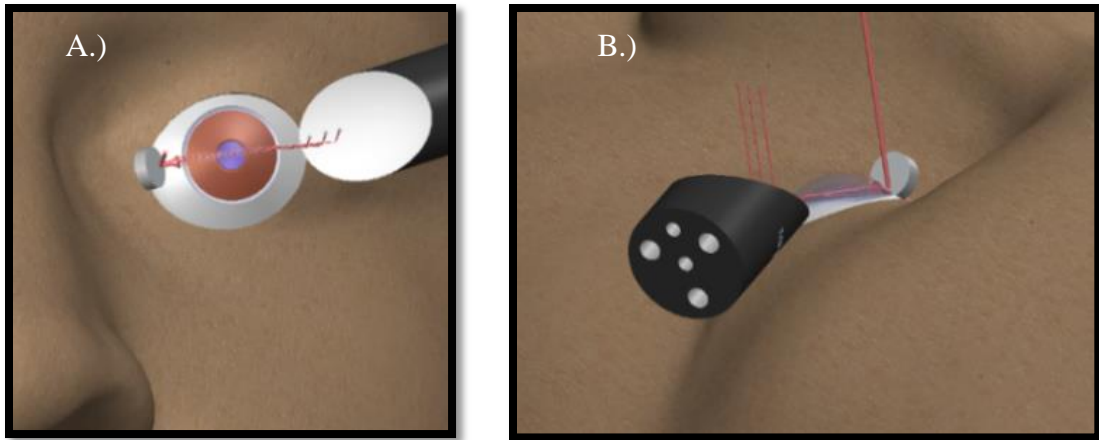


Figure E3: 3D anatomical analysis for proposed non-index matched design configuration utilizing CODE V ray trace exported in CAD format. (A) 3D rendering top view of proposed design coupled to eye with facial anatomy included and (B) additional side view of proposed setup illustrating the collimated beam profile for input and output beams.

Based on the results illustrated in Figures. 4A and 4B it appears that the proposed non-index matched coupling scheme could be achieved without being limited anatomically by the facial structure. It also appears significant room is available to modify the position of the input and output mirrors for varying anthropometric requirements that exist between people.

APPENDIX F

ZEMAX EYE MODELING

The design consisted of two round mirrors guiding the input beam into the eye at a glancing angle and two 90-degree off-axis parabolic mirrors collecting and re-collimating the beam output from the eye. All optical parameters included in the models were downloaded from THORLABS for each of the mirrors in the setup. The eye model described by our group previously was then imported into Zemax and the optical parameters were designated as described above. The position of each optical element was then optimized to provide the most consistent and collimated beam profile at the point of detection. Figure F4A is a screen capture of the optical simulation design in Zemax for the non-index matched design. Figure F4B represents a modeled image of the beam pattern at the detector for both wavelengths over multiple simulated runs.

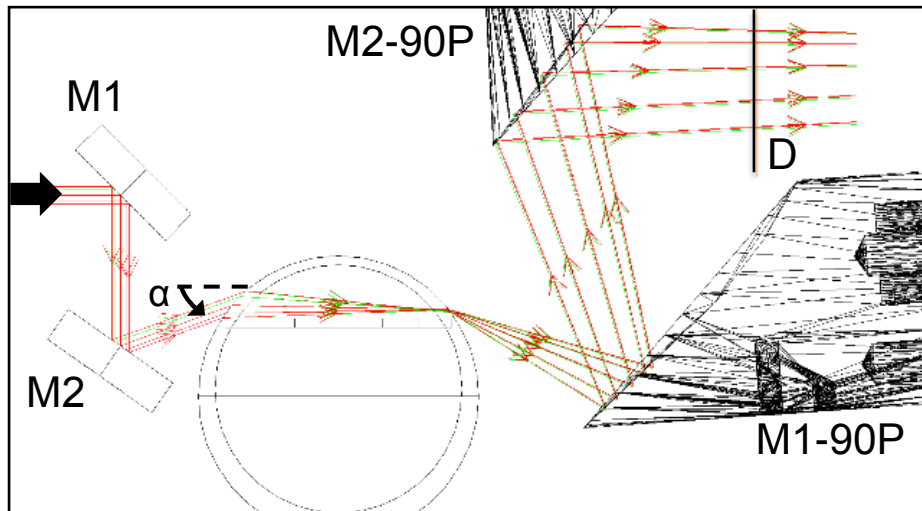


Figure F1: Zemax simulation of proposed non-index matched eye-coupling scheme utilizing two 90 degree off-axis parabolic mirrors re-collimating the beam exiting the cornea in addition to a round mirror guiding the entrance beam into the cornea at a specified glancing angle.

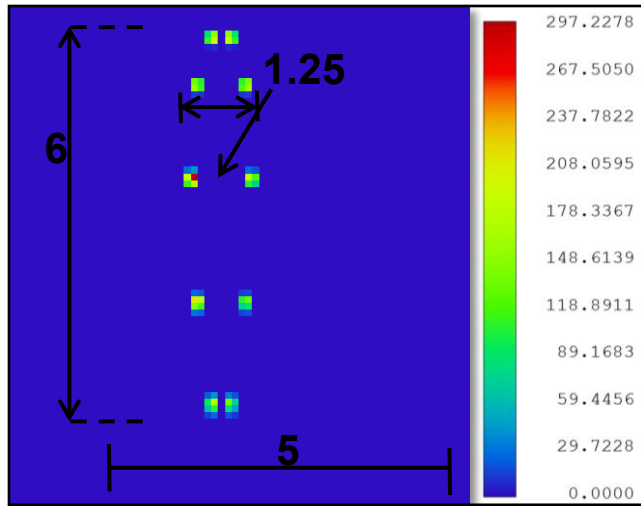


Figure F2: Zemax simulation spot ray trace simulation output at the detector for model shown in Figure E1 profile showing repeatable beam shape under 6 mm x 5 mm which is the current size of the detector surface.

Glancing angle (α): 16°
 Beam Width (mm): 1 x 1
 Wavelengths (nm): 635 & 532
 # of rays: 5 x 2

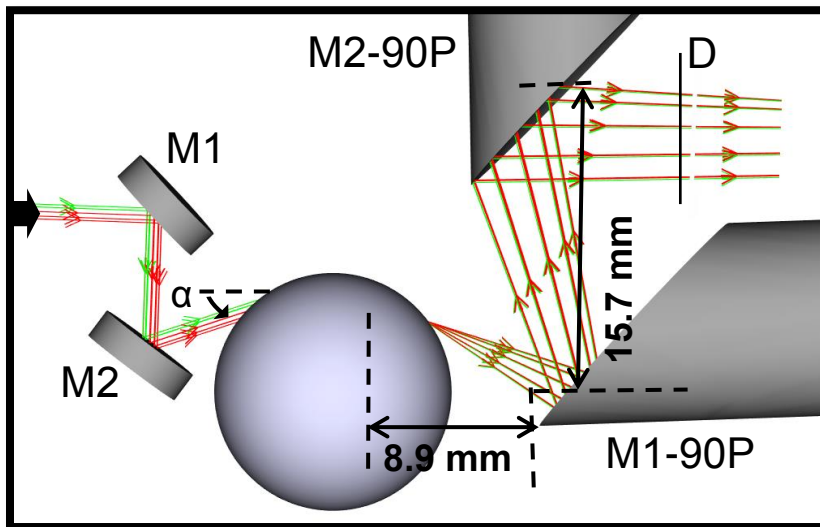


Figure F3: Zemax simulation of proposed non-index matched eye-coupling scheme utilizing two 90 degree off-axis parabolic mirrors re-collimating the beam exiting the cornea in addition to a round mirror guiding the entrance beam into the cornea at a specified glancing angle where, M1 & M2 are round mirrors; α is glancing angle of input beam; M1-90P & M2-90P are 90 degree off-axis parabolic mirrors; and D is detector.

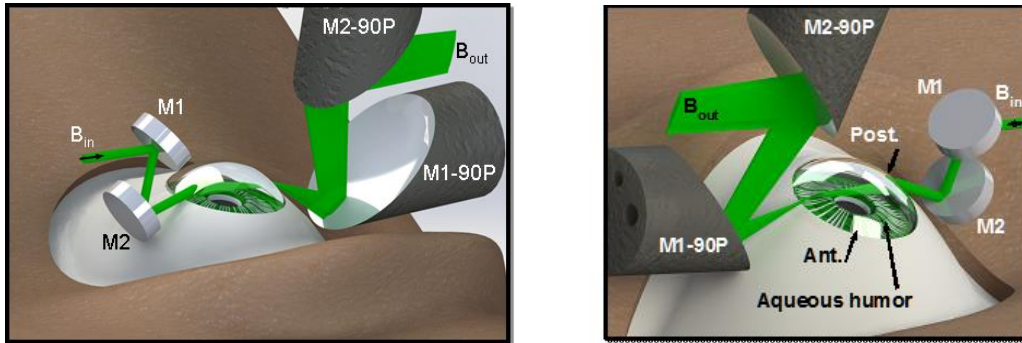


Figure F4: (A) Zemax simulation of proposed non-index matched eye-coupling scheme utilizing two 90 degree off-axis parabolic mirrors re-collimating the beam exiting the cornea in addition to two round mirrors guiding the entrance beam into the cornea at a specified glancing angle and (B) the beam profile at the detector for an optimized setup configuration. Multiple simulation runs were conducted and minimal change in the profile was observed.

APPENDIX G

LABVIEW FPGA CONTROL

For near real-time measurement and PID closed-loop response of the glucose polarimeter design described in Chapters 2-4 below, an FPGA based LabVIEW PID control program was constructed to control the feedback provided to the Faraday Compensators in the system. A screen capture of the block diagram for the FPGA LabVIEW PID controller is illustrated below in addition to the user interface for the VI.

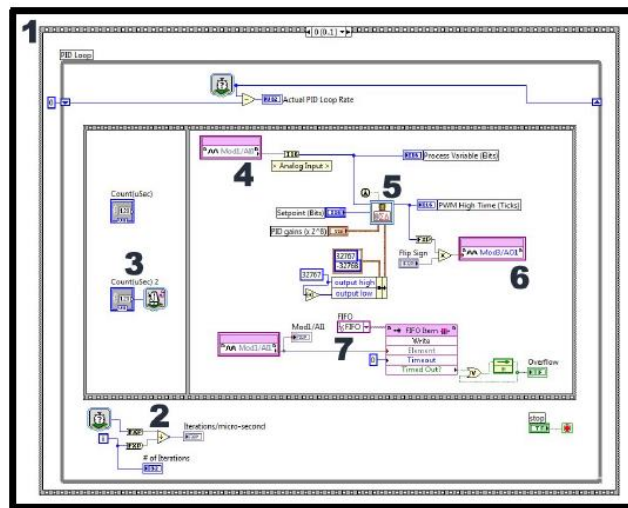


Figure G1: A screen capture of the block diagram for the FPGA LabVIEW PID controller is illustrated below in addition to the user interface for the VI.

The section marked (1) in the block diagram above marks a stacked sequence containing two frames. One frame is the diagram displayed above and the second sequence is a re-initialization control re-setting the DAQ output voltages to zero prior to stopping the VI. In the VI the PID control is implemented in a while loop design. The program design marked with 2 in the image above is used in the VI to keep track of the number of iterations that are cycled of the while loop in addition to keeping track of the amount of time the while loop is running. By dividing the values, the rate the VI is running and is displayed on the front panel.

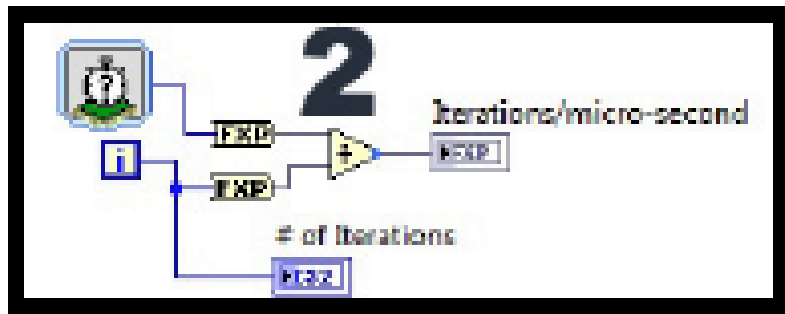


Figure G2: (A screen capture of the block diagram for the FPGA LabVIEW PID controller. Area marked with 2 in the image above is used in the VI to keep track of the number of iterations that are cycled of the while loop in addition to keeping track of the amount of time the while loop is running.

Once the PID VI is initiated, the section marked (3) in the diagram above is a timer implemented to allow the user control over the amount of wait time between executing the next sequence, regulating the rate of the overall VI. Sections (4), (5), and (6) in the block diagram represent the PID loop on the FPGA side. The Analog Input from the cRio expansion chassis is illustrated by the box in the block diagram just above the section 4 label. Using analog inputs (1) and (2) from the cRio chassis module, the signal from the photodiodes in the polarimetric system are collected and processed with the VI. The signal from the photodiode represents the process variable component of the closed-loop feedback control within the system.

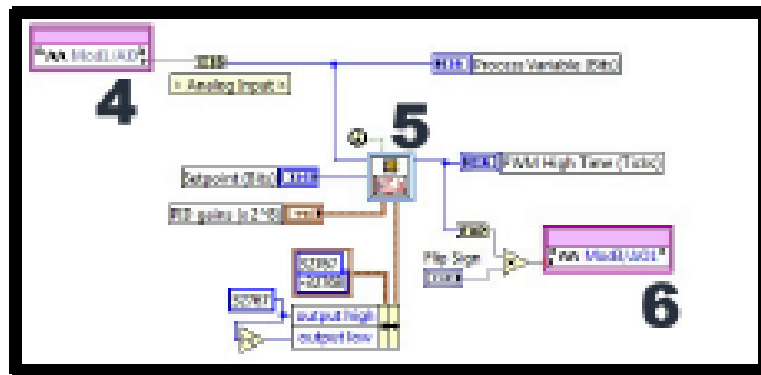


Figure G3: (A screen capture of the block diagram for the FPGA LabVIEW PID controller. Sections 4, 5, and 6 in the block diagram represent the PID loop on the FPGA side is illustrated below in addition to the user interface for the VI.

Section (5) represents the PID FPGA VI provided by National Instruments. The modifiable parameters of the PID system which include; PID gains, setpoint values to which the lasers are maintained and the output range, and the output itself are shown in the block diagram. Further, the output value from the PID VI (represented by (6) in the block diagram) is the input provided to the optical polarimeter Faraday compensators. Prior to generating the specified rotation in the system the voltage is generated by the third Module Analog Output (1) and then supplied to a gain circuit followed by the Faraday Compensators. In addition to the PID control and feedback voltage generation the VI also collects the output value specified and the system time it was specified and stores the values in an output file through the section marked (7) in the block diagram. Data collection and output occurs through implementation of a FIFO output methodology.

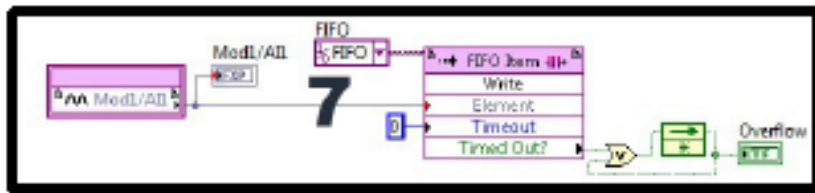


Figure G4: (A screen capture of the block diagram for the FPGA LabVIEW PID controller. Section marked 7 in the block diagram. Data collection and output occurs through implementation of a FIFO output methodology.

The front panel for the FPGA VI is shown below in Figure G5. Section (1) indicated in the front panel VI is an indicator for the speed the VI is operating at in iterations/microsecond, controlled by part (2) of the block diagram. Directly below this indicator is a control where the user can specify the loop time found in part 3 of the block diagram. The indicator labeled (2) in the front panel of the FPGA represents the component of the closed-loop feedback control that requires adjusting, which in this project is the polarization angle measured at the detector after traversing a sample. The determined output voltage required by the cRio module to maintain the specified setpoint of the control system is presented in the indicator field marked with the number

(3). For tuning the PID controller for optimal response profile and speed the gain values are adjusted by the user, shown in section 4 on front panel.

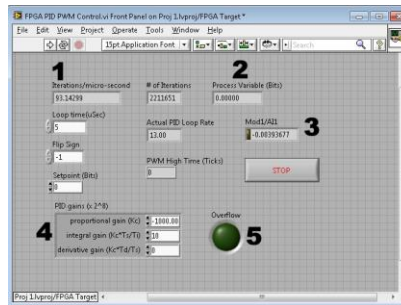


Figure G5: A screen capture of the front panel for the FPGA VI.

The block diagram and front panel schematic for the host PC PID control VI is shown in Figures G6 and G7 below. The section marked (1) in the block diagram is used to connect this VI with the FPGA VI and cRio chassis. This section opens a reference to the FPGA VI, initializes important variable values of the loop, and then runs the FPGA VI embedded on the cRio device. The bulk of the host PC VI function is shown in the section marked (2) on the block diagram. This section allows the user to specify changes in the PID parameters in real-time during operation of the PID controller. The second function of the host VI is illustrated in section (3) on the block diagram. This portion of the VI takes the data acquired from FPGA modules, organizes the data into a desired output format and generates the output file containing the PID feedback values calculated by the PID controller.

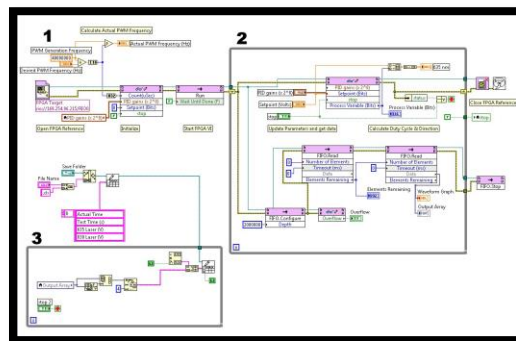


Figure G6: A screen capture of the block diagram schematic for the host PC PID control VI.

The front panel of the VI is shown in Figure G7. To tune the PID gain settings in real-time while operating the VI the user can vary the control boxes in section (1) of the front panel. The path specified in section (2) of the front panel and file name provided in the control box specify the path and filename for the output data file for the PID controller. A graph of the process variable and desired set-point are plotted in section (3). The frequency control specified in section (5) determines the duration the output voltage is supplied via the cRio module. The indicators on the front panel in section (6) provide real-time values for the operating frequency, output voltages, and the remaining number of elements that need to be written to the host PC.



Figure G7: A screen capture of the front panel schematic for the host PC PID control VI.

For the dual-wavelength polarimeter setup the diagram shown above was essentially duplicated allowing for two PID loops to run simultaneously, for the respective wavelengths lasers in the system.